1. Report No.	2. Government Accession No.	3. Recipient's Catalog No.
FHWA/TX-07/ 0-4759-1		

4. Title and Subtitle	5. Report Date
Rational Shear Provisions for AASHTO LRFD Specifications: TECHNICAL REPORT	October 2006 Published: January 2007
	6. Performing Organization Code

7. Author(s)	8. Performing Organization Report No.
Arghadeep Laskar, Jun Wang, Thomas T. C. Hsu, and Y. L. Mo	Report 0-4759-1

9. Performing Organization Name and Address	10. Work Unit No. (TRAIS)
Department of Civil & Environmental Engineering Cullen College of Engineering University of Houston Houston, TX 77204-4003	11. Contract or Grant No. Project 0-4759

12. Sponsoring Agency Name and Address	13. Type of Report and Period Covered
Texas Department of Transportation Research and Technology Implementation Office P. O. Box 5080 Austin, Texas 78763-5080	Technical Report: September 2003 – August 2006
	14. Sponsoring Agency Code

15. Supplementary Notes

Project performed in cooperation with the Texas Department of Transportation and the Federal Highway Administration
Project title: Rational Shear Provisions for AASHTO LRFD Specifications
URL: http:// www.egr.uh.edu/structurallab/

16. Abstract

Prestressed concrete I-beams are used extensively as the primary superstructure components in Texas highway bridges. This research intends to solve one of the most troublesome problems in prestressed concrete, namely shear. The problem arises from the lack of a rational model to predict the behavior of prestressed concrete structures under shear action and the various modes of shear failures. Because of this deficiency, all the guidelines for shear design, such as ACI Codes and AASHTO Specifications, are empirical and have severe limitations.

The research work was divided into two phases: **Phase One** consisted of developing the constitutive laws for prestressed concrete membrane elements and developing an analytical model for predicting the shear behavior of such elements. Crack simulation tests were first performed on rectangular prestressed beams to find the same cracking pattern of post-tensioned concrete with conduits as that in pre-tensioned concrete without conduits. Ten prestressed concrete panels (two series of five panels each) were tested. The first series of five panels was tested under sequential loading. The results of these tests were used to establish the constitutive relationships of materials (concrete and prestressing tendons). The second series of panels was tested under pure shear (a special case of proportional loading) to study the shear behavior of prestressed concrete membrane elements. Finally the Softened Membrane Model for Prestressed Concrete (SMM-PC) was developed to predict the response of prestressed concrete membrane elements under shear loading.

Phase Two of the research dealt with testing of full-scale prestressed concreted I-beams and developing a new simplified equation for the shear design of prestressed concrete girders. Five TxDOT Type-A beams were designed, cast and tested to study their behavior in web shear and flexural shear failures. The results of these tests, along with the constitutive laws of prestressed concrete (developed in Phase One), were used to develop a new simplified equation for shear design of prestressed girders. Results of other prestressed beams available in literature were also considered to validate the design equation. The shear capacities of all the tested and referred beams were obtained using the new design equation and compared with the shear capacities obtained using ACI and AASHTO guidelines. Four design examples were prepared to illustrate the application of the new equation for design of prestressed girders. The new design equation was thereby extended to include non-prestressed girders. An example showing the design of a non-prestressed girder using the new equation was also completed.

The research findings proved that the shear capacities of prestressed beams depended mainly on the compressive strength of concrete and the shear span to depth ratio of the beams. The effect of the amount of prestressing force and the angle of the failure planes of the beams on their shear capacities is insignificant.

17. Key Words	18. Distribution Statement
Beams, Constitutive Laws, Shear Provisions, Prestressed Concrete, Membrane Elements, Full-Scale Tests, Design Equation	No restrictions. This document is available to the public through NTIS: National Technical Information Service Springfield, Virginia 22161. www.ntis.gov and University of Houston, Houston, Texas 77204 www.egr.uh.edu/structurallab/

19. Security Classif.(of this report)	20. Security Classif.(of this page)	21. No. of Pages	22. Price
Unclassified	Unclassified	216	

Rational Shear Provisions for AASHTO LRFD Specifications: Technical Report

by

Arghadeep Laskar
Research Assistant

Jun Wang
Research Assistant

Thomas T. C. Hsu
Moores Professor

and

Y. L. Mo
Professor

Report 0-4759-1
Project 0-4759
Project Title: Rational Shear Provisions for AASHTO LRFD Specifications

Performed in cooperation with the
Texas Department of Transportation
and the
Federal Highway Administration

October 2006
Published: January 2007

Department of Civil and Environmental Engineering

University of Houston

Houston, Texas

DISCLAIMER

This research was performed in cooperation with the Texas Department of Transportation and the U.S. Department of Transportation, Federal Highway Administration. The contents of this report reflect the views of the authors, who are responsible for the facts and accuracy of the data presented herein. The contents do not necessarily reflect the official view or policies of the FHWA or TxDOT. This report does not constitute a standard, specification, or regulation, nor is it intended for construction, bidding, or permit purposes. Trade names were used solely for information and not product endorsement.

ACKNOWLEDGEMENTS

This research, Project 0-4759, was conducted in cooperation with the Texas Department of Transportation and the U.S. Department of Transportation, Federal Highway Administration. The project monitoring committee consisted of J. C. Liu (Program Coordinator), Jon Holt (Project Director), Tim Bradberry (Project Advisor), Amy Eskridge (Project Advisor), Mark Holt (Project Advisor), John Vogel (Project Advisor), and Tom Yarbrough (Project Advisor).

The researchers would like to thank the Texas Concrete Company, Victoria, Texas, for continued co-operation during this project. The researchers are grateful to Chaparrel Steel Co. of Midlothian, Texas, for supplying the steel bars for this research.

TABLE OF CONTENTS

Page

CHAPTER 1 Introduction 1
1.1 Overview of Research 1
1.2 Objectives of Research 4
1.3 Outline of Report 4

PART I: PRESTRESSED CONCRETE ELEMENTS

CHAPTER 2 Backgrounds on Shear Theories of Reinforced and Prestressed Concrete Panels 9
2.1 Introduction 9
2.2 Shear Theories of Reinforced Concrete in Literature 9
2.3 Previous Studies by Research Group at UH 12
2.3.1 Rotating-Angle Softened Truss Model (RA-STM) 15
2.3.2 Fixed-Angle Softened Truss Model (FA-STM) 17
2.3.3 Softened Membrane Model (SMM) 20
2.4 Literature Survey on Shear Behavior of Prestressed Concrete Panels 27

CHAPTER 3 Crack Simulation Tests 29
3.1 General Description 29
3.2 Test Program 31
3.3 Test Specimens 33
3.3.1 Fabrication of Specimens 33
3.3.2 Tendon Jacking System 37
3.4 Materials 40
3.4.1 Concrete 40
3.4.2 Reinforcements 40
3.5 Loading Procedure 42
3.6 Test Results 42
3.7 Conclusions 46

CHAPTER 4 Prestressed Concrete 0-deg Panels Under Sequential Loading 47
4.1 Test Program (Group TE) 47
4.2 Test Specimens (Group TE) 48
4.2.1 Layout of Specimens 48
4.2.2 Fabrication of Specimens 53
4.2.3 Tendon Jacking System 56
4.3 Materials (Group TE) 56
4.3.1 Concrete 56
4.3.2 Reinforcements 57
4.4 Loading Procedure (Group TE) 57
4.5 General Behavior of Test Panels in Group TE 58
4.5.1 Applied Tensile Stress-Strain Relationships 59
4.5.2 Applied Compressive Stress-Strain Relationships 61
4.6 Smeared (Average) Stress-Strain Relationships of Concrete in Tension 62
4.6.1 Decompression 62

4.6.2 Post-Decompression Behavior 65
4.6.3 Mathematical Modeling of Smeared (Average) Stress-Strain Curve of Concrete in Tension 65
4.7 Smeared (Average) Stress-Strain Relationships of Prestressing Tendons Embedded in Concrete 71
4.8 Smeared (Average) Stress-Strain Relationships of Concrete in Compression 76

CHAPTER 5 Prestressed Concrete 45-deg Panels Under Pure Shear (Proportional Loading) 83
5.1 Test Program (Group TA) 83
5.2 Test Specimens (Group TA) 84
5.2.1 Layout of Specimens 84
5.2.2 Fabrication of Specimens 87
5.2.3 Tendon Jacking System 90
5.3 Materials (Group TA) 92
5.3.1 Concrete 92
5.3.2 Reinforcements 92
5.4 Loading Procedure (Group TA) 93
5.5 General Behavior of Test Panels in Group TA 94
5.5.1 Cracking Behavior 94
5.5.2 Yielding of Steel 95
5.5.3 Shear Stress vs. Shear Strain Relationships ($\tau_{\ell t} - \gamma_{\ell t}$ Curves) 97
5.5.4 Shear Stress vs. Principal Tensile Strain Relationships ($\tau_{\ell t} - \varepsilon_1$ Curves) 98
5.5.5 Shear Stress vs. Principal Compressive Strain Relationships ($\tau_{\ell t} - \varepsilon_2$ Curves) 100
5.6 Smeared (Average) Stress-Strain Relationships of Concrete in Compression 102
5.6.1 Experimental Curves for Prestressed Concrete 102
5.6.2 Mathematical Modeling of Smeared (Average) Stress-Strain Curve of Prestressed Concrete in Compression 105

CHAPTER 6 Analytical Models of Prestressed Concrete Panels 115
6.1 Introduction 115
6.2 Fundamentals of Softened Membrane Model for Prestressed Concrete 115
6.2.1 Equilibrium and Compatibility Equations 116
6.2.2 Biaxial Strains vs. Uniaxial Strains 117
6.2.3 Constitutive Relationships of Concrete in Prestressed Elements 118
6.2.4 Constitutive Relationships of Reinforcements 120
6.2.5 Solution Algorithm 121
6.3 Applications of SMM-PC to Test Panels TA-1 to TA-5 124

PART II: SHEAR IN PRESTRESSED CONCRETE BEAMS

CHAPTER 7 Shear Tests of Prestressed Concrete Beams 129
7.1 Introduction 129
7.2 Test Program 129
7.3 Test Specimens 135

7.4 Manufacturing of Test Specimens 138
7.5 Test Setup 140
7.6 Test Results 145

CHAPTER 8 Analysis of Prestressed Beams 149
8.1 Flexural Analysis 149
8.2 Shear Analysis 150
8.2.1 Analytical Model 150
8.2.2 V_c and V_s terms in the Analytical Model 153

CHAPTER 9 Shear Design of Prestressed Beams 155
9.1 Design Method 155
9.2 Shear Capacities of Beams According to ACI and AASHTO Provisions 161
9.3 Design Examples for Prestressed Beams 165
9.3.1 Example 1 165
9.3.2 Example 2 167
9.3.3 Example 3 170
9.3.4 Example 4 172
9.4 Shear Design of Non-prestressed Beams 174
9.4.1 Design Example for Non-Prestressed T-Beam 174

CHAPTER 10 Conclusions and Suggestions 179
10.1 Conclusions 179
10.2 Suggestions 180

References 181

Appendix: Recommendations for Shear Design of Prestressed and Non-prestressed Bridge Girders 185

LIST OF FIGURES

Page

Fig. 1.1.1 Three Types of Bridge Girders 3
(a) I-Girder 3
(b) Box Girder 3
(c) Trapezoidal Girder 3
(d) Web Element 3
Fig. 1.1.2 Shear Failure Modes and Shear Panel Elements 3
(a) Girder Test 3
(b) Panel Test 3
Fig. 2.3.1 Reinforced Concrete Membrane Elements Subjected to In-Plane Stresses 14
(a) Reinforced Concrete 14
(b) Concrete 14
(c) Reinforcement 14
(d) Principal Axes 1-2 for Applied Stresses 14
(e) Principal Axes r-d for Stresses on Concrete 14
(f) Assumed Crack Direction in Fixed-Angle Model 14
(g) Assumed Crack Direction in Rotating-Angle Model 14
Fig. 2.3.2 Constitutive Laws of Concrete in Tension and Compression 24
Fig. 2.3.3 Constitutive Law of Steel Bars 25
Fig. 2.3.4 Flow Chart of Solution Procedure for Softened Membrane Model 26
Fig. 3.1.1 Arrangement of Reinforcement in Trial Panel TE-2 30
Fig. 3.1.2 Crack Pattern of Trial Panel TE-2 at 2% Tensile Strain 31
Fig. 3.3.1 Formwork for Crack Simulation Tests (TSB1 to TSB5) 34
Fig. 3.3.2 Formwork for Crack Simulation Tests (TSB6 to TSB10) 34
Fig. 3.3.3 Dimensions of U-Shape Inserts (Unit: in.) 36
(a) Perspective View 36
(b) Top View 36
(c) Side View 36
Fig. 3.3.4 Specimens after Casting Concrete 37
Fig. 3.3.5 Tendon Jacking System 39
Fig. 3.4.1 Stress-Strain Curve of Bare Strands 41
Fig. 3.5.1 Test Setup for a Typical Specimen 42
Fig. 3.6.1 Crack Patterns of Specimens TSB2 and TSB3 43
(a) TSB2-North 43
(b) TSB3-North 43
Fig. 3.6.2 Crack Patterns of Specimens TSB6 and TSB8 44
(a) TSB6-South 44
(b) TSB8-South 44
Fig. 4.2.1 Steel Layout and Dimensions of Test Panels in Group TE 50
(a) Steel Layout and Dimensions of Panels TE-4, 3, and 5 50
(b) Steel Layout and Dimensions of Panel TE-6 51
(c) Steel Layout and Dimensions of Panel TE-7 52
Fig. 4.2.2 Formworks of Panels in Group TE 54
(a) Formwork of Panel TE-4 54

(b) Formwork of Panel TE-6 54
(c) Formwork of Panel TE-7 55
Fig. 4.2.3 Special Steel Jig 55
Fig. 4.3.1 Typical Stress-Strain Curve from Concrete Cylinder Compression Test 57
Fig. 4.4.1 Sequential Loading Path used in Group TE 58
Fig. 4.5.1 $\sigma_1 - \varepsilon_1$ Relationships of Panels TE-4, 3, and 5 60
Fig. 4.5.2 $\sigma_1 - \varepsilon_1$ Relationships of Panels TE-6, 3, and 7 60
Fig. 4.5.3 $\sigma_2 - \varepsilon_2$ Relationships of Panels TE-4, 3, and 5 61
Fig. 4.5.4 $\sigma_2 - \varepsilon_2$ Relationships of Panels TE-6, 3, and 7 62
Fig. 4.6.1 Experimental $\sigma_c - \bar{\varepsilon}_c$ Relationships of Concrete in Decompression 64
Fig. 4.6.2 Experimental Smeared (Average) Tensile Stress-Strain Curves of Concrete 65
Fig. 4.6.3 Smeared Stress-Strain Relationships of Concrete in Tension 67
Fig. 4.6.4 Smeared (Average) Stress-Strain Relationships of Concrete in Tension (TE-3) 68
Fig. 4.6.5 Smeared (Average) Stress-Strain Relationships of Concrete in Tension (TE-4) 69
Fig. 4.6.6 Smeared (Average) Stress-Strain Relationships of Concrete in Tension (TE-5) 69
Fig. 4.6.7 Smeared (Average) Stress-Strain Relationships of Concrete in Tension (TE-6) 70
Fig. 4.6.8 Smeared (Average) Stress-Strain Relationships of Concrete in Tension (TE-7) 70
Fig. 4.7.1 Comparison of Experimental Stress-Strain Curve of Prestressing Tendons Embedded in Concrete in Panel TE-4 with that of Bare Strands 72
Fig. 4.7.2 Comparison of Theoretical Smeared (Average) Stress-Strain Curve of Prestressing Tendons with Experimental Curve for Panel TE-4 74
Fig. 4.7.3 Comparison of Theoretical Smeared (Average) Stress-Strain Curve of Prestressing Tendons with Experimental Curve for Panel TE-3 74
Fig. 4.7.4 Comparison of Theoretical Smeared (Average) Stress-Strain Curve of Prestressing Tendons with Experimental Curve for Panel TE-5 75
Fig. 4.7.5 Comparison of Theoretical Smeared (Average) Stress-Strain Curve of Prestressing Tendons with Experimental Curve for Panel TE-6 75
Fig. 4.7.6 Comparison of Theoretical Smeared (Average) Stress-Strain Curve of Prestressing Tendons with Experimental Curve for Panel TE-7 76
Fig. 4.8.1 Smeared (Average) Stress-Strain Relationships of Concrete in Compression in Panels TE-4, 3, and 5 77

Fig. 4.8.2 Smeared (Average) Stress-Strain Relationships of Concrete in Compression in Panels TE-6, 3, and 7 78
Fig. 4.8.3 Crack Pattern of Panel TE-6 81
Fig. 4.8.4 Crack Pattern of Panel TE-3 81
Fig. 5.2.1 Steel Layout and Dimensions of Test Panels in Group TA 85
(a) Steel Layout and Dimensions of Panels TA-1, 2, 3, and 4 85
(b) Steel Layout and Dimensions of Panel TE-5 86
Fig. 5.2.2 Dimensions of V-Shape Inserts (Unit: in.) 88
(a) Perspective View 88
(b) Top View 88
(c) Bearing Plate 88
Fig. 5.2.3 Formworks of Panels in Group TA 89
(a) Formwork of Panel TA-3 89
(b) Formwork of Panel TA-5 89
Fig. 5.2.4 Tendon Jacking System for Panels in Group TA 91
(a) Setup of Pulling End 91
(b) Details of Supporting Chair 91
Fig. 5.3.1 Stress-Strain Curves of Bare Steel Bars 93
Fig. 5.4.1 Proportional Loading Path used in Group TA 94
Fig. 5.5.1 Shear Stress-Strain Curves of Panels TA-1, 2, and 3 96
Fig. 5.5.2 Shear Stress-Strain Curves of Panels TA-2, 4, and 5 96
Fig. 5.5.3 Shear Stress vs. Principal Tensile Strain Curves of Panels TA-1, 2, and 3 99
Fig. 5.5.4 Shear Stress vs. Principal Tensile Strain Curves of Panels TA-2, 4, and 5 100
Fig. 5.5.5 Shear Stress vs. Principal Compressive Strain Curves of Panels TA-1, 2, and 3 101
Fig. 5.5.6 Shear Stress vs. Principal Compressive Strain Curves of Panels TA-2, 4, and 5 102
Fig. 5.6.1 Experimental Concrete Compressive Stress-Strain Curves of Panels TA-1, 2, and 3 104
Fig. 5.6.2 Experimental Concrete Compressive Stress-Strain Curves of Panels TA-2, 4, and 5 104
Fig. 5.6.3 Constitutive Laws of Concrete in Compression 106
Fig. 5.6.4 $f(\beta)$ versus β Relationships for Reinforced and Prestressed Concrete Panels 108
Fig. 5.6.5 W_p versus β Relationships for Prestressed Concrete Panels 110
Fig. 5.6.6 Comparison of SMM-PC predicted Concrete Compressive Stress-Strain Curves with Experimental Data of Panels TA-1 to TA-5 111
Fig. 6.2.1 Coordinate System in a Prestressed Concrete Membrane Element 116
(a) Prestressed Concrete 116
(b) Concrete 116
(c) Reinforcement 116
(d) Prestressed Concrete Element 116
(e) Principal Coordinate 2-1 for Applied Stresses 116

Fig. 6.2.2 Flow Chart of Solution Procedure for SMM-PC 123
Fig. 6.3.1 Applied Shear Stress $\tau_{\ell t}$ versus Shear Strain $\gamma_{\ell t}$ of Panel TA-1 124
Fig. 6.3.2 Applied Shear Stress $\tau_{\ell t}$ versus Shear Strain $\gamma_{\ell t}$ of Panel TA-2 125
Fig. 6.3.3 Applied Shear Stress $\tau_{\ell t}$ versus Shear Strain $\gamma_{\ell t}$ of Panel TA-3 125
Fig. 6.3.4 Applied Shear Stress $\tau_{\ell t}$ versus Shear Strain $\gamma_{\ell t}$ of Panel TA-4 126
Fig. 6.3.5 Applied Shear Stress $\tau_{\ell t}$ versus Shear Strain $\gamma_{\ell t}$ of Panel TA-5 126
Fig. 7.2.1 Cross Section of Type-A Beams 131
(a) Cross Section of Beams B1, B2, and B4 131
(b) Cross Section of Beams B3 and B5 132
Fig. 7.2.2 Elevation and Reinforcement Details of Beam B1 133
Fig. 7.2.3 Elevation and Reinforcement Details of Beams B2 and B3 133
Fig. 7.2.4 Elevation and Reinforcement Details of Beams B4 and B5 134
Fig. 7.3.1 Reinforcement and Instrumentation Details of Beams B1, B2, and B3 (Web Shear Specimens) 135
(a) Beam B1 135
(b) Beam B2 136
(c) Beam B3 136
Fig. 7.3.2 Reinforcement and Instrumentation Details of Beams B4 and B5 (Flexural Shear Specimens) 137
(a) Beam B4 137
(b) Beam B5 137
Fig. 7.4.1 Casting of Test Specimens 138
(a) Concrete Placed in Beam B4 by a Hopper 138
(b) Compaction using Needle Vibrators in Beam B4 139
(c) Removal of Anchors of Hold-down Rod from Beam B3 139
Fig. 7.5.1 Test Setup 140
Fig. 7.5.2 Loading Positions of Beams 142
(a) Loading Point and LVDT Locations for Beams B1, B2, and B3 142
(b) Loading Point and LVDT Locations for Beams B4 and B5 142
Fig. 7.5.3 LVDT Setup on Beam B4 143
Fig. 7.5.4 Location of Strain Gages on L Bars in Beam B1 144
Fig. 7.5.5 Location of Strain Gages on R Bars in Beams B2 and B3 144
Fig. 7.5.6 Location of Strain Gages on L Bars in Beams B4 and B5 145
Fig. 7.5.7 Tracking and Measuring Shear Cracks on the Web of Beam B4 145
Fig. 7.6.1 Load Deformation Curves of the Specimens B1 to B5 147
Fig. 8.2.1 Analytical Model used for Calculating Web Shear Capacities of Beams 150
Fig. 8.2.2 Variation of Normalized Concrete Shear of Beams Tested in Web Shear 154
Fig. 8.2.3 Determination of Number of Stirrups for "Contribution of Steel" V_s 154
(a) Average Spacing Method 154
(b) Minimum Shear Resistance Method 154
Fig. 9.1.1 Details of Beams Tested by Other Researchers 156
(a) Cross Section of Beams Tested by Lyngberg 156
(b) Elevation of Beams Tested by Lyngberg 156
(c) Cross Section of Beams Tested by Rangan 157

(d) Elevation of Beams Tested by Rangan 157
(e) Details of CI Specimens Tested by Elzanaty 158
(f) Details of CW Specimens Tested by Elzanaty 158
Fig. 9.1.2 Variation of Normalized Concrete Shear with a/d 159
Fig. 9.1.3 Variation of Normalized Ultimate Shear Capacities of Beams with a/d 160
Fig. 9.3.1 Layout of Girders and Roadway Slab considered in Design Examples 165
Fig. 9.3.2 Dimensional Details of Beam and Overlaying Slab 165

LIST OF TABLES

Page

Table 3.2.1 Variables of 10 Specimens 32
Table 3.4.1 Mechanical Properties of Steel Bars 41
Table 3.6.1 Average Crack Spacing of 10 Specimens 45
Table 4.1.1 Two Variables of Test Panels in Group TE 48
Table 4.8.1 Experimental Softening Coefficients 79
Table 4.8.2 Comparison of Experimental Softening Coefficients with Analytical Model 80
Table 5.1.1 Principal Variables of Test Panels in Group TA 84
Table 5.3.1 Mechanical Properties of Steel Bars 92
Table 5.6.1 Calculation of β and $f(\beta)$ for Prestressed Concrete Panels 107
Table 5.6.2 Calculation of W_p for Prestressed Concrete Panels 109
Table 7.2.1 Test Specimens 130
Table 7.6.1 Failure Loads of Beams 146
Table 7.6.2 Experimental Ultimate Strains in Specimens B1 to B5 measured by LVDTs 147
Table 7.6.3 Experimental Ultimate Strains in Strain Gages for Specimens B1 to B5 148
Table 8.2.1 Angles of Failure Planes Corresponding to Beam Shear Capacities as per Model 153
Table 8.2.2 Normalized Concrete Shear Contributions of Beams B1 through B3 154
Table 9.2.1 Comparison of Test Results for UH Specimens 162
Table 9.2.2 Comparison of Test Results for Lyngberg's Specimens 162
Table 9.2.3 Comparison of Test Results for Rangan's Specimens 163
Table 9.2.4 Comparison of Test Results for Elzanaty's Specimens 164
Table 9.3.1 Beam Design 1 167
Table 9.3.2 Beam Design 2 169
Table 9.3.3 Beam Design 3 172
Table 9.3.4 Beam Design 4 174
Table 9.4.1 Design of Non-Prestressed Beam 177

NOTATIONS

1	=	direction of applied principal tensile stress
2	=	direction of applied principal compressive stress
a	=	shear span of prestressed beams
A	=	cross-sectional areas of prestressed beams
A_c	=	cross-sectional areas of concrete
A_v	=	cross-sectional areas of single stirrup in prestressed beam
A_{ps}	=	cross-sectional areas of prestressing tendons
A_{incl}	=	cross-sectional areas of prestressing beams along failure plane
b_w	=	width of web of prestressed I-beams
c	=	constant in stress-strain relationship of concrete after cracking
d	=	depth of c.g.s. of tendons from top concrete fiber in prestressed beams
d_{bv}	=	diameter of stirrups used in prestressed beams
$d-$	=	direction of principal compressive stress of concrete
E_c	=	elastic modulus of concrete
E_c'	=	decompression modulus of concrete, given as $2f_c'/\varepsilon_0$
E_c''	=	modulus of concrete in tension before cracking
E_{ps}	=	modulus of elasticity of prestressing strands
E_{ps}'	=	modulus of bare prestressing strands in inelastic stage
E_{ps}''	=	modulus of prestressing tendons embedded in concrete in inelastic stage
E_s	=	modulus of elasticity of mild steel bars
f_c'	=	cylinder compressive strength of concrete
$\sqrt{f'}_c$	=	square root of cylinder compressive strength of concrete (same units as f_c')

f_{cr} = cracking tensile strength of concrete

f_{ℓ} = smeared (average) stress in longitudinal steel bars

$f_{\ell p}$ = smeared (average) stress in longitudinal prestressing tendons

f_n = apparent yield strength of mild steel bars embedded in concrete

f_p = smeared (average) stress in mild steel bars at peak

f_{pi} = initial stress of prestressing tendons

f_{ps} = stress of prestressing tendons

f_{pu} = stress in prestressing tendons at nominal strength

f'_{pu} = revised ultimate strength of prestressing tendons

f_s = smeared (average) stress in mild steel bars, becomes f_{ℓ} or f_t when applied to longitudinal and transverse steel, respectively

f_t = smeared (average) stress in transverse steel bars

f_{tp} = smeared (average) stress in transverse prestressing tendons

f_y = yield strength of bare mild steel bars

G = shear modulus of concrete

h = depth of prestressed beam

H = tensile load or strain to represent load stages in crack simulation tests

K_r = reduction factor for concrete contribution in non-prestressed concrete

ℓ = direction of longitudinal reinforcements

L_n = span of prestressed beam

m = constant in stress-strain relationships of prestressing tendons

M = bending moment at design section of prestressed beams

P = total tensile load on panels

r = direction of principal tensile stress of concrete

t = direction of transverse reinforcements

s = spacing of stirrups in prestressed beams

S = shear force along failure plane in prestressed beams

T = tensile force in tendons in prestressed beams

$\sum F_V$ = summation of stirrup forces lying on the failure plane in prestressed beams

V = shear capacity of prestressed beams

V_{cal} = shear capacity of prestressed beams calculated from shear theory

$V_{\exp}$ = experimental shear capacity of beams

V_c = concrete contribution in shear resistance of beams

V_s = steel contribution in shear resistance of beams

V_u = design shear force acting on beams

$V_{c.\max}$ = maximum concrete shear capacity in beams

$V_{u.\max}$ = maximum design shear capacity of beams

w_u = uniformly distributed load acting on beams

W_p = prestress factor in softening coefficient

x = distance of design section from support of prestressed beam

α = angle of the principal tensile stress of concrete ($r-$axis) with respect to the longitudinal steel bars ($\ell-$axis)

α_1 = angle of the applied principal tensile stress ($1-$axis) with respect to the longitudinal steel bars ($\ell-$axis)

β = deviation angle of the direction of concrete principal tensile stress ($r-$axis) and the direction of $1-$axis, $\alpha-\alpha_1$

$\gamma_{\ell t}$ = smeared (average) shear strain in $\ell-t$ coordinates

γ_{hv} = smeared (average) shear strain in horizontal-vertical plane in beam tests

γ_{12} = smeared (average) shear strain in $1-2$ coordinates

ε_0 = concrete cylinder strain corresponding to peak cylinder strength, f_c'

ε_1 = biaxial smeared (average) principal strain in $1-$direction

ε_h = smeared (average) horizontal strain in beam tests

ε_v = smeared (average) vertical strain in beam tests

ε_d = smeared (average) diagonal strain in beam tests

ε_{H1} = ultimate strain recorded in LVDT H1 during beam tests

ε_{H2} = ultimate strain recorded in LVDT H2 during beam tests

ε_{V1} = ultimate strain recorded in LVDT V1 during beam tests

ε_{V2} = ultimate strain recorded in LVDT V2 during beam tests

ε_{D1} = ultimate strain recorded in LVDT D1 during beam tests

ε_{D2} = ultimate strain recorded in LVDT D2 during beam tests

ε_{SG1} = ultimate strain recorded in strain gage SG1 during beam tests

ε_{SG2} = ultimate strain recorded in strain gage SG2 during beam tests

ε_{SG3} = ultimate strain recorded in strain gage SG3 during beam tests

ε_{SG4} = ultimate strain recorded in strain gage SG4 during beam tests

$\bar{\varepsilon}_1$ = uniaxial smeared (average) principal strain in $1-$direction

ε_2 = biaxial smeared (average) principal strain in $2-$direction

$\bar{\varepsilon}_2$ = uniaxial smeared (average) principal strain in $2-$direction

$\bar{\varepsilon}_c$ = uniaxial strain in concrete

$\bar{\varepsilon}_{ci}$ = initial strain in concrete

ε_{cr} = concrete cracking strain taken as 0.00008

$\bar{\varepsilon}_{cx}$ = extra strain in concrete after decompression

ε_d = smeared (average) concrete compressive strain in concrete principal $d-$direction

ε_ℓ = biaxial smeared (average) strain in the direction of longitudinal steel bars ($\ell-$axis)

$\bar{\varepsilon}_\ell$ = uniaxial smeared (average) strain in the direction of longitudinal steel bars ($\ell-$axis)

$\bar{\varepsilon}_n$ = uniaxial smeared (average) yielding strain of steel bars embedded in concrete

$\bar{\varepsilon}_p$ = uniaxial smeared (average) strain in mild steel at peak

$\bar{\varepsilon}_{pi}$ = initial uniaxial strain of prestressing tendons

ε_r = smeared (average) concrete tensile strain in concrete principal $r-$direction

ε_s = smeared (average) strain in mild steel, ε_s becomes ε_ℓ or ε_t, when applied to the longitudinal or transverse steel, respectively

ε_{sf} = smeared (average) strain of steel bars which yields first, taking into account the Hsu/Zhu ratios

ε_t = biaxial smeared (average) strain in the direction of transverse steel bars ($t-$axis)

$\bar{\varepsilon}_t$ = uniaxial smeared (average) strain in the direction of transverse steel bars ($t-$axis)

ε_y = yielding strain in bare steel bars

ϕ = angle between the horizontal and the diagonal LVDTs in beam tests

ζ = softening coefficient

ζ_ε = strain softening coefficient

ζ_σ = stress softening coefficient

η = reinforcement index, taken as $\left(\rho_t f_{ty} - \sigma_t\right)/\left(\rho_\ell f_{\ell y} - \sigma_\ell\right)$

η' = η or its reciprocal whichever is less than unity

ν_{12} = Hsu/Zhu ratio (increment of strain in $1-$direction due to a strain in $2-$direction)

ν_{21} = Hsu/Zhu ratio (increment of strain in $2-$direction due to a strain in $1-$direction)

ρ_ℓ = longitudinal steel ratio

$\rho_{\ell p}$ = longitudinal prestressing steel ratio

ρ_t = transverse steel ratio

σ_1 = applied principal stress in $1-$direction

σ_1^c = smeared (average) concrete stress in $1-$direction

σ_2 = applied principal stress in $2-$direction

σ_2^c = smeared (average) concrete stress in $2-$direction

σ_c = smeared (average) stress in concrete

σ_{ci} = initial compressive stress in concrete due to prestress

σ_d = smeared (average) compressive stress in concrete principal $d-$direction

σ_ℓ = applied normal stress in $\ell-$direction

σ_p = prestress on concrete

σ_{pk} = peak compressive stress on panels in vertical direction

σ_r = smeared (average) tensile stress in concrete principal $r-$direction

σ_t = applied normal stress in $t-$direction

τ_{12}^{c} = smeared shear stress of cracked concrete in $1-2$ coordinates

$\tau_{\ell t}$ = applied shear stress in $\ell - t$ coordinates

CHAPTER 1

INTRODUCTION

1.1 Overview of Research

The idea of prestressing concrete structures was first applied in 1928 by Eugene Freyssinet (1956) in his effort to save the Le Veurdre Bridge over the Allier River near Vichy, France. The primary purpose of using prestressed concrete was to eliminate/reduce cracking at service load and to fully utilize the capacity of high-strength steel. After the Second World War, prestressed concrete became prevalent due to the needs of reconstruction and the availability of high-strength steel. Today, prestressed concrete has become the predominant material in highway bridge construction. It is also widely used in the construction of buildings, underground structures, TV towers, floating storages and offshore structures, power stations, nuclear reactor vessels, etc.

This research intends to solve one of the most troublesome problems in prestressed concrete, namely shear. The problem arises from the lack of a rational model to predict the behavior of prestressed concrete structures under shear action and the various modes of shear failures. Because of this deficiency, all the guidelines for shear design, such as ACI Codes and AASHTO Specifications, are empirical and have severe limitations.

Hsu (2002) pointed out the deficiency in the shear design guidelines for reinforced and prestressed concrete bridge girders. By comparing the fixed-angle model with the rotating-angle model, he showed that the "concrete contribution" V_c for the shear resistance can be derived from the shear resistance of cracked concrete, rather than from the tensile strength of concrete as assumed in ACI Codes (2005) or the tensile stress of cracked concrete in AASHTO Specifications (2004).

In Loov's "shear friction" theory (Loov, 1978, 1997, and 2002) for girders, V_c was derived from the shear resistance of cracked concrete along a shear failure plane. Based on the "shear friction" principle, Loov established a shear design method and illustrated it with a detailed example. However, the determination of V_c by a "shear friction" principle was not widely accepted. Hsu (2002) noted that Loov's method can be modified and be applicable to prestressed concrete girders, as long as the constitutive laws of prestressed concrete membrane elements are clarified. These constitutive laws would allow us to understand the effect of prestress on the "concrete contribution" V_c.

Similar to reinforced concrete structures, wall-type or shell-type prestressed concrete structures can be visualized as assemblies of membrane elements subjected to normal and shear stresses in the plane of elements. Taking bridge girders as examples, Fig. 1.1.1(a) to (c) show three main types of prestressed bridge girders: I-girder, box girder, and trapezoidal girder. The webs of the girders, which are shear-governed, can be analyzed using finite element methods if there is a rational shear model for plane stress elements (Fig. 1.1.1(d)). Therefore, the key to

solving the shear problem of prestressed concrete structures is to thoroughly understand the shear behavior of prestressed concrete membrane elements.

Figure 1.1.2(a) shows a typical I-girder used in highway bridges. The girder may encounter two major kinds of shear failure modes: (1) web shear failure near the supports where the shear force is large and the bending moment is small, and (2) flexural-shear failure near the one-third or quarter point of the span where both the shear force and the bending moment are large. A typical membrane element subjected to in-plane stresses can be isolated from the failure region of the girder, as shown in Fig. 1.1.2(b). The research in this project focuses on the shear behavior of prestressed concrete membrane elements (panels).

Many researchers have developed various types of analytical models of reinforced concrete, such as truss models, orthotropic models, nonlinear elastic models, plastic models, micro models, etc. As compared with the other models, the orthotropic model stands out both in accuracy and in efficiency. Over the past 20 years, extensive experimental and theoretical studies on the shear behavior of reinforced concrete have been carried out by a research group at the University of Houston (UH). A series of analytical models was established to predict the nonlinear shear behavior of reinforced concrete membrane elements. These models are: the Rotating-Angle Softened Truss Model (RA-STM) by Hsu (1993), Belarbi and Hsu (1995), and Pang and Hsu (1995); the Fixed-Angle Softened Truss Model (FA-STM) by Pang and Hsu (1996) and Hsu and Zhang (1997); and the Softened Membrane Model (SMM) by Hsu and Zhu (2002). All these models are rational because they satisfy Navier's three principles of mechanics of materials: stress equilibrium, strain compatibility, and constitutive relationships of materials.

The Softened Membrane Model has been proven to be successful in predicting the entire shear behavior of reinforced concrete panels including both the pre-peak and the post-peak regions. In this research, the SMM is extended to prestressed concrete panels. Ten prestressed concrete panels were tested to obtain the constitutive laws of concrete and prestressing strands. These constitutive laws, which take into account the effect of prestress, were then incorporated into the SMM. The new model established in this dissertation will be called the Softened Membrane Model for Prestressed Concrete (SMM-PC).

Another major part of this project involved development of a new simple shear design equation for girders. For this a series of five prestressed concrete I-beams were designed, cast, and tested to study their behavior in web shear as well as flexural shear failure modes. The results obtained from these tests were analyzed and a new simple equation was developed for the shear design of prestressed concrete girders. Results from other tests available in the literature (Lyngberg, 1976; Elzanaty et al., 1986; and Rangan, 1991) were used to verify the new design equation and make necessary modifications to the same. The new design equation was also extended to include non-prestressed girders.

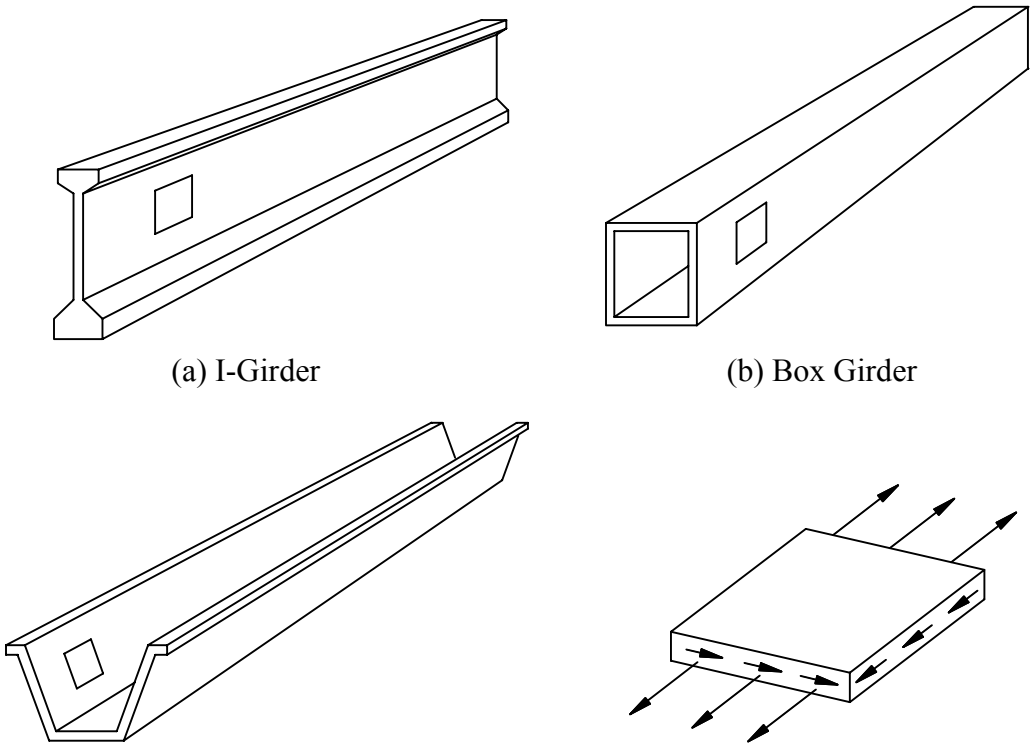

(a) I-Girder (b) Box Girder

(c) Trapezoidal Girder (d) Web Element

Fig. 1.1.1 Three Types of Bridge Girders

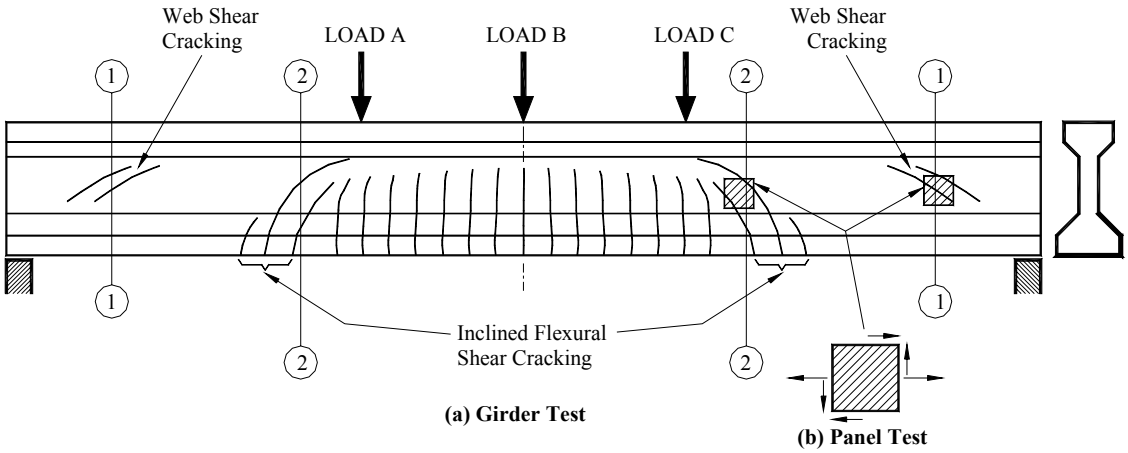

Fig. 1.1.2 Shear Failure Modes and Shear Panel Elements

1.2 Objectives of Research

The objectives of this research can be summarized as follows:

(1) To investigate experimentally the behavior of prestressed concrete panels subjected to sequential loading and proportional loading (pure shear).

(2) To develop the constitutive laws of concrete in tension and compression and prestressing strands in panels under pure shear, focusing particularly on the effect of prestress on the stress-strain relationship of concrete in compression.

(3) To establish a shear model (SMM-PC) to predict the shear behavior of prestressed concrete membrane elements (panels).

(4) To perform tests on prestressed concrete beams subjected to shear so that the analytical model developed in this research can be validated.

(5) To propose a practical equation for shear design of prestressed concrete beams based on tests performed in this project and those from literature.

1.3 Outline of Report

This report is divided into 10 chapters, which include parts: (I) Prestressed Concrete Elements and (II) Shear in Prestressed Concrete Beams. Part I covers Chapters 2 through 6 and Part II covers Chapters 7 through 9.

Chapter 1 introduces the overview of the research, the objectives of the research, and the outline of this report.

Chapter 2 describes a literature study on the shear models of reinforced concrete panels with emphasis on the models developed at the University of Houston. A background survey on shear behavior of prestressed concrete panels is also included in this chapter.

Chapter 3 describes the crack simulation tests that were conducted in this project to simulate the effect of pre-tensioned tendons using grouted post-tensioned strands. Ten axially prestressed beams were cast with different types of grouts to find the optimal method of prestressing and grouting the tendons in the laboratory.

Chapters 4 and 5 describe the experimental program on 10 prestressed concrete panels. To analyze the responses of prestressed concrete structures using finite element methods, it is necessary to fully understand the behavior of prestressed concrete membrane elements subjected to various types of loading. According to the orientation of the steel grids and the loading procedure, the panels were divided into two groups: TE and TA. Chapter 4 describes the TE panels, which are subjected to sequential loading and are used to determine the constitutive laws of materials taking into account the effect of prestress. Chapter 5 describes the TA panels, which are subjected to proportional loading and are used to study the shear behavior of prestressed concrete membrane elements, including the effects of the percentages of mild steel bars and prestressing tendons.

Chapter 6 presents the analytical model to predict the behavior of prestressed concrete panels. To analyze the responses of prestressed concrete structures using finite element methods, the

Softened Membrane Model (SMM) for reinforced concrete (RC) was extended for the application to prestressed concrete (PC). This generalized analytical model includes the following three new constitutive laws: (1) A new constitutive relationship of concrete in tension, which includes the decompression stage; (2) A new prestress factor W_p for incorporation into the softening coefficient for the constitutive relationship of concrete in compression; and (3) A new smeared (average) stress-strain relationship of prestressing tendons embedded in concrete. To verify the model SMM for PC, the predictions of the model are compared with the test results for prestressed concrete panels subjected to shear.

Chapter 7 describes the full-scale load tests of five I-beams to study the structural behavior with regard to ultimate shear strength, ductility, and failure mechanism. The results obtained from the tests are also presented in this chapter.

Chapter 8 presents two analytical models to predict the behavior of prestressed concrete beams. The first one is used to predict the flexural behavior, and the second one is used to predict the shear behavior.

Chapter 9 presents a new and simple equation for shear in prestressed concrete beams. The development of this equation is based on the results of the beams tested at UH and the results from other beam tests available in literature (Lyngberg, 1976; Elzanaty et al., 1986; and Rangan, 1991). The shear capacities predicted by the new equation are compared to those predicted by the ACI Code and the AASHTO Specifications. Four design examples are included to illustrate the practical use of the new equation for design of prestressed girders. Four design examples were prepared to illustrate the application of the new shear equation for prestressed concrete girders. The shear equation was also extended for application to non-prestressed girders, including an example showing the design of a non-prestressed girder.

Chapter 10 provides the conclusions of this research and suggests further studies in the area.

PART I

PRESTRESSED CONCRETE ELEMENTS

CHAPTER 2

BACKGROUNDS ON SHEAR THEORIES OF REINFORCED AND PRESTRESSEED CONCRETE PANELS

2.1 Introduction

Section 2.2 of this chapter reviews the shear models for reinforced concrete in the literature. Section 2.3 summarizes a series of the shear models developed at the University of Houston in the past 20 years with emphasis on the Softened Membrane Model (SMM). The last section 2.4 contains a literature survey on shear behavior of prestressed concrete panels.

2.2 Shear Theories of Reinforced Concrete in Literature

The post cracking behavior of a reinforced concrete member subjected to shear and bending was first simulated by a truss model more than a century ago by Ritter (1899) and Morsch (1902). The model assumed that the concrete was separated by diagonal cracks into a series of concrete struts. The shear resistance of the reinforced concrete beams was provided by an internal truss mechanism, consisting of two longitudinal parallel chords connected to a composite web made of web steel bars and diagonal concrete struts. The diagonal concrete struts were assumed to be subjected to direct axial compression, while the web steel bars were treated as the tensile web members of the truss. Since the cracks were assumed to be inclined at 45 degrees with respect to the longitudinal reinforcement, this model was referred to as the "45-degree truss model."

Robinson and Demorieux (1968) realized that a reinforced concrete element subjected to shear stresses was actually subjected to biaxial compression-tension stresses in the 45-degree direction. Viewing the shear action as a two dimensional problem, they discovered that the compressive strength in one direction was reduced by cracking due to tension in the perpendicular direction. Applying this softening effect of concrete struts to the webs of eight tested beams with I-section, they were able to explain the equilibrium of stresses in the webs according to the truss model. However, they were not able to quantify this reduction of strength in the concrete struts.

Vecchio and Collins (1981) built a so-called "shear rig," used to quantify a softening coefficient for the compressive stress-strain curve of concrete and then developed the compression field theory (CFT), which was applicable throughout the post-cracking range up to the ultimate. CFT assumed that the inclination of the principal compressive stress in concrete coincided with the inclination of the principal compressive strain, and cracks developed in the principal direction of concrete (rotating-crack model). CFT satisfied the three fundamental principles of mechanics of materials and represented a major breakthrough in the prediction of shear behavior of RC elements. However, the compression field theory assumed that no tensile

stress of concrete exists after cracking. This assumption is contradicted by many tests, which demonstrated that concrete stresses in tension increased significantly the stiffness of the cracked reinforced concrete structures. By taking into account the tensile strength of concrete, Vecchio and Collins (1986) further developed the modified compression field theory (MCFT) so it could predict the post-cracking stiffness. However, the theory had two deficiencies as pointed out by Hsu (1998). First, the MCFT violated the basic principle of mechanics by imposing concrete shear stresses in the principal directions. Second, it used the local stress-strain curve of steel bars embedded in concrete, rather than the smeared (average) stress-strain curves.

Balakrishnan and Murray (1988c) also applied a rotating crack model to predict the monotonic behavior of shear panels and deep beams using their own constitutive relationships (Balakrishnan and Murray, 1988a and 1988b). Poisson's ratio was set to be zero when the concrete cracking began. The model was used to predict the behavior of a number of reinforced concrete panels tested by Vecchio and Collins (1982).

Crisfield and Wills (1989) performed analyses of a number of reinforced concrete panels tested by Vecchio and Collins (1982) using different material models. The models included a fixed crack model, a swinging-crack model, and a simple plasticity model. In the fixed crack model, the directions of orthogonal cracks were governed by the direction of the first principal stress that exceeded the tensile stress of the uncracked concrete. The swinging-crack model was a rotating crack model. The plasticity model had a square yield surface in compression in which no tension was allowed. The authors conducted extensive studies of the three proposed models on the panels and compared the analytical results with the experimental results. The authors also demonstrated the differences between the fixed crack and the swinging crack models.

A Rotating-Angle Softened Truss Model (RA-STM) was developed at the University of Houston (Belarbi and Hsu, 1994 and 1995; Pang and Hsu, 1995), which truly treated the cracked reinforced concrete as a smeared, continuous material. In this model, a new smeared (average) stress-strain curve of steel bars embedded in concrete (Belarbi and Hsu, 1994) was proposed. Moreover, a new algorithm was developed to significantly improve the iteration procedure in solving the 11 equilibrium, compatibility, and constitutive equations. As a result this model has two advantages. First, it produces a single and unique solution instead of multiple solutions as in the case of the modified compression field theory. Second, there is no need to perform the so-called "crack check," which is difficult to apply in finite element methods.

These studies also showed that all theories that are based on rotating-angle could not logically produce the "concrete contribution" V_c because shear stresses could not exist along the rotating-angle cracks. In order to predict the "concrete contribution," Hsu and his colleagues (Pang and Hsu, 1996; Hsu and Zhang, 1997; Zhang and Hsu, 1998) proposed the Fixed-Angle Softened Truss Model (FA-STM). In the FA-STM, the direction of cracks is assumed to be perpendicular to the applied principal tensile stresses at initial cracking rather than following the rotating cracks. The constitutive laws of concrete were set in the principal coordinate of the applied stresses at initial cracking. The only shortcoming of the FA-STM is that it is more complicated than the RA-STM because of the complexity in the stress-strain relationship of concrete in shear.

Ayoub and Filippou (1998) presented a rotating crack model that was an extension of the orthotropic models by Vecchio (1990) and Balakrishnan and Murray (1988a, 1988b, and 1988c). The panels tested by Vecchio and Collins (1982) were used in the correlation studies. Reasonable comparison was obtained between the analytical and experimental results.

Kaufmann and Marti (1998) proposed the Cracked Membrane Model (CMM), which was a combination of CFT (Vecchio and Collins, 1981) and a concrete tension stiffening model. The tension stiffening of concrete was modeled using a stepped, rigid-perfectly plastic concrete-steel bond slip relationship between the cracks with equilibrium maintained at the crack faces. Foster and Marti (2003) implemented the CMM into a finite element formulation and compared its predictions against experimental data from the shear panel tests by Meyboom (1987) and Zhang (1992).

Vecchio (2000 and 2001a) developed the Disturbed Stress Field Model (DSFM) based on the rotating crack model. The DSFM was a partially smeared model, which included shear slips along crack surfaces and required a "crack check" as in MCFT. The DSFM was more complicated when compared with the MCFT (Vecchio and Collins 1986). The predictions by the DSFM were compared to the experimental results of their panels and to the analytical results by MCFT (Vecchio et al., 2001b). The predictions using the DSFM and MCFT were found to be close in most cases.

Belletti et al. (2001) proposed a fixed crack model by adopting the stress-strain relationships of concrete and steel, aggregate interlock, and dowel action. The softening coefficient ζ proposed by Pang and Hsu (1995) was adopted in the model, which represented the softening effect of tensile strains on the perpendicular compression behavior of concrete. The panels tested at the University of Toronto (Vecchio and Collins 1982 and 1986; Collins et al., 1985; Bhide and Collins, 1989) and the panels tested at the University of Houston (Belarbi and Hsu, 1995; Pang and Hsu, 1995 and 1996; Hsu and Zhang, 1996) were analyzed. The predictions of the proposed model showed good agreement with the test results.

Although the rational models given above were able to predict the pre-peak behavior of shear elements, none of them could explain the existence of the post-peak load-deformation curves (descending branches). The Softened Membrane Model (SMM) (Hsu and Zhu, 2002) was therefore developed to predict the entire monotonic shear stress-strain curves of reinforced concrete panels including the descending branches. The capability of SMM to predict the descending branches was achieved by taking into account the Poisson effect (mutual effects of the two normal strains) of cracked reinforced concrete. This Poisson effect is characterized by two Hsu/Zhu ratios (Zhu and Hsu, 2002). In addition, a very simple stress-strain equation for concrete in shear was also derived using the equilibrium and compatibility equations and then incorporated in the model (Zhu, Hsu, and Lee, 2001). This new shear modulus significantly simplified the solution algorithm of fixed model theories, including SMM and FA-STM. It also increased the accuracy of these models.

To date, SMM has been proven to be capable of successfully predicting the entire behavior of RC panels under pure shear. In this research, SMM will be extended to predict the behavior of prestressed concrete panels.

2.3 Previous Studies by Research Group at UH

In the past 20 years, Hsu and his colleagues performed over 130 panel tests using the Universal Panel Tester (Hsu, Belarbi, and Pang, 1995) at the University of Houston. A series of three rational models for the monotonic shear behavior of the reinforced concrete elements (panels) was developed.

A reinforced concrete membrane element subjected to in-plane shear and normal stresses is shown in Fig. 2.3.1(a). The directions of the longitudinal and the transverse steel bars are designated as $\ell-$ and $t-$ axes, respectively, constituting the $\ell-t$ coordinate system. The normal stresses are designated as σ_l and σ_t in the $\ell-$ and the $t-$ directions, respectively, and the shear stresses are represented by τ_{lt} in the $\ell-t$ coordinate system. For Mohr's circles, a positive shear stress τ_{lt} is the one that causes clockwise rotation of a reinforced concrete element (Hsu, 1993).

The applied principal stresses for the reinforced concrete element are defined as σ_1 and σ_2 based on the $1-2$ coordinate system as shown in Fig. 2.3.1(d). The angle between the direction of the applied principal tensile stress ($1-$axis) and the direction of the longitudinal steel ($\ell-$axis) is defined as the fixed-angle α_1, because this angle does not change when the three in-plane stresses, σ_l, σ_t, and τ_{lt}, increase proportionally. This angle α_1 is also called the steel bar angle because it defines the direction of the steel bars with respect to the applied principal stresses.

The principal stresses in concrete coincide with the applied principal stresses σ_1 and σ_2 before cracking. When the principal tensile stress σ_1 reaches the tensile strength of concrete, cracks will form and the concrete will be separated by the cracks into a series of concrete struts in the $2-$direction as shown in Fig. 2.3.1(f). If the element is reinforced with different amounts of steel in the $\ell-$ and the $t-$ directions, i.e., $\rho_\ell f_\ell \neq \rho_t f_t$ in Fig. 2.3.1(c), the direction of the principal stresses in concrete after cracking will deviate from the directions of the applied principal stresses. The new directions of the post-cracking principal stresses in concrete are defined by the $r-d$ coordinate system shown in Fig. 2.3.1(e). Accordingly, the principal tensile stress and the principal compressive stress in the cracked concrete are defined as σ_r and σ_d, respectively.

The angle between the direction of the principal tensile stress in the cracked concrete ($r-$axis) and the direction of the longitudinal steel ($\ell-$axis) is defined as the rotating-angle α. The angle α is dependent on the relative amount of "smeared steel stresses," $\rho_l f_l$ and $\rho_t f_t$, in the longitudinal and the transverse directions as shown in Fig. 2.3.1(c). When $\rho_\ell f_\ell > \rho_t f_t$, the $r-d$ coordinate gradually rotates away from the $2-1$ coordinate and α becomes smaller with increasing load. With increasing applied proportional stresses (σ_l, σ_t, and τ_{lt}), the deviation between the angle α and the angle α_1 increases. This deviation angle β is defined as $\alpha-\alpha_1$. The

angle was determined by Hsu, Zhu and Lee (2001) for reinforced concrete and extended by Wang (2006) to prestressed concrete, as shown in Eq. 2.3-1.

$$\beta = \frac{1}{2}\tan^{-1}\left[\frac{\gamma_{12}}{(\varepsilon_1 - \varepsilon_2)}\right] \tag{2.3-1}$$

where ε_1, ε_2, and γ_{12} are the strains in the $1-2$ coordinate of the applied principal stresses. When the percentages of reinforcement are the same in the $\ell-$ and the $t-$ directions, the rotating angle α is equal to the fixed-angle α_1.

The Rotating-Angle Softened Truss Model is based on the assumption that the direction of cracks coincides with the direction of the principal compressive stress in the cracked concrete, as shown in Fig. 2.3.1(g). The derivations of all the equilibrium and compatibility equations are based on the rotating-angle α. In contrast, the Fixed-Angle Softened Truss Model is based on the assumption that the direction of the cracks coincides with the direction of the applied principal compressive stress as shown in Fig. 2.3.1(f). In the fixed-angle softened-truss model, all the equations are derived based on the fixed-angle α_1.

The three stress components σ_l, σ_t, and τ_{lt} shown in Fig. 2.3.1(a) are the applied stresses on the reinforced concrete element viewed as a whole. The stresses on the concrete struts are denoted as σ_ℓ^c, σ_t^c, and $\tau_{\ell t}^c$ as shown in Fig. 2.3.1(b). The longitudinal and the transverse

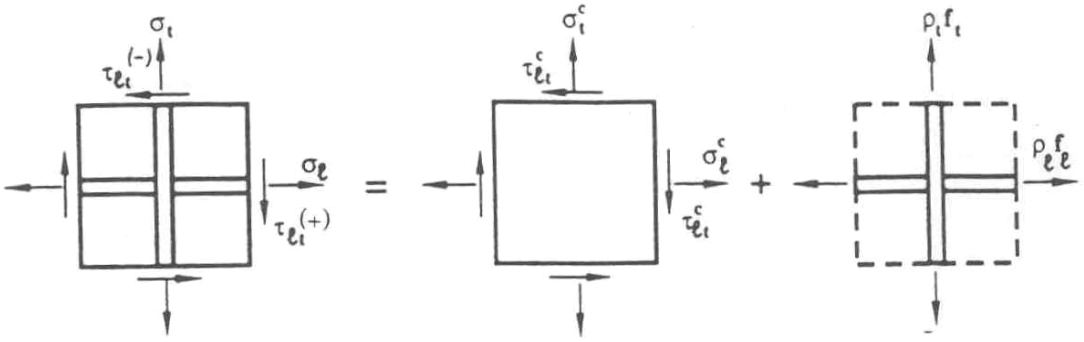

(d) Principal Axes 1-2 for Applied Stresses

(e) Principal Axes r-d for Stresses on Concrete

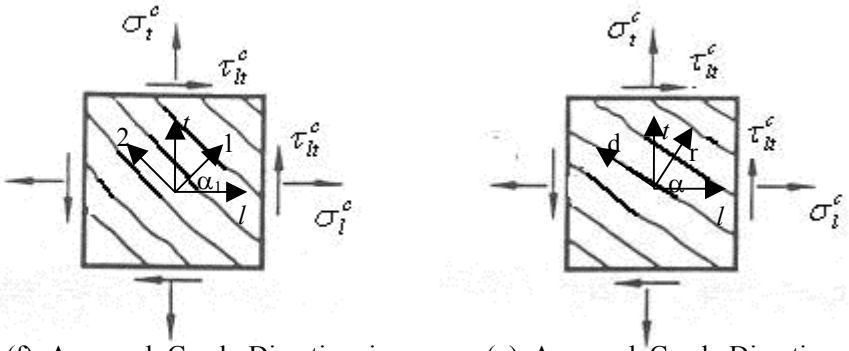

(f) Assumed Crack Direction in Fixed-Angle Model

(g) Assumed Crack Direction in Rotating-Angle Model

Fig. 2.3.1 Reinforced Concrete Membrane Elements Subjected to In-Plane Stresses

steel provide the smeared (average) stresses of $\rho_\ell f_\ell$ and $\rho_t f_t$ as shown in Fig. 2.3.1(c). The reinforcements are assumed to take only axial stresses, neglecting any possible dowel action. Summing the concrete stresses and the steel stresses in the $\ell-$ and the $t-$ directions and maintaining the equilibrium of forces and moments give the following equations:

$$\sigma_\ell = \sigma_\ell^c + \rho_\ell f_\ell \tag{2.3-2}$$

$$\sigma_t = \sigma_t^c + \rho_t f_t \tag{2.3-3}$$

$$\tau_{\ell t} = \tau_{\ell t}^c \tag{2.3-4}$$

Eqs. 2.3-2 to 2.3-4 are the basic equilibrium equations for both RA-STM and FA-STM. When the three concrete stresses (σ_ℓ^c, σ_t^c, and $\tau_{\ell t}^c$) in the $\ell - t$ coordinate are transformed to the principal $r-d$ coordinate of concrete, Fig. 2.3.1(g), we obtain the RA-STM derived in Section 2.3.1. When the three concrete stresses (σ_ℓ^c, σ_t^c, and $\tau_{\ell t}^c$) are transformed to the principal $1-2$ coordinate of the applied stresses, Fig. 2.3.1(f), we obtain the FA-STM derived in Section 2.3.2.

2.3.1 Rotating-Angle Softened Truss Model (RA-STM)

Equilibrium and Compatibility Equations

In the Rotating-Angle Softened-Truss Model (RA-STM), the direction of cracks is defined by the rotating-angle α in the principal $r-d$ coordinate of concrete as shown previously in Fig. 2.3.1(e). The three equilibrium equations are obtained from Eqs. 2.3-2 to 2.3-4 by expressing the concrete stresses (σ_ℓ^c, σ_t^c, and $\tau_{\ell t}^c$) in terms of concrete stresses (σ_r and σ_d) in the principal $r-d$ direction through transformation (Hsu, 1993):

$$\sigma_\ell = \sigma_r \cos^2\alpha + \sigma_d \sin^2\alpha + \rho_\ell f_\ell \tag{2.3-5}$$

$$\sigma_t = \sigma_r \sin^2\alpha + \sigma_d \cos^2\alpha + \rho_t f_t \tag{2.3-6}$$

$$\tau_{\ell t} = (-\sigma_r + \sigma_d)\sin\alpha\cos\alpha \tag{2.3-7}$$

where

σ_r, σ_d = smeared (average) principal tensile and compressive stresses of cracked concrete in $r-$ and $d-$ directions, respectively,

ρ_l, ρ_t = steel ratio in $\ell-$ and $t-$ directions, respectively,

f_l, f_t = smeared (average) stresses of steel bars in $\ell-$ and $t-$ directions, respectively, and

α = angle of principal tensile concrete stress ($r-$axis) with respect to longitudinal steel bars ($\ell-$axis).

The three compatibility equations, which represent the relationship through transformation between the strains (ε_l, ε_t, and γ_{lt}) in the $\ell-t$ coordinate of the reinforcement and the strains (ε_r and ε_d) in the $r-d$ coordinate of the concrete, are expressed as follows:

$$\varepsilon_\ell = \varepsilon_r \cos^2\alpha + \varepsilon_d \sin^2\alpha \tag{2.3-8}$$

$$\varepsilon_t = \varepsilon_r \sin^2\alpha + \varepsilon_d \cos^2\alpha \tag{2.3-9}$$

$$\frac{\gamma_{\ell t}}{2} = (-\varepsilon_r + \varepsilon_d)\sin\alpha\cos\alpha \tag{2.3-10}$$

where

ε_r, ε_d = smeared (average) principal tensile and compressive strains in $r-$ and $d-$ directions, respectively.

The solution of the above six equilibrium and compatibility equations requires constitutive laws of materials for concrete and reinforcements.

Constitutive Relationship of Cracked Concrete in Compression

The softened compressive stress-strain relationship of concrete is established in the $r-d$ coordinate as follows (Zhang and Hsu, 1998):

$$\sigma_d = \zeta f_c' \left[2\left(\frac{\varepsilon_d}{\zeta\varepsilon_0}\right) - \left(\frac{\varepsilon_d}{\zeta\varepsilon_0}\right)^2 \right], \qquad \frac{\varepsilon_d}{\zeta\varepsilon_0} \le 1 \tag{2.3-11a}$$

or

$$\sigma_d = \zeta f_c' \left[1 - \left(\frac{\varepsilon_d/\zeta\varepsilon_0 - 1}{4/\zeta - 1}\right)^2 \right], \qquad \frac{\varepsilon_d}{\zeta\varepsilon_0} > 1 \tag{2.3-11b}$$

where

$$\zeta = \frac{5.8}{\sqrt{f_c'}} \frac{1}{\sqrt{(1+400\varepsilon_r)}} \le 0.9 \tag{2.3-12}$$

Constitutive Relationship of Cracked Concrete in Tension

The tensile stress-strain relationship of concrete in the $r-d$ coordinate is given as follows (Belarbi and Hsu, 1994):

$$\sigma_r = E_c \varepsilon_r, \qquad \varepsilon_r \le \varepsilon_{cr} \tag{2.3-13a}$$

or

$$\sigma_r = f_{cr}\left(\frac{\varepsilon_{cr}}{\varepsilon_r}\right)^{0.4}, \qquad \varepsilon_r > \varepsilon_{cr} \tag{2.3-13b}$$

where

E_c = elastic modulus of concrete taken as $3875\sqrt{f_c'}$ (f_c' and $\sqrt{f_c'}$ are in MPa),

ε_{cr} = concrete cracking strain taken as 0.00008, and

f_{cr} = concrete cracking stress taken as $0.31\sqrt{f'_c}$ (f'_c and $\sqrt{f'_c}$ are in MPa).

Constitutive Relationship of Steel Bars Embedded in Cracked Concrete

The smeared (average) tensile stress-strain relationship of steel embedded in concrete in the $\ell - t$ coordinate can be expressed as follows (Pang and Hsu, 1995):

$$f_s = E_s \varepsilon_s, \qquad \varepsilon_s \le \varepsilon_n \qquad (2.3\text{-}14a)$$

$$f_s = f_y \left[(0.91 - 2B) + (0.02 + 0.25B) \frac{\varepsilon_s}{\varepsilon_y} \right], \qquad \varepsilon_s > \varepsilon_n \qquad (2.3\text{-}14b)$$

where $$\varepsilon_n = \varepsilon_y (0.93 - 2B) \qquad (2.3\text{-}15)$$

and $$B = \frac{1}{\rho} \left(\frac{f_{cr}}{f_y} \right)^{1.5} \qquad (2.3\text{-}16)$$

In the above equations, ℓ replaces s in the subscript of symbols for the longitudinal steel, and t replaces s for the transverse steel.

2.3.2 Fixed-Angle Softened Truss Model (FA-STM)

Equilibrium and Compatibility Equations

In the Fixed-Angle Softened Truss Model (FA-STM), the direction of cracks is defined by the fixed angle α_1 in the principal $1-2$ coordinate of the applied stresses as shown in Fig. 2.3.1(d). The three equilibrium equations are obtained from Eqs. 2.3-2 to 2.3-4 by expressing the concrete stresses (σ^c_ℓ, σ^c_t, and $\tau^c_{\ell t}$) in terms of concrete stresses (σ^c_1, σ^c_2 and τ^c_{12}) in the principal $1-2$ direction through transformation (Pang and Hsu, 1996):

$$\sigma_\ell = \sigma^c_1 \cos^2 \alpha_1 + \sigma^c_2 \sin^2 \alpha_1 + \tau^c_{12} 2 \sin \alpha_1 \cos \alpha_1 + \rho_\ell f_\ell \qquad (2.3\text{-}17)$$

$$\sigma_t = \sigma^c_1 \sin^2 \alpha_1 + \sigma^c_2 \cos^2 \alpha_1 - \tau^c_{12} 2 \sin \alpha_1 \cos \alpha_1 + \rho_t f_t \qquad (2.3\text{-}18)$$

$$\tau_{\ell t} = (-\sigma^c_1 + \sigma^c_2) \sin \alpha_1 \cos \alpha_1 + \tau^c_{12} (\cos^2 \alpha_1 - \sin^2 \alpha_1) \qquad (2.3\text{-}19)$$

where

σ^c_1, σ^c_2 = smeared (average) stresses of concrete in $1-$ and $2-$ directions, respectively,

τ^c_{12} = smeared (average) shear stress of concrete in $1-2$ coordinate, and

α_1 = angle of applied principal tensile stress ($1-$axis) with respect to longitudinal steel bars ($\ell-$axis).

The three compatibility equations, which represent the relationship through transformation between the strains (ε_l, ε_t, and γ_{lt}) in the $\ell-t$ coordinate of the reinforcement and the strains (ε_1, ε_2, and γ_{12}) in the $1-2$ coordinate of the applied principal stresses, are expressed as follows (Pang and Hsu, 1996):

$$\varepsilon_\ell = \varepsilon_1 \cos^2\alpha_1 + \varepsilon_2 \sin^2\alpha_1 + \frac{\gamma_{12}}{2} 2\sin\alpha_1 \cos\alpha_1 \tag{2.3-20}$$

$$\varepsilon_t = \varepsilon_1 \sin^2\alpha_1 + \varepsilon_2 \cos^2\alpha_1 - \frac{\gamma_{12}}{2} 2\sin\alpha_1 \cos\alpha_1 \tag{2.3-21}$$

$$\frac{\gamma_{\ell t}}{2} = (-\varepsilon_1 + \varepsilon_2)\sin\alpha_1 \cos\alpha_1 + \frac{\gamma_{12}}{2}(\cos^2\alpha_1 - \sin^2\alpha_1) \tag{2.3-22}$$

where

ε_1, ε_2, = smeared (average) strains in $1-2$ directions, respectively, and

γ_{12} = smeared (average) shear strain in $1-2$ coordinate.

Constitutive Relationship of Cracked Concrete in Compression

The softened compressive stress-strain relationship of concrete is established in the $1-2$ coordinate as follows (Zhang and Hsu, 1998):

$$\sigma_2^c = \zeta f_c' \left[2\left(\frac{\varepsilon_2}{\zeta\varepsilon_0}\right) - \left(\frac{\varepsilon_2}{\zeta\varepsilon_0}\right)^2 \right], \qquad \frac{\varepsilon_2}{\zeta\varepsilon_0} \le 1 \tag{2.3-23a}$$

or

$$\sigma_2^c = \zeta f_c' \left[1 - \left(\frac{\varepsilon_2/\zeta\varepsilon_0 - 1}{4/\zeta - 1} \right)^2 \right], \qquad \frac{\varepsilon_2}{\zeta\varepsilon_0} > 1 \tag{2.3-23b}$$

where

$$\zeta = \frac{5.8}{\sqrt{f_c'}} \frac{1}{\sqrt{\left(1 + \frac{400\varepsilon_1}{\eta'}\right)}} \le 0.9 \tag{2.3-24}$$

and

$$\eta = \frac{\rho_t f_{ty} - \sigma_t}{\rho_\ell f_{ly} - \sigma_\ell}, \qquad 0.2 < \eta < 5 \tag{2.3-25}$$

η' in Eq. 2.3-24 is η or its reciprocal whichever is less than unity.

Constitutive Relationship of Cracked Concrete in Tension

The tensile stress-strain relationship of concrete in the $1-2$ coordinate is given as follows (Belarbi and Hsu, 1994):

$$\sigma_1 = E_c \varepsilon_1, \qquad \varepsilon_1 \le \varepsilon_{cr} \tag{2.3-26a}$$

or

$$\sigma_1 = f_{cr}\left(\frac{\varepsilon_{cr}}{\varepsilon_1}\right)^{0.4}, \qquad \varepsilon_1 > \varepsilon_{cr} \tag{2.3-26b}$$

where

E_c = elastic modulus of concrete taken as $3875\sqrt{f_c'}$ (f_c' and $\sqrt{f_c'}$ are in MPa),

ε_{cr} = concrete cracking strain taken as 0.00008, and

f_{cr} = concrete cracking stress taken as $0.31\sqrt{f_c'}$ (f_c' and $\sqrt{f_c'}$ are in MPa).

Constitutive Relationship of Steel Bars Embedded in Cracked Concrete

The smeared (average) tensile stress-strain relationship of steel embedded in concrete is the same as that given in RA-STM in Section 2.3.1.

Constitutive Relationship of Cracked Concrete in Shear

The constitutive law of concrete in shear in the $1-2$ coordinate is quite complicated as given below:

$$\tau_{12}^c = \tau_{12m}^c\left[1-\left(1-\frac{\gamma_{12}}{\gamma_{120}}\right)^6\right] \tag{2.3-27}$$

where τ_{12m}^c and γ_{120} are the maximum shear stress of cracked concrete and the corresponding shear strain, respectively. τ_{12m}^c and γ_{120} are obtained initially in the first phase of the solution algorithm using the empirical equation,

$$\gamma_{120} = -0.85\varepsilon_{10}(1-\eta) \tag{2.3-28}$$

where

ε_{10} = maximum principal tensile strain of cracked concrete,

and the equilibrium equation,

$$\tau_{12m}^c = \frac{1}{2}\left[\left(\sigma_\ell - \rho_\ell f_{\ell y}'\right) - \left(\sigma_t - \rho_t f_{ty}'\right)\right]\sin 2\alpha_1 + \tau_{\ell tm}\cos 2\alpha_1 \tag{2.3-29}$$

where

τ_{ltm} = maximum applied shear stress in the $\ell - t$ coordinate,

f'_{ly} = smeared (average) yield stress of longitudinal steel bars embedded in concrete given by Eq. 2.3-14b, and

f'_{ty} = smeared (average) yield stress of transverse steel bars embedded in concrete given by Eq. 2.3-14b.

2.3.3 Softened Membrane Model (SMM)

The RA-STM and the FA-STM are two rational models that can satisfy Navier's three principles of mechanics of materials. Although these two models are successful in predicting the pre-peak behavior of reinforced concrete membrane elements subjected to monotonic shear stresses, they cannot explain the existence of the post-peak load-deformation curves (descending branches). The reason, as pointed out by Hsu and Zhu (2002), is because the Poisson effect is neglected in those theories.

In order to predict the descending branches of the shear stress-strain curves of membrane elements, a new theory known as the softened membrane model (SMM) was developed by Hsu and Zhu (2002) that did take the Poisson effect into account. In this model, two Hsu/Zhu ratios, ν_{12} and ν_{21}, were obtained from tests (Zhu and Hsu, 2002) to characterize the Poisson effect of cracked concrete in the $1-2$ coordinate system using the smeared crack concept. Hsu/Zhu ratio ν_{21} is defined as the ratio $\Delta\varepsilon_1/\Delta\varepsilon_2$, where $\Delta\varepsilon_1$ is the resulting increment of strain in $1-$direction and $\Delta\varepsilon_2$ is the source increment of strain in $2-$direction. Similarly, Hsu/Zhu ratio ν_{21} is defined as the ratio $\Delta\varepsilon_2/\Delta\varepsilon_1$, where $\Delta\varepsilon_2$ is the resulting increment of strain in $2-$direction and $\Delta\varepsilon_1$ is the source increment of strain in $1-$direction. It is to be mentioned that the $1-$direction is the direction of the applied principal tensile stresses, and the $2-$direction is the direction of the applied principal compressive stresses.

The SMM is an extension of the FA-STM with two improvements. One is the inclusion of the two Hsu/Zhu ratios to consider the Poisson effect, and the other is the derivation of a simple, but rational, shear modulus of concrete.

Equilibrium and Compatibility Equations

The equations for stress equilibrium and strain compatibility are identical to those in the FA-STM, which are repeated as follows:

$$\sigma_\ell = \sigma_1^c \cos^2\alpha_1 + \sigma_2^c \sin^2\alpha_1 + \tau_{12}^c 2\sin\alpha_1\cos\alpha_1 + \rho_\ell f_\ell \qquad (2.3\text{-}30)$$

$$\sigma_t = \sigma_1^c \sin^2\alpha_1 + \sigma_2^c \cos^2\alpha_1 - \tau_{12}^c 2\sin\alpha_1\cos\alpha_1 + \rho_t f_t \qquad (2.3\text{-}31)$$

$$\tau_{\ell t} = (-\sigma_1^c + \sigma_2^c)\sin\alpha_1\cos\alpha_1 + \tau_{12}^c(\cos^2\alpha_1 - \sin^2\alpha_1) \tag{2.3-32}$$

$$\varepsilon_\ell = \varepsilon_1\cos^2\alpha_1 + \varepsilon_2\sin^2\alpha_1 + \frac{\gamma_{12}}{2}2\sin\alpha_1\cos\alpha_1 \tag{2.3-33}$$

$$\varepsilon_t = \varepsilon_1\sin^2\alpha_1 + \varepsilon_2\cos^2\alpha_1 - \frac{\gamma_{12}}{2}2\sin\alpha_1\cos\alpha_1 \tag{2.3-34}$$

$$\frac{\gamma_{\ell t}}{2} = (-\varepsilon_1 + \varepsilon_2)\sin\alpha_1\cos\alpha_1 + \frac{\gamma_{12}}{2}(\cos^2\alpha_1 - \sin^2\alpha_1) \tag{2.3-35}$$

Although Eqs. 2.3-33 to 2.3-35 appear to be the same as Eqs. 2.3-20 to 2.3-22, the concepts involved in these two sets of equations are quite different. In Eqs. 2.3-33 to 2.3-35, the set of strains, ε_1, ε_2, ε_ℓ, and ε_t, are the biaxial strains, taking into account the Hsu/Zhu ratios. In Eqs. 2.3-20 to 2.3-22 of the FA-STM, however, these same strains are taken as the uniaxial strains, because the Hsu/Zhu ratios were assumed to be zero. In other words, the set of Eqs. 2.3-20 to 2.3-22 are actually special cases of the set of Eqs. 2.3-33 to 2.3-35.

Biaxial Strains vs. Uniaxial Strains (Hsu/Zhu Ratios)

The three basic compatibility equations used in the SMM are based on the biaxial strains, rather than on the uniaxial strains as assumed in the FA-STM and the RA-STM. Since the relationships between the stresses in the equilibrium equations and the biaxial strains in the compatibility equations depend on the Hsu/Zhu ratios, the constitutive laws relating the stresses to the biaxial strains are not unique and thus cannot be determined directly from experiments. All previous constitutive laws for cracked concrete and embedded steel bars as used in the RA-STM and the FA-STM, were based on uniaxial loading (Belarbi and Hsu, 1994; Zhang and Hsu, 1998). Therefore, equations relating the uniaxial strains to the biaxial strains need to be derived, so that the uniaxial strains of cracked concrete can serve as the bridge to connect the biaxial strains in the $\ell - t$ directions to the stresses in the steel. The relationships between the uniaxial strains and the biaxial strains are given as follows (Zhu, 2000):

$$\bar{\varepsilon}_1 = \frac{1}{1-\nu_{12}\nu_{21}}\varepsilon_1 + \frac{\nu_{12}}{1-\nu_{12}\nu_{21}}\varepsilon_2 \tag{2.3-36}$$

$$\bar{\varepsilon}_2 = \frac{\nu_{21}}{1-\nu_{12}\nu_{21}}\varepsilon_1 + \frac{1}{1-\nu_{12}\nu_{21}}\varepsilon_2 \tag{2.3-37}$$

$$\bar{\varepsilon}_\ell = \bar{\varepsilon}_1\cos^2\alpha_1 + \bar{\varepsilon}_2\sin^2\alpha_1 + \frac{\gamma_{12}}{2}2\sin\alpha_1\cos\alpha_1 \tag{2.3-38}$$

$$\bar{\varepsilon}_t = \bar{\varepsilon}_1\sin^2\alpha_1 + \bar{\varepsilon}_2\cos^2\alpha_1 - \frac{\gamma_{12}}{2}2\sin\alpha_1\cos\alpha_1 \tag{2.3-39}$$

where

ε_1, ε_2 = biaxial smeared (average) strains in $1-$ and $2-$ directions, respectively,

$\bar{\varepsilon}_1$, $\bar{\varepsilon}_2$ = uniaxial smeared (average) strains in $1-$ and $2-$ directions, respectively,

$\bar{\varepsilon}_\ell$, $\bar{\varepsilon}_t$ = uniaxial smeared (average) strains in $\ell-$ and $t-$ directions, respectively, and

γ_{12} = biaxial smeared (average) shear strains in $1-2$ coordinate system.

The Hsu/Zhu ratios are given by (Zhu and Hsu, 2002):

$$\nu_{12} = 0.2 + 850\varepsilon_{sf}, \qquad \varepsilon_{sf} \le \varepsilon_y \tag{2.3-40a}$$

or

$$\nu_{12} = 1.9, \qquad \varepsilon_{sf} > \varepsilon_y \tag{2.3-40b}$$

$$\nu_{21} = 0 \tag{2.3-41}$$

where

ε_{sf} = smeared (average) tensile strain of steel bars in $\ell-$ and $t-$ directions, whichever yields first, taking into account Hsu/Zhu ratios.

Eqs. 2.3-36 to 2.3-39 can be used to obtain the uniaxial strains from the biaxial strains, and these uniaxial strains, in turn, will be used to calculate the stresses in cracked concrete (σ_1^c and σ_2^c) and in the steel (f_ℓ and f_t) in the equilibrium Eqs. 2.3-30 to 2.3-32 using the uniaxial constitutive laws of the materials as will be shown hereafter.

Constitutive Relationship of Cracked Concrete in Compression

The constitutive relationships of concrete compressive stress σ_2^c and the uniaxial compressive strain $\bar{\varepsilon}_2$, shown in Fig. 2.3.2, are given as follows:

$$\sigma_2^c = \zeta f_c' \left[2\left(\frac{\bar{\varepsilon}_2}{\zeta\varepsilon_0}\right) - \left(\frac{\bar{\varepsilon}_2}{\zeta\varepsilon_0}\right)^2 \right], \qquad \frac{\bar{\varepsilon}_2}{\zeta\varepsilon_0} \le 1 \text{ (stage C1)} \tag{2.3-42a}$$

or

$$\sigma_2^c = \zeta f_c' \left[1 - \left(\frac{\bar{\varepsilon}_2/\zeta\varepsilon_0 - 1}{4/\zeta - 1}\right)^2 \right], \qquad \frac{\bar{\varepsilon}_2}{\zeta\varepsilon_0} > 1 \text{ (stage C2)} \tag{2.3-42b}$$

where

$$\zeta = \frac{5.8}{\sqrt{f_c'}} \frac{1}{\sqrt{\left(1 + \dfrac{400\bar{\varepsilon}_1}{\eta'}\right)}} \le 0.9 \tag{2.3-43}$$

and $$\eta = \frac{\rho_t f_{ty} - \sigma_t}{\rho_\ell f_{ly} - \sigma_\ell}, \qquad 0.2 < \eta < 5 \qquad (2.3\text{-}44)$$

η' in Eq. 2.3-43 is η or its reciprocal whichever is less than unity.

Constitutive Relationship of Cracked Concrete in Tension

Based on the previous uniaxial tests, the smeared (average) stress-strain relationship of concrete in tension, shown in Fig. 2.3.2, was obtained as follows (Belarbi and Hsu, 1994):

$$\sigma_1 = E_c \bar{\varepsilon}_1, \qquad \bar{\varepsilon}_1 \le \varepsilon_{cr} \ \text{(stage T1)} \qquad (2.3\text{-}45a)$$

or $$\sigma_1 = f_{cr}\left(\frac{\varepsilon_{cr}}{\bar{\varepsilon}_1}\right)^{0.4}, \qquad \bar{\varepsilon}_1 > \varepsilon_{cr} \ \text{(stage T2)} \qquad (2.3\text{-}45b)$$

where

E_c = elastic modulus of concrete taken as $3875\sqrt{f'_c}$ (f'_c and $\sqrt{f'_c}$ are in MPa),

ε_{cr} = concrete cracking strain taken as 0.00008, and

f_{cr} = concrete cracking stress taken as $0.31\sqrt{f'_c}$ (f'_c and $\sqrt{f'_c}$ are in MPa).

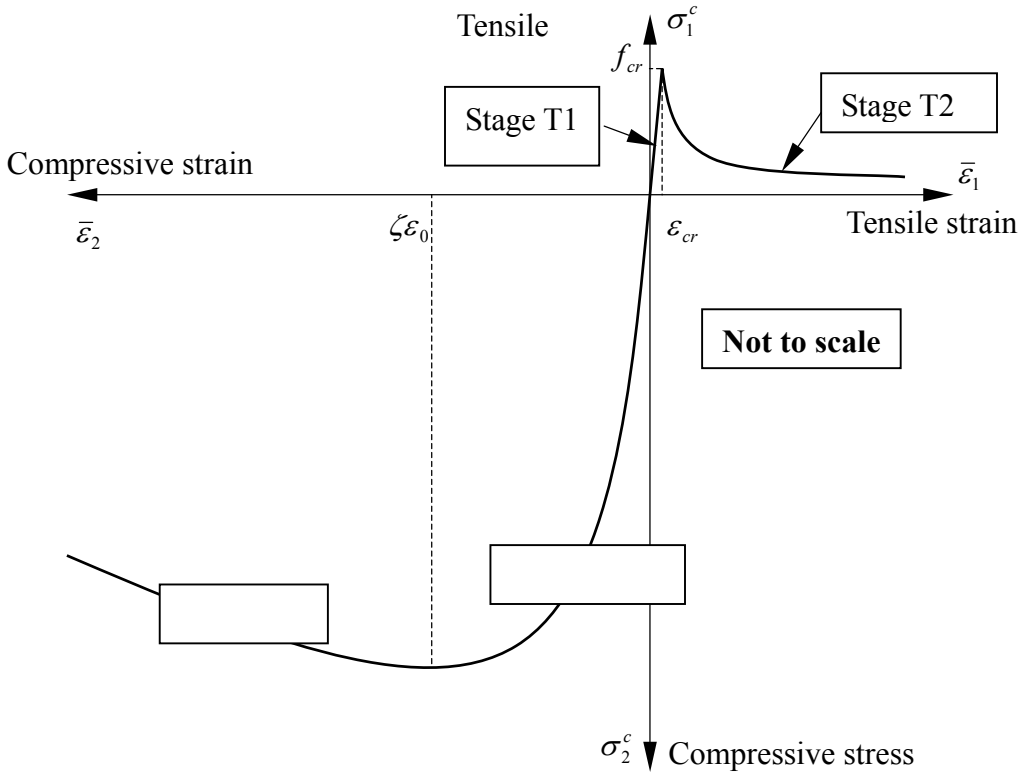

Fig. 2.3.2 Constitutive Laws of Concrete in Tension and Compression

Constitutive Relationship of Cracked Concrete in Shear

Zhu, Hsu, and Lee (2001) showed that the relationship between the shear stress and the shear strain of cracked concrete in the $1-2$ coordinate system could be rationally derived from the equilibrium equations and the compatibility equations by assuming that the direction of principal stresses coincides with the direction of principal strains. The new constitutive law of concrete in shear is given as:

$$\tau_{12}^c = \frac{\sigma_1^c - \sigma_2^c}{2(\varepsilon_1 - \varepsilon_2)}\gamma_{12} \qquad (2.3\text{-}46)$$

Constitutive Relationship of Steel Bars Embedded in Cracked Concrete

The smeared (average) tensile stress-strain relationship of steel embedded in concrete in the $\ell - t$ coordinate, shown in Fig. 2.3.3, can be expressed as follows:

$$\text{Stage 1:}\quad f_s = E_s\bar{\varepsilon}_s, \qquad \bar{\varepsilon}_s \le \bar{\varepsilon}_n \qquad (2.3\text{-}47a)$$

$$\text{Stage 2:}\quad f_s = f_y\left[(0.91-2B)+(0.02+0.25B)\frac{\bar{\varepsilon}_s}{\varepsilon_y}\right], \qquad \bar{\varepsilon}_s > \bar{\varepsilon}_n \qquad (2.3\text{-}47b)$$

Stage 3 (unloading): $f_s = f_p - E_s(\bar{\varepsilon}_p - \bar{\varepsilon}_s)$, $\bar{\varepsilon}_s < \bar{\varepsilon}_p$ (2.3-47c)

where $\bar{\varepsilon}_n = \varepsilon_y(0.93 - 2B)$ (2.3-48)

and $B = \frac{1}{\rho}\left(\frac{f_{cr}}{f_y}\right)^{1.5}$ (2.3-49)

In the above equations, ℓ replaces s in the subscript of symbols for the longitudinal steel, and t replaces s for the transverse steel. In Eq. 2.3-48, recent tests (Chintrakarn, 2001) show that the originally specified minimum ρ of 0.5% can be reduced to 0.25%.

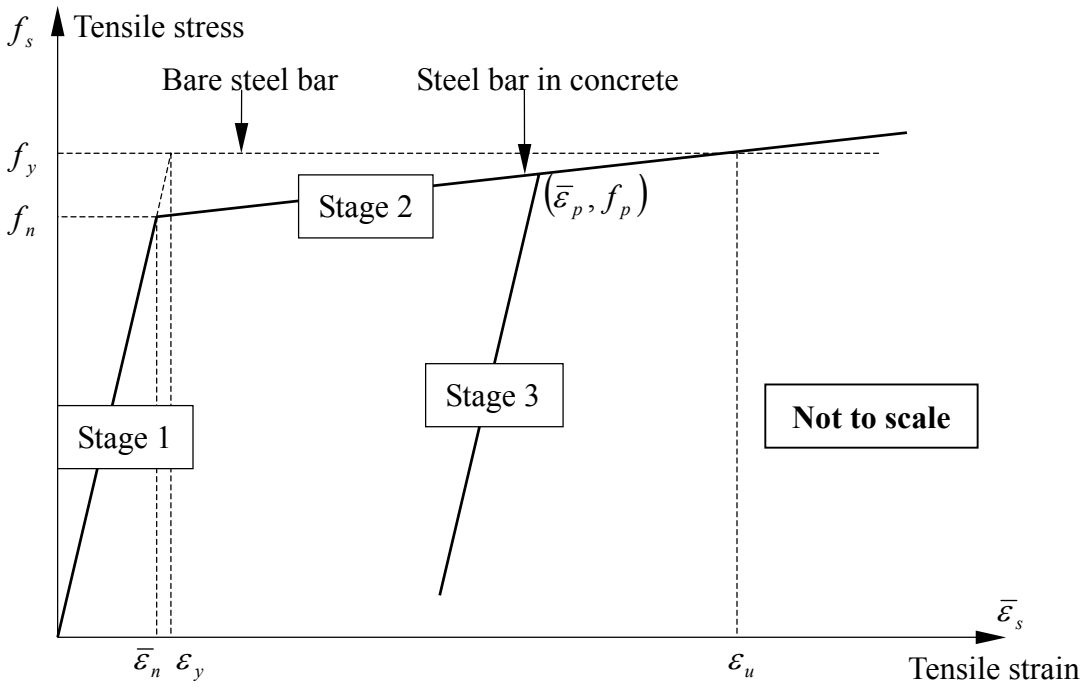

Fig. 2.3.3 Constitutive Law of Steel Bars

Solution Algorithm

The solution procedure for the softened membrane model is given by the flow chart in Fig. 2.3.4. The following two equilibrium equations, which make the solution procedure more efficient, are derived from the basic equilibrium equations 2.3-30 and 2.3-31:

$$\rho_\ell f_\ell + \rho_t f_t = (\sigma_\ell + \sigma_t) - (\sigma_1^c + \sigma_2^c) \quad (2.3\text{-}50)$$

$$\rho_\ell f_\ell - \rho_t f_t = (\sigma_\ell - \sigma_t) - (\sigma_1^c - \sigma_2^c)\cos 2\alpha_1 - 2\tau_{12}^c \sin 2\alpha_1 \quad (2.3\text{-}51)$$

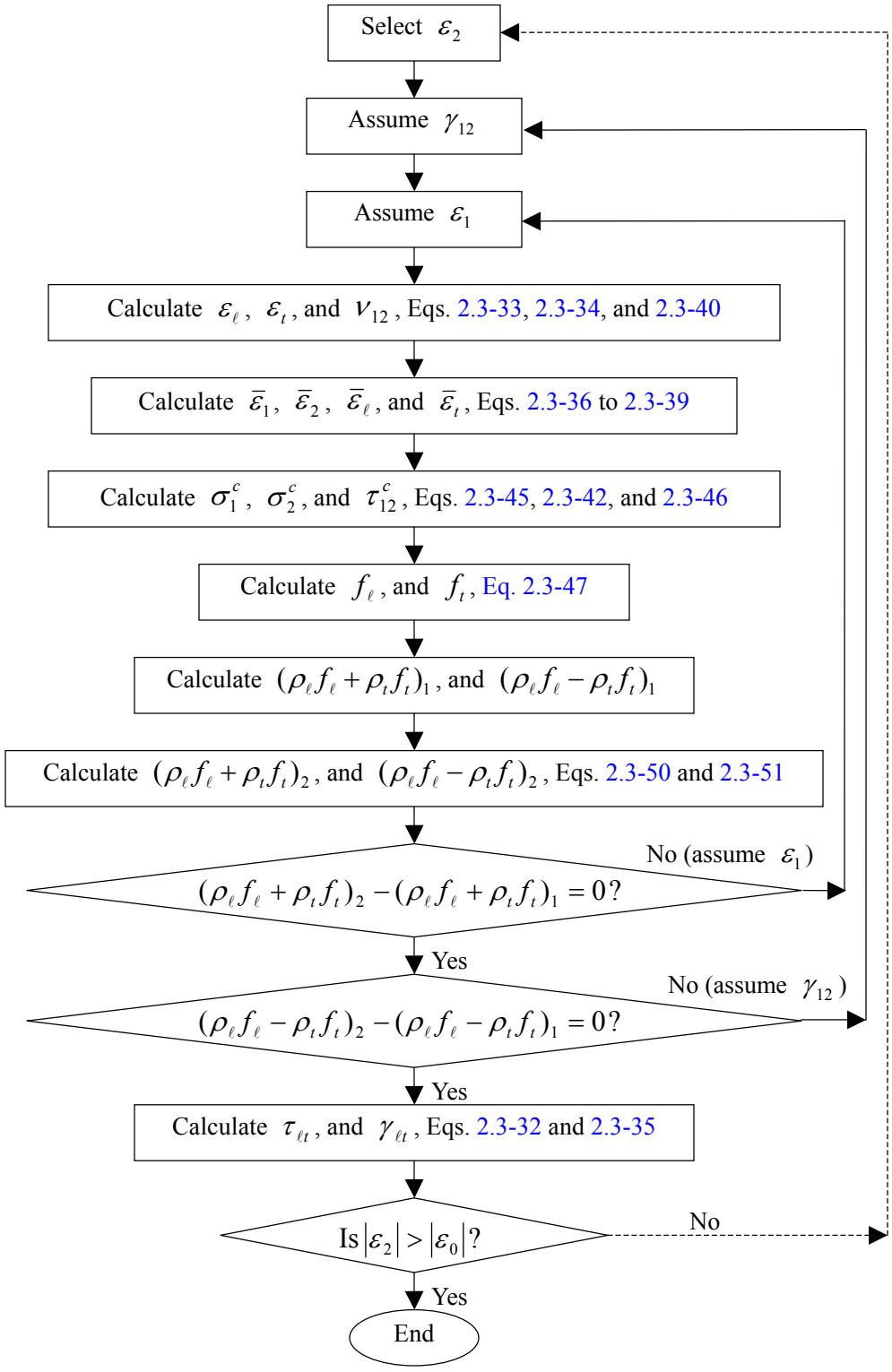

Fig. 2.3.4 Flow Chart of Solution Procedure for Softened Membrane Model

2.4 Literature Survey on Shear Behavior of Prestressed Concrete Panels

Very little experimental research has been done on the behavior of prestressed concrete membrane elements (panels) under shear stresses. The main difficulties involved in performing these kinds of tests were the high cost of testing equipment and the complexity in fabricating prestressed concrete panels.

Marti and Meyboom (1992) discussed the influence of prestressing on the behavior of orthogonally reinforced concrete elements subjected to in-plane shear forces. Meyboom (1987) reported three tests performed on the University of Toronto's shell element tester. All three specimens had identical dimensions of $1626\,\text{mm} \times 1626\,\text{mm} \times 287\,\text{mm}$ $(64\,\text{in.} \times 64\,\text{in.} \times 11.3\,\text{in.})$. The only variable was the amount of prestressing in the 45-degree direction: Specimen PP1 was not prestressed, Specimen PP2 was prestressed to 2.07 MPa (301 psi), and Specimen PP3 was prestressed to 4.40 MPa (638 psi). Based on these test results, the authors concluded that prestressing results in higher cracking loads, reduced reorientation of the internal forces after cracking, delayed degradation of the concrete, smaller strains in the reinforcements at ultimate, and higher ultimate loads. The experimental responses were compared with the predicted responses made by linear, nonlinear, and limit analyses as given in the paper. However, there were several deficiencies in the study: First, they did not give the properties of materials in prestressed concrete panels, so only a qualitative analysis could be performed. The effect of prestressing on the constitutive laws of the concrete was not clarified. Second, since mild steel bars were oriented in the direction of the unbonded prestressing bars, the crack patterns were caused mainly by the distribution of the mild steel bars. Finally, the descending branches for the shear stress-strain curve could not be obtained because the tester was not equipped with a servo-controlled system.

Rahal (2002) proposed a method for the analysis and design of concrete membrane elements subjected to in-plane shear and normal stresses, which is a simplification of the modified compression field theory (Vecchio and Collins, 1986). In this method, a prestress force was simply considered as a superimposed normal stress on the panels. The experimental results of Meyboom (1987) were used to check his method. It was concluded that a significant increase of prestressing stresses produced only a slight increase in shear strength. Also, the effect of prestressing on the shear behavior of the prestressed concrete elements could not be verified due to the limitation of experimental results.

CHAPTER 3

CRACK SIMULATION TESTS

3.1 General Description

Prestressed concrete is classified into "pre-tensioned concrete" and "post-tensioned concrete" by the sequence of concrete placement and tensioning of high-strength steel. Pre-tensioning technology is more commonly used than post-tensioning in highway bridges, because it is more convenient for mass production. According to ACI 318-02 Eq. 12-2, the transfer length in concrete pre-tensioned by 270K (1862 MPa) strands with an assumed effective stress of 965 MPa (140 ksi) is 50 times the strand diameter, giving 750 mm (30 in.) and 625 mm (25 in.) for diameters of 0.6 in. (15 mm) and 0.5 in. (13 mm) strands, respectively. The corresponding development lengths in pre-tensioned concrete are 2692 mm (106 in.) and 2235 mm (88 in.), respectively. Since these transfer lengths and development lengths are too large for the test panels of 1398 mm × 1398 mm (55 in. × 55 in.), the post-tensioning method was chosen for the test panels in this research. The post-tensioned strands were placed in flexible conduits and then grouted.

A trial panel, labeled TE-2, was first tested. The arrangement of the reinforcements of panel TE-2 is shown in Fig. 3.1.1. Prestressing tendons were placed in the longitudinal direction and the post-tensioning technology was used. This panel was tested under applied tensile forces in the longitudinal direction. The crack pattern of panel TE-2 at 2% tensile strain is shown in Fig. 3.1.2. The crack spacing, approximately 610 mm (24 in.), was excessive due to the weak bond between the prestressing tendons and the cementitious grout. The smeared-crack concept as an average quantity of strain could not be applied in this case with only two big cracks occurring in the measurement zone. Therefore, a series of crack simulation tests was performed to improve the bond condition between the steel tendons and the cementitious grout. The purpose of the study was to find the same cracking pattern of post-tensioned concrete with conduits as that in pre-tensioned concrete without conduits.

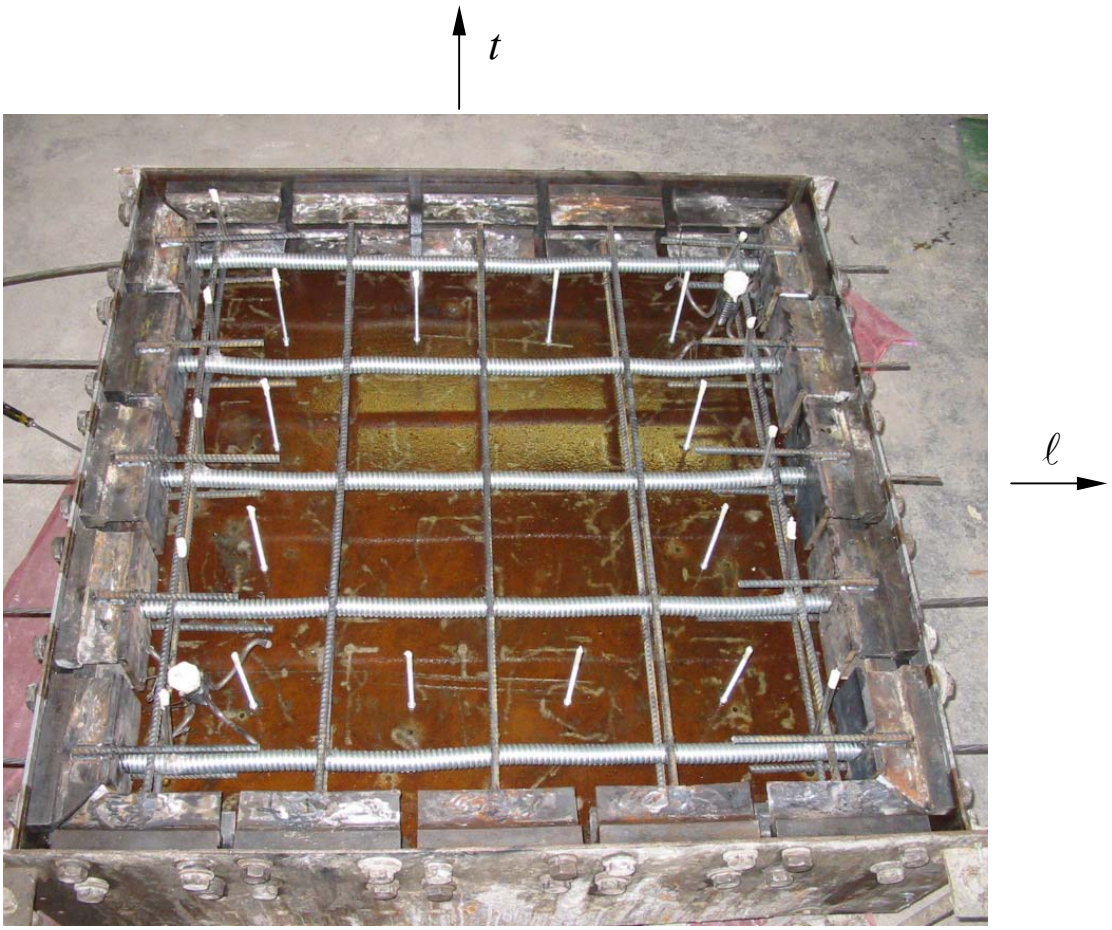

Fig. 3.1.1 Arrangement of Reinforcement in Trial Panel TE-2

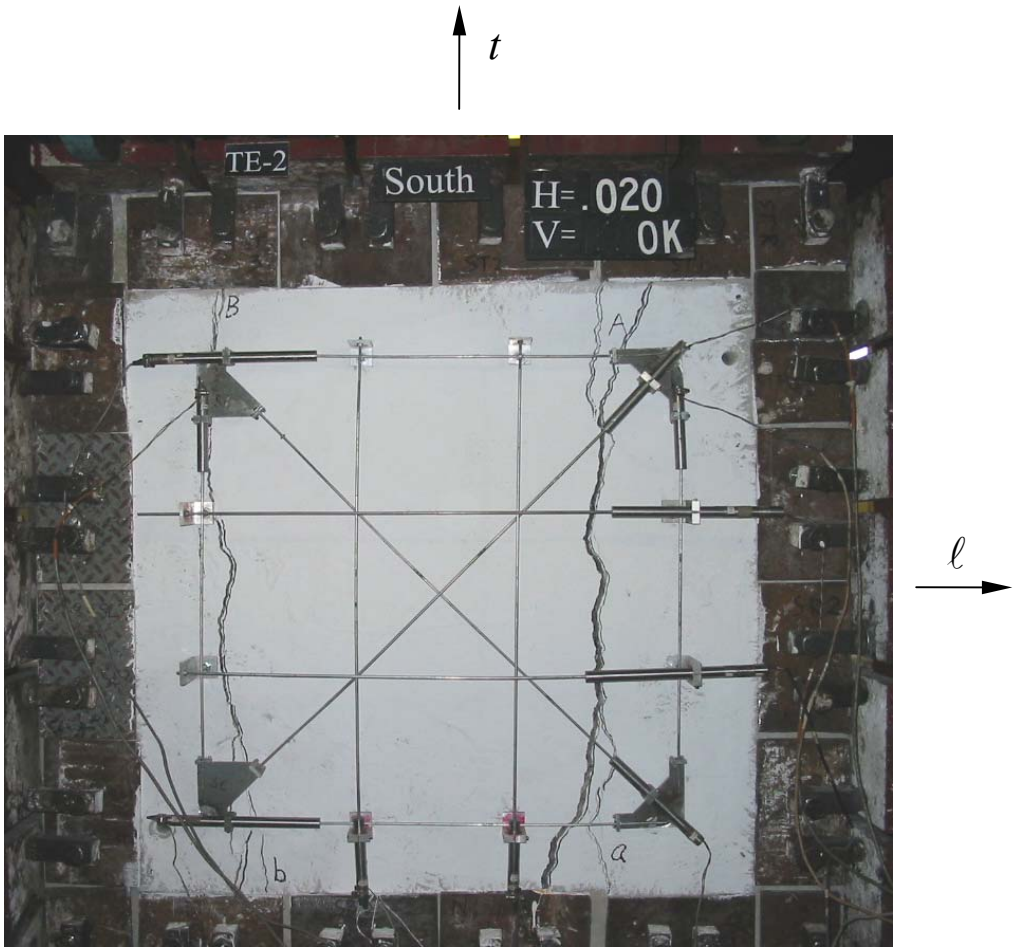

Fig. 3.1.2 Crack Pattern of Trial Panel TE-2 at 2% Tensile Strain

3.2 Test Program

Bond stress is primarily the result of the shear interlock between the reinforcing element and the enveloping concrete. According to Nawy's textbook (1985) for reinforced concrete, bond strength is controlled by the following major factors: (1) adhesion between the concrete and the reinforcement; (2) gripping effect resulting from the drying shrinkage of the surrounding concrete; (3) frictional resistance to sliding and interlock as the reinforcement is subjected to tensile stress; (4) effect of concrete quality and strength in tension and compression; and (5) diameter, shape, and spacing of reinforcement as they effect crack development. Three types of tests can be used to determine the bond quality of the reinforcement: the pull-out test, the embedded-rod test, and the beam test. The concept of the embedded-rod test was used in this research.

Ten specimens were designed to study the cracking patterns as related to the bond condition between the prestressing tendons and the concrete. Four variables were included in the study as

shown in Table 3.2.1: namely, the number of tendons, the presence or absence of flexible conduit, the strength of cementitious grout, and the percentage of the mild steel in the concrete. In order to provide a high prestress force on concrete, the prestressing tendons with 0.6 in. (15 mm) iameter were used. The corrugated flexible conduit, which has a diameter of 32 mm (1-1/4 in.), is assumed to carry no axial loading, but is capable of transferring bond stresses. The specimens without the flexible conduits have the same bond condition as that in the pre-tensioned concrete. Three types of grouts were injected into the flexible conduits after prestressing. LSG represents Low Strength Grout with 6.9 MPa (1000 psi) compressive strength at two to three days. HSG means High Strength Grout with 13.8 MPa (2000 psi) compressive strength at two to three days. SCCG stands for Self-Compacting Concrete Grout with 41.4 MPa (6000 psi) compressive strength at two to three days and with great workability.

Table 3.2.1 Variables of 10 Specimens

Specimen	Number of Prestressing Tendons	Flexible Conduit	Cementitious Grout*	Mild Steel
TSB1	1	w	LSG	w/o
TSB2	1	w/o	N/A	w/o
TSB3	1	w	HSG	w/o
TSB4	1	w	HSG	2 #2
TSB5	1	w	HSG	2 #4
TSB6	2	w/o	N/A	w/o
TSB7	4	w/o	N/A	w/o
TSB8	2	w	SCCG	w/o
TSB9	2	w	SCCG	w/o
TSB10	4	w	SCCG	w/o

* LSG = Low Strength Grout,
HSG = High Strength Grout, and
SCCG = Self-Compacting Concrete Grout

3.3 Test Specimens

Ten test specimens were cast in two groups and had the same dimensions of 1398 mm × 257 mm × 178 mm (55 in. × 10.125 in. × 7 in.).

In the first group, specimens TSB1 to TSB5, a single prestressing tendon was placed in the center plane of each specimen. All specimens were cast with flexible conduits, except specimen TSB2, in which a prestressing tendon was directly embedded in the concrete to simulate the bond condition in the pre-tensioned concrete. LSG was used as the grouting material in specimen TSB1; and HSG was employed in specimens TSB3, TSB4, and TSB5. Specimen TSB2 had no grout at all. Two #2 and two #4 mild steel bars were placed in specimens TSB4 and TSB5, respectively. The concrete compressive strength was 398 MPa (5776 psi) in this group.

In the second group, specimens TSB6 to TSB10, each specimen was designed with two layers of prestressing tendons in the 178 mm (7 in.) thickness direction, and no mild steel bars. Two prestressing tendons were designed in specimens TSB6, TSB8, and TSB9, while four were in specimens TSB7 and TSB10. No flexible conduit was placed in specimens TSB6 and TSB7 to simulate the pre-tensioned concrete. Specimens TSB8, TSB9, and TSB10 had flexible conduits which were injected with SCCG. The concrete compressive strength was 36.7 MPa (5323 psi) in this group.

3.3.1 Fabrication of Specimens

The first group of specimens TSB1 to TSB5 and the second group of specimens TSB6 to TSB10 were cast separately as shown in Fig. 3.3.1 and Fig. 3.3.2, respectively. All 10 specimens were cast in a precisely made steel form, which was initially used to cast tested panels with sizes of 1398 mm × 1398 mm (55 in. × 55 in.). The steel form was separated into five strips of 257 mm (10.125 in.) width, divided by six steel plates sized 1398 mm × 191 mm × 10 mm (55 in. × 7.5 in. × 0.375 in.).

Specimens TSB1 to TSB5 were cast and tested first. At each end of the specimen, there were two regular horizontal anchor-inserts welded together by a 13 mm (0.5 in.) thick steel bearing plate (Grade A36) with a 38 mm (1.5 in.) diameter hole at its center. This set of inserts can hold and anchor a tendon so that the tensile forces from the jacks can be transferred to the prestressing tendon.

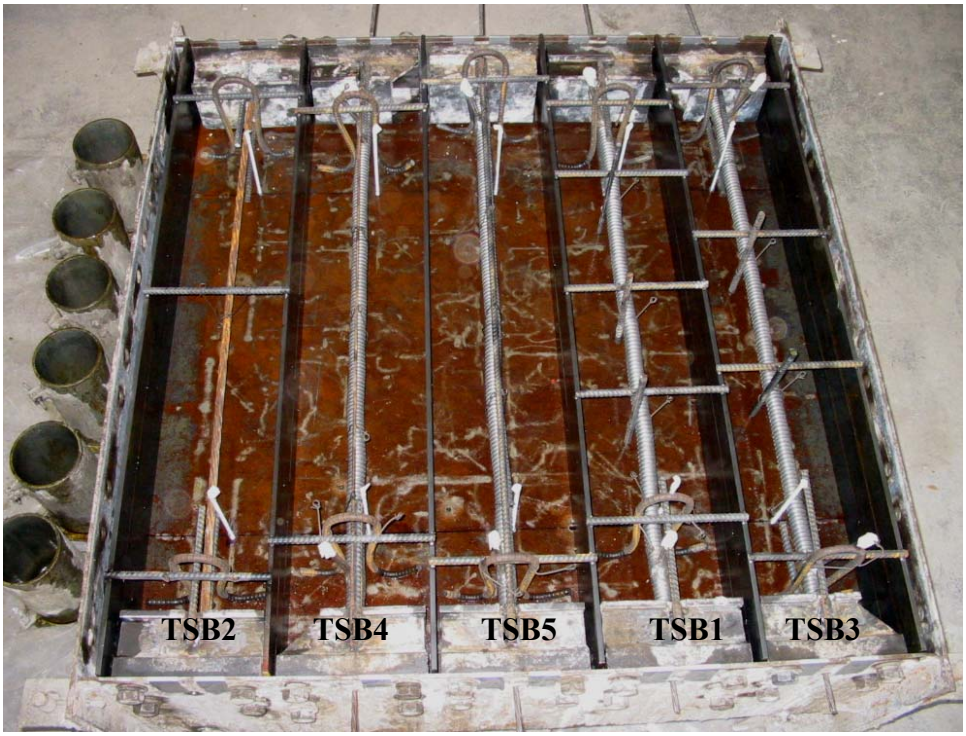

Fig. 3.3.1 Formwork for Crack Simulation Tests (TSB1 to TSB5)

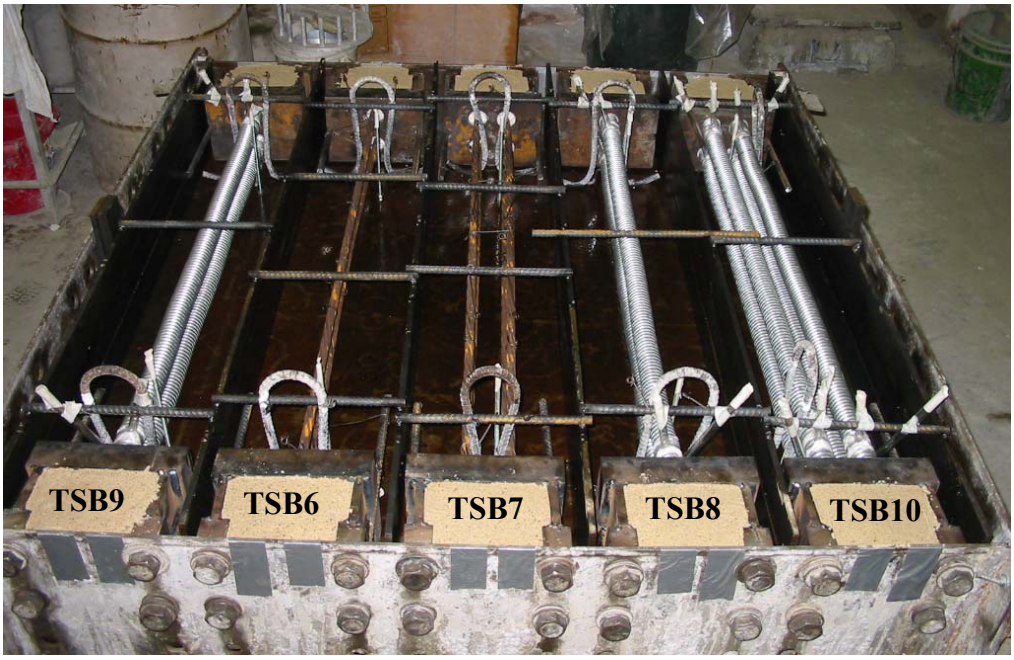

Fig. 3.3.2 Formwork for Crack Simulation Tests (TSB6 to TSB10)

To provide a higher prestress force on concrete, more tendons had to be placed in the specimens. A new U-shape insert, Fig. 3.3.3, was designed which consisted of two vertical anchor-inserts and a bearing plate. The new U-shape inserts can provide more space for multiple tendons, up to four tendons in one specimen. Three threaded holes of 25 mm (1 in.) diameter were needed on each vertical anchor-insert to ensure the connection between the yokes and the specimens.

After testing specimens TSB1 to TSB5, permanent deformations were observed on their bearing plates. Therefore, higher strength or thicker bearing plates were indicated. A finite element software, SAP2000, was applied to analyze the stress distribution on the bearing plates with different thickness. As a result, the high strength steel (A572-50) with a nominal yielding strength of 345 MPa (50 ksi) was chosen to make the bearing plates. The thickness was designed to be 25 mm (1 in.) for the plates with one tendon and 51 mm (2 in.) for those with two or four tendons. The two anchor-inserts were made of the high-strength steel of 448 MPa (65 ksi) yield strength instead of the regular Grade A36 steel. Fig. 3.3.3 shows the dimensions and the photo of U-shape inserts for four tendons.

The whole procedure of assembling and casting is summarized as follows. First, the steel casting form and the six dividing plates were oiled. U-shape inserts were then installed in the casting form by tightening the bolts to ensure the accurate positions. Sand was used to fill the space between the inserts and the form, leaving room for the tendon chucks. After that, the flexible conduits were placed in the specimens between the U-shape inserts at two ends; and steel pipes with 19 mm (3/4 in.) diameters were put inside the flexible conduits to make them straight. Near each end of the flexible conduits, a hole on the conduits was connected to a plastic tube, which was used to inject grout into the flexible conduits after the tendons were stressed. Next, 10 threaded rods, used to fasten the brackets of LVDTs during testing, were attached to the bottom plate of the form. Two pick-up hooks were fixed in each specimen. Finally, all the positions were checked and the concrete was cast. The concrete was divided into two batches for casting each group. Fig 3.3.4 shows the specimens after casting concrete.

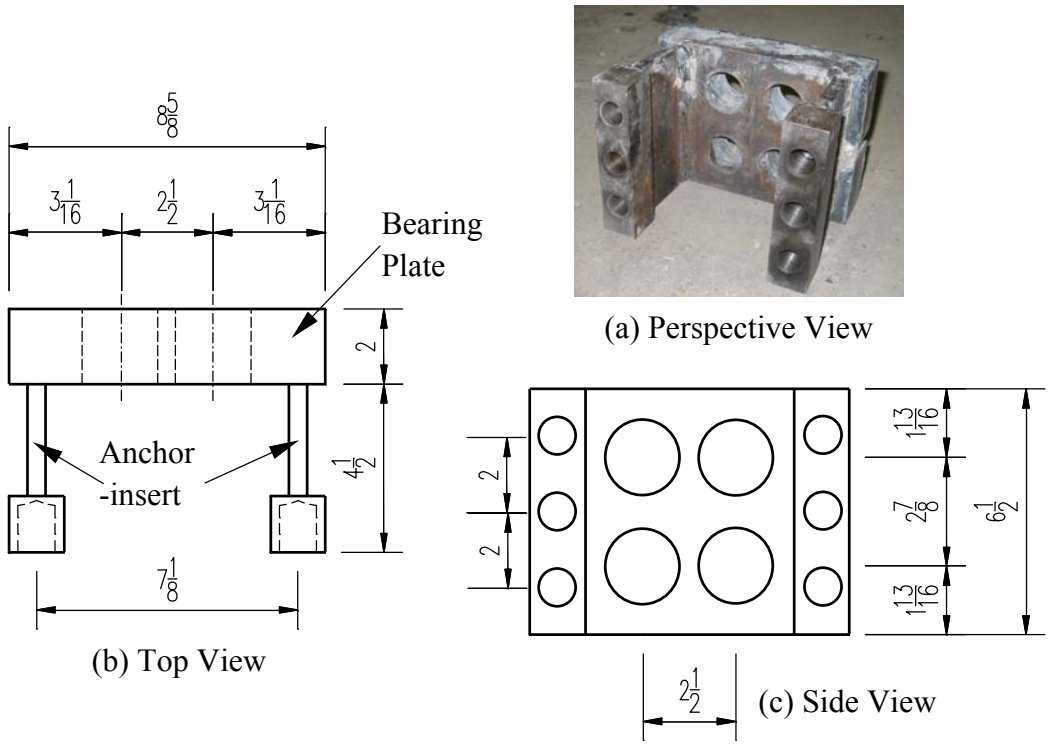

Fig. 3.3.3 Dimensions of U-Shape Inserts (Unit: in.)

Fig. 3.3.4 Specimens after Casting Concrete

3.3.2 Tendon Jacking System

The jacking system, as shown in Fig. 3.3.5, applies the prestressing force to the steel tendons. In the post-tensioning method, the tendons were jacked sequentially. The equipment for the jacking system includes: a hydraulic jack, a pump, a pressure relief valve, load cells, a strain indicator, a data acquisition system, a home-made supporting chair, and three chucks.

The hydraulic jack used in this research is the double-acting hollow plunger cylinder RRH-3010 from Enerpac Co. The advance cylinder capacity is 351 kN (79 kips). The stroke is 254 mm (10 in.), and the diameter of the center hole is 33 mm (1.31 in.). An electric pump with a four-way valve, made by Owatonna Tool Co., MN, was used to power the hydraulic jack with an oil pressure up to 69 MPa (10,000 psi). A model V-152 pressure relief valve, manufactured by Enerpac Co., is able to control the pressure developed by the pump within a range of 5.5 to 69 MPa (800 to 10,000 ksi), thus controlling the force in the hydraulic jack.

Two types of load cells, manufactured by Transducer Techniques Inc., CA, were used in the jacking system, namely, THD-50 and LWO-60. THD-50 is a "thru-hole" load cell 25 mm (1 in.) thick, with a 76 mm (3 in.) outer diameter and a 41 mm (1.6 in.) inner diameter. The compressive capacity is 222 kN (50 kips). It was used to measure the tensile force in the prestressing tendons during the jacking procedure. The reading was indicated by a strain indicator.

LWO-60 is a thru-hole "load washer" load cell with a compressive capacity of 267 kN (60 kips). The outer and inner diameters are 44 mm (1.75 in.) and 23 mm (0.897 in.), respectively. The thickness is only 13 mm (0.5 in.). This type of load cells can be placed inside the specimens between the chucks and the bearing plates to monitor the tensile forces in the tendons during and

after prestressing. A data acquisition system called Spider 8 was used to collect the readings from all the LWO-60 load cells.

The supporting chair consists of two 25 mm (1 in.) thick steel plates, four threaded bolts, and eight nuts. The chair is designed to transfer the force of the hydraulic jack to the test specimen. The height of the chair is adjustable.

Fig. 3.3.5(a) is a sketch of the tendon jacking system. Three chucks are used in the jacking system. The first chuck on the left end, which is next to a load cell LWO-60, grips one end of the tendon. On the right end, the second chuck holds the tendon against the hydraulic jack. Load cell THD-50 is placed between this chuck and the jack piston (Fig. 3.3.5(c)). The jack sits on the supporting chair against the specimen. The third chuck is located in the space enclosed by U-shape inserts. This chuck is kept loose during the jacking process, but catches the tendon once the releasing procedure starts.

After all the setup was ready, the pump would be turned on to increase the pressure in the jack. The whole jacking procedure was summarized into five steps. First, a small force was applied to tighten the setup, and the positions of all the components were checked. Second, the tendon was pulled until the desired tensile force was reached. The pulling stage was divided into about 15 steps. At each step, the readings from load cells THD-50 and LWO-60 were recorded. Because the thickness of LWO-60 was very small, the reading was very sensitive to the eccentricity of the load (did not happen on THD-50). Therefore, the data from THD-50 would be used to calibrate the LWO-60 load cells.

In the third step, the nut bearing against the right plate of the supporting chair was turned to push and tighten the chuck against the test specimen, as shown in Fig. 3.3.5(b). This is one of the two methods to reduce the prestress loss due to the anchorage slippage. The other method is to utilize the pressure relief valve. Fourth, the pressure relief valve was turned to slowly release the pressure in the hydraulic jack. By applying those two methods, the prestress loss could be minimized. These two methods not only reduced the prestress loss, but also stabilized the loss, which could make the forces in the tendons more uniform in the test panel. The data showed that the effective stress in 0.6 in. tendons was approximately 965 MPa (140 ksi) with a jacking stress of 1303 MPa (189 ksi). Upon release, the middle chuck served to catch the tendon. Finally, all equipment was removed from the specimen and the redundant parts of the tendons were cut off.

In addition to slippage and elastic loss, prestress losses also include time-related losses, such as creep and shrinkage in the concrete and relaxation in the steel. To limit these time-dependent losses and to keep the high prestressed forces on the specimens, tests were conducted as soon as possible after the tensioning procedure. Experience shows that two to three days would be needed to inject grout into the flexible conduits, to install yokes, to put specimens in the Univers-

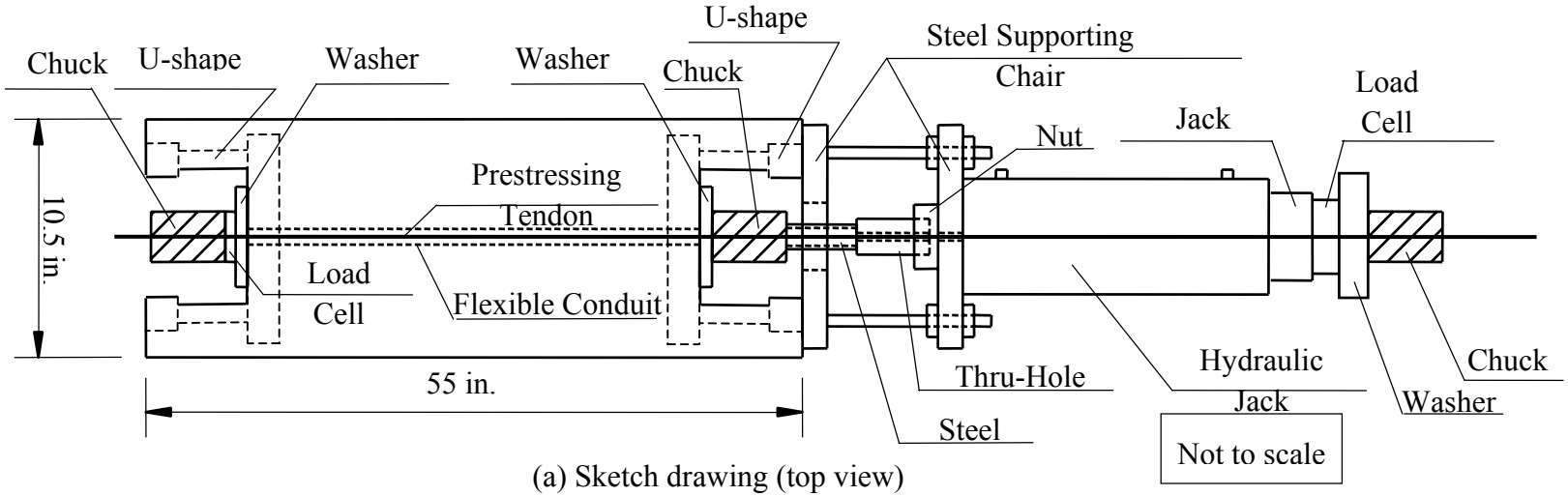

(a) Sketch drawing (top view)

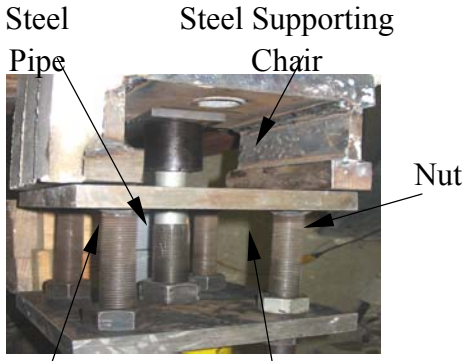

(b) Details inside supporting chair

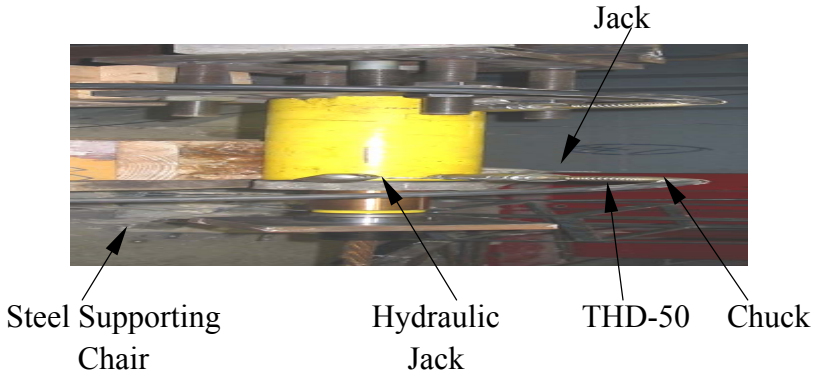

(c) Setup of pulling end

Fig. 3.3.5 Tendon Jacking System

al Panel Tester, and to install Linear Voltage Displacement Transducers (LVDTs), etc. For this reason, the strength of grouting materials at two to three days was important and was taken as the criterion for choosing suitable grout.

3.4 Materials

3.4.1 Concrete

A cylinder compressive strength of 41.4 MPa (6000 psi) was chosen as the target strength of the concrete in the test specimens. The concrete mix proportion (based on weight) was 1:2.64:2.93, corresponding to cement, sand, and coarse aggregate, respectively. The water-cement ratio was about 0.6. Since sand always contains some water, the water-cement ratio was controlled by the slump test. The desired slump was 178 mm (7 in.). Type I Portland cement was used. Concrete sand conformed to ASTM C33, while the graded limestone aggregate had a maximum size of 19 mm (3/4 in.).

Six standard cylinders, with the dimensions of 152 mm × 305 mm (6 in. × 12 in.), were cast along with each group of specimens. The cylinders were cured under the same environmental conditions as that of the specimens, that is, seven days under moist environment covered by the plastic sheet and the remaining time in the air-conditioned laboratory until testing. A Tinius Olsen Universal testing machine with a capacity of 1779 kN (400 kips) was used to test the cylinders using a strain rate of around 400 micro strains per minute. The standard cylinders were tested at the same age as the test specimens and capped with a high strength sulfur compound before testing.

Three types of grouting materials were used in the test specimens: LSG, HSG, and SCCG. The mix proportion was 1:1:0.5 for LSG, corresponding to cement, sand, and water, respectively; 1:0.3:0.5 for HSG; and 1:1.5:0.37 for SCCG. In addition, 0.126 oz (3.57 g) of High Ratio Water Reduction (HRWR) agent was used for every 1 pound (454 g) of cement in SCCG. To obtain a high concrete strength in two to three days, Type III Portland cement was used in all three grouting materials. The compressive strength of grout was obtained from the tests of 76 mm × 152 mm (3 in. × 6 in.) cylinders.

3.4.2 Reinforcements

The stress-relieved strands, grade 270 (1862 MPa), which conformed to ASTM A-416, were donated by Texas Concrete Company, Victoria, TX. Each strand was made from seven wires by twisting six of them around a slightly larger, straight central wire. In this experiment, the strands had a nominal diameter of 0.6 in. (15 mm), a cross-sectional area of 140 mm^2 (0.217 $in.^2$), an ultimate strength of 1862 MPa (270 ksi), and an elastic limit of 1396 MPa (203 ksi) (75% of the ultimate strength). The solid line in Fig. 3.4.1 shows the typical stress-strain relationship of the strands, which is the average of three color lines representing the stress-strain curves from three strand tests.

The low-alloy, grade 60 (415 MPa) steel bars, which satisfied ASTM 716, were used in the specimens. Two sizes of deformed bars #2 and #4, with cross-sectional areas of 32 mm^2 and 129 mm^2 (0.05 in^2 and 0.2 in^2), were placed in TSB4 and TSB5, respectively. The #2 bars were manufactured in Sweden (could be purchased from Portland Cement Association in the United States) and the #4 bars were custom-made and donated by Chaparral Steel Co. of Midlothian, TX. At least three coupons for each size of steel bars were tested in the Tinus Olsen Universal testing machine to obtain the stress-strain curves. The tensile strains were measured by an extensometer capable of measuring strains up to 0.25. The mechanical properties of the steel bars used in the test program are listed in Table 3.4.1.

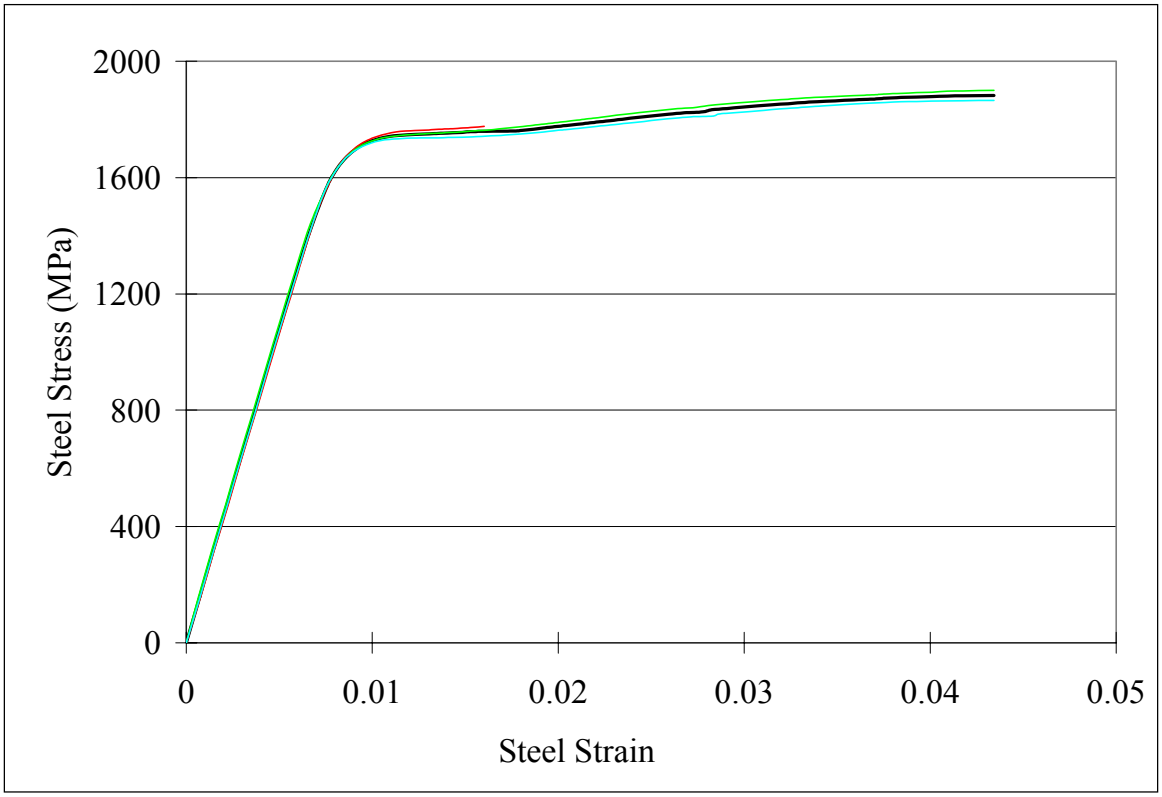

Fig. 3.4.1 Stress-Strain Curve of Bare Strands

Table 3.4.1 Mechanical Properties of Steel Bars

Steel Bar	f_y (MPa)	ε_y	E_s (GPa)	ε_h
#2	419.2	0.00250	187.5	-
# 4	415.1	0.00216	192.2	0.0176

Note: ε_h is the strain at the beginning of the strain hardening region

3.5 Loading Procedure

The specimens in the test program were tested using the Universal Panel Tester. Two yokes were first attached to the ends of a specimen by high-strength bolts. Then the specimen was connected to jack N10, S10, N16, and S16, while a roller was placed at the bottom to support the specimen. The roller was removed when the test began. The test setup for a typical specimen is shown in Fig. 3.5.1, where the photo in (a) shows the specimen installed in the Universal Panel Tester and (b) shows the axial tensile forces on the embedded-rod specimen.

The 10 specimens were each subjected to a uniaxial tensile load supplied by four jacks (jacks N10, S10, N16, and S16) controlled by manifold 4. Two LVDTs were installed on the two opposite faces of a specimen to measure the smeared strains. The average values of the two LVDT signals were collected and sent to controller 4 as strain feedback. Once all the jacks and the LVDTs were ready, the horizontal tensile load was applied to the specimen using the load-control method and the strain-control method before and after the elastic limit of prestressing tendons, respectively. The elastic limit is taken as 1303 MPa (189 ksi), the peak of the elastic stage in the stress-strain relationship of bare prestressing tendons.

(a)

(b)

Fig. 3.5.1 Test Setup for a Typical Specimen

3.6 Test Results

In the embedded-rod test specimens, the number of cracks, their widths, and their spacing at various loading levels were a measure of the bond stress development between the concrete and the tendons. The crack widths were measured by microscopes with a precision of 0.025 mm

(0.001 in.). The average crack spacings of the specimens were taken as the main criterion for the comparisons.

Fig. 3.6.1 shows the crack patterns of specimens TSB2 and TSB3, and Fig. 3.6.2 shows those for specimens TSB6 and TSB8. In these two figures, the photos for each specimen under various loading were pasted together and the load stages H were labeled by either tensile loads or tensile strains. Fig. 3.6.1 and Fig. 3.6.2 show that the number of cracks remained constant beyond a certain load (named the critical load), and further increase of loading only increased the crack widths. Half of the crack spacing beyond the critical load represents the minimum length for a tendon to transfer its stresses to the surrounding concrete to cause cracking. This crack spacing is a direct function of the bond strength. The smaller the crack spacing, the stronger the bond strength. Therefore, the average crack spacings of the specimens were calculated based on the measured crack spacings after the critical loads and are listed in Table 3.6.1.

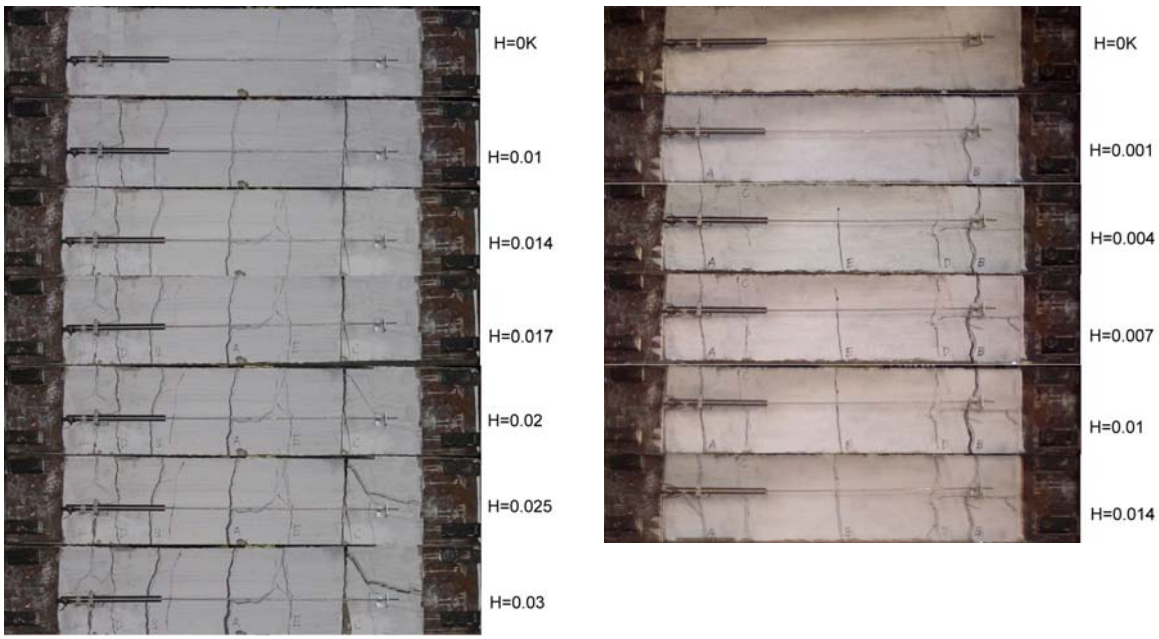

(a) TSB2-North (b) TSB3-North

Fig. 3.6.1 Crack Patterns of Specimens TSB2 and TSB3

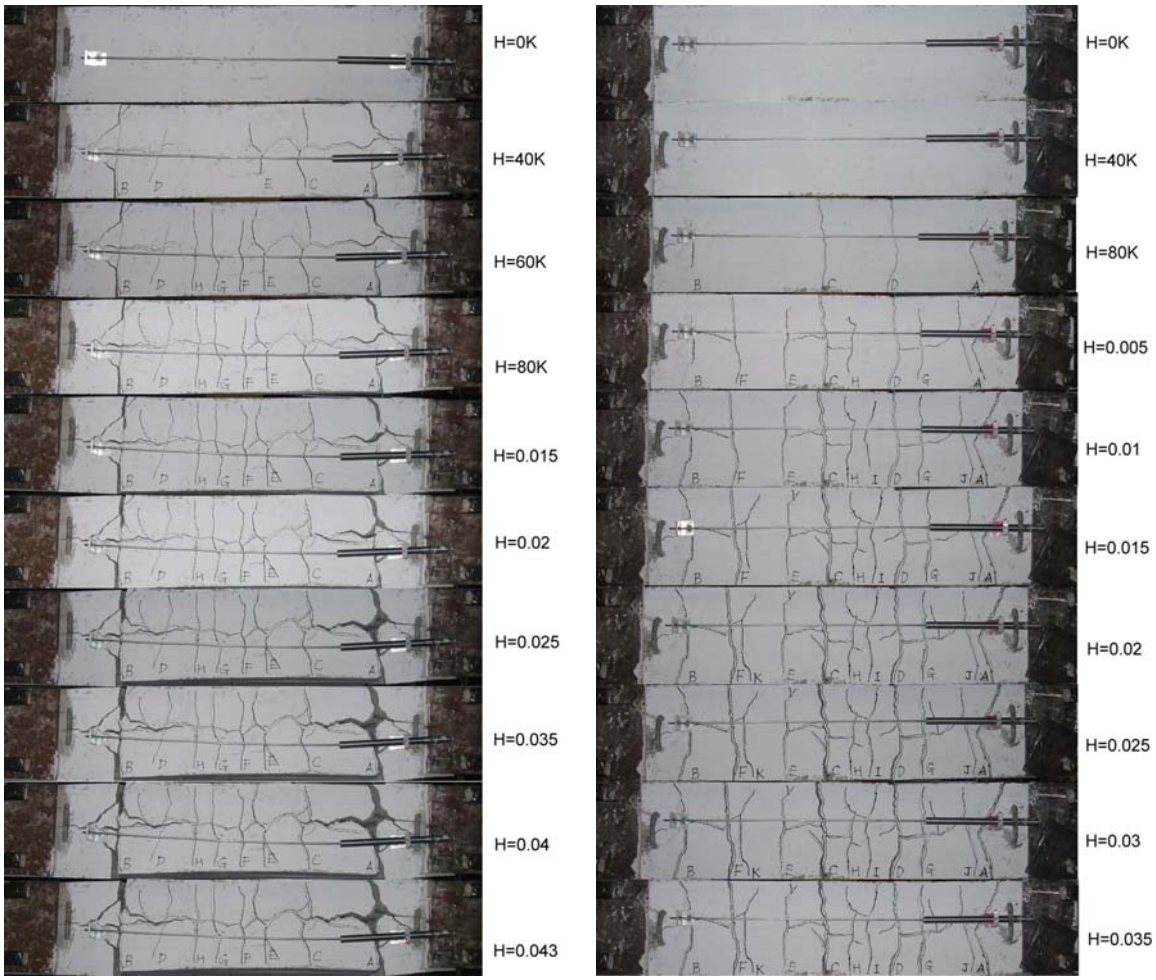

(a) TSB6-South (b) TSB8-South

Fig. 3.6.2 Crack Patterns of Specimens TSB6 and TSB8

Table 3.6.1 Average Crack Spacing of 10 Specimens

Specimen	Average Crack Spacing		Specimen	Average Crack Spacing	
	(in.)	(cm)		(in.)	(cm)
TSB1	20	50.8	TSB6	3.1	7.9
TSB2	6.5	16.5	TSB7	3.0	7.6
TSB3	11.0	27.9	TSB8	3.1	7.9
TSB4	7.8	19.8	TSB9	3.3	8.4
TSB5	3.9	9.9	TSB10	Bond Failure	Bond Failure

Several sets of the specimens were compared as follows:

(1) Comparison of specimens TSB3, TSB4, and TSB5.

Table 3.6.1 shows that these three specimens have the same number of tendons, the same flexible conduit, and the same cementitious grout, but differ in the percentage of mild steel. Because the bond between the deformed mild steel bars and the concrete is very strong, the crack spacings decreased significantly with the increase of mild steel. Table 3.6.1 shows that the width of crack spacing decreased from TSB3 to TSB4 and to TSB5, as the mild steel bars increased from none to two #2 bars then to two #4 bars.

(2) Comparison of specimens TSB2, TSB6, and TSB7.

These three specimens have the same three variables, differing only in the number of prestressing tendons. The increase of the number of prestressing tendons from one to two in specimens TSB2 and TSB6 helped to reduce the crack spacings from 6.5 in. to 3.1 in. However, further increase of tendons from two to four reduced the crack spacing very slightly in specimens TSB6 and TSB7. Apparently, there is a minimum crack spacing for specimens with a certain thickness of concrete cover.

(3) Comparison of specimens TSB1, TSB2, and TSB3.

Specimen TSB3 with conduits and a grout of 2000 psi had crack spacing (11.0 in.) much smaller than the crack spacing (20.0 in.) for specimen TSB1 with the same flexible conduit but a grout of 1000 psi. However, specimen TSB2, which was without conduit and grout, had even smaller crack spacing (6.5 in.). To further reduce the crack spacing of specimens with conduits, grout of even higher strength must be devised.

(4) Comparison of specimens TSB6, TSB8, and TSB9.

Self-Compacting Concrete Grout (SCCG) with 41.4 MPa (6000 psi) compressive strength at two to three days was used in specimens TSB8 and TSB9. Their crack spacings of 3.1 in. and

3.3 in., respectively, were essentially the same as the 3.1 in. spacing for specimen TSB6 devoid of conduit and grout. In other words, post-tensioned specimens with flexible conduits and SCC grout of 41.4 MPa (6000 psi) (TSB8 and TSB9) can be used to simulate the bond condition in the pre-tensioned specimen (TSB6).

3.7 Conclusions

According to the test results of 10 embedded-rod specimens, it can be concluded that (1) the bond condition in pre-tensioned concrete can be simulated by post-tensioned concrete with flexible conduits and SCC grout of 41.4 MPa (6000 psi); (2) the new U-shape insert was proven to be capable of carrying up to four prestressing tendons; and (3) the jacking system was successful in applying and controlling the prestress forces on the concrete. All these proven technologies will be applicable to test panels described in Chapters 4 and 5.

CHAPTER 4

PRESTRESSED CONCRETE 0-DEGREE PANELS UNDER SEQUENTIAL LOADING

To establish a rational model for the action of shear on prestressed concrete, a total of 10 membrane elements (panels) were tested in this research. The panels were divided into two groups: TE and TA, according to the angle of steel bar orientation α_1 with respect to the applied principal stresses. The α_1 angles of groups TE and TA are 0^o and 45^o respectively. Panels with $\alpha_1 = 0^o$ are subjected to sequential loading to study the constitutive relationships of materials (concrete and prestressing tendons). Panels with $\alpha_1 = 45^o$ are subjected to pure shear (a special case of proportional loading) to study the shear behavior of prestressed concrete membrane elements. The test program and testing results of the five panels in Group TE are described and discussed in this chapter, while those of the five panels in Group TA are presented in Chapter 5.

4.1 Test Program (Group TE)

The purpose of testing the five panels in Group TE is to obtain the constitutive laws of concrete and steel tendons in prestressed concrete membrane elements. The five panels were designed with two variables: (1) percentage of prestressing tendons $\rho_{\ell p}$ in the panels and (2) tensile strain in the horizontal direction $\bar{\varepsilon}_1$, which was maintained constant during the second stage of the loading (see Section 4.4) in each panel. The two variables of Group TE are listed in Table 4.1.1.

The labels of all five specimens in Group TE start with the letter "T", which signifies that these panels are reinforced with prestressing **T**endons. The second letter "E" means that the steel grid was set parallel to the applied principal stresses, resulting in $\alpha_1 = 0^o$.

All the panels were subjected to sequential loading. Tensile forces were first applied in the horizontal direction. After attaining the desired smeared (average) tensile strain in the panels, compressive stresses were gradually applied in the vertical direction until failure. During the first stage of the tensile loading, the constitutive laws of concrete in tension and prestressing tendons embedded in concrete were obtained. In the second stage of the compressive loading, the stress-strain relationships of concrete in compression were recorded, from which the experimental softening coefficients were obtained.

Table 4.1.1 Two Variables of Test Panels in Group TE

Specimen	Concrete		Steel in ℓ direction		Prestress MPa (ksi)	$\bar{\varepsilon}_1$
	f_c' (MPa)	ε_0	Tendons	$\rho_{\ell p}$		
TE-3	32.52	0.0020	2 ϕ0.6 @267 mm	0.59%	5.52 (0.8)	2%
TE-4	38.69	0.0024	2 ϕ0.6 @267 mm	0.59%	5.52 (0.8)	1%
TE-5	34.76	0.0022	2 ϕ0.6 @267 mm	0.59%	5.52 (0.8)	3%
TE-6	36.81	0.0018	1 ϕ0.6 @267 mm	0.30%	2.76 (0.4)	2%
TE-7	42.39	0.0021	4 ϕ0.6 @267 mm	1.18%	11.0 (1.6)	2%

Based on the two variables, the five panels were divided into two series. In the first series of panels TE-4, 3, and 5, the prestressing tendons have a percentage of 0.59% in the horizontal direction and a vertical spacing of 267 mm (10.5 in.). The desired horizontal tensile strains in the second stage of loading were 1%, 2%, and 3% for TE-4, 3, and 5, respectively. This series of panels produced the relationship between the softening coefficients and the tensile strains in the perpendicular direction.

The second series of panels consists of panels TE-6, 3, and 7. In this series of panels the desired tensile strains were kept constant at 2%, while the number of prestressing tendons in these three panels varied from 1 to 4 as shown in Table 4.1.1. The effect of prestress on the softening coefficients was clarified from this series of tests.

4.2 Test Specimens (Group TE)

4.2.1 Layout of Specimens

The dimensions and steel arrangements of the panels in Group TE are shown in Fig. 4.2.1. Two coordinate systems ($\ell - t$ and $1 - 2$) were used for all the test panels. The first coordinate system $\ell - t$ was used to represent the directions of the longitudinal (ℓ) and the transverse (t) steel, while the second coordinate system $1 - 2$ was used to represent the directions of the applied principal stresses.

In Group TE, the longitudinal reinforcements (prestressing tendons) were placed parallel to the applied horizontal principal tensile stress, while the transverse reinforcements (mild steel) were placed parallel to the applied vertical principal compressive stress, i.e., the angle between the $\ell -$ axis and the $1 -$ axis is $\alpha_1 = 0^o$. All the panels had the same sizes of 1398 mm × 1398 mm × 178 mm (55 in. × 55 in. × 7 in.). The transverse reinforcements were #4 mild steel bars. The spacing of reinforcing bars was kept constant at 267 mm (10.5 in.) and the percentage of steel was 0.54% in all the panels.

The arrangement of the reinforcements in panels TE-4, 3, and 5 was identical as shown in Fig. 4.2.1(a). Five prestressing tendons (in the form of pairs) were placed in the horizontal direction in two layers. The center-to-center spacing between the two layers of tendons was 73 mm (2.88 in). The prestress force in each tendon was about 138 kN (31 kips), resulting in the prestress on the concrete of about 5.52 MPa (0.8 ksi). Fig. 4.2.1(b) shows the steel grid of panel TE-6, which had only one layer of prestressing tendons. Five tendons with the spacing of 267 mm (10.5 in.) provided about 2.76 MPa (0.4 ksi) prestress on the concrete. In Fig. 4.2.1(c), panel TE-7 has a total of 20 prestressing tendons divided into five groups of four tendons each. The four tendons were held and tensioned together as a group by a U-shape insert at each end. The U-shape inserts are shown in Fig. 3.3.3. The center-to-center spacing of the inserts was 267 mm (10.5 in.). The prestressing force in each tendon was also about 138 kN (31 kips), resulting in a concrete compressive stress of 11 MPa (1.6 ksi).

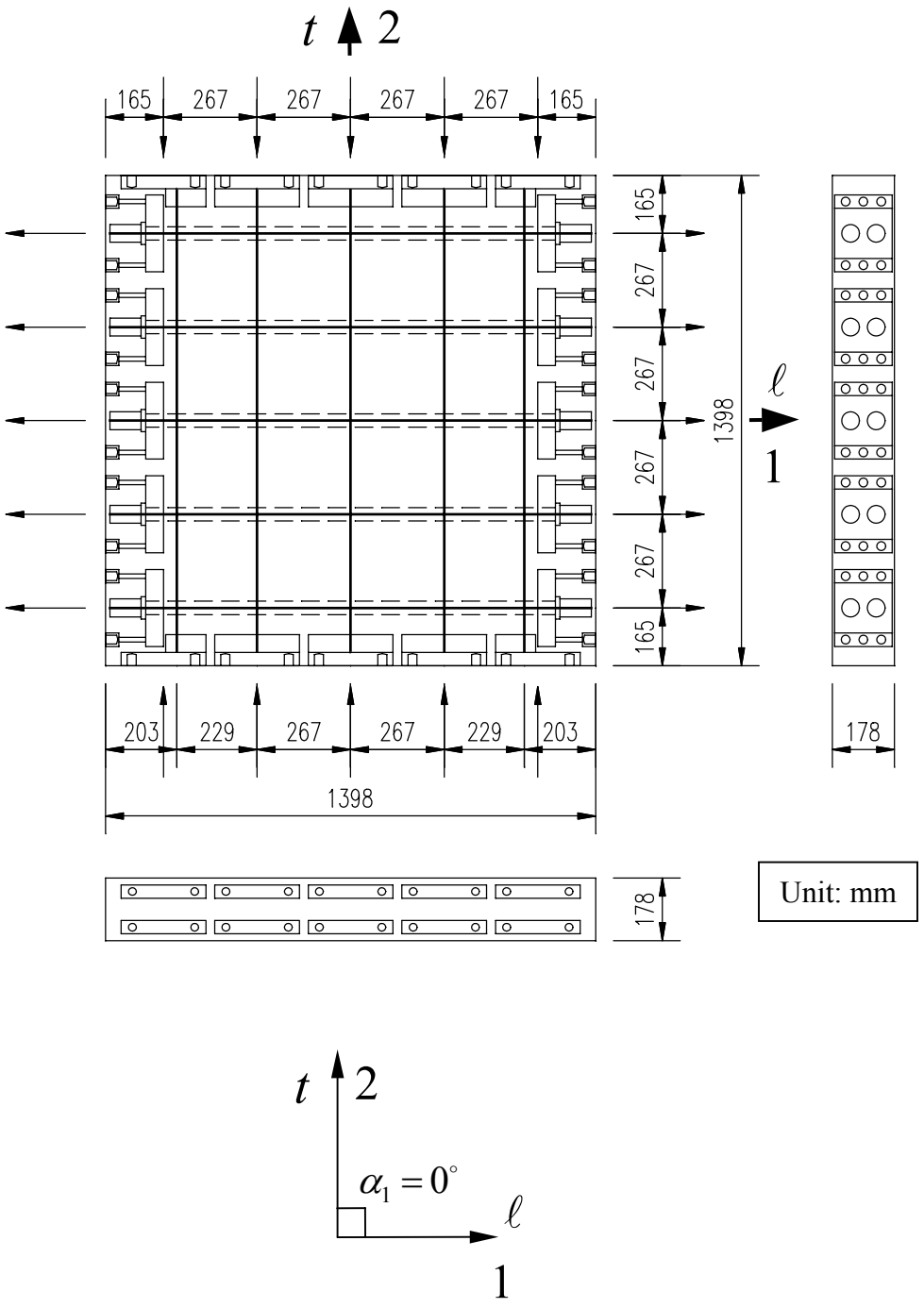

(a) Steel Layout and Dimensions of Panels TE-4, 3, and 5

Fig. 4.2.1 Steel Layout and Dimensions of Test Panels in Group TE

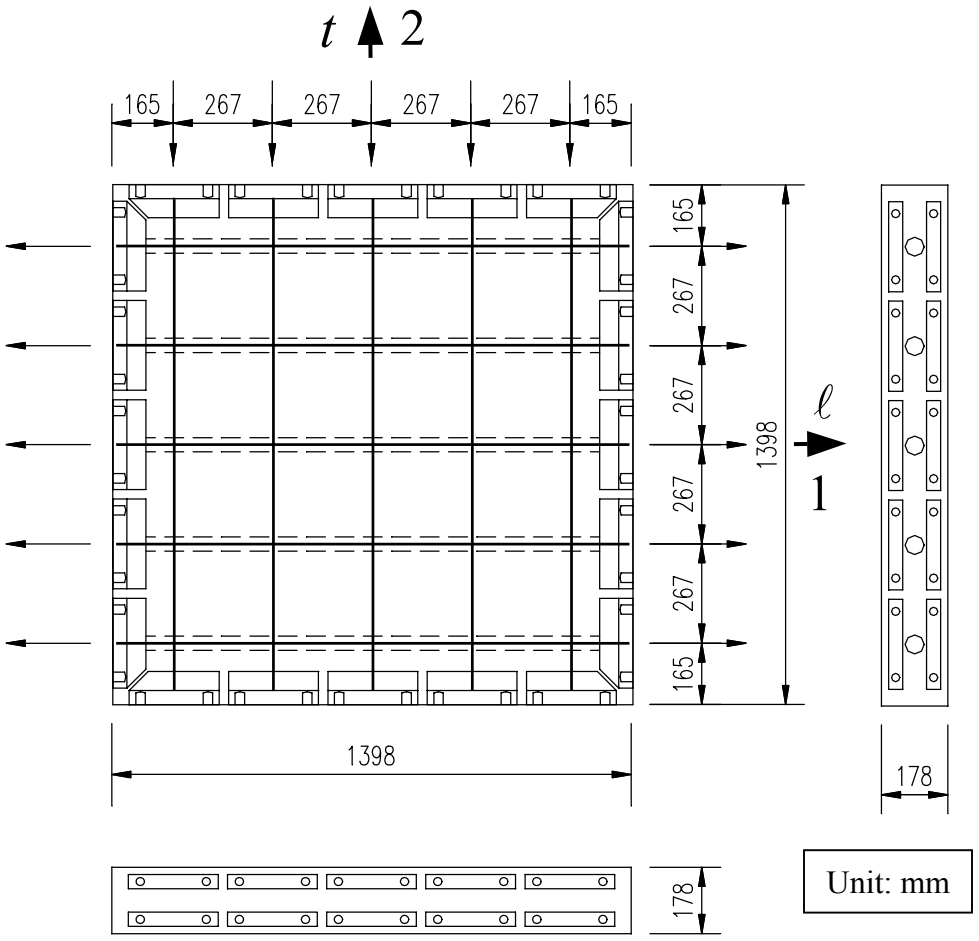

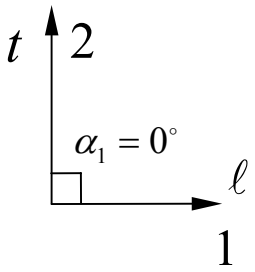

(b) Steel Layout and Dimensions of Panel TE-6

Fig. 4.2.1 Steel Layout and Dimensions of Test Panels in Group TE (continued)

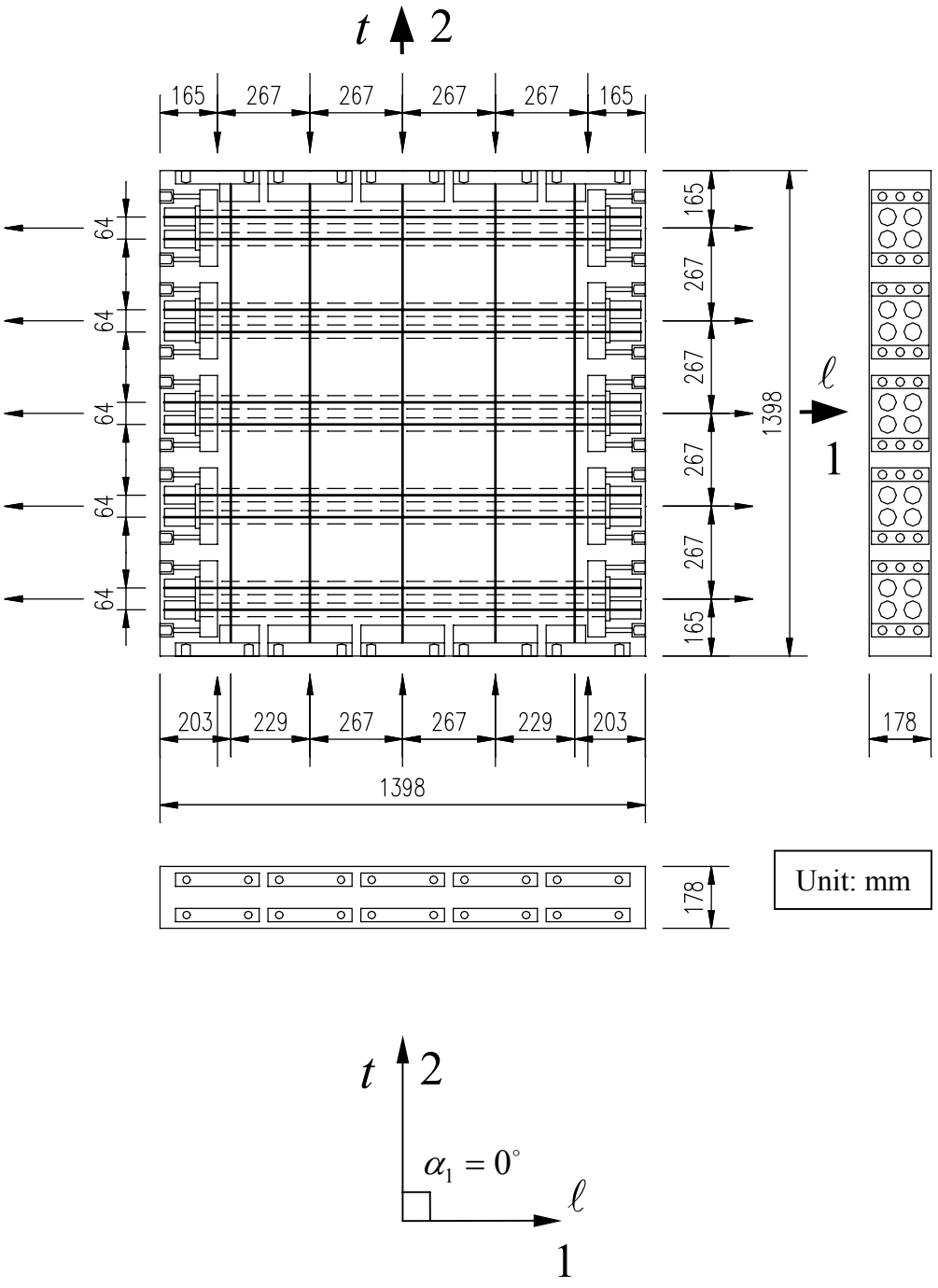

(c) Steel Layout and Dimensions of Panel TE-7

Fig. 4.2.1 Steel Layout and Dimensions of Test Panels in Group TE (continued)

4.2.2 Fabrication of Specimens

All the specimens were cast in the steel form as shown in Fig. 4.2.2(a) to (c). Each panel had two layers of #4 steel bars in the transverse direction and two layers of prestressing tendons in the longitudinal direction, except panel TE-6, shown in Fig. 4.2.2(b) which had only one mid-layer of prestressing tendons. The two layers of #4 steel bars in the transverse direction were first welded to the regular anchor-inserts in a special steel jig with the sizes of 1398 mm × 1398 mm (55 in. × 55 in.) as shown in Fig. 4.2.3.

The reinforcement and accessories were installed in the casting form in the following six steps. (1) The bottom layer of the #4 steel bars was transferred from the steel jig to the oiled casting form. The anchor-inserts at the ends of the steel bars were aligned and bolted to the side faces of the casting form. (2) Ten U-shape inserts for each panel were bolted onto the two sides of the casting form, and the flexible conduits were placed between the U-shape inserts. To support the flexible conduits, steel pipes were placed inside the conduits and through the holes on the U-shape inserts. (3) The top layer of #4 steel bars with the anchor-inserts was bolted onto the casting form.

In step (4) the threaded rods for fastening LVDT brackets were attached onto the bottom of the casting form, and two pick-up rings were installed. (5) Sand was poured into the space between the U-shape inserts and the side form to prevent concrete from entering the space during casting. Panel TE-6 was the exception; here styrofoam blocks were used instead of sand. (6) The top tips of the threaded rods were taped to protect the threads, and cylinder molds were cleaned and oiled. The formwork was done and ready for the casting of concrete.

With the reinforcing bars and flexible conduits secured inside the casting form, each panel was cast in a horizontal position using two batches of concrete of approximately 0.184 m^3 (6.5 ft^3) each. Each batch was mixed in a 0.34 m^3 (12 ft^3) capacity mixer available in the laboratory and then spread uniformly in the casting form. The concrete had an average slump of 178 mm (7 in.) with good workability.

After the form was filled, the concrete was shaken by an internal spud vibrator. The concrete adjacent to the perimeter of the casting form was more intensively vibrated so that the ultimate failure of the panels would occur away from the edges. The cylinder molds were also filled and vibrated in a manner similar to the central portion of the panels. The concrete in the companion cylinders was cured in the same way as the test panels.

Once the concrete was cast, a smooth finish was obtained on the top surface of the panels and the cylinders; thereafter they were covered with a plastic sheet. The concrete was kept in a humid condition for the first seven days. Then the panels and the cylinders were stripped from the molds and cured in the air-conditioned laboratory for about 28 days.

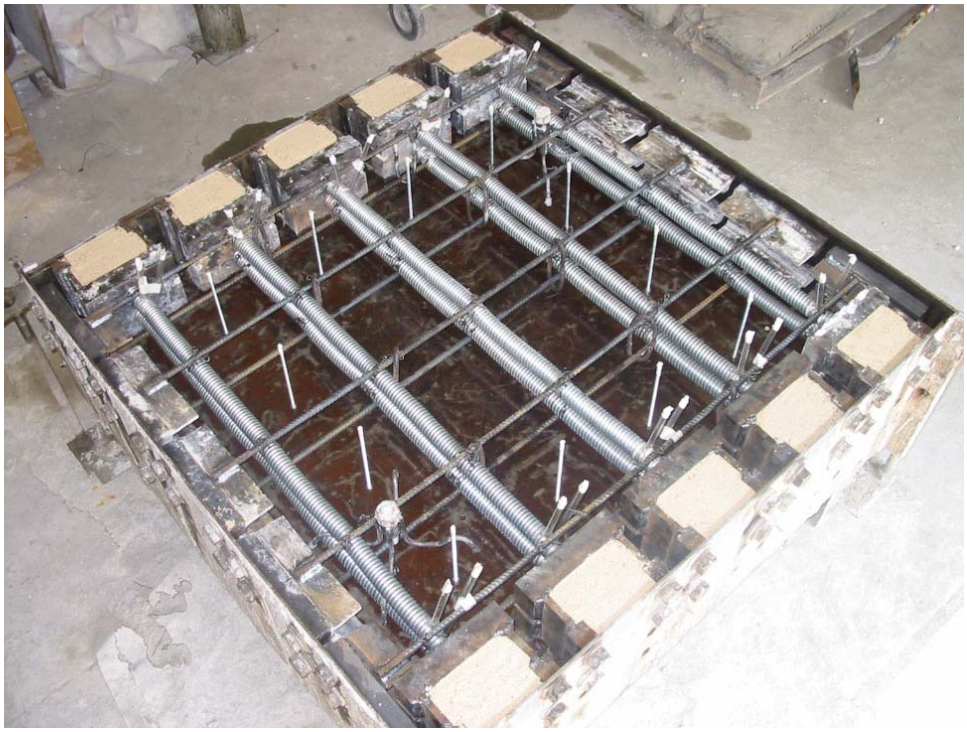

(a) Formwork of Panel TE-4

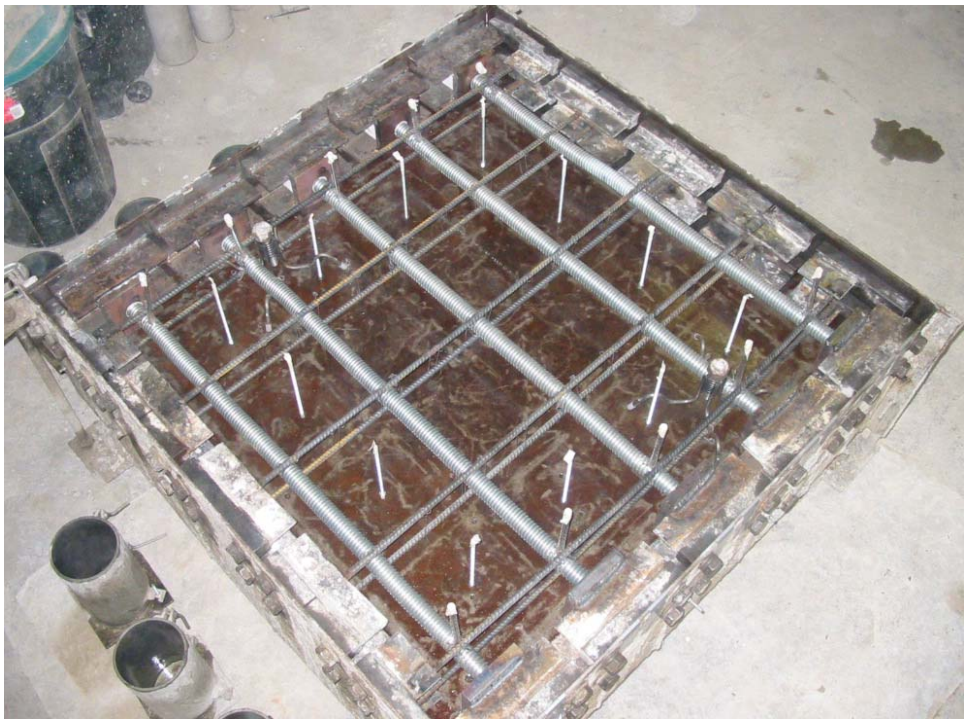

(b) Formwork of Panel TE-6

Fig. 4.2.2 Formworks of Panels in Group TE

(c) Formwork of Panel TE-7

Fig. 4.2.2 Formworks of panels in Group TE (continued)

Fig. 4.2.3 Special Steel Jig

4.2.3 Tendon Jacking System

The tendon jacking system for the panels in Group TE was the same as that described in Section 3.3.2 for the crack simulation tests.

The tendon jacking procedure was performed about four days before the panel was tested. Ten load cells (LWO-60) were used to monitor the tensile forces of the tendons in the panels, except that five load cells were used in panel TE-6. The average readings of the load cells right before testing were taken as the prestress forces on each panel. Following the jacking of the tendons, the grouting materials (SCCG) were injected into the flexible conduits. Then the panels were mounted in the Universal Panel Tester, and LVDTs were attached on both surfaces of the panels. The panels were ready for testing.

4.3 Materials (Group TE)

4.3.1 Concrete

A cylinder compressive strength of 41.4 MPa (6000 psi) was chosen as the target strength of the concrete in the panels of Group TE. This concrete was the same as that used in the crack simulation tests. The concrete mix proportion (based on weight) was 1:2.64:2.93, corresponding to cement, sand, and coarse aggregate, respectively. The water-cement ratio was 0.6 and the slump for each batch was 178 mm (7 in.). The cement was Type I Portland cement, the sand conformed to ASTM C33, and the graded limestone aggregate had a maximum size of 19 mm (3/4 in.).

Six standard concrete cylinders, with the dimensions of 152 mm × 305 mm (6 in. × 12 in.), were cast along with each panel. The cylinders were tested at the same age as the panels using the Tinius Olsen Universal testing machine. The compressive stresses and strains were recorded up to the peak point. Fig. 4.3.1 shows that the typical compressive stress-strain relationship of concrete was clearly in the form of a parabolic curve. Thus, a parabolic equation was used to represent the compressive stress-strain relationship of plain concrete in the ascending branch.

The actual compressive strength of the concrete and the strain at peak stress in each panel are listed in Table 4.1.1. The strengths in some panels were a little lower than the target. The small differences in concrete strength could be remedied by the normalization of concrete strength in the analysis.

The Self-Compacting Concrete Grout (SCCG), used to grout the flexible ducts, had a mix proportion of 1:1.5:0.37 for Type III Portland cement, sand, and water, respectively. A ratio of 0.126 oz (3.57 g) of High Ratio Water Reduction (HRWR) agent was used for every 1 pound (454 g) of cement in the SCCG.

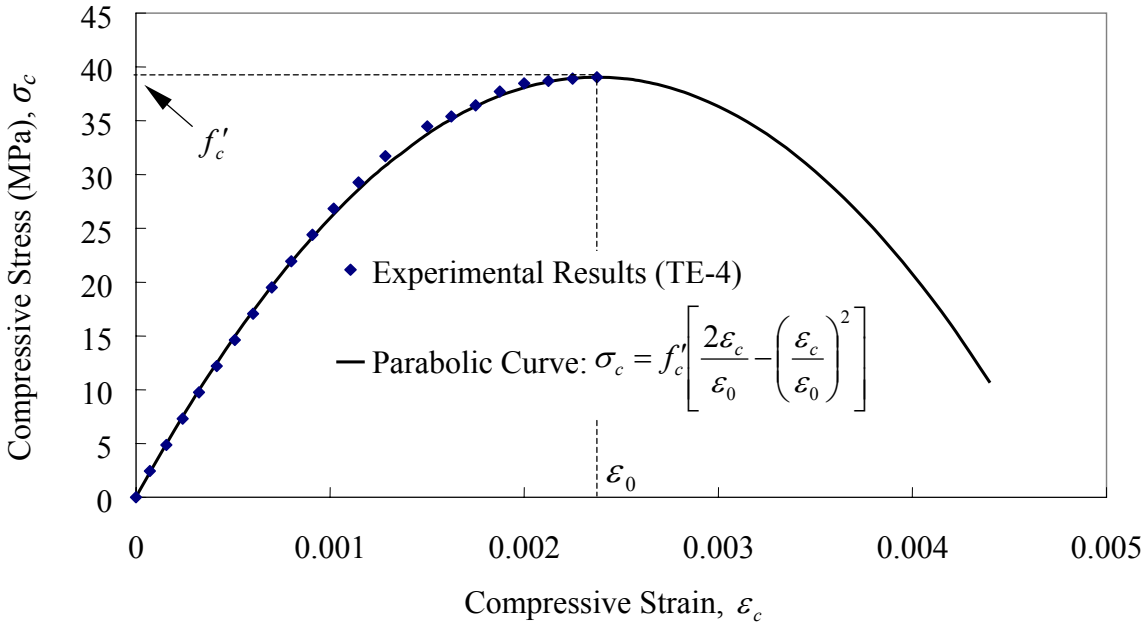

Fig. 4.3.1 Typical Stress-Strain Curve from Concrete Cylinder Compression Test

4.3.2 Reinforcements

The prestressing tendons with a nominal diameter of 0.6 in. (15 mm) were used in the longitudinal direction of the panels. Size #4 mild steel bars were used in the transverse direction. The properties of these two kinds of reinforcements are specified in Section 3.4.2.

4.4 Loading Procedure (Group TE)

The test program was carried out using the Universal Panel Tester. The panel was subjected to in-plane forces, supplied by 20 pairs of in-plane hydraulic jacks placed around the four sides of a square panel. The loading procedure was well designed by controlling the pressures in the jacks, using a servo-control system.

Figure 4.4.1 shows the typical sequential loading path used in the panels of Group TE. The sequential loading path included two stages: (1) the horizontal tensile loading was first applied, and (2) the vertical compressive loading was applied until the failure of the panels, while the horizontal strain was maintained constant. In each stage, the load-control mode was first used, followed by the strain-control mode.

In the first stage, the load-control mode was used until the stresses in the tendons were close to the elastic limit of 1303 MPa (189 ksi). Then the control mode was switched to the strain-control until the desired principal tensile strain was obtained. In this stage of uniaxial tensile loading, we can obtain the smeared (average) constitutive law of concrete in tension and the smeared (average) constitutive law of prestressing tendons embedded in concrete.

In the second stage of vertical compressive loading, the horizontal tensile strain was kept constant using the servo-control system. As the first stage, the load-control mode was first applied until the peak stress was approached. Then the control mode was shifted to the strain-control, which allows us to measure the strains in the descending branches of the stress-strain curves. In this second stage, we can study the smeared (average) compressive constitutive law of concrete in compression, particularly the softening coefficients.

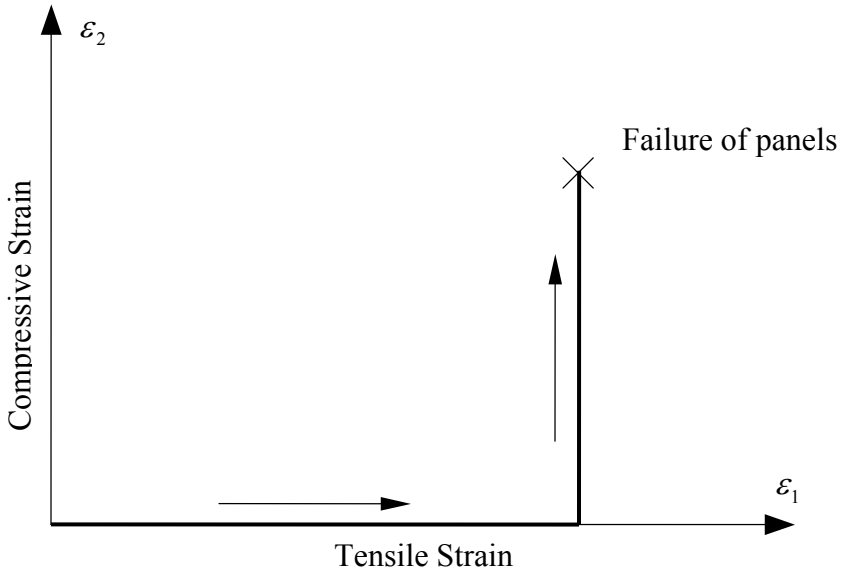

Fig. 4.4.1 Sequential Loading Path used in Group TE

4.5 General Behavior of Test Panels in Group TE

According to the test program in Section 4.1, five prestressed concrete panels in Group TE were successfully tested under the sequential loading. The data in the two loading stages are recorded separately. The crack widths for each panel were recorded and the crack patterns at selected load stages were photographed.

In the first stage of tensile loading, all five panels were used to obtain the tensile constitutive laws of concrete and prestressing tendons. In the second stage of compressive loading, the softening coefficients of prestressed concrete were studied as related to the perpendicular tensile strains and to the prestress.

In the first series of panels TE-4, 3, and 5, the constant tensile strains were 0.0146, 0.0194, and 0.0293, respectively. The relationship between the softening coefficient, ζ, and the tensile strain, $\bar{\varepsilon}_1$, could be obtained. It should be noted that in testing panel TE-4, during the first stage of the loading, one of the top prestressing tendons was broken at one end due to a large

deformation. After restarting the test, the target tensile strain was revised to 0.0146 rather than 0.01 as indicated in Table 4.1.1.

In the second series of panels TE-6, 3, and 7, the constant tensile strains were approximately the same, being 0.0203, 0.0194, and 0.0205, respectively. With the different prestress of 2.76 MPa , 5.52 MPa , and 11.0 MPa , respectively, the effect of prestress on the softening coefficients was studied as described below.

4.5.1 Applied Tensile Stress-Strain Relationships

To describe the panel behavior the horizontal principal stress, σ_1, is plotted against the horizontal principal strain, ε_1. The two series of panels TE-4, 3, 5 and TE-6, 3, 7 are shown in Fig. 4.5.1 and Fig. 4.5.2, respectively.

As shown in Fig. 4.5.1, the panels in the first series (TE-4, 3, and 5) had the same number of prestressing tendons. Hence, these three panels had almost the same tensile stress-strain curves up to their target strains.

In the second series of panels TE-6, 3, and 7, Fig. 4.5.2, the tensile loads carried by the panels increased with the increase of prestressing tendons. The tensile stresses of 5.5, 11.0, and 21.5 MPa (800, 1600, and 3120 psi) at a strain of 0.02 for panels TE-6, 3, and 7 were approximately proportional to the tendon percentages of 0.30%, 0.59%, and 1.18%, respectively. The corresponding cracking stresses were 4.48, 7.56, and 12.75 MPa (650, 1096, and 1849 psi), respectively.

The smeared (average) stress-strain relationships of concrete in tension and prestressing steel embedded in concrete are derived in Sections 4.6 and 4.7, respectively.

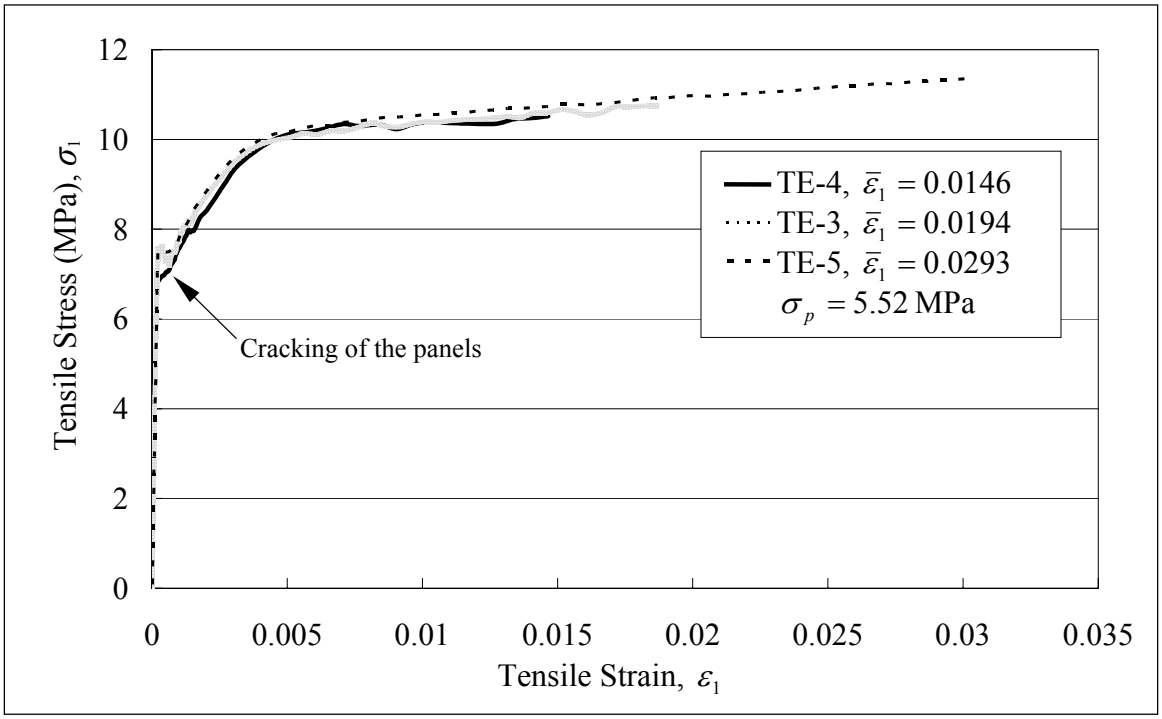

Fig. 4.5.1 $\sigma_1 - \varepsilon_1$ Relationships of Panels TE-4, 3, and 5

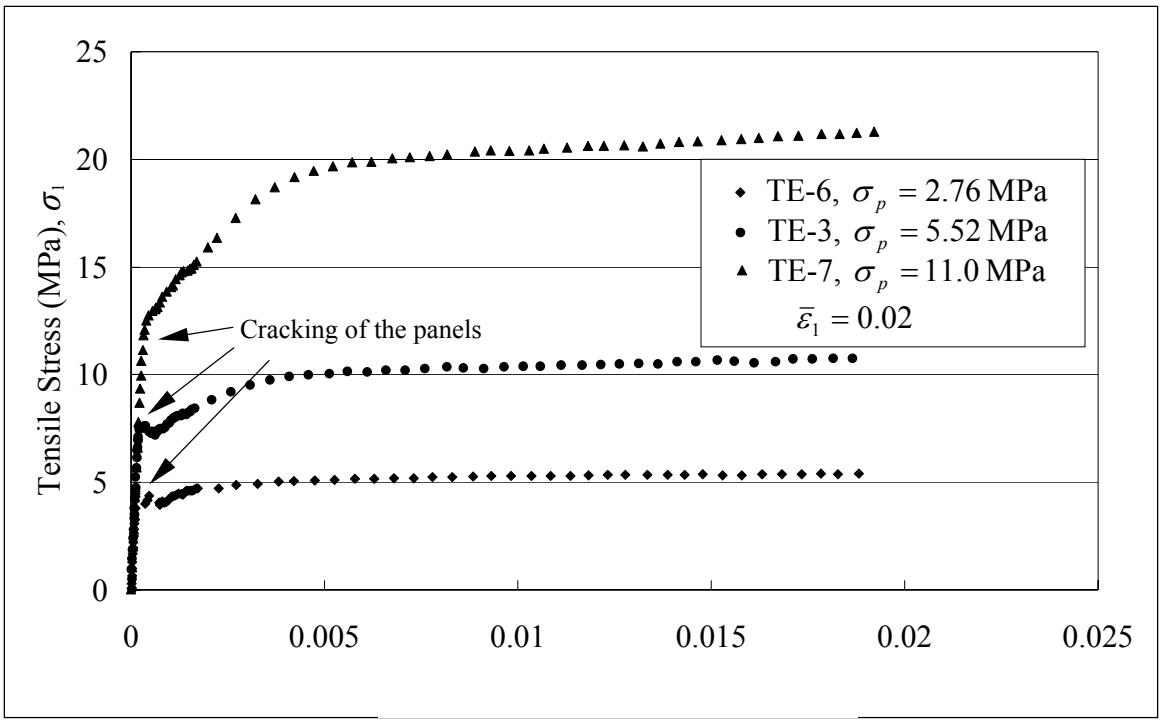

Fig. 4.5.2 $\sigma_1 - \varepsilon_1$ Relationships of Panels TE-6, 3, and 7

4.5.2 Applied Compressive Stress-Strain Relationships

The compressive stress-strain relationships of the panels in Group TE are given in Fig. 4.5.3 and Fig. 4.5.4.

In the first series (panels TE-4, 3, and 5), Fig.4.5.3, the same number of prestressing tendons was placed while the constant tensile strains in the horizontal direction were changed from 0.0146 to 0.0194, then to 0.0293. The curves show that the compressive strength of the panel is indeed a function of the tensile strain in the perpendicular direction.

In the second series (panels TE-6, 3, and 7), Fig. 4.5.4, the panels had different amounts of prestressing steel and the desired tensile strains were designed to be the same. The compressive strengths of the three panels were 23.52, 17.74, and 17.1 MPa (3.41, 2.57, and 2.48 ksi), respectively. It is clear that the compressive strength of panels TE-3 and TE-7 are almost the same, but the strength of panel TE-6 was much higher than those of panels TE-3 and TE-7.

The smeared (average) stress-strain relationships of concrete in compression are further discussed in Section 4.8.

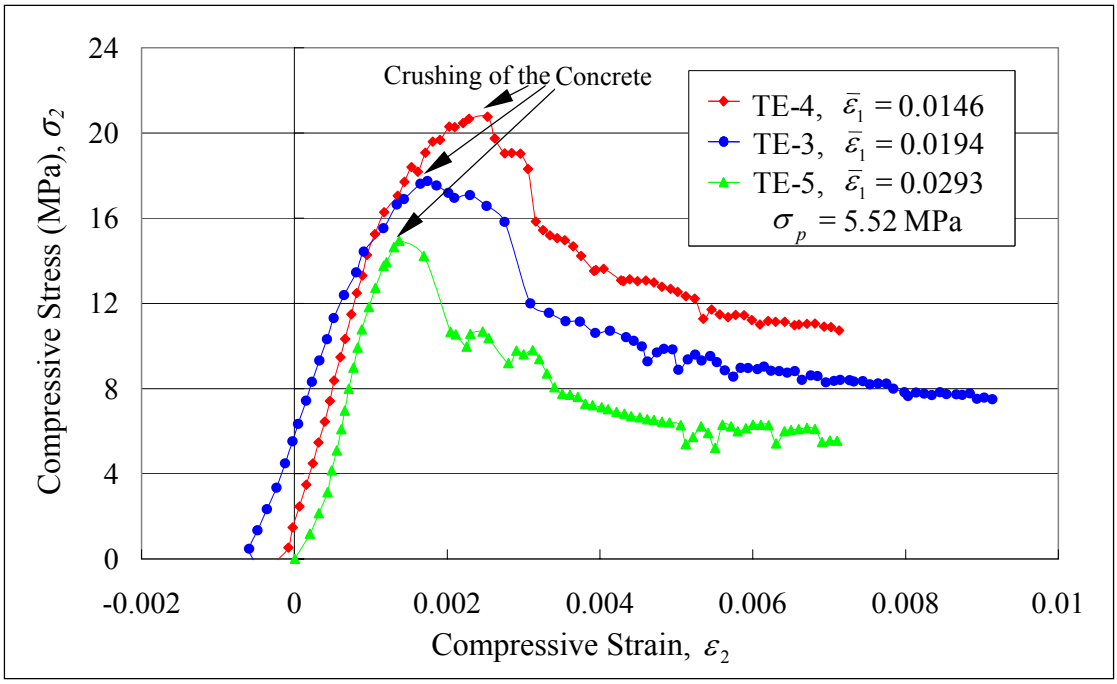

Fig. 4.5.3 $\sigma_2 - \varepsilon_2$ Relationships of Panels TE-4, 3, and 5

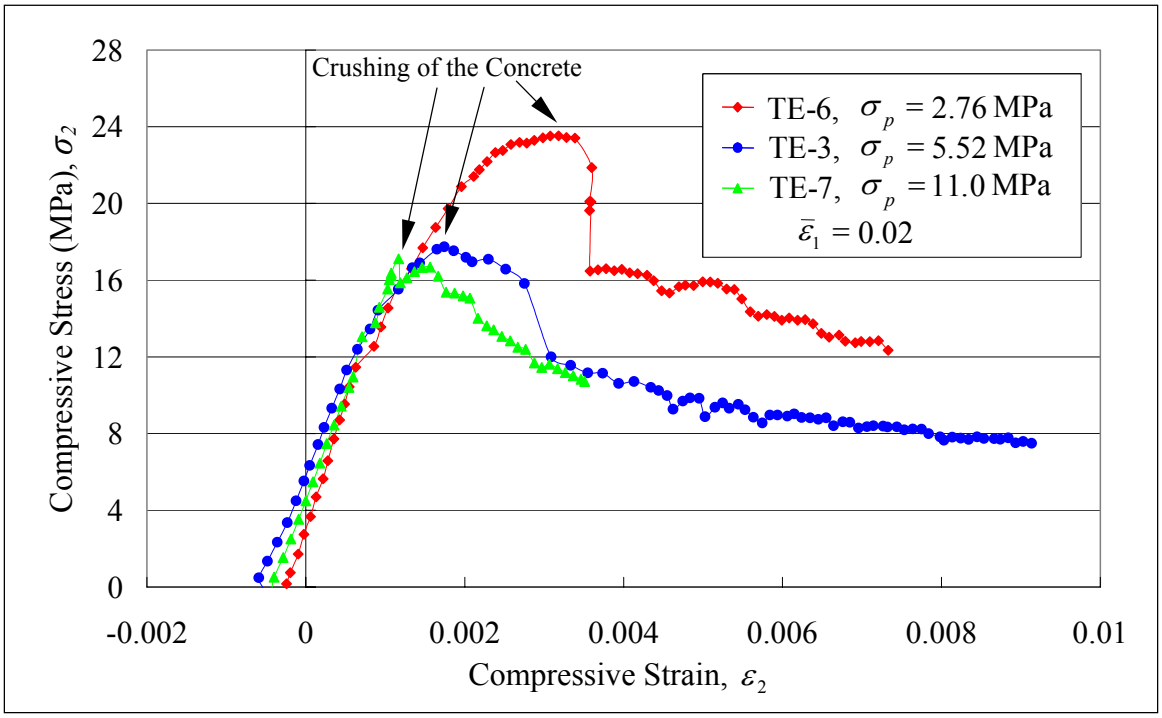

Fig. 4.5.4 $\sigma_2 - \varepsilon_2$ Relationships of Panels TE-6, 3, and 7

4.6 Smeared (Average) Stress-Strain Relationships of Concrete in Tension

Plain concrete cannot resist any tensile stresses after a crack is formed, but the concrete between the cracks of reinforced concrete can still take some tensile stress. This contribution of concrete between cracks is known as "tension stiffening" (Carreira and Chu, 1986). Taking into account this phenomenon, the smeared (average) stress-strain relationships of concrete and mild steel were studied (Belarbi and Hsu, 1994; Hsu and Zhang, 1996).

Tension stiffening can also be observed in prestressed concrete. From the first stage of the panel tests, we obtained the smeared (average) constitutive laws of concrete in tension discussed in Section 4.6.1 to 4.6.3. The smeared (average) stress-strain relationship of prestressing tendons is discussed in Section 4.7.

4.6.1 Decompression

Before applying loads, initial compressive stress and strain exist in the concrete due to the prestress. Upon applying a tensile load, the first stage of the stress-strain relationship of concrete, called "decompression," begins.

The initial stress and the initial uniaxial strain in concrete are denoted as σ_{ci} and $\bar{\varepsilon}_{ci}$, respectively, while the initial stress and the initial uniaxial strain of prestressing tendons are f_{pi} and $\bar{\varepsilon}_{pi}$, respectively. These stresses are in equilibrium as follows:

$$\sigma_{ci} A_c + f_{pi} A_{ps} = 0 \tag{4.6-1}$$

where

A_c, A_{ps} = cross-sectional areas of concrete and tendons, respectively.

Prior to concrete cracking, both the concrete and the prestressing tendons can be considered as elastic materials. When stretched to the same strain ε_1, the concrete stress σ_c and the tendon stress f_{ps} are given as follows:

$$\sigma_c = \sigma_{ci} + E_c' \varepsilon_1 \tag{4.6-2}$$

$$f_{ps} = f_{pi} + E_{ps} \varepsilon_1 \tag{4.6-3}$$

where

E_{ps} = modulus of prestressing steel tendons, and

E_c' = decompression modulus of concrete, given as $2f_c'/\varepsilon_0$. See Eq. 4.6-8.

The total load P is the sum of the concrete force and the tendon force:

$$P = A_c \sigma_c + A_{ps} f_{ps}$$

$$= \left(E_c' A_c + E_{ps} A_{ps}\right)\varepsilon_1 + \left(\sigma_{ci} A_c + f_{pi} A_{ps}\right)$$

In view of Eq. 4.6-1,

$$P = \left(E_c' A_c + E_{ps} A_{ps}\right)\varepsilon_1 \tag{4.6-4}$$

Substituting the cross-sectional area of tendons $A_{ps} = \rho_{\ell p} A_c$ into Eq. 4.6-4 and rearranging the terms, a general form of equilibrium equation before cracking is given as:

$$E_c' \varepsilon_1 = \frac{P}{A_c} - \rho_{\ell p} E_{ps} \varepsilon_1 \tag{4.6-5}$$

Substituting Eq. 4.6-5 into Eq. 4.6-2, the concrete stress is obtained as follows:

$$\sigma_c = \sigma_{ci} + \frac{P}{A_c} - \rho_{\ell p} E_{ps} \varepsilon_1 \qquad (4.6\text{-}6)$$

The concrete uniaxial strain $\bar{\varepsilon}_c$ is given by:

$$\bar{\varepsilon}_c = \bar{\varepsilon}_{ci} + \varepsilon_1 \qquad (4.6\text{-}7)$$

Using Eqs. 4.6-6 and 4.6-7, the experimental stress-strain relationship of concrete in decompression can be plotted as shown in Fig. 4.6.1. It is obvious that the relationship is close to a straight line.

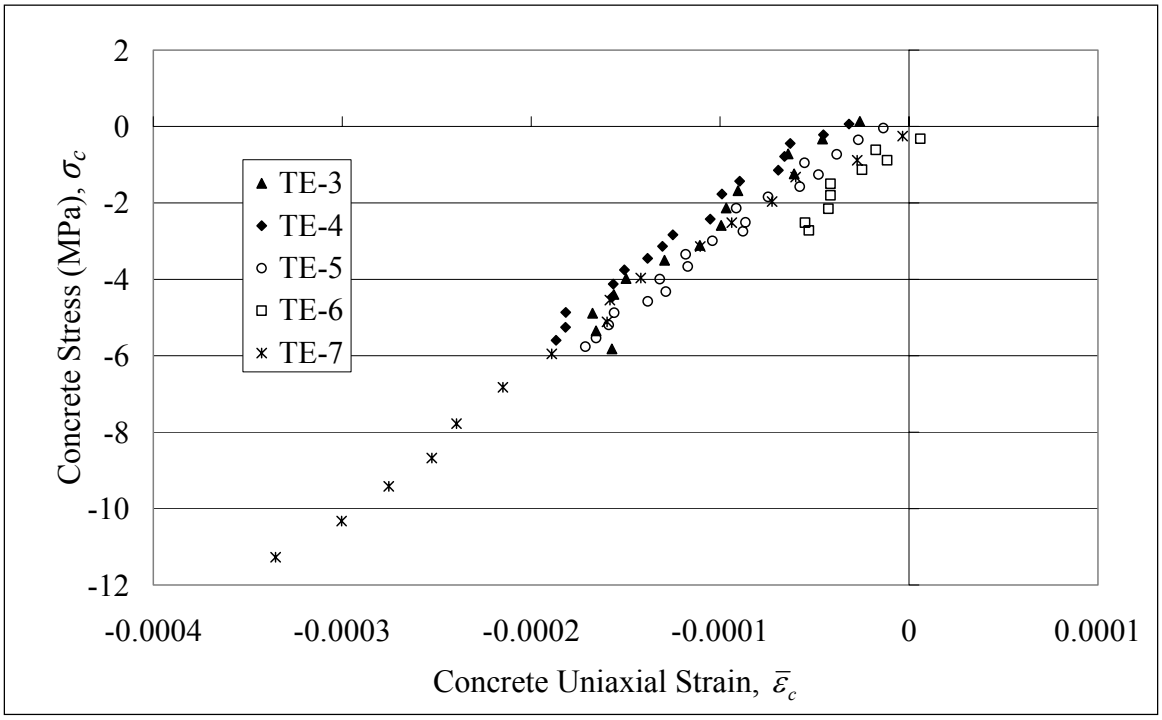

Fig. 4.6.1 Experimental $\sigma_c - \bar{\varepsilon}_c$ Relationships of Concrete in Decompression

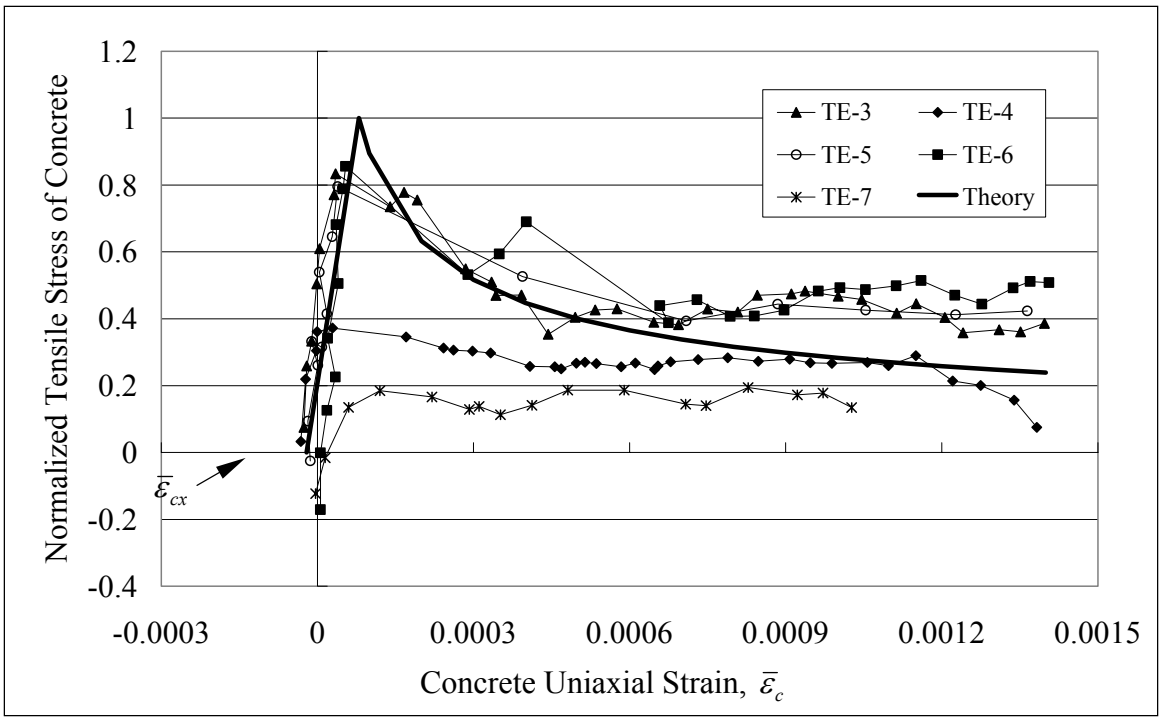

Fig. 4.6.2 Experimental Smeared (Average) Tensile Stress-Strain Curves of Concrete

4.6.2 Post-Decompression Behavior

After the decompression of the concrete and before the yielding of the tendons, Eqs. 4.6-6 and 4.6-7 can still be applied to obtain the experimental stress-strain relationship of the concrete. After cracking, the applied strain ε_1 becomes the smeared (average) strain. Fig. 4.6.2 shows the stress-strain curves of the concrete in tension. The stresses are normalized by dividing the tensile stresses by the crack strength of the concrete. It is noted that a small extra strain $\bar{\varepsilon}_{cx}$ is formed at the end of the decompression.

4.6.3 Mathematical Modeling of Smeared (Average) Stress-Strain Curve of Concrete in Tension

The experimental stress-strain relationship of concrete in decompression is close to a straight line as shown in Fig. 4.6.1. Therefore, a linear equation is proposed. The slope of the line is taken as the unloading modulus of the concrete in compression E_c'. Because the slope of the unloading part is the tangential slope of a parabolic compressive stress-strain relationship of concrete at the origin, the modulus, E_c', is given as:

$$E_c' = \frac{2f_c'}{\varepsilon_0} \tag{4.6-8}$$

Complete decompression to a zero tensile stress stage would result in an extra strain of $\bar{\varepsilon}_{cx}$ as shown in Fig. 4.6.3.

The stress-strain relationships of concrete after decompression are similar to those of reinforced concrete (Belarbi and Hsu, 1994) except that the curve starts at a point $(0, \bar{\varepsilon}_{cx})$. Assuming the same concrete cracking stress f_{cr} and the same cracking strain ε_{cr} as those of reinforced concrete, the relationship prior to cracking is expressed as a straight line, starting from the point $(0, \bar{\varepsilon}_{cx})$ and ending at the point $(f_{cr}, \varepsilon_{cr})$. Therefore, the slope is taken as the modulus of concrete E_c'' defined by $f_{cr}/(\varepsilon_{cr} - \bar{\varepsilon}_{cx})$. After cracking, the curve is similar to that of reinforced concrete proposed by Tamai et al. (1987),

$$\sigma_c = f_{cr}\left(\frac{\varepsilon_{cr}}{\bar{\varepsilon}_c}\right)^c \tag{4.6-9}$$

where

c = a constant taken as 0.5, obtained from this research.

The constant c in Eq. 4.6-9 for reinforced concrete was 0.4. It is changed to 0.5 in Eq. 4.6-9 as the bond between prestressing tendons and concrete is weaker than that between deformed bars and concrete. Fig. 4.6.2 shows a reasonable fit by using the new constant, 0.5.

In summary, the smeared (average) stress-strain relationships of concrete in tension for prestressed concrete, shown in Fig. 4.6.3, are expressed by the following equations:

Stage UC: $\sigma_c = E_c'(\bar{\varepsilon}_c - \bar{\varepsilon}_{ci}) + \sigma_{ci}$, $\bar{\varepsilon}_c \le \bar{\varepsilon}_{cx}$ (4.6-10a)

Stage T1: $\sigma_c = E_c''(\bar{\varepsilon}_c - \bar{\varepsilon}_{cx})$, $\bar{\varepsilon}_{cx} < \bar{\varepsilon}_c \le \varepsilon_{cr}$ (4.6-10b)

Stage T2: $\sigma_c = f_{cr}\left(\frac{\varepsilon_{cr}}{\bar{\varepsilon}_c}\right)^{0.5}$, $\bar{\varepsilon}_c > \varepsilon_{cr}$ (4.6-10c)

where

E_c' = decompression modulus of concrete taken as $\frac{2f_c'}{\varepsilon_0}$,

$\bar{\varepsilon}_{ci}$ = initial strain in concrete due to prestress,

σ_{ci} = initial stress in concrete,

$\bar{\varepsilon}_{cx}$ = extra strain calculated by $\bar{\varepsilon}_{ci} - \dfrac{\sigma_{ci}}{E_c'}$,

E_c'' = modulus of concrete taken as $\dfrac{f_{cr}}{\varepsilon_{cr} - \bar{\varepsilon}_{cx}}$,

ε_{cr} = concrete cracking strain taken as 0.00008, and

f_{cr} = concrete cracking stress taken as $0.31\sqrt{f_c'}$ (f_c' and $\sqrt{f_c'}$ are in MPa).

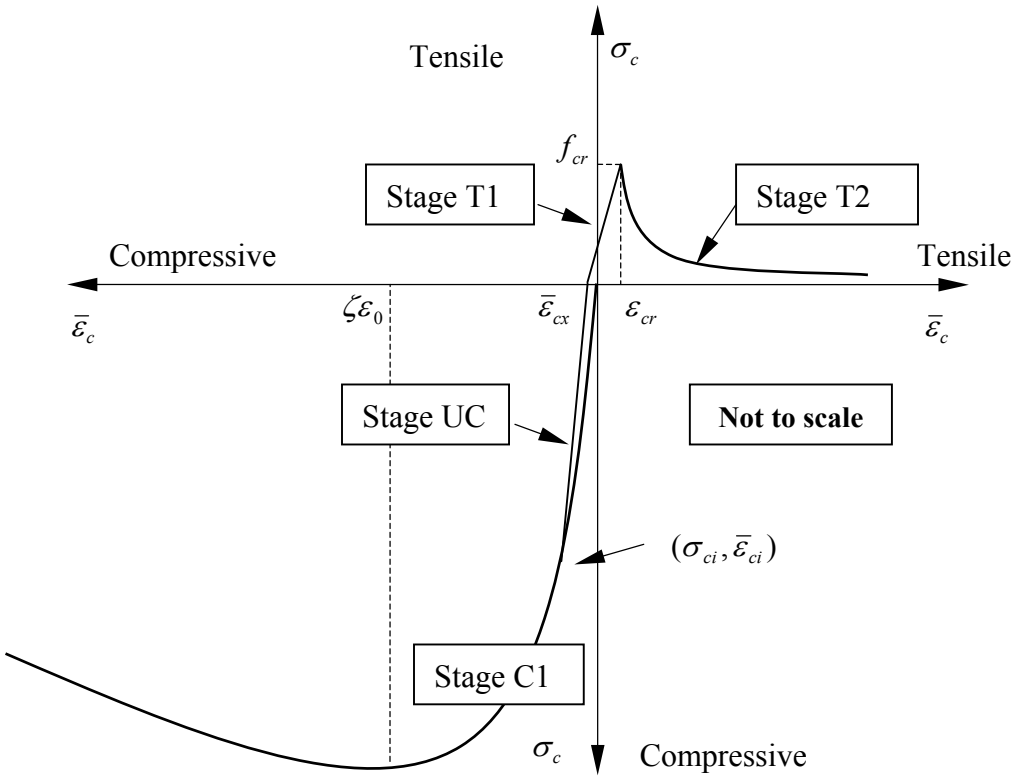

Fig. 4.6.3 Smeared Stress-Strain Relationships of Concrete in Tension

Stage C1: $\sigma_c = 0.9 f_c' \left[2\left(\dfrac{\bar{\varepsilon}_c}{\varepsilon_0}\right) - \left(\dfrac{\bar{\varepsilon}_c}{\varepsilon_0}\right)^2 \right]$, $\qquad \dfrac{\bar{\varepsilon}_c}{\varepsilon_0} \le 1$ (4.6-11)

The constant 0.9 in Eq. 4.6-11 takes care of the size effect between the large panels and the 6 in. by 12 in. standard cylinders.

Using the proposed Eqs. 4.6-10a, b, and c, the smeared (average) stress-strain relationships of concrete in tension are plotted in Fig. 4.6.4 to Fig. 4.6.8 and compared to the test data of the five panels TE-3 to TE-7. It can be seen that the agreements are acceptable.

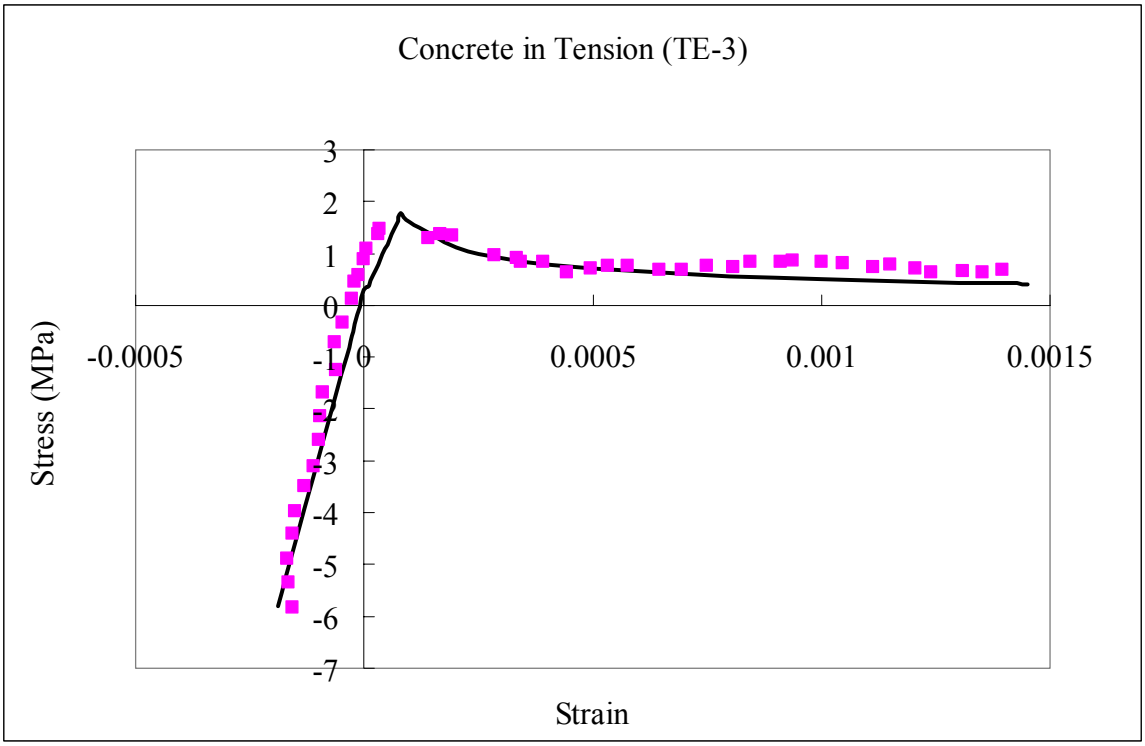

Fig. 4.6.4 Smeared (Average) Stress-Strain Relationships of Concrete in Tension (TE-3)

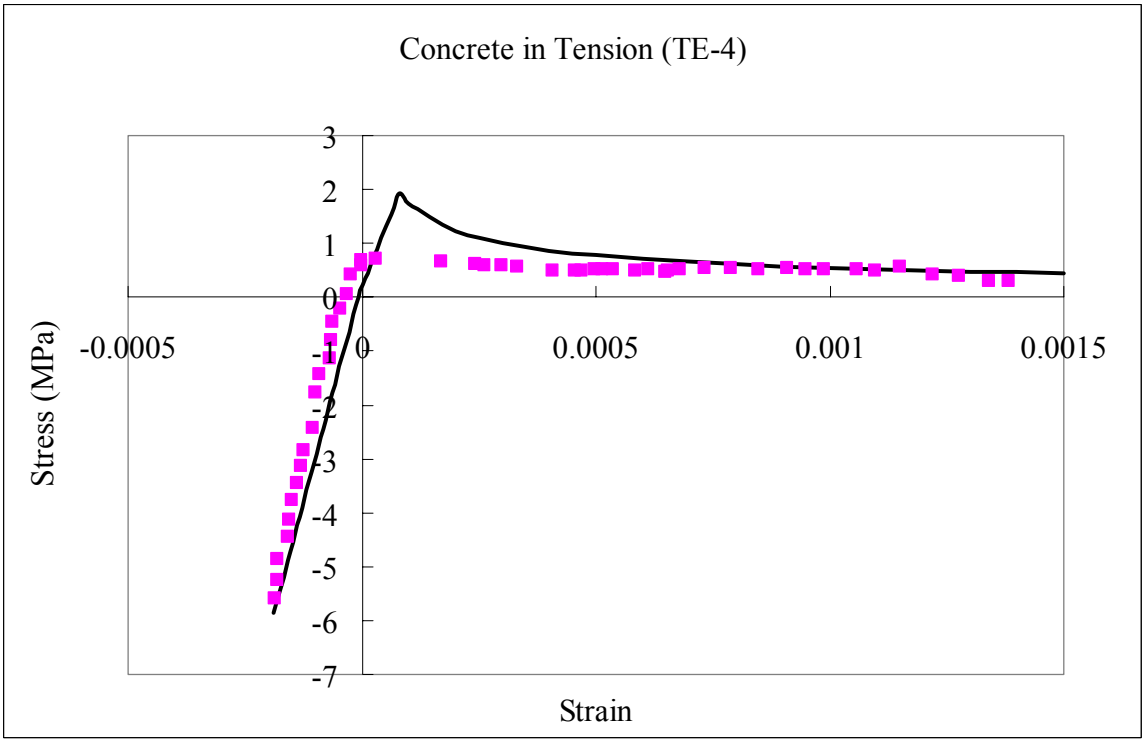

Fig. 4.6.5 Smeared (Average) Stress-Strain Relationships of Concrete in Tension (TE-4)

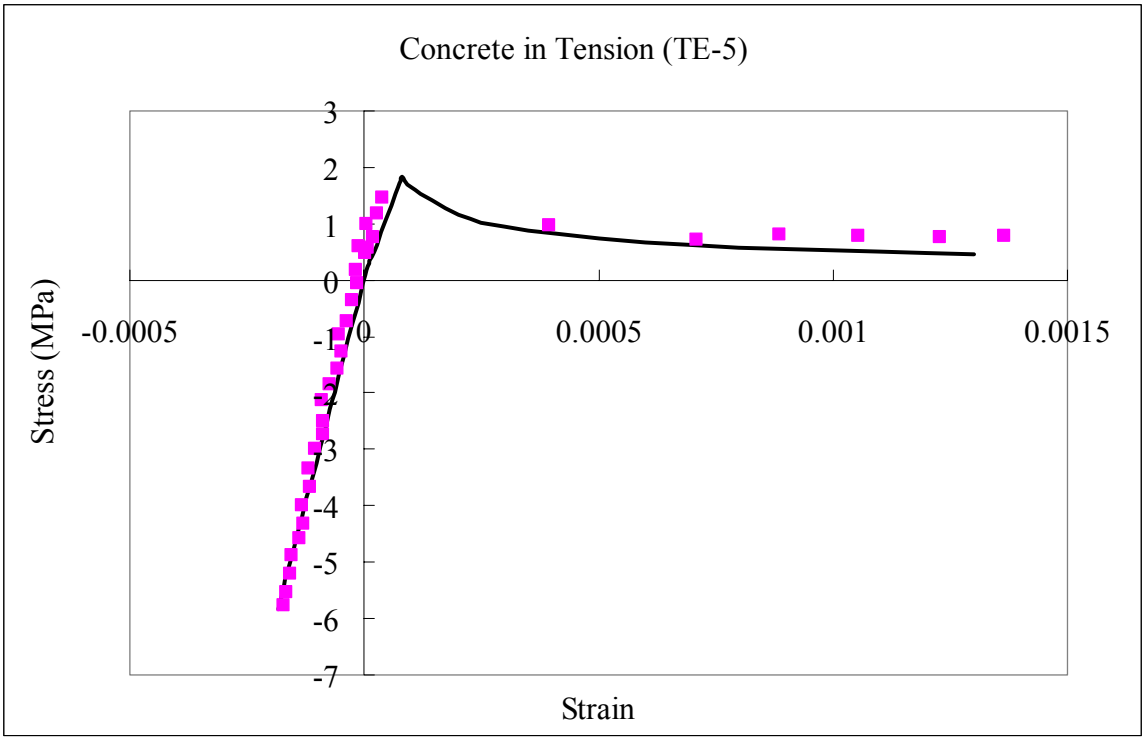

Fig. 4.6.6 Smeared (Average) Stress-Strain Relationships of Concrete in Tension (TE-5)

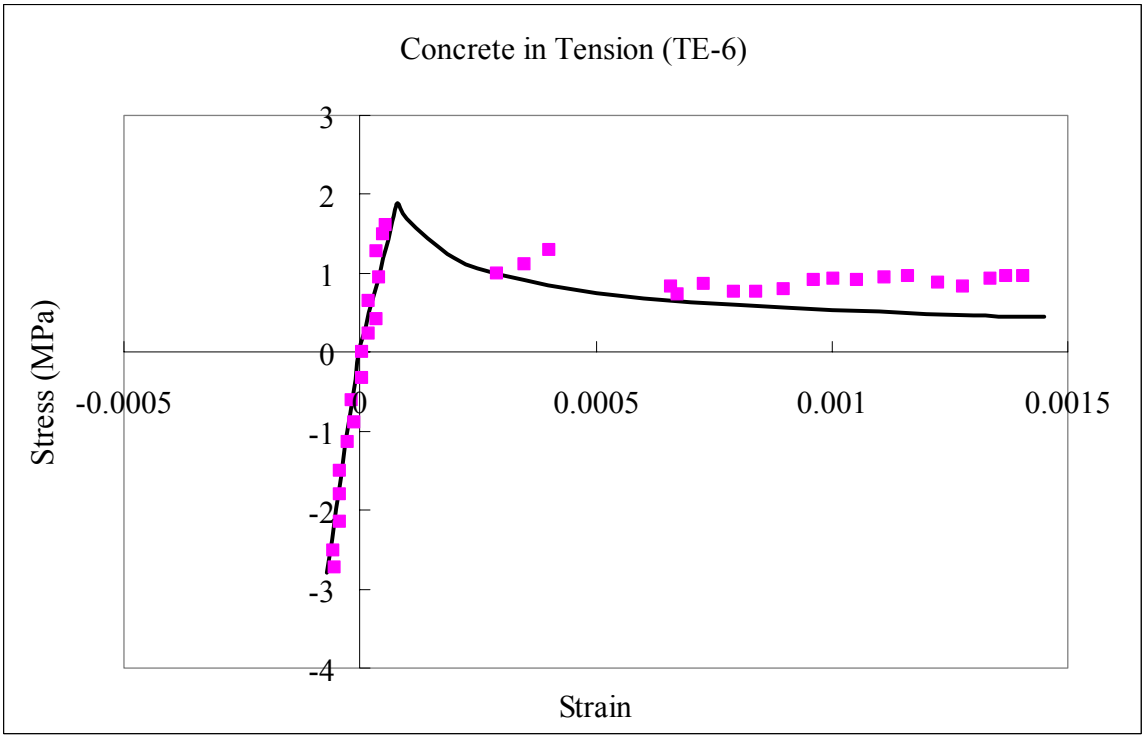

Fig. 4.6.7 Smeared (Average) Stress-Strain Relationships of Concrete in Tension (TE-6)

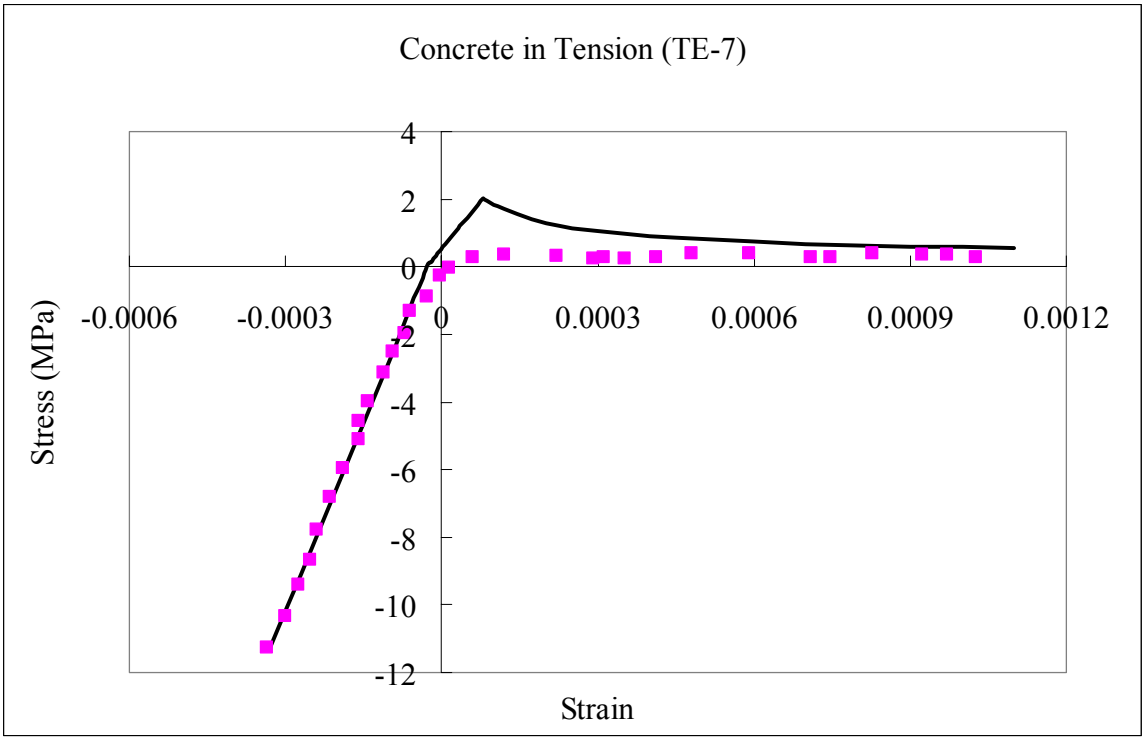

Fig. 4.6.8 Smeared (Average) Stress-Strain Relationships of Concrete in Tension (TE-7)

4.7 Smeared (Average) Stress-Strain Relationships of Prestressing Tendons Embedded in Concrete

When mild steel bars with a yield plateau are stiffened by concrete as in the non-prestressed reinforced concrete panels, the smeared (average) yield stress f_n is lower than the yield stress f_y of a bare steel bar, because of "concrete stiffening." The smeared yield stress f_n was derived and expressed analytically by Belarbi and Hsu (1994) and Zhang and Hsu (1998). Prestressing strands, however, have no clear yielding point, and the effect of "concrete stiffening" will have to be expressed in a different way.

In this research, the elastic limit of prestressing tendons embedded in concrete is approximately 70% of the ultimate strength f_{pu}, which is lower than that of bare prestressing strands. Therefore, the stress-strain relationship of prestressing tendons prior to $0.7f_{pu}$ is given by:

$$f_{ps} = E_{ps}\bar{\varepsilon}_s, \qquad \bar{\varepsilon}_s < \frac{0.7 f_{pu}}{E_{ps}} \tag{4.7-1}$$

where

E_{ps} = elastic modulus of prestressing tendons taken as 200 GPa (29000 ksi),

and f_{pu} = ultimate strength of prestressing tendons taken as 1862 MPa (270 ksi).

After the cracking of the concrete, the experimental stress and strain of prestressing tendons can be obtained by the following derivation.

Recalling Eq. 4.6-4, the total load is given as:

$$P = A_c\sigma_c + A_{ps}f_{ps}$$

The smeared (average) stress of concrete σ_c can be obtained from Eq. 4.6-10c. Substituting Eq. 4.6-10c into Eq. 4.6-4, rearranging the terms, and then using Eq. 4.6-7, the stress of prestressing tendons is given as:

$$f_{ps} = \frac{P}{A_{ps}} - \frac{f_{cr}\left(\dfrac{\varepsilon_{cr}}{\bar{\varepsilon}_{ci}+\varepsilon_1}\right)^{0.5}}{\rho_{lp}} \tag{4.7-2}$$

The strain of the tendons is:

$$\bar{\varepsilon}_s = \bar{\varepsilon}_{pi} + \varepsilon_1 \tag{4.7-3}$$

Using Eqs. 4.7-2 and 4.7-3, the experimental stress-strain curve of prestressing tendons in panel TE-4 is plotted in Fig. 4.7.1, as well as the stress-strain curve of bare strands. The experimental curves in the other four panels are similar to that in panel TE-4.

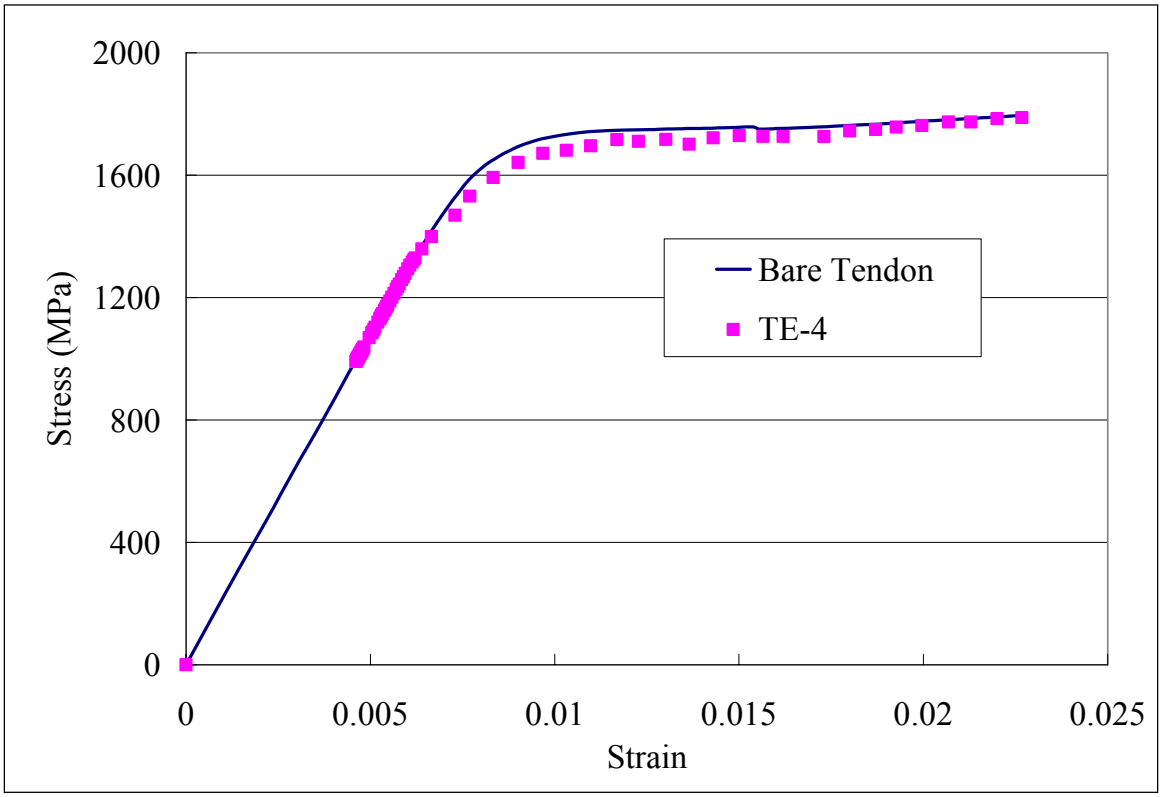

Fig. 4.7.1 Comparison of Experimental Stress-Strain Curve of Prestressing Tendons Embedded in Concrete in Panel TE-4 with that of Bare Strands

The stress-strain relationship of bare prestressing strands beyond the elastic limit (75% of the ultimate strength) has been represented by the following equation,

$$f_{ps} = \frac{E'_{ps}\bar{\varepsilon}_s}{\left[1+\left(\frac{E'_{ps}\bar{\varepsilon}_s}{f_{pu}}\right)^m\right]^{\frac{1}{m}}} \qquad (4.7\text{-}4)$$

where

E'_{ps} = modulus of prestressing tendons taken as 211 GPa (30600 ksi),

f_{pu} = ultimate strength of prestressing tendons taken as 1862 MPa (270 ksi), and

m = a constant describing the curvature at knee portion, taken as 6.

Because of the contribution of the concrete in tension, the smeared (average) stress-strain curve of prestressing tendons embedded in concrete should be lower than that of bare tendons (shown in Fig. 4.7.1). The elastic limit also reduced from 75% to 70% of the ultimate strength.

Replacing f_{pu} by f'_{pu} (260 ksi), and the constant m by 5, Eq. 4.7-5 was obtained to fit the experimental results (Fig. 4.7.1) of prestressing strands embedded in concrete:

$$f_{ps} = \frac{E''_{ps}\bar{\varepsilon}_s}{\left[1+\left(\frac{E''_{ps}\bar{\varepsilon}_s}{f'_{pu}}\right)^5\right]^{\frac{1}{5}}}, \qquad \bar{\varepsilon}_s \geq \frac{0.7 f_{pu}}{E_{ps}} \tag{4.7-5}$$

where

E''_{ps} = modulus of prestressing tendons taken as 209.2 GPa (30345 ksi), and

f'_{pu} = revised strength of prestressing tendons taken as 1793 MPa (260 ksi).

Based on Eqs. 4.7-1 and 4.7-5, a comparison of the theoretical smeared (average) stress-strain curve of prestressing tendons with the experimental curve in panel TE-4 is shown in Fig. 4.7.2. It can be seen that the two proposed equations are satisfactory. Fig. 4.7.3 to Fig. 4.7.6 show the comparisons for the other four panels, TE-3, 5, 6, and 7.

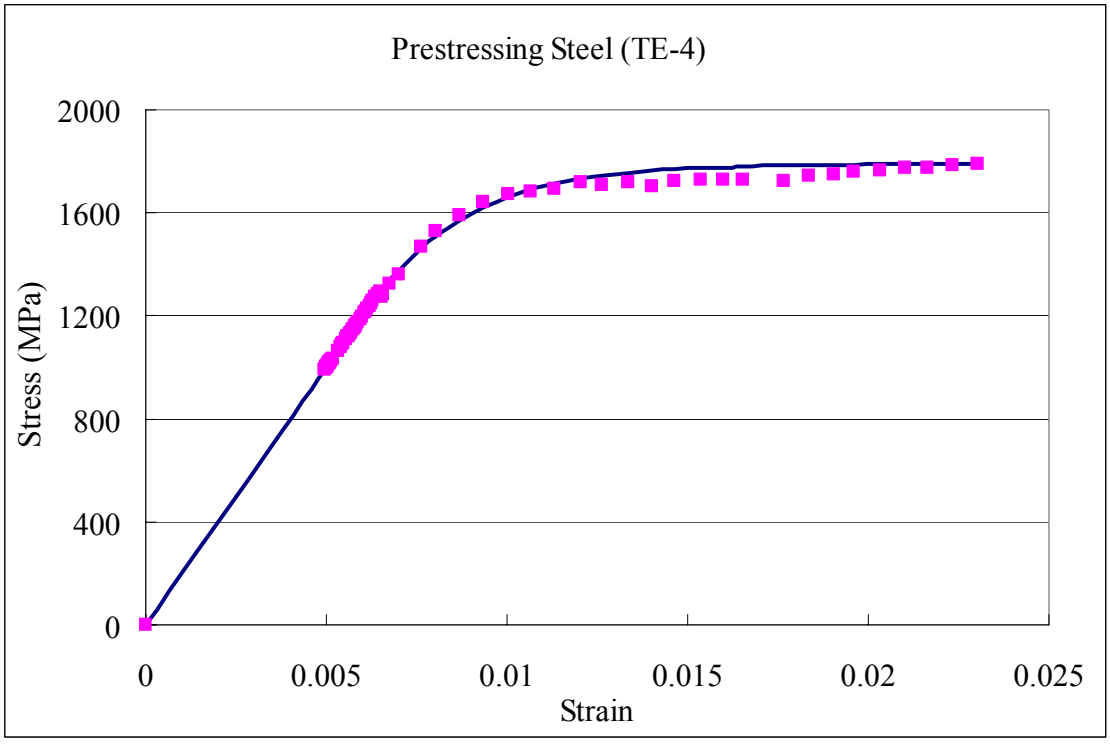

Fig. 4.7.2 Comparison of Theoretical Smeared (Average) Stress-Strain Curve of Prestressing Tendons with Experimental Curve for Panel TE-4

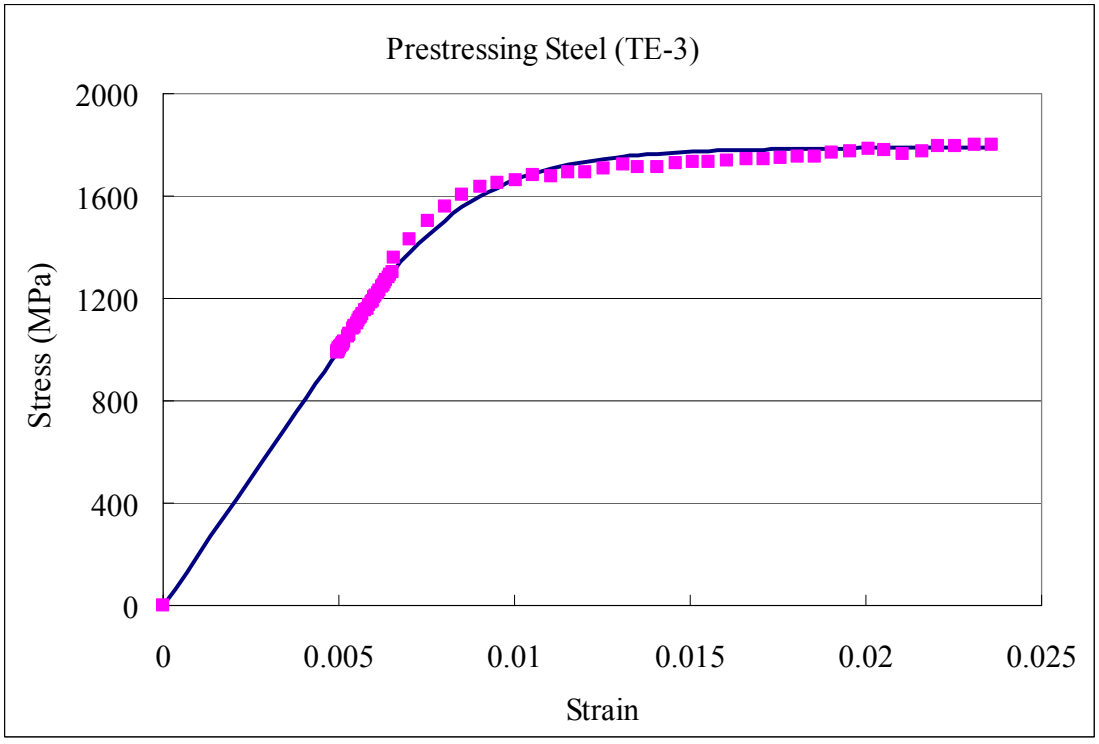

Fig. 4.7.3 Comparison of Theoretical Smeared (Average) Stress-Strain Curve of Prestressing Tendons with Experimental Curve for Panel TE-3

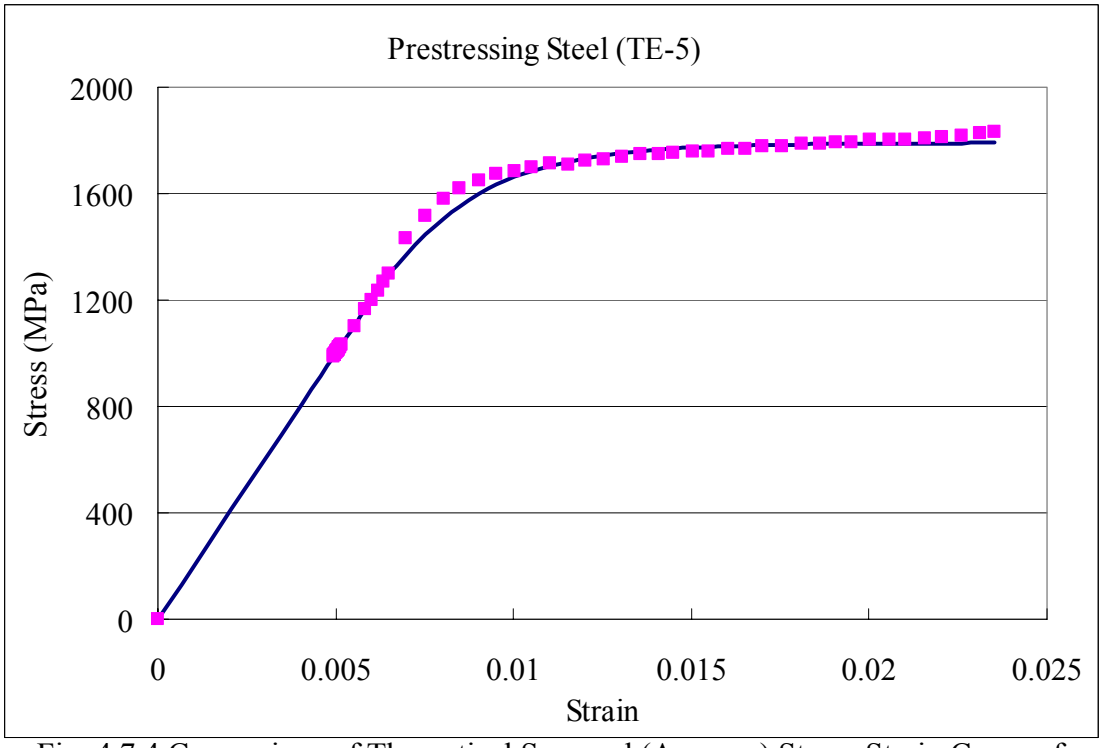

Fig. 4.7.4 Comparison of Theoretical Smeared (Average) Stress-Strain Curve of Prestressing Tendons with Experimental Curve for Panel TE-5

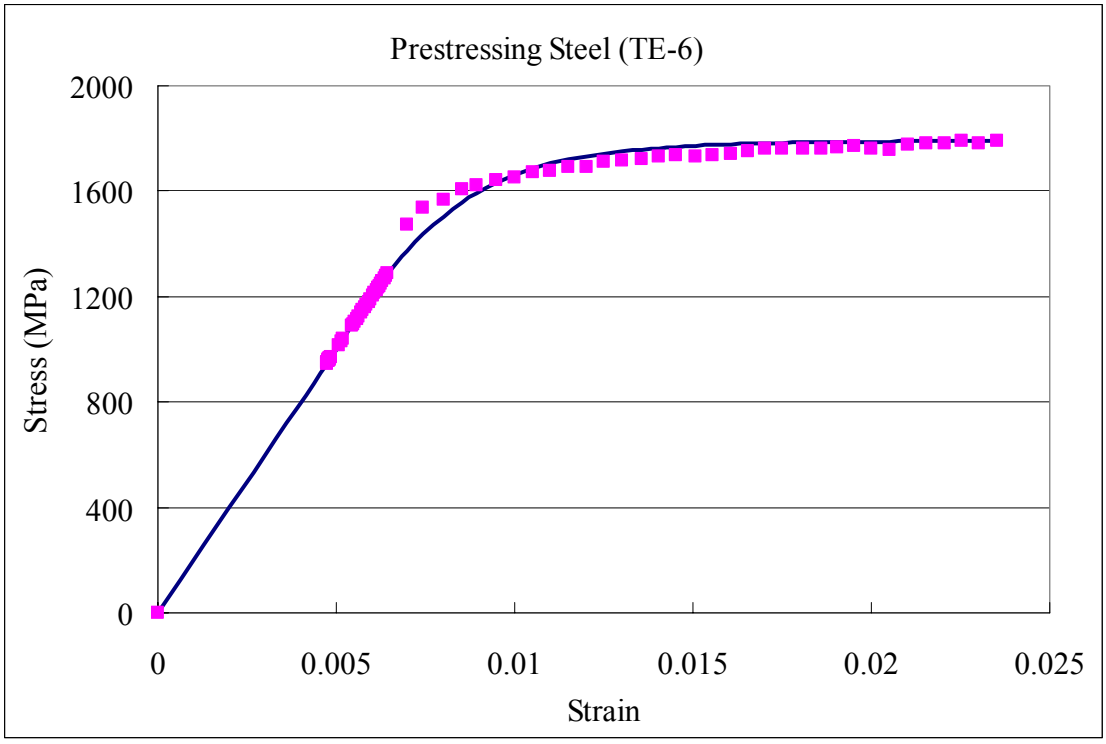

Fig. 4.7.5 Comparison of Theoretical Smeared (Average) Stress-Strain Curve of Prestressing Tendons with Experimental Curve for Panel TE-6

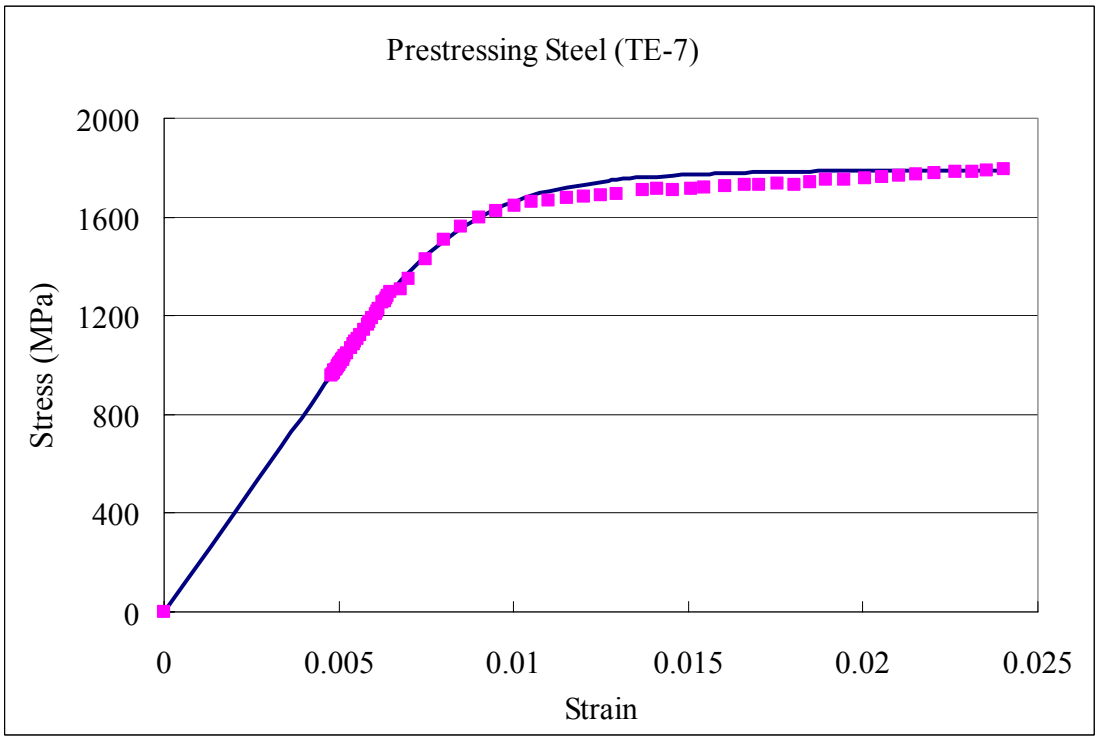

Fig. 4.7.6 Comparison of Theoretical Smeared (Average) Stress-Strain Curve of Prestressing Tendons with Experimental Curve for Panel TE-7

4.8 Smeared (Average) Stress-Strain Relationships of Concrete in Compression

Figures 4.5.3 and 4.5.4 give the compressive stress-strain curves of the panels in Group TE. To obtain the compressive stress-strain relationship of the concrete, the stresses in Fig. 4.5.3 and Fig. 4.5.4 are subtracted by the mild steel stresses, while the strains remain the same. The stress-strain relationship of mild steel bars in compression is the same as that of a bare steel bar. That is, the stress is proportional to the strain with the slope of E_s until yielding and becomes a constant of 415.1 MPa (60.2 ksi) after yielding.

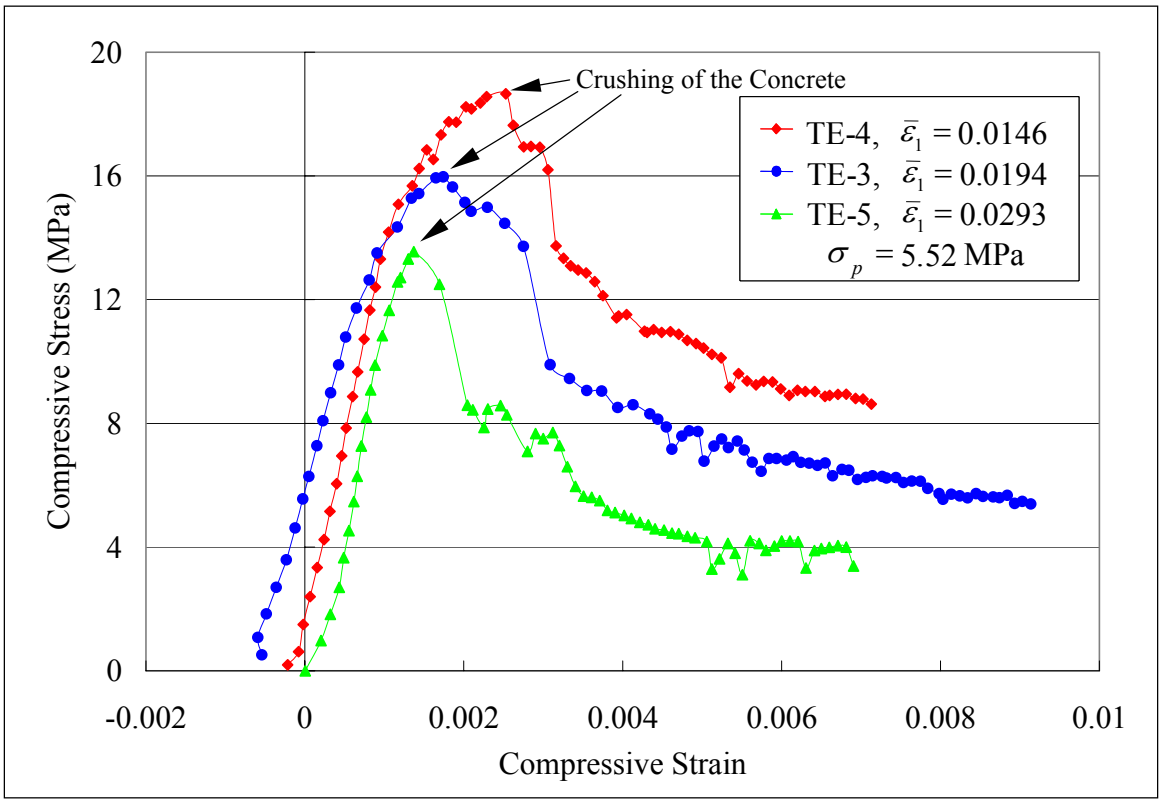

Fig. 4.8.1 Smeared (Average) Stress-Strain Relationships of Concrete in Compression in Panels TE-4, 3, and 5

The experimental smeared (average) stress-strain curves of the concrete in compression are shown in Fig. 4.8.1 and Fig. 4.8.2.

To be consistent with the non-prestressed reinforced concrete, a parabolic equation is proposed here for the compressive stress-strain curve of the prestressed concrete:

$$\sigma_c = \zeta_\sigma f_c' \left[2\left(\frac{\varepsilon_c}{\zeta_\varepsilon \varepsilon_0}\right) - \left(\frac{\varepsilon_c}{\zeta_\varepsilon \varepsilon_0}\right)^2 \right], \quad \frac{\varepsilon_c}{\zeta_\varepsilon \varepsilon_0} \le 1 \qquad (4.8\text{-}1a)$$

or

$$\sigma_c = \zeta_\sigma f_c' \left[1 - \left(\frac{\varepsilon_c/\zeta_\varepsilon \varepsilon_0 - 1}{4/\zeta_\varepsilon - 1}\right)^2 \right], \quad \frac{\varepsilon_c}{\zeta_\varepsilon \varepsilon_0} > 1 \qquad (4.8\text{-}1b)$$

where

ε_0 = concrete cylinder strain corresponding to cylinder strength f_c', and

ζ_σ, ζ_ε = stress and strain softening coefficients, respectively.

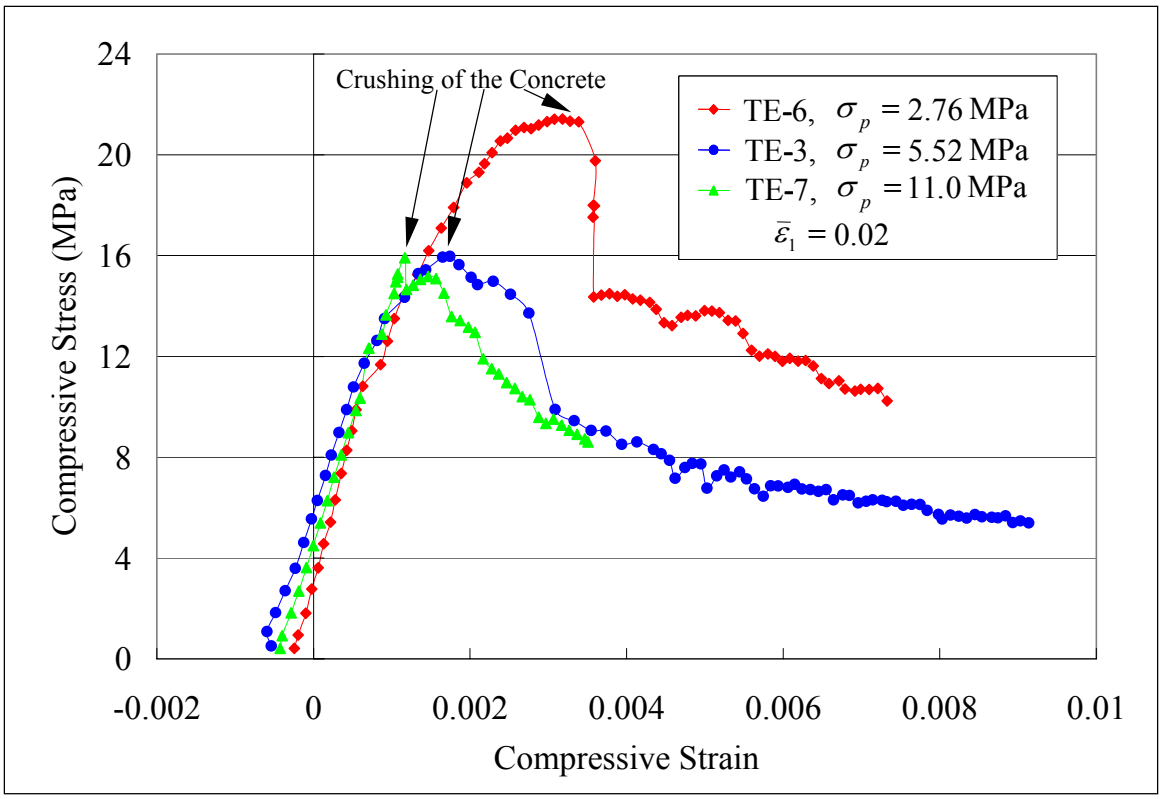

Fig. 4.8.2 Smeared (Average) Stress-Strain Relationships of Concrete in Compression in Panels TE-6, 3, and 7

Based on the experimental research conducted by Belarbi and Hsu (1994 and 1995), the strain softening coefficient ζ_ε for 0^o panels under sequential loading is equal to unity. The same phenomenon can also be observed in the test panels of Group TE. The discussion in this section, however, focuses on the stress softening coefficient, ζ_σ.

The stress softening coefficient ζ_σ is defined as the ratio of the peak compressive stress σ_p of the panel to the companion cylinder strength f_c' as follows:

$$\zeta_\sigma = \frac{\sigma_p}{f_c'} \qquad (4.8\text{-}2)$$

Based on the above equation, the experimental softening coefficients ζ_σ of the panels are calculated and listed in Table 4.8.1. The softening coefficients in the two series of panels are compared.

Table 4.8.1 Experimental Softening Coefficients

Panel No.	$\rho_{\ell p}$	$\bar{\varepsilon}_1$	f_c' (MPa)	σ_{pk} (MPa)	ζ_σ (exp.)
[1]	[2]	[3]	[4]	[5]	[6]=[5]/[4]
TE-4	0.59%	1.46%	38.69	18.65	**0.482**
TE-3	0.59%	1.94%	32.52	15.98	**0.492**
TE-5	0.59%	2.93%	34.76	13.55	**0.390**
TE-6	0.295%	2.03%	36.81	21.42	**0.582**
TE-3	0.59%	1.94%	32.52	15.98	**0.492**
TE-7	1.18%	2.05%	42.39	15.13	**0.357**
TE-1	0.21%	2.11%	48.46	16.68	**0.344**

Table 4.8.1 also lists a part of the test results of panel TE-1 that related to the softening coefficient. Panel TE-1 was a trial panel, not included in the test program because of premature failure at the edges of the panel. The layout of panel TE-1 is similar to that of panel TE-6. The reinforcements in the longitudinal direction were five seven-wire strands with the diameter of 0.5 in. The mild steel ratio was 0.54%. The compressive loading was applied with a constant horizontal tensile strain of 2.11%.

In the first series of panels (TE-4, 3, and 5), the effect of the tensile strain $\bar{\varepsilon}_1$ in the perpendicular direction on the softening coefficient was studied. It was clear that the softening coefficient is a function of the tensile strain; the larger the tensile strain, the lower the softening coefficient. This tendency is well described in published data on the expression of the softening coefficient for 0^o reinforced concrete panels under sequential loading (Belarbi and Hsu, 1994 and 1995; Zhang and Hsu, 1998):

$$\zeta_\sigma = \frac{5.8}{\sqrt{f_c'}\sqrt{1+250\bar{\varepsilon}_1}} \qquad (4.8\text{-}3)$$

In Table 4.8.2 the predicted results from Eq. 4.8-3, given in columns 4 and 5, are compared to the new test data on prestressed panels, column 3. The difference between the two sets of results can be considered as the effect of prestress and can be represented by a prestress factor W_p.

In the second series of panels (TE-6, 3, and 7), the effect of the percentage of prestressing tendons, as well as the prestress in the concrete, was studied. Similar to the first series, the experimental results are compared with those from Eq. 4.8-3 and listed in Table 4.8.2, including

the prestress factor W_p. Neglecting panel TE-6 in Table 4.8.2, the average prestress factor W_p is 1.15.

Table 4.8.2 Comparison of Experimental Softening Coefficients with Analytical Model

Panel No.	$\bar{\varepsilon}_1$	ζ_σ (exp.)	$\frac{5.8}{\sqrt{f'_c}} \le 0.9$	$\frac{1}{\sqrt{1+250\bar{\varepsilon}_1}}$	W_p
[1]	[2]	[3]	[4]	[5]	$[6]=\frac{[3]}{[4][5]}$
TE-4	1.46%	0.482	0.90	0.464	**1.16**
TE-3	1.94%	0.492	0.90	0.413	**1.32**
TE-5	2.93%	0.390	0.90	0.347	**1.25**
TE-6	2.03%	0.582	0.90	0.406	**1.59***
TE-3	1.94%	0.492	0.90	0.413	**1.32**
TE-7	2.05%	0.357	0.89	0.404	**0.99**
TE-1	2.11%	0.344	0.83	0.399	**1.04**

* Not included in the average. The average is 1.15.

The result from panel TE-6 is neglected for the following two reasons: First, there was only one layer of prestressing tendons in the longitudinal direction. When the tensile loading was applied, only three main cracks were created as shown in Fig. 4.8.3. In the other panels, such as panel TE-3, two layers of tendons were used which induced more uniform cracks as shown in Fig. 4.8.4. Since panel TE-6 had much fewer cracks than TE-3, the concrete between the cracks in panel TE-6 was stronger than that in panel TE-3, resulting in a higher load capacity. Thus, neglecting panel TE-6 is on the conservative side. Second, in actual structures, such as prestressed concrete bridge girders, many tendons are placed creating more uniform cracks. Neglecting the effects exhibited by panel TE-6 in determining the value of the prestress factor is valid in practice.

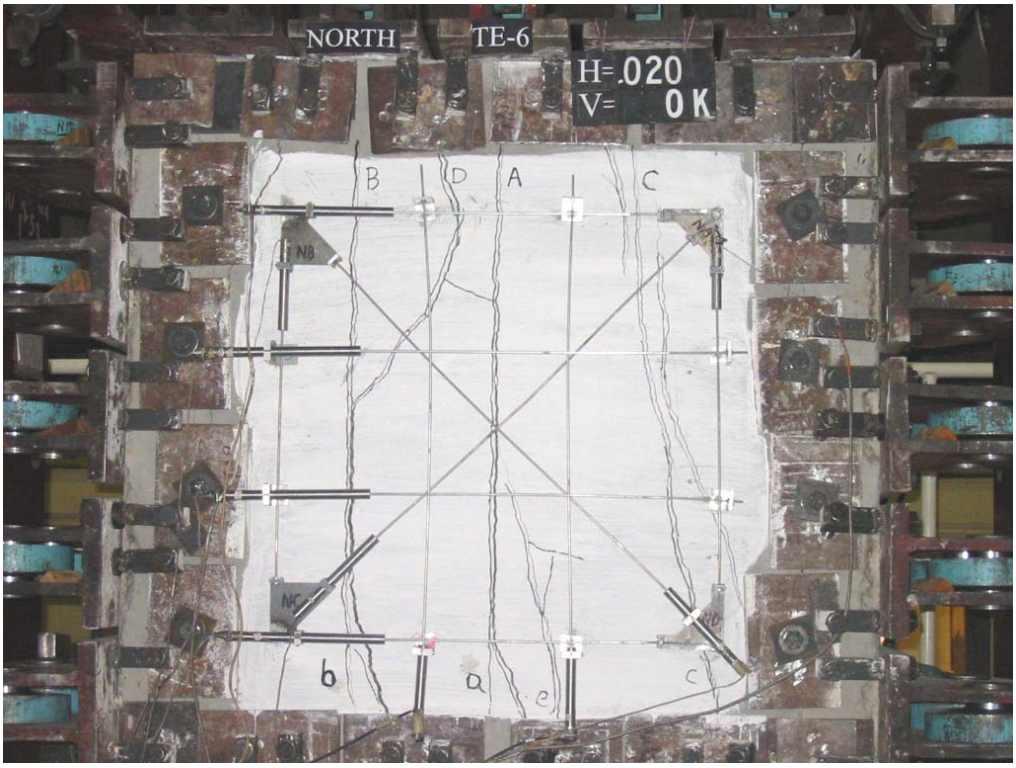

Fig. 4.8.3 Crack Pattern of Panel TE-6

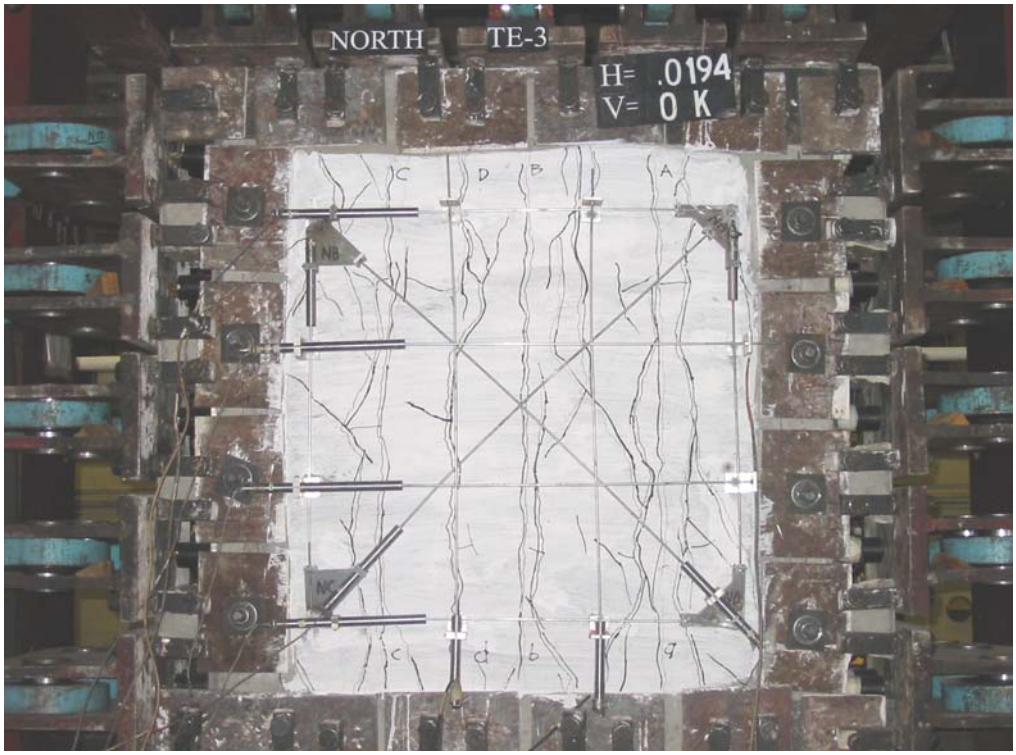

Fig. 4.8.4 Crack Pattern of Panel TE-3

In summary, the smeared (average) stress-strain relationships of concrete in compression are expressed as:

$$\sigma_c = \zeta_\sigma f_c' \left[2\left(\frac{\varepsilon_c}{\varepsilon_0}\right) - \left(\frac{\varepsilon_c}{\varepsilon_0}\right)^2 \right], \qquad \frac{\varepsilon_c}{\varepsilon_0} \le 1 \tag{4.8-4a}$$

and

$$\sigma_c = \zeta_\sigma f_c' \left[1 - \left(\frac{\varepsilon_c/\varepsilon_0 - 1}{3}\right)^2 \right], \qquad \frac{\varepsilon_c}{\varepsilon_0} > 1 \tag{4.8-4b}$$

where

$$\zeta = f(f_c')f(\bar{\varepsilon}_1)f(\beta)W_p \le 0.9 \tag{4.8-5}$$

$$f(f_c') = \frac{5.8}{\sqrt{f_c'}} \le 0.9 \ \ (f_c' \text{ in MPa}) \tag{4.8-6}$$

$$f(\bar{\varepsilon}_1) = \frac{1}{\sqrt{1 + 250\bar{\varepsilon}_1}} \tag{4.8-7}$$

$$f(\beta) = 1 - \frac{|\beta|}{24^\circ} = 1 \text{ because } \beta = 0 \tag{4.8-8}$$

and

$$W_p = 1.15 \tag{4.8-9}$$

CHAPTER 5

PRESTRESSED CONCRETE 45-DEGREE PANELS UNDER PURE SHEAR (PROPORTIONAL LOADING)

As Chapter 4 describes the test results of the panels in Group TE, Chapter 5 addresses the studies done on Group TA. Group TA panels with 45^o steel bars were subjected to pure shear, a special case of proportional loading. The test program, test specimens, and test results of the panels in Group TA are described. The shear behavior of prestressed concrete was studied, and the stress-strain relationship of concrete in compression is further discussed. Particular attention is given to the new prestress factor in the softening coefficient.

5.1 Test Program (Group TA)

Five full-size panels with steel bars oriented at 45^o were designed to study the shear behavior of prestressed concrete membrane elements. Two variables were studied in this group: (1) percentage of prestressing tendons in the longitudinal direction ρ_{lp} and (2) percentage of mild steel bars in the transverse direction ρ_t. The details are listed in Table 5.1.1. The panels in this group are identified first with the letter "T", which signifies that the panels are designed with prestressing **T**endons. The second letter "A" means that the steel grid was oriented at a 45^o angle to the applied principal stresses.

The panels in this group were divided into two series based on the two variables. The first series included panels TA-1, 2, and 3. In this series, the percentage of the prestressing steel in the longitudinal direction was kept constant at 0.84%. The mild steel in the transverse direction varied from 0.42% to 0.77% then to 1.54%. The second series included panels TA-2, 4, and 5. The percentages of the mild steel in the transverse direction were 0.77% in the three panels, and the percentages of the prestressing tendons were 0.84%, 0.59%, and 0.42%, respectively. The effects of the percentages of prestressing tendons and the percentage of mild steel on the shear behavior of prestressed concrete membrane elements were studied in the test program.

Table 5.1.1 Principal Variables of Test Panels in Group TA

Specimen	Concrete		Steel in ℓ direction		Steel in t direction	
	f'_c (MPa)	ε_0	Tendons	$\rho_{\ell p}$	Mild Steel	ρ_t
TA-1	41.47	0.0021	2 ϕ0.6 @189 mm	0.84%	2#3@189 mm	0.42%
TA-2	41.33	0.0019	2 ϕ0.6 @189 mm	0.84%	2#4@189 mm	0.77%
TA-3	42.21	0.0019	2 ϕ0.6 @189 mm	0.84%	4#4@189 mm	1.54%
TA-4	42.54	0.0021	2 ϕ0.5 @189 mm	0.59%	2#4@189 mm	0.77%
TA-5	41.08	0.0021	1 ϕ0.6 @189 mm	0.42%	2#4@189 mm	0.77%

5.2 Test Specimens (Group TA)

5.2.1 Layout of Specimens

As in the case of the specimens in Group TE, the same two coordinate systems ($\ell - t$ and $1-2$) were used in the panels in Group TA, Fig. 5.2.1. All the panels had the same size of 1398 mm × 1398 mm × 178 mm (55 in. × 55 in. × 7 in.). The longitudinal reinforcements (prestressing tendons) and the transverse reinforcements (mild steel) were oriented at an angle of 45^o to the principal $1-2$ coordinate of the applied stresses, i.e. $\alpha_1 = 45^o$.

As shown in Fig. 5.2.1(a), two layers of the prestressing tendons were placed in the longitudinal direction with a spacing of 188 mm (7.4 in.) in panels TA-1, 2, 3, and 4. Since the stresses in 0.6 in. prestressing tendons were kept constant at about 986 MPa (143 ksi) in the first three panels, the prestress on the concrete was approximately 8.3 MPa (1.2 ksi). In panel TA-4, 0.5 in. prestressing tendons were used to replace the 0.6 in. tendons. The smaller tendons produced a prestress of 5.8 MPa (0.84 ksi). At two of the corners of the panels, the regular anchor-inserts were used because there was no space to place the prestressing tendons.

Figure 5.2.1(b) shows panel TA-5 to have only one layer of 0.6 in. diameter prestressing tendons. This single layer of 0.6 in. diameter tendons produced a prestress of about 4.1 MPa (0.6 ksi).

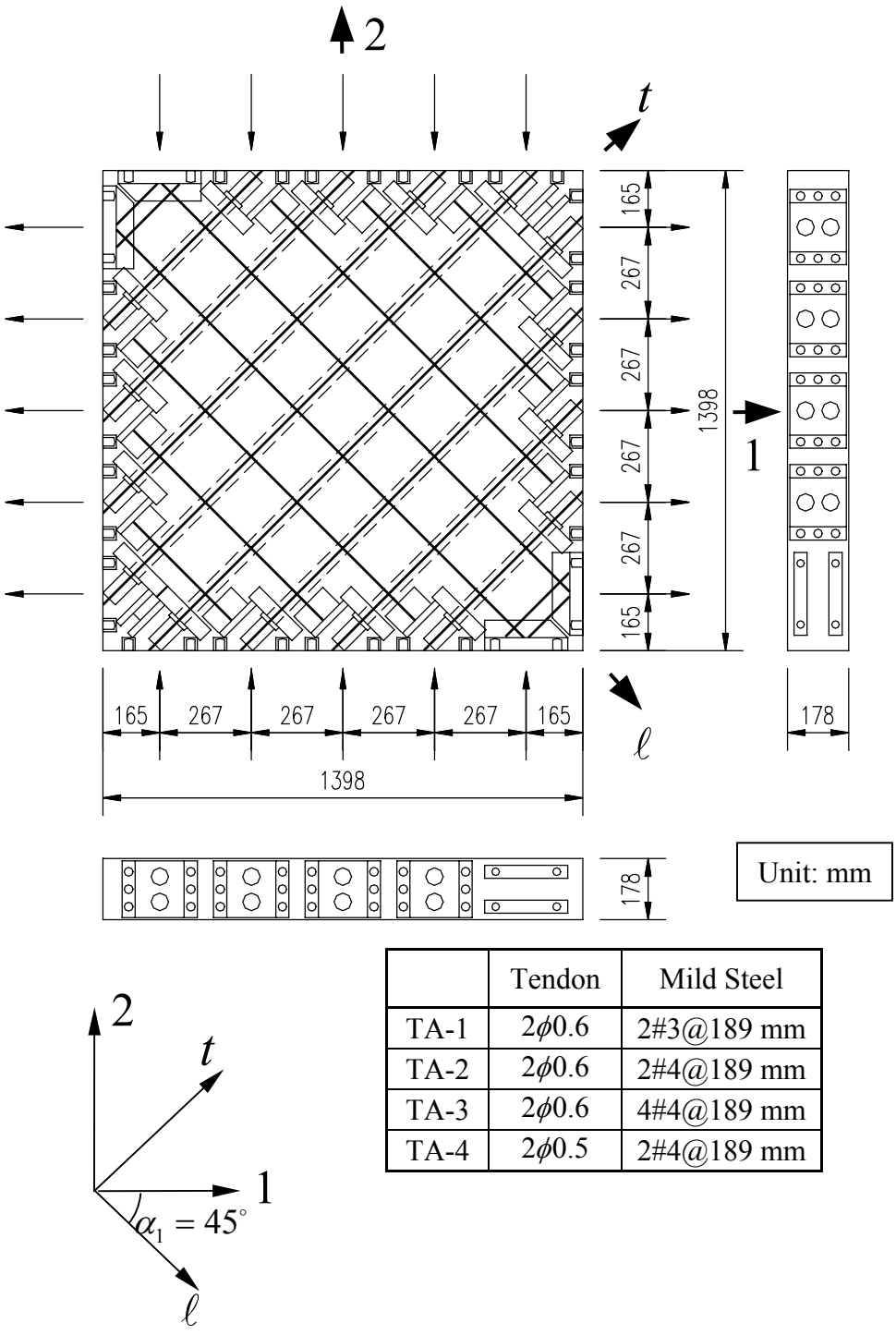

	Tendon	Mild Steel
TA-1	2ϕ0.6	2#3@189 mm
TA-2	2ϕ0.6	2#4@189 mm
TA-3	2ϕ0.6	4#4@189 mm
TA-4	2ϕ0.5	2#4@189 mm

(a) Steel Layout and Dimensions of Panels TA-1, 2, 3, and 4

Fig. 5.2.1 Steel Layout and Dimensions of Test Panels in Group TA

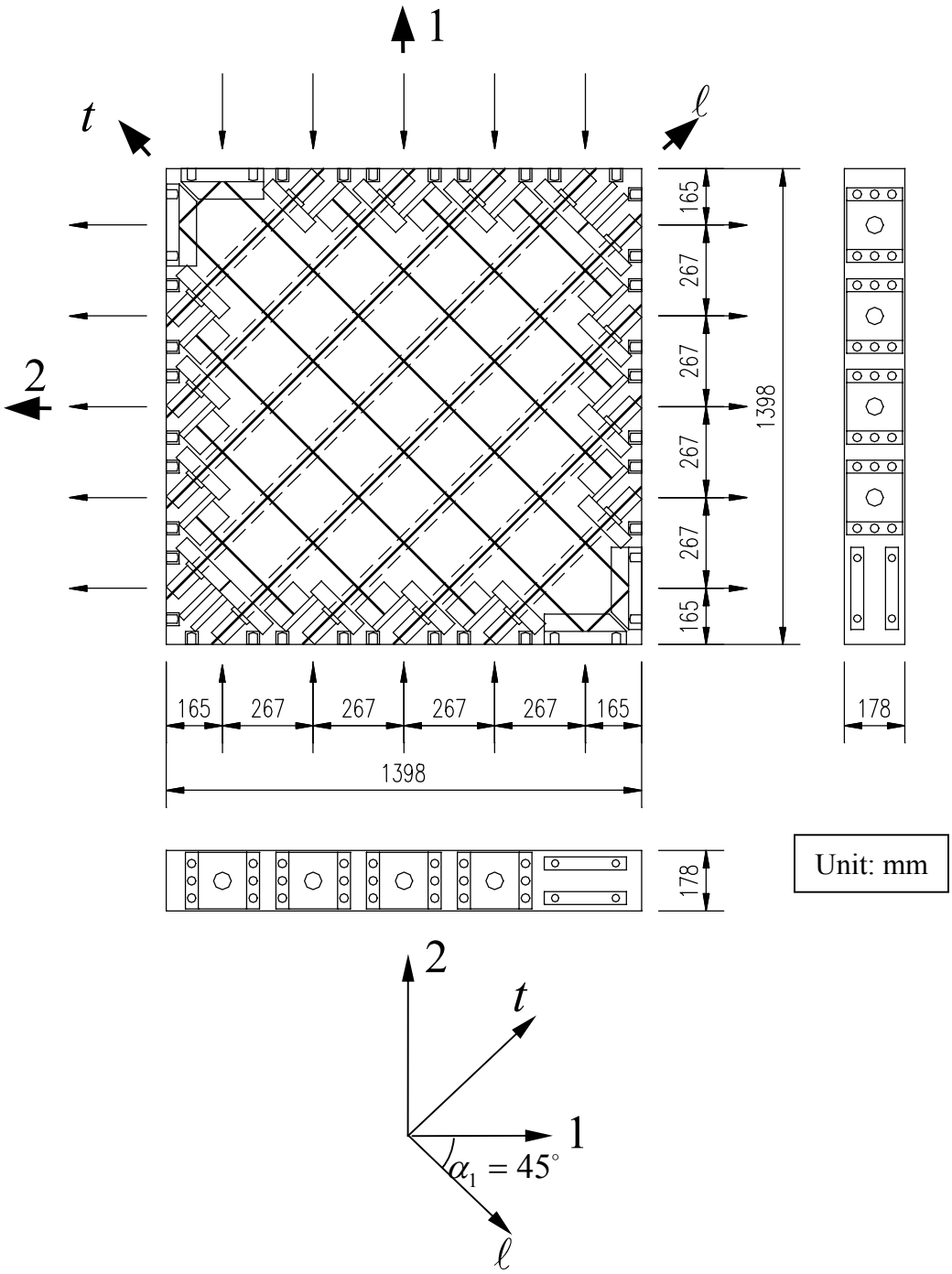

(b) Steel Layout and Dimensions of Panel TA-5

Fig. 5.2.1 Steel Layout and Dimensions of Test Panels in Group TA (continued)

5.2.2 Fabrication of Specimens

To hold the tendons at 45°, new V-shape inserts were designed and manufactured as shown in Fig. 5.2.2(a). Each V-shape insert consists of two perpendicular plates. One is the bearing plate with a thickness of 38 mm (1.5 in.) for anchoring the prestressing tendons. The other is a connecting plate with a thickness of 25 mm (1 in.) for connecting to the two layers of mild steel bars. The detailed dimensions of a typical V-shape insert are shown in Fig. 5.2.2(b). The bearing plate could hold two prestressing tendons as shown in Fig. 5.2.2(c). The connecting plate was connected to the two transverse mild steel bars via two steel plates 9.5 mm (3/8 in.) thick, 64 mm (2.5 in.) wide, and 127 mm (5 in.) long. V-shape inserts at the corners of a panel are different in that there are no plates connecting the transverse steel bars which were directly welded onto the bearing plates. All the steel plates in the V-shape inserts were assembled by welding.

The two layers of the transverse mild steel bars were welded to the V-shape inserts in the steel casting form in the following manner: the 16 V-shape inserts were first bolted to the steel casting form, and the first layer of the steel bars was welded. Then the V-shape inserts were flipped over, and fastened again. The second layer of the steel bars could then be welded. The two V-shape inserts at the corners were connected by welding four #4 steel bars on the surfaces of the adjacent bearing plates.

After finishing the welding work, the steel casting form was emptied and cleaned. The whole steel assembly and the flexible conduits were then placed into the casting form, as shown in Fig. 5.2.3. The casting and curing procedure were the same as those described in Section 4.2.2.

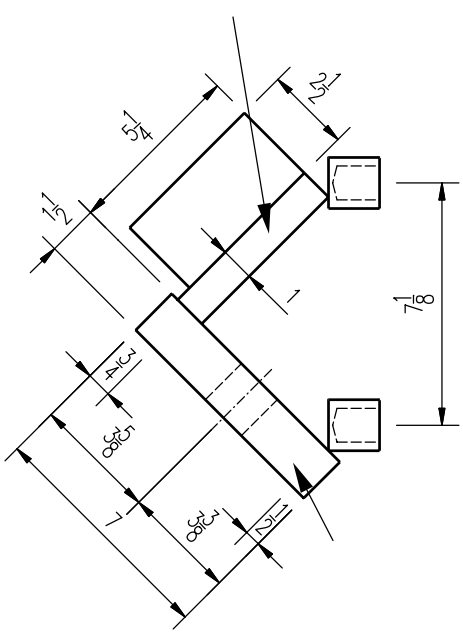

(b) Top View

(a) Perspective View

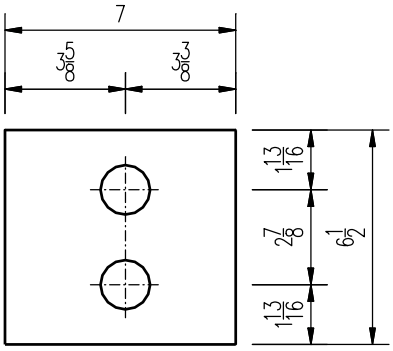

(c) Bearing Plate

Fig. 5.2.2 Dimensions of V-shape Inserts (Unit: in.)

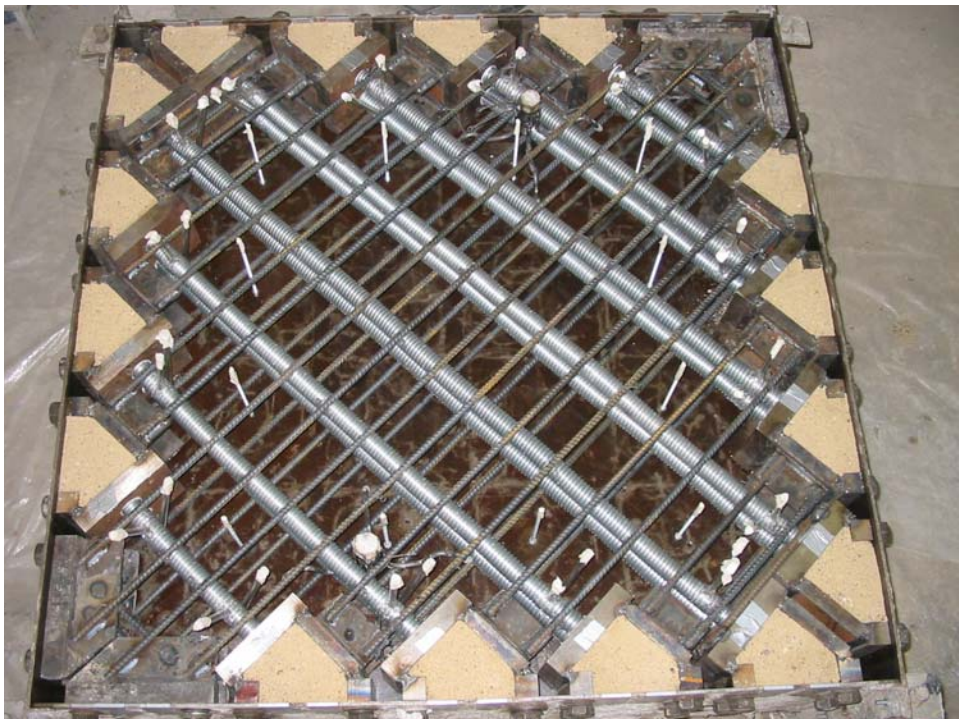

(a) Formwork of Panel TA-3

(b) Formwork of Panel TA-5

Fig. 5.2.3 Formworks of Panels in Group TA

5.2.3 Tendon Jacking System

The tendon jacking system for the panels in Group TA is the same as that for the panels in Group TE except that different supporting chairs were used. Fig. 5.2.4(a) shows the pulling end in the jacking system.

The supporting chair consisted of two supporting legs of unequal lengths and one connecting plate, as shown in Fig. 5.2.4(b). Each supporting leg was made by welding two threaded rods of 25 mm (1 in.) diameter to a steel bearing plate at an angle of 45^{o}. The bearing plate has a 25 mm (1 in.) diameter hole at the center for a connecting bolt to the panel. The connecting plate was attached to the threaded rods by four holes at the corners and four nuts. The nuts on the four threaded rods could be adjusted to make the connecting plate perpendicular to the direction of the prestressing tendons. Three holes with a diameter of 16 mm (5/8 in.) were drilled near the center of the connecting plate along the plane of flexible conduits to accommodate both the two-layer and the single-layer arrangements of the prestressing tendons. For the corner tendons, the sizes of the supporting legs and the connecting plate were slightly different from those of the other tendons.

The tendon jacking system, including hydraulic jack, pump, pressure relief valve, load cells, etc, was the same as that used in the cracking simulation tests in Chapter 3. The jacking procedure for the tendons was also explained.

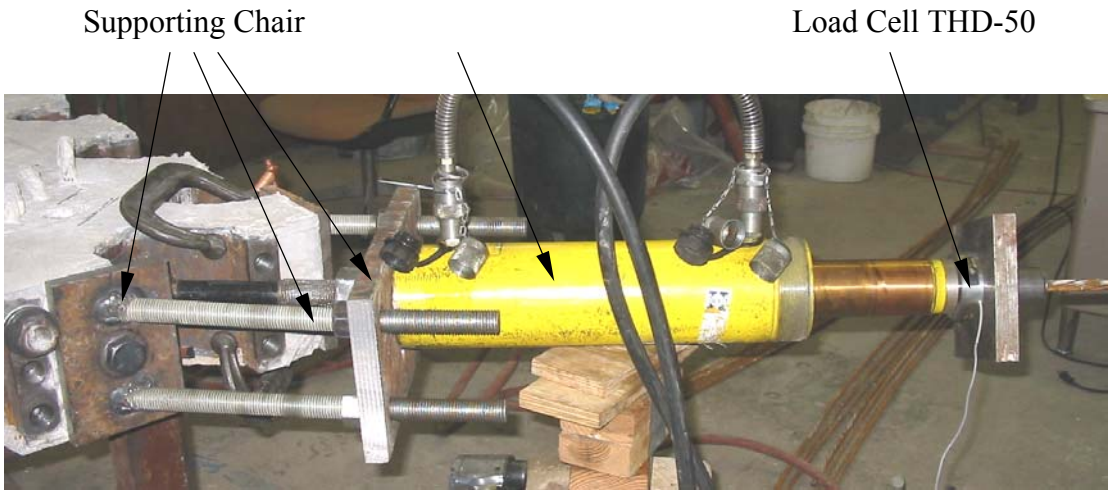

(a) Setup of Pulling End

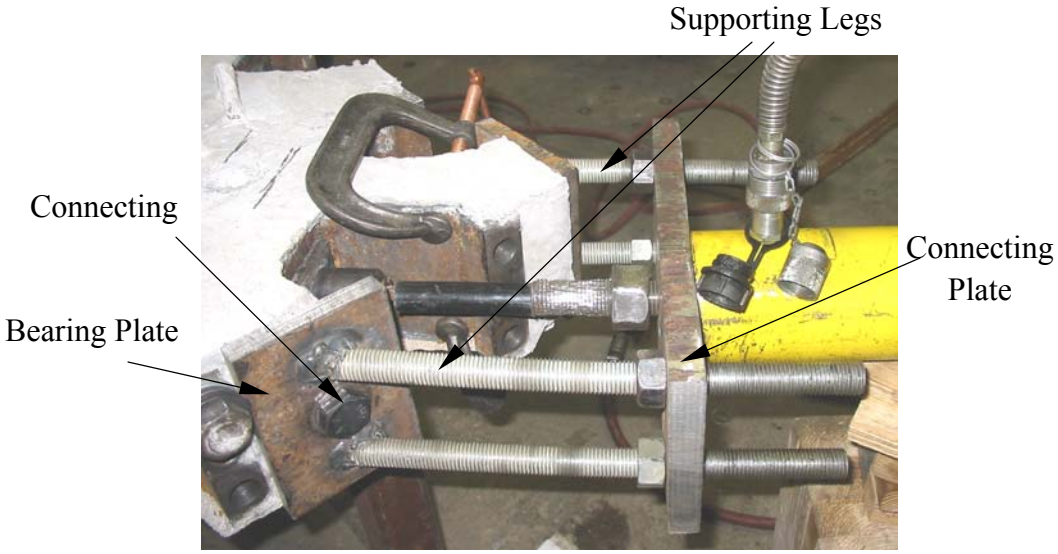

(b) Details of Supporting Chair

Fig. 5.2.4 Tendon Jacking System for Panels in Group TA

5.3 Materials (Group TA)

5.3.1 Concrete

The materials for the concrete used in Group TA were the same as those used in Group TE described in Section 4.3.1. The compressive strength of the concrete for each panel is listed in Table 5.1.1. The strength was very close to the target strength of 41.4 MPa (6000 psi). The grouting material, SCCG, was the same as that described in Section 4.3.1.

5.3.2 Reinforcements

The stress-relieved strands, grade 270 (1862 MPa), which conformed to ASTM A-416, were used in the specimens. Two sizes of strands were used. Strands with 0.5 in. (13 mm) nominal diameter and a cross-sectional area of 99 mm^2 (0.153 in^2) were used in panel TA-4, while strands with 0.6 in. (15 mm) nominal diameter and a cross-sectional area of 140 mm^2 (0.217 in^2) were used in the other four panels.

The mild steel bars used in the Group TA panels were #3 and #4 bars, which were low-alloy grade 60 (415 MPa) steel bars and satisfied ASTM 716. The deformed bars #3 and #4 had cross-sectional areas of 71 mm^2 and 129 mm^2 (0.11 $in.^2$ and 0.20 $in.^2$), respectively. The mechanical properties of the steel bars are shown in Table 5.3.1. Fig. 5.3.1 shows two typical stress-strain relationships of #3 and #4 steel bars.

Table 5.3.1 Mechanical Properties of Steel Bars

Steel Bar	f_y (MPa)	ε_y	E_s (GPa)	ε_h
#3	413.8	0.00210	197.0	0.0200
# 4	415.1	0.00216	192.2	0.0176

Note: ε_h is the strain at the beginning of the strain hardening region.

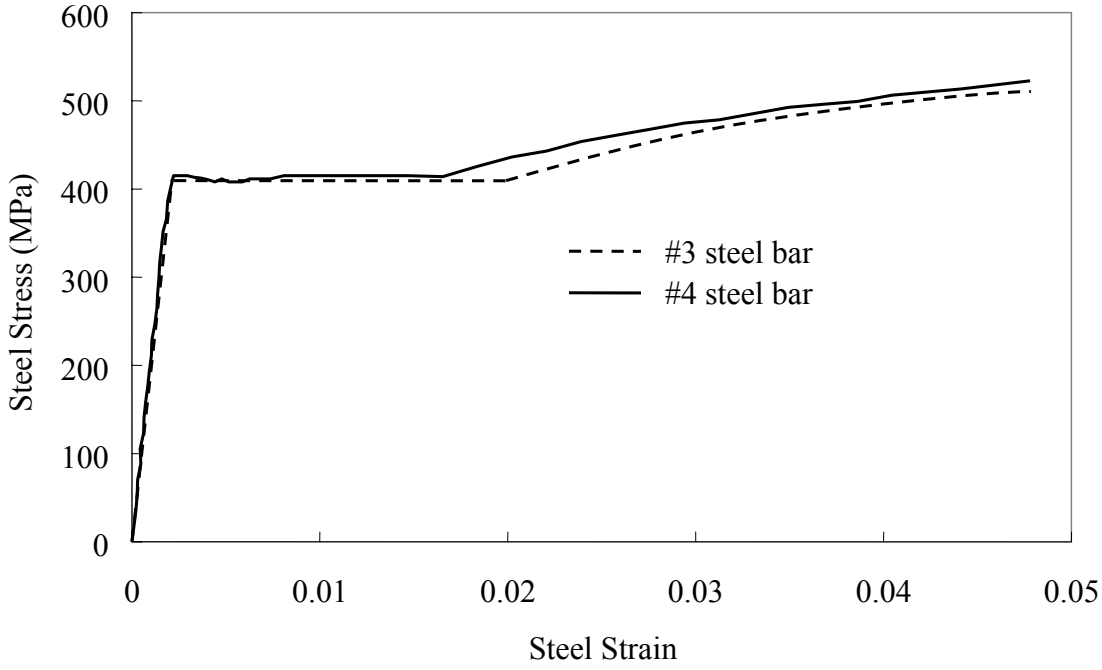

Fig. 5.3.1 Stress-Strain Curves of Bare Steel Bars

5.4 Loading Procedure (Group TA)

A proportional load path was used in the tests of panels in Group TA, as shown in Fig. 5.4.1. In these tests, all horizontal tensile stresses and vertical compressive stresses were applied with equal magnitude, $\sigma_2 = -\sigma_1$, to create a pure shear state in the 45° direction.

In applying the loads, either the horizontal or the vertical loading could be used to control the loading of the other direction. The average reading of the LVDTs for tensile strains was chosen as the controlling feedback because the compressive strains were much more sensitive and scattered than the tensile strains. In this control scheme, the horizontal tensile strain, ε_1, controls the horizontal tensile stress, σ_1, which, in turn, controls the vertical compressive stress, σ_2.

In these five panel tests, load-control mode was first applied. Just before the yielding of the steel, the strain-control mode was initiated, which could well control the non-linear part of the shear behavior.

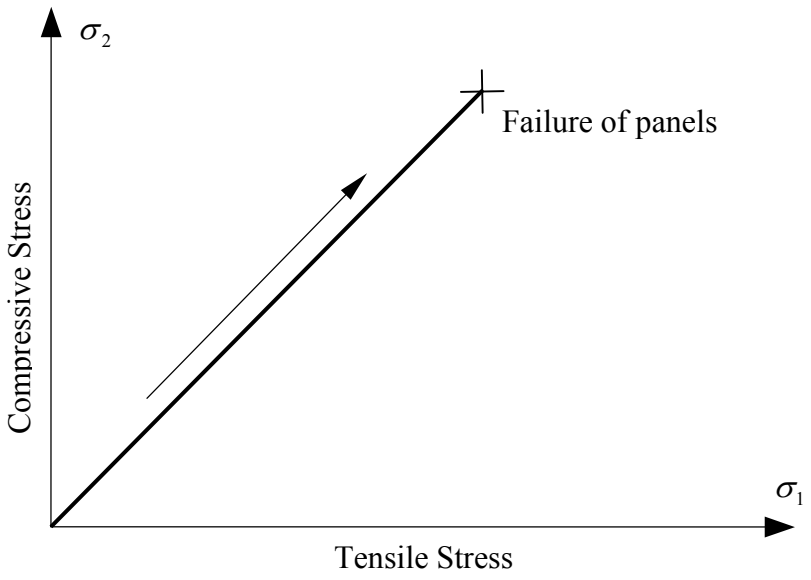

Fig. 5.4.1 Proportional Loading Path used in Group TA

5.5 General Behavior of Test Panels in Group TA

Five panels in Group TA were tested under pure shear conditions. As described in Section 5.1, the panels were designed to have various reinforcement ratios in the two orthogonal directions. The panels TA-1, 2, and 3 were used to study the effect of transverse mild steel percentage on the shear behavior of prestressed concrete elements, while the panels TA-2, 4, and 5 were used to study the effect of prestressing tendon percentage.

The raw test data of the panels, which includes the applied tensile and compressive forces and the strains of all 20 LVDTs in each panel, can be found in Wang's dissertation (2006). Wang's dissertation also gives the test data for these panels analyzed with the equilibrium and the compatibility equations in the Softened Membrane Model, the crack widths for each panel, and the crack patterns at certain stages.

5.5.1 Cracking Behavior

For non-prestressed reinforced concrete elements, initial cracks form in the direction of applied principal tensile stress, regardless of the orientation of the reinforcing bars. Under pure shear, the direction of cracks is oriented at an angle of 45^o to the longitudinal steel. With increasing load, new cracks may "rotate" if the steel ratios are different in the two directions.

The prestressed concrete panels, however, displayed a different type of crack formation and development. First, the initial cracks formed at angles of less than 45^o to the longitudinal prestressing tendons: approximately 26.5^o in panels TA-1, 2, and 3; and 31.6^o and 34.2^o in panels

TA-4 and 5, respectively. These angles are close to the angle of the principal compressive stress at the cracking of each panel.

Second, the "rotation" of cracks was not observed with the increase of the applied loads. All the cracks formed during a short "cracking stage." Beyond the peak point of the shear stress-strain curves, slippage of cracks and spalling of the concrete gradually occurred along the prestressing tendons in the middle part of the panels TA-1, 2, and 3 until the failures. In panels TA-4 and 5, only spalling was seen on one face of the panel.

Figures 5.5.1 and 5.5.2 give the shear stress-strain relationships of panels in Group TA. It can be seen that the cracking strength of the prestressed concrete panels is related to the prestressing tendons in the panels rather than the mild steel in the transverse direction. The cracking strengths of panels TA-1, 2, and 3 are approximately the same with a value of 3.7 MPa (0.54 ksi). The cracking strengths of panels TA-4 and 5 are given as 3.45 MPa and 2.84 MPa (0.50 ksi and 0.41 ksi), respectively. They are smaller than that of TA-2 because of fewer prestressing tendons, i.e., less prestress on the concrete. In other words, the prestress delays the cracking of the concrete, which is parallel to the conclusion of the panel tests in Group TE (Chapter 4).

5.5.2 Yielding of Steel

Upon the cracking of concrete, the steel bars started to resist the shear loading and the stresses in the steel increased dramatically. From the shear stress-strain relationships shown in Fig. 5.5.1, the yield point of the mild steel in the transverse direction could be discerned in panels TA-1 and TA-2 with the transverse steel ratios of 0.42% and 0.77%, respectively. In contrast, the yield point could not be discerned in panel TA-3 with a transverse steel ratio of 1.54%. Apparently, the yielding of mild steel could occur only when the transverse steel force is much less than the longitudinal prestressing force.

The yielding of prestressing tendons could not be observed in any of the panel tests of Group TA for two reasons. First, prestressing tendons have a high elastic limit. Second, there is no clear yielding plateau for prestressing tendons. Even beyond the limit of the elastic stage (0.7 f_{pu}), the stiffness decreases very slowly until reaching 85% to 90% of the ultimate strength. It was frequently observed that prestressing tendons in bridge girders did not yield under shear failure modes, because crushing of concrete occurred before the yielding of the longitudinal prestressing tendons.

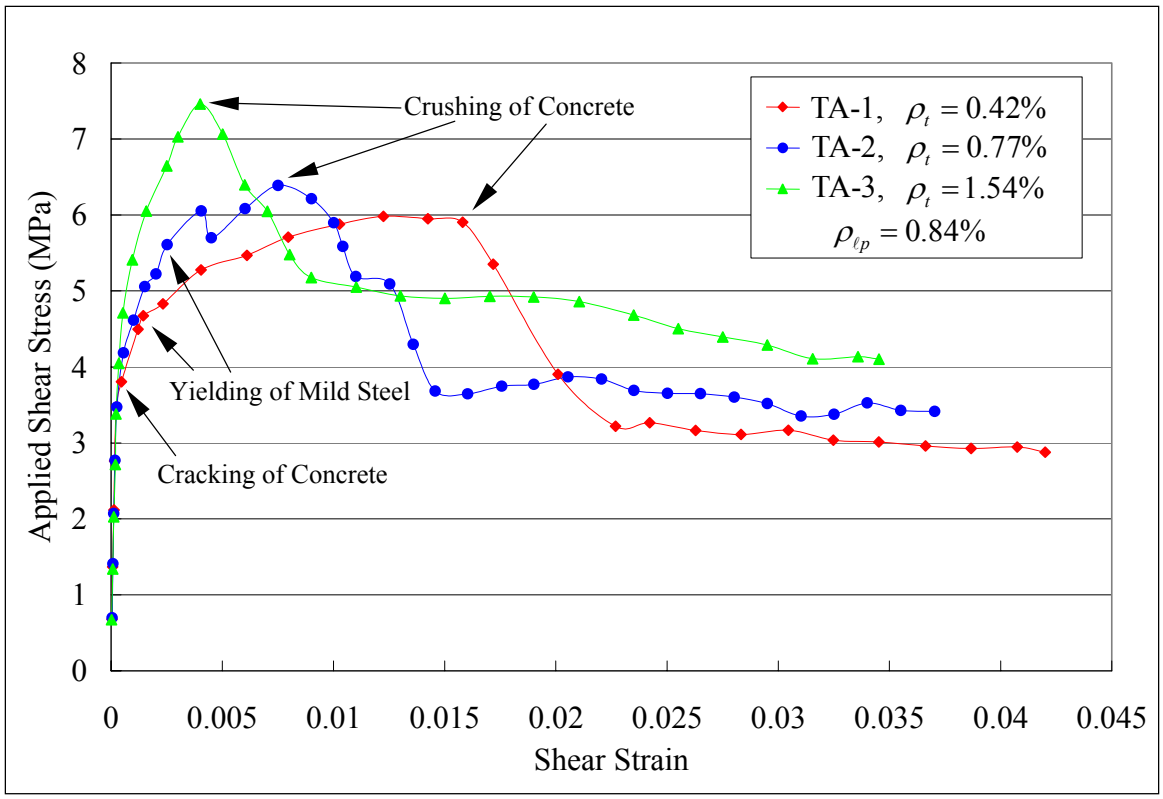

Fig. 5.5.1 Shear Stress-Strain Curves of Panels TA-1, 2, and 3

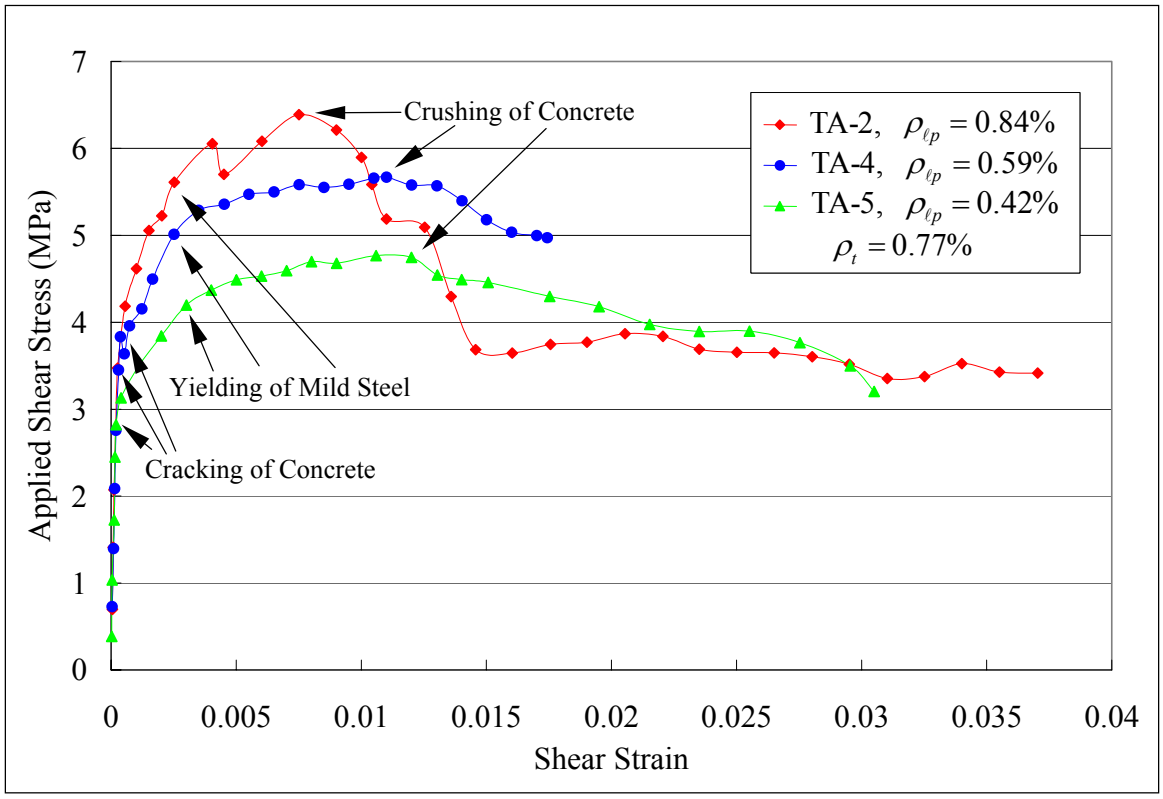

Fig. 5.5.2 Shear Stress-Strain Curves of Panels TA-2, 4, and 5

5.5.3 Shear Stress vs. Shear Strain Relationships ($\tau_{\ell t} - \gamma_{\ell t}$ Curves)

In the five panels, TA-1 to TA-5, the prestressing tendons and the mild steel were oriented at an angle of 45° to the principal $1-2$ coordinate of the applied stresses, i.e. $a_1 = 45^o$.

The stress transformation equations of the element in terms of principal applied stresses are given as:

$$\sigma_\ell = \sigma_1 \cos^2 \alpha_1 + \sigma_2 \sin^2 \alpha_1 \tag{5.5-1}$$

$$\sigma_t = \sigma_1 \sin^2 \alpha_1 + \sigma_2 \cos^2 \alpha_1 \tag{5.5-2}$$

$$\tau_{\ell t} = (-\sigma_1 + \sigma_2) \sin \alpha_1 \cos \alpha_1 \tag{5.5-3}$$

The strain transformation equations of the element in terms of principal strains are given as:

$$\varepsilon_\ell = \varepsilon_1 \cos^2 \alpha_1 + \varepsilon_2 \sin^2 \alpha_1 \tag{5.5-4}$$

$$\varepsilon_t = \varepsilon_1 \sin^2 \alpha_1 + \varepsilon_2 \cos^2 \alpha_1 \tag{5.5-5}$$

$$\gamma_{\ell t} = (-\varepsilon_1 + \varepsilon_2) \sin \alpha_1 \cos \alpha_1 \tag{5.5-6}$$

Substituting $\alpha_1 = 45^o$ into Eqs. 5.5-3 and 5.5-6, the shear stress $\tau_{\ell t}$ and the shear strain $\gamma_{\ell t}$ of the element can be calculated by the following simple equation in terms of the principal stresses and strains (σ_2, σ_1, ε_2, and ε_1):

$$\tau_{\ell t} = \frac{1}{2}(-\sigma_1 + \sigma_2) \tag{5.5-7}$$

$$\gamma_{\ell t} = \frac{1}{2}(-\varepsilon_1 + \varepsilon_2) \tag{5.5-8}$$

The principal stresses and strains were calculated using the readings from jack load cells and LVDTs, respectively. The shear stress-strain curves of the panels in the two series are plotted in Fig. 5.5.1 and Fig. 5.5.2, respectively.

As described in Section 5.5.2, each of the curves for panels TA-1, 2, 4, and 5 exhibits three critical points, namely, cracking of concrete, yielding of transverse mild steel, and crushing of concrete. Before the cracking of the concrete, the shear behavior of the panels was elastic and the $\tau_{\ell t} - \gamma_{\ell t}$ curves were essentially linear. After cracking, the approximately linear increase of the shear stresses continued with smaller slopes until the yielding of the mild steel. After the mild steel yielded, the shear strains increased dramatically with a very small increase of shear stresses. The prestressed concrete panels reached their peak shear strengths when the crushing of the

concrete occurred. The shear stresses started to decline with the increase of the deformations beyond the peak points.

Test panel TA-3 exhibited a different shear behavior from the other panels. Because this panel had the highest percentages of prestressing tendons and mild steel, the steel in both longitudinal and transverse directions did not yield. There were only two critical points, the cracking and the crushing of the concrete, that divided the shear stress-strain curve into three stages.

From the two series of curves, it is obvious that the maximum shear capacity of the prestressed concrete panels is related to its reinforcement ratios. The experimental shear strengths of the test panels TA-1, 2, and 3 are 5.96 MPa, 6.40 MPa, and 7.47 MPa (0.86 ksi, 0.93 ksi, and 1.08 ksi), respectively. The shear strengths are 6.40 MPa, 5.67 MPa, and 4.77 MPa (0.93 ksi, 0.82 ksi, and 0.69 ksi) for test panels TA-2, 4, and 5, respectively. The shear strength increases with an increase of either prestressing tendon or mild steel ratios.

The shear ductility factor is defined as the ratio of the strain at 80% of peak stress in the descending branch to the strain at the yielding point. It is evident from Fig. 5.5.1 and Fig. 5.5.2 that a prestressed concrete element subjected to shear could exhibit good ductility if properly reinforced. The ductility factors of the panels TA-1, 2, and 3 in the first series are 12.7, 5.0, and less than 1.0 (no steel yielding in panel TA-3), respectively. It is obvious that the ductility increases dramatically with the decrease of the mild steel ratios in the transverse direction. In the second series, the ductility factors are 5.0, 6.9, and 8.6 for panels TA-2, 4, and 5, respectively. The strain at 87% of peak stress is used because of the limited test data for panel TA-4. Obviously, the ductility increases with the reduction of prestressing tendons in the longitudinal direction.

The descending branches of those shear stress-strain curves right after the crushing of the concrete exhibit an interesting phenomenon. In panels TA-1 and TA-2, after the crushing of concrete, the shear stresses dropped rapidly below 80% of peak stress in a short period. Even under strain-control mode, only one or two points within this period were caught. In panels TA-4 and 5, however, there was no sudden drop after the crushing of concrete. The shear stresses gradually decreased with the increase of the shear strains.

5.5.4 Shear Stress vs. Principal Tensile Strain Relationships ($\tau_{\ell t} - \varepsilon_1$ Curves)

Figures 5.5.3 and 5.5.4 show the experimental shear stress vs. principal tensile strain relationships. The principal tensile strains, ε_1, of the prestressed concrete panels are obtained by averaging the horizontal LVDT readings.

The shapes of the two figures are similar to Figs. 5.5.1 and 5.5.2 because the shear strain $\gamma_{\ell t}$ is governed predominantly by the principal tensile strain, especially before the crushing of the concrete. Each $\tau_{\ell t} - \varepsilon_1$ curve also has four stages jointed by three characteristic points. The first

stage is the elastic stage before concrete cracking. The second stage is the post-cracking elastic branch. The third stage is the plastic stage starting from the yielding of the mild steel to the peak point. The last stage is the descending branch.

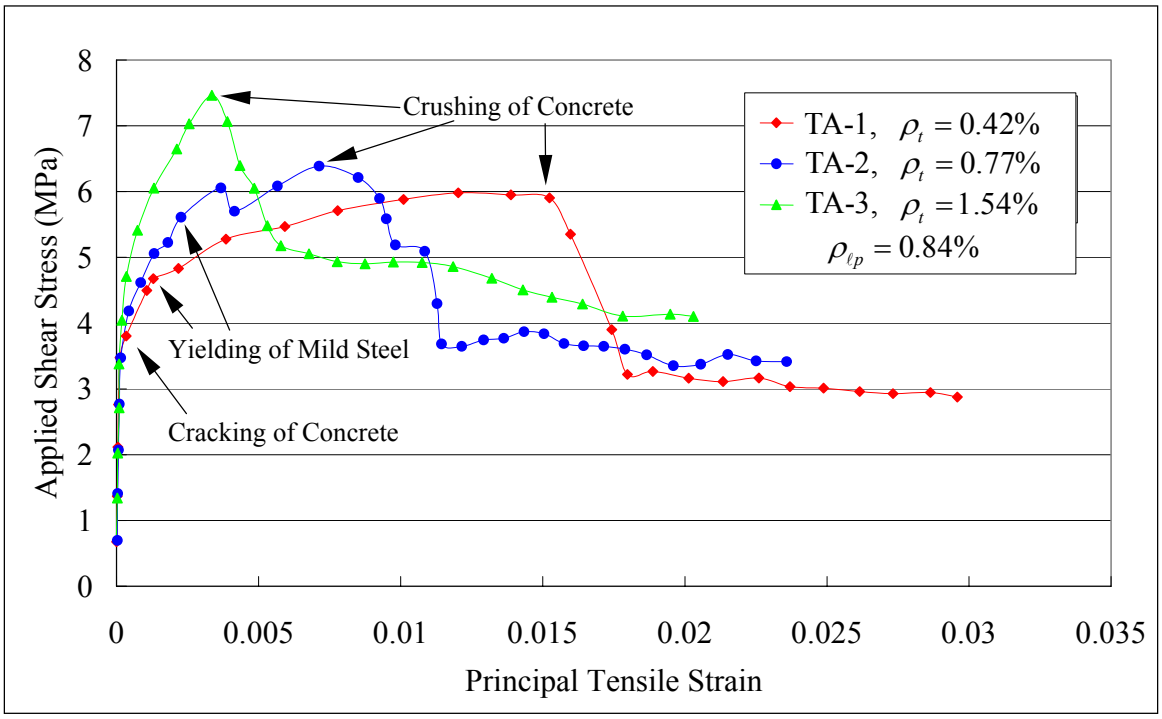

Fig. 5.5.3 Shear Stress vs. Principal Tensile Strain Curves of Panels TA-1, 2, and 3

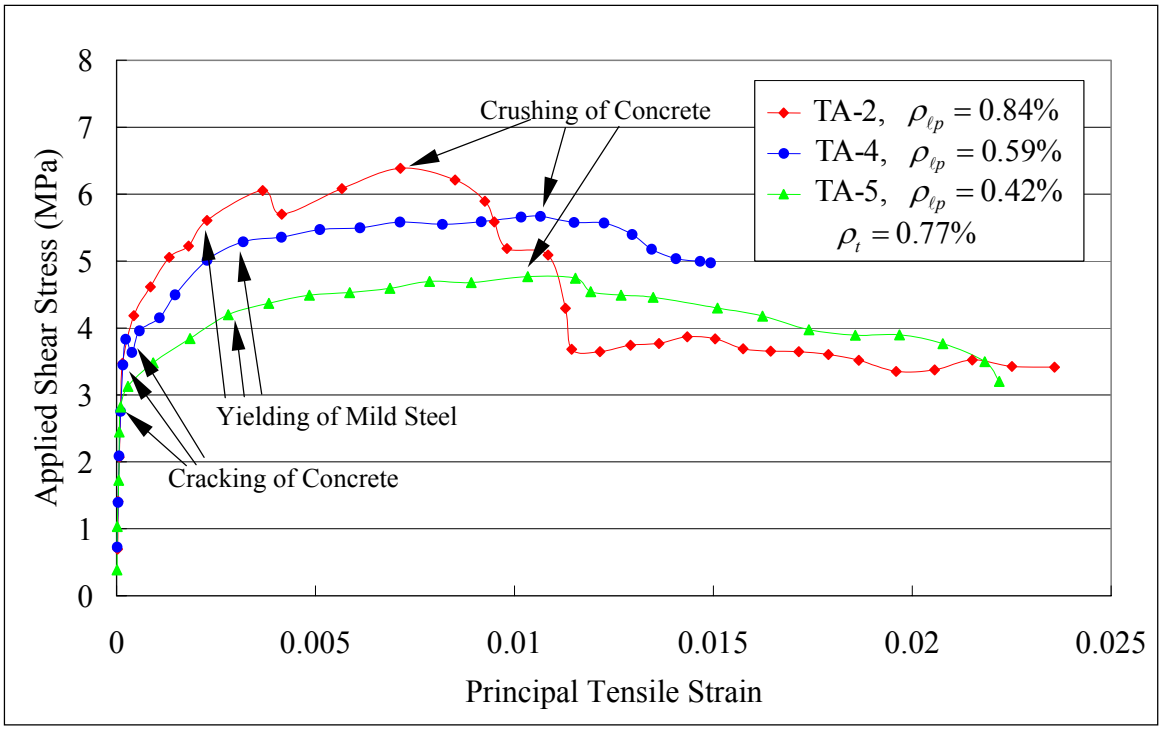

Fig. 5.5.4 Shear Stress vs. Principal Tensile Strain Curves of Panels TA-2, 4, and 5

5.5.5 Shear Stress vs. Principal Compressive Strain Relationships ($\tau_{\ell t} - \varepsilon_2$ Curves)

Figures 5.5.5 and 5.5.6 show the two series of experimental shear stress vs. principal compressive strain relationships. The principal compressive strains, ε_2, of the prestressed concrete panels are obtained by averaging the vertical LVDT readings.

Unlike the τ_{lt}–γ_{lt} curves, the cracking of the concrete had a lesser effect on the post-cracking slope of the τ_{lt}–ε_2 curves. With the increase of the applied shear stress after cracking, the compressive strain continued to increase linearly up to the yielding of the mild steel and became nonlinear until the peak point. After the crushing of concrete, the compressive strain rapidly increased with a decrease of applied shear stress.

It should be noted that the compressive strains of panels TA-1 and 5 had a slight reduction after the yielding of the mild steel. Two reasons to explain the phenomenon were advanced by Pang (1991). First, the direction of the principal compressive strain of the concrete (d – direction) deviated significantly from the original 2 – direction after the yielding of steel. This deviation of the principal compressive direction reduced the compressive strain in the 2 – direction. Second, the direction of cracks was not perpendicular to the direction of the principal tensile stresses of the elements. The inclined cracks crossed the line connecting the two measuring points of a LVDT in the 2 – direction. The development of the crack widths gave a tensile component in the 2 – direction, which counteracted the compressive strain caused by the external shear forces.

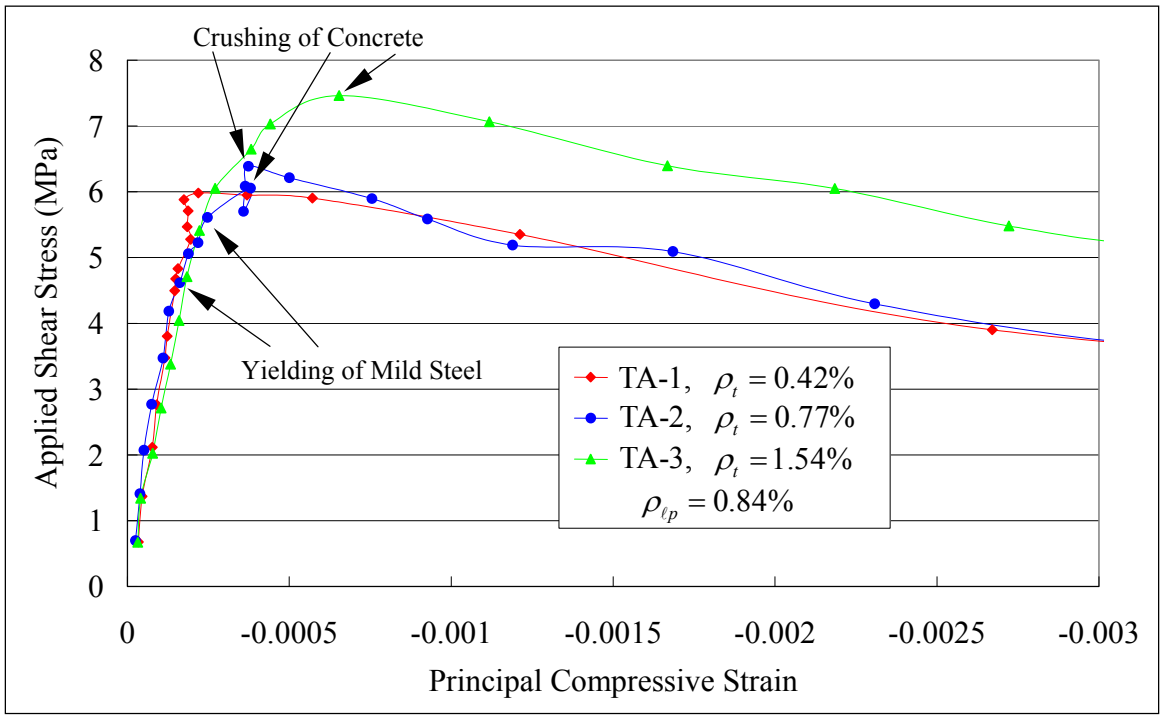

Fig. 5.5.5 Shear Stress vs. Principal Compressive Strain Curves of Panels TA-1, 2, and 3

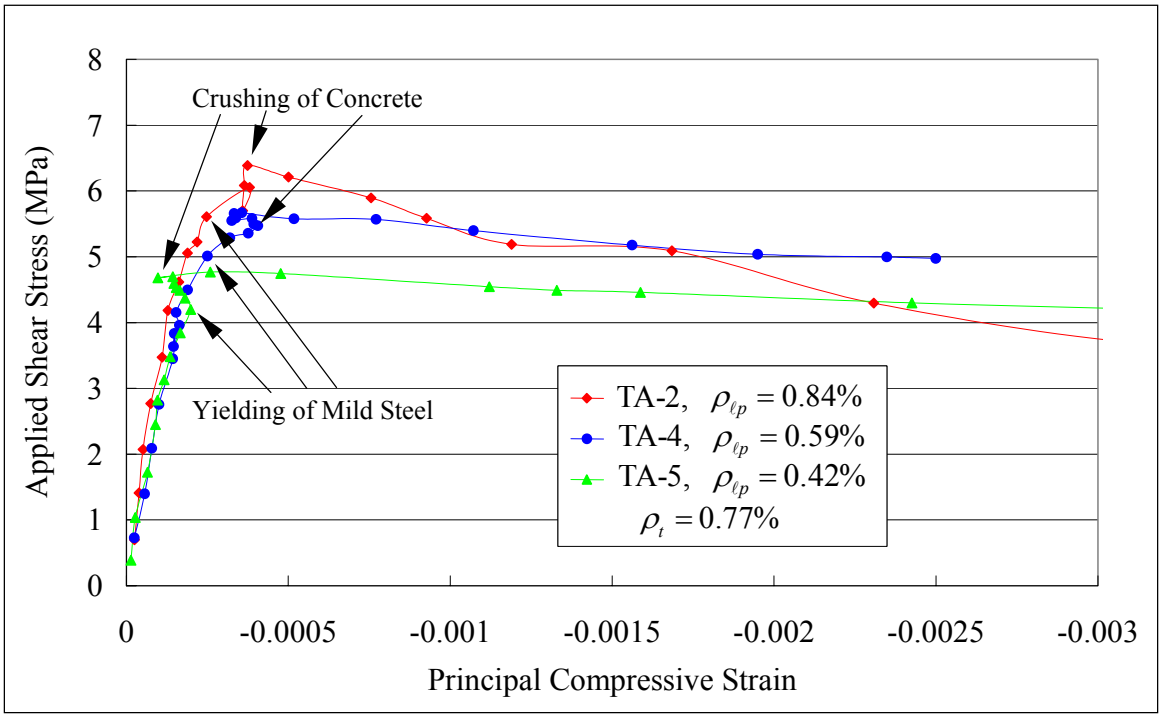

Fig. 5.5.6 Shear Stress vs. Principal Compressive Strain Curves of Panels TA-2, 4, and 5

5.6 Smeared (Average) Stress-Strain Relationships of Concrete in Compression

The softening coefficient is the most important property of the smeared (average) stress-strain relationships of concrete in compression.

5.6.1 Experimental Curves for Prestressed Concrete

In the Softened Membrane Model, the equilibrium equations for panels in Group TA are given as:

$$\sigma_\ell = \sigma_1^c \cos^2 \alpha_1 + \sigma_2^c \sin^2 \alpha_1 + \tau_{12}^c 2\sin\alpha_1 \cos\alpha_1 + \rho_{\ell p} f_{\ell p} \qquad (5.6\text{-}1)$$

$$\sigma_t = \sigma_1^c \sin^2 \alpha_1 + \sigma_2^c \cos^2 \alpha_1 - \tau_{12}^c 2\sin\alpha_1 \cos\alpha_1 + \rho_t f_t \qquad (5.6\text{-}2)$$

$$\tau_{\ell t} = (-\sigma_1^c + \sigma_2^c)\sin\alpha_1 \cos\alpha_1 + \tau_{12}^c (\cos^2 \alpha_1 - \sin^2 \alpha_1) \qquad (5.6\text{-}3)$$

Substituting α_1=45° into Eq. 5.6-3 and rearranging the equation, the compressive stress of the concrete is given as follows:

$$\sigma_1^c = \sigma_2^c - 2\tau_{\ell t} \qquad (5.6\text{-}4)$$

In Eq. 5.6-4, the applied shear stress $\tau_{\ell t}$ can be calculated from the applied principal stresses measured from the panel testing, as expressed by Eq. 5.5-7. The average tensile stress of the concrete σ_1^c is relatively small in magnitude and can be calculated from the tensile stress-strain relationships of the concrete expressed by Eq. 4.6-10c. This equation was established from the panels in Group TE described in Section 4.6.3.

In the SMM, the relationships between the uniaxial strains and the biaxial strains are given as follows (Zhu, 2000):

$$\bar{\varepsilon}_1 = \frac{1}{1-\nu_{12}\nu_{21}}\varepsilon_1 + \frac{\nu_{12}}{1-\nu_{12}\nu_{21}}\varepsilon_2 \tag{5.6-5}$$

$$\bar{\varepsilon}_2 = \frac{\nu_{21}}{1-\nu_{12}\nu_{21}}\varepsilon_1 + \frac{1}{1-\nu_{12}\nu_{21}}\varepsilon_2 \tag{5.6-6}$$

The Hsu/Zhu ratio ν_{21}, which is the tensile strain caused by the perpendicular compressive strain, is zero. Substituting $\nu_{21} = 0$ into Eq. 5.6-6, the uniaxial compressive strain of the concrete is obtained as follows:

$$\bar{\varepsilon}_2 = \varepsilon_2 \tag{5.6-7}$$

The biaxial compressive strain ε_2 in Eq. 5.6-7 can be calculated directly from the tests by averaging the vertical LVDT readings.

It should be noted that the longitudinal prestresses were induced into the concrete before the application of the load. This 45° prestress induced identical initial compressive strains in the $1-$ and the $2-$ directions, labeled as ε_i. The strain in the $1-$direction is considered when calculating σ_1^c in Eq. 5.6-4. The strain in the $2-$direction is added to $\bar{\varepsilon}_2$ to get the uniaxial compressive strain $\bar{\varepsilon}_c$ in the concrete, as follows:

$$\bar{\varepsilon}_c = \bar{\varepsilon}_2 + \varepsilon_i \tag{5.6-8}$$

Using Eqs. 5.6-4 and 5.6-8, the experimental smeared (average) stress-strain curves of the concrete in compression in the two series of panels are plotted in Fig. 5.6.1 and Fig. 5.6.2.

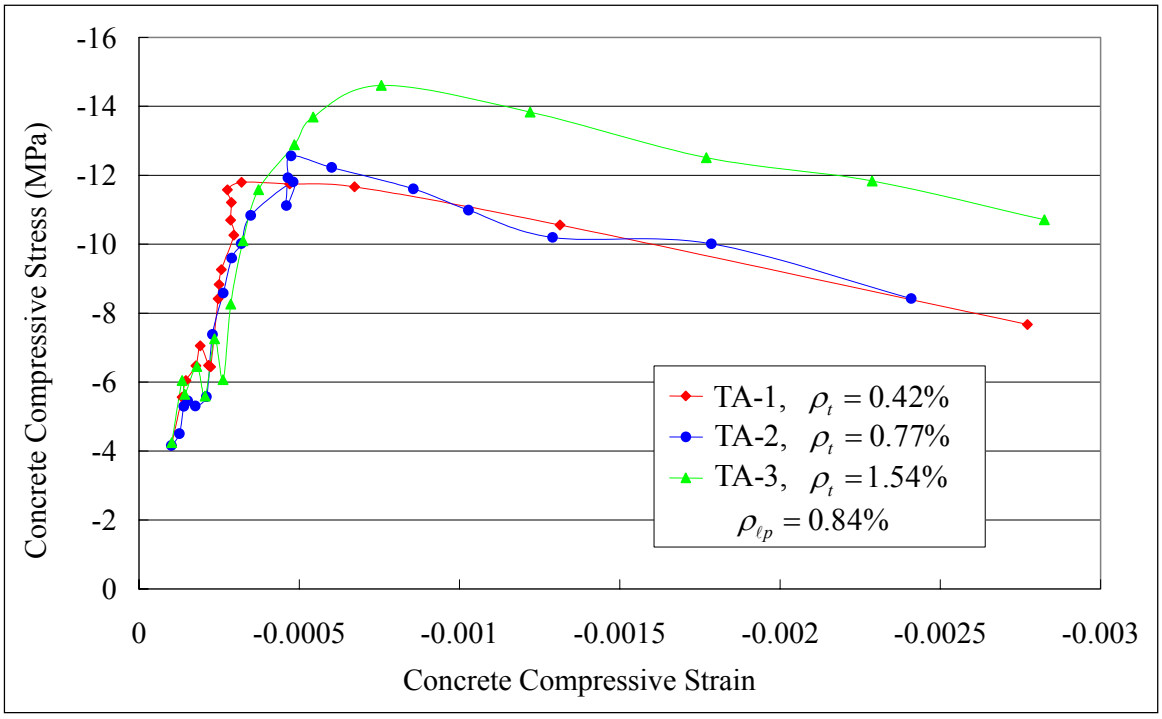

Fig. 5.6.1 Experimental Concrete Compressive Stress-Strain Curves of Panels TA-1, 2, and 3

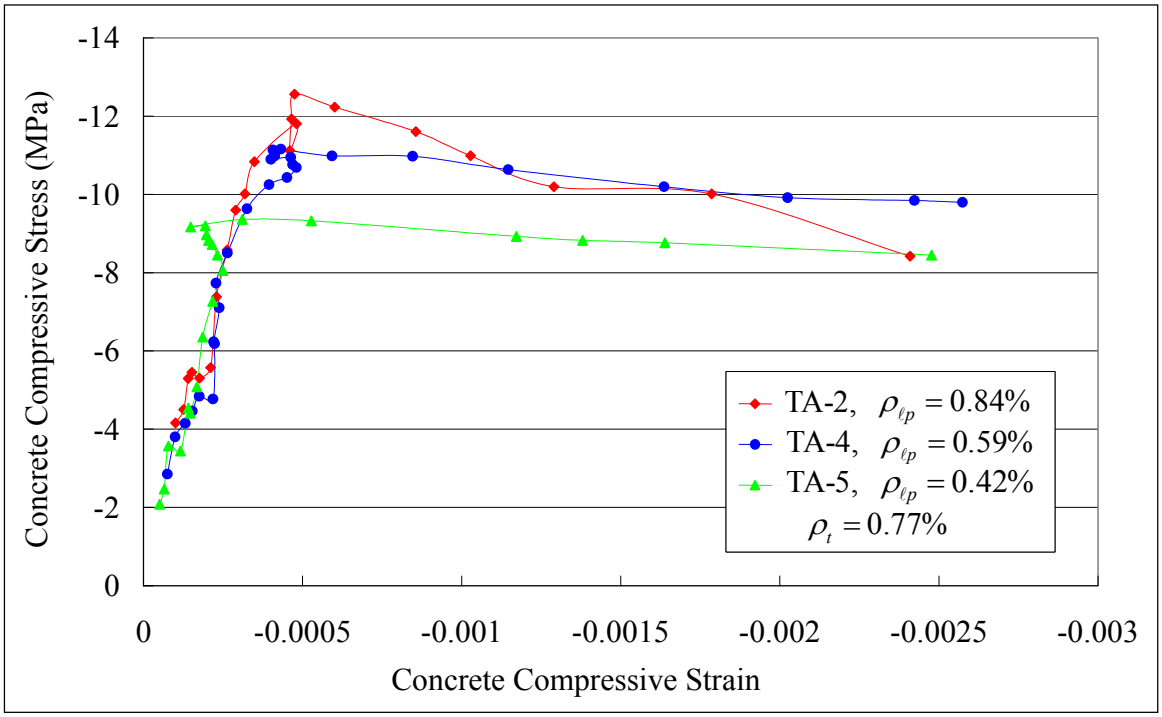

Fig. 5.6.2 Experimental Concrete Compressive Stress-Strain Curves of Panels TA-2, 4, and 5

The effect of loading paths on the concrete compressive softening was first observed by Belarbi and Hsu (1995). By comparing the test results from their two series, E and F, they found that the loading path had a significant effect on the softening behavior. Unlike sequential loading, in which only the stress was softened, both the stress and the strain were softened for the panels tested under proportional loading. The stress and strain softening coefficients were approximately the same. Later experiments at the University of Houston (Pang and Hsu, 1995; Zhang and Hsu, 1998) confirmed this observation. From this research, Fig. 5.6.1 and Fig. 5.6.2, similar conclusion could be drawn for prestressed concrete, i.e., both the stress and the strain of concrete were softened under proportional loading.

5.6.2 Mathematical Modeling of Smeared (Average) Stress-Strain Curve of Prestressed Concrete in Compression

In the Softened Membrane Model, the smeared (average) constitutive relationships of concrete compressive stress σ_2^c versus uniaxial compressive strain $\bar{\varepsilon}_2$, shown in Fig. 5.6.3, are given as follows:

$$\sigma_2^c = \zeta f_c' \left[2\left(\frac{\bar{\varepsilon}_2}{\zeta\varepsilon_0}\right) - \left(\frac{\bar{\varepsilon}_2}{\zeta\varepsilon_0}\right)^2 \right], \qquad \frac{\bar{\varepsilon}_2}{\zeta\varepsilon_0} \le 1 \text{ (stage C1)} \tag{5.6-9a}$$

or

$$\sigma_2^c = \zeta f_c' \left[1 - \left(\frac{\bar{\varepsilon}_2/\zeta\varepsilon_0 - 1}{4/\zeta - 1}\right)^2 \right], \qquad \frac{\bar{\varepsilon}_2}{\zeta\varepsilon_0} > 1 \text{ (stage C2)} \tag{5.6-9b}$$

As discussed in Section 4.8, the softening coefficient ζ in Eq. 5.6-9 is expressed as the product of the functions of concrete compressive strength f_c', uniaxial tensile strain $\bar{\varepsilon}_1$, and deviation angle β, i.e.

$$\zeta = f(f_c')f(\bar{\varepsilon}_1)f(\beta) \le 0.9 \tag{5.6-10}$$

where

$$f(f_c') = \frac{5.8}{\sqrt{f_c'}} \le 0.9 \quad (f_c' \text{ in MPa}) \tag{5.6-11}$$

$$f(\bar{\varepsilon}_1) = \frac{1}{\sqrt{1 + 400\bar{\varepsilon}_1}} \tag{5.6-12}$$

and

$$f(\beta) = 1 - \frac{|\beta|}{24^\circ} \tag{5.6-13}$$

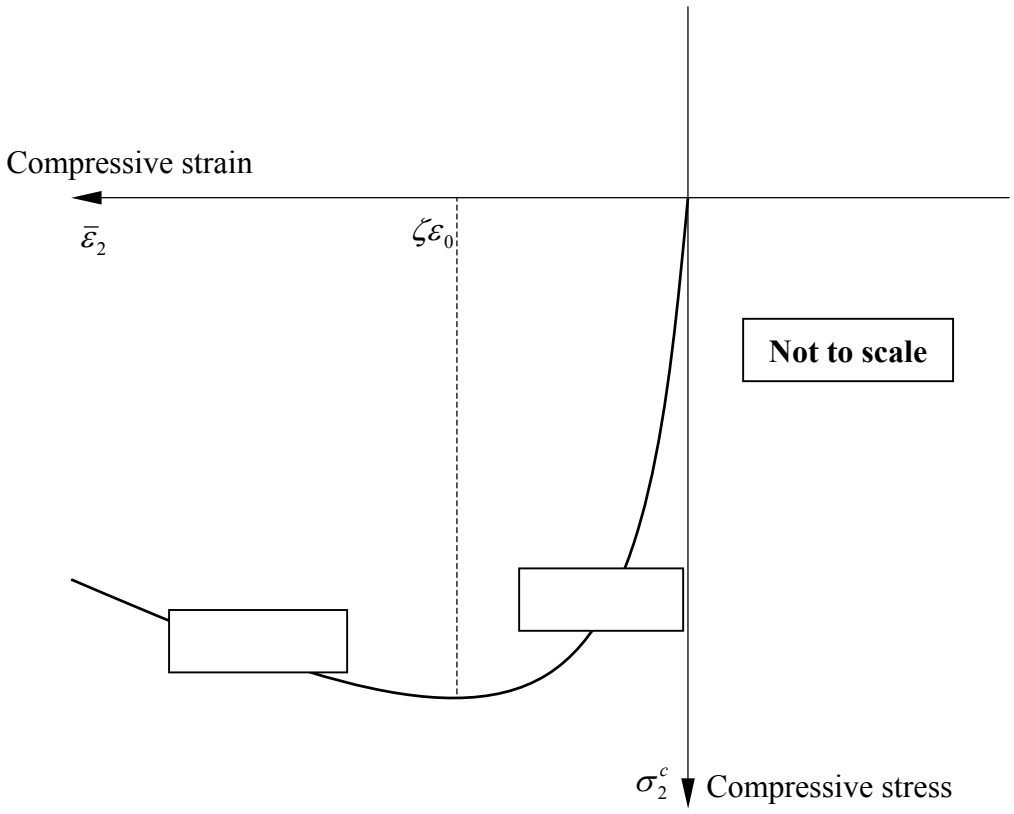

Fig. 5.6.3 Constitutive Laws of Concrete in Compression

To express the smeared (average) stress-strain curves of the concrete in compression in prestressed elements, the same parabolic equation, Eq. 5.6-9, is used. The three functions used to calculate the softening coefficient are expressed by Eqs. 5.6-10 to 5.6-13.

For consistency, $f(f_c')$ and $f(\bar{\varepsilon}_1)$ remain the same as those for reinforced concrete. By dividing the experimental values of ζ by $f(f_c')$ and $f(\bar{\varepsilon}_1)$, the experimental $f(\beta)$ for prestressed concrete elements are calculated and listed in Table 5.6.1. The experimental β for the prestressed concrete elements listed in Table 5.6.1 are obtained using Eq. 2.3-1.

Table 5.6.1 Calculation of β and $f(\beta)$ for Prestressed Concrete Panels

Specimen	ζ (exp.)	f'_c (MPa)	$f(f'_c)$	$\bar{\varepsilon}_1$	$f(\bar{\varepsilon}_1)$	$f(\beta)$	β (Degree)
[1]	[2]	[3]	[4]	[5]	[6]	[7]=[2]/([4][6])	[8]
TA-1	0.284	41.47	0.900	0.012277	0.411	0.767	17.6
TA-2	0.308	41.33	0.900	0.005242	0.568	0.602	13.8
TA-3	0.361	42.21	0.893	0.002743	0.691	0.585	7.6
TA-4	0.265	42.54	0.889	0.008603	0.475	0.628	12.4
TA-5	0.229	41.08	0.900	0.007187	0.508	0.501	9.7
TE-3	0.492	32.52	0.900	0.019400	0.413	1.321	0
TE-4	0.482	38.69	0.900	0.014600	0.464	1.155	0
TE-5	0.390	34.76	0.900	0.029300	0.347	1.249	0
TE-6	0.582	36.82	0.900	0.020300	0.406	1.593	0
TE-7	0.357	42.39	0.891	0.020500	0.404	0.992	0

Note: Eq. 5.6-12) was used to calculate $f(\bar{\varepsilon}_1)$ for the panels in Group TA.

Eq. 4.8-7 was used to calculate $f(\bar{\varepsilon}_1)$ for the panels in Group TE.

According to the data in Table 5.6.1, the *f(β)* versus β relationship for the prestressed concrete panels is plotted in Fig. 5.6.4 along with the data for the reinforced concrete panels and the straight line by Eq. 5.6-13. Two points should be noted. First, the average *f(β)* at β=0 (Group TE) is 1.15, which is the prestress factor W_p obtained from Section 4.8. Second, the *f(β)* versus β relationship for prestressed concrete panels in Group TA shows a different trend than that for reinforced concrete panels. In other words, Eq. 5.6-13 for reinforced concrete must be modified before it can be applied to prestressed concrete elements.

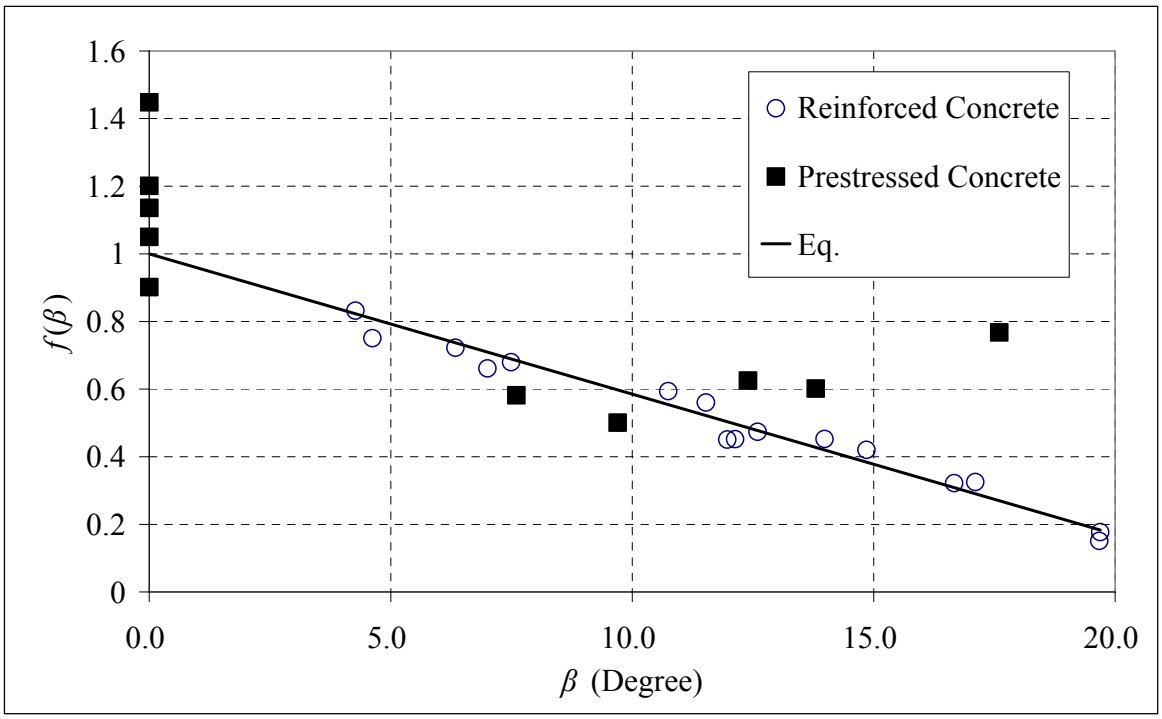

Fig. 5.6.4 *f(β)* versus *β* Relationships for Reinforced and Prestressed Concrete Panels

Introducing a new "prestressed factor W_p" into the softening coefficient to take care of the effect of prestress, Eq. 5.6-10 becomes:

$$\zeta = f(f_c')f(\bar{\varepsilon}_1)f(\beta)W_p \le 0.9 \qquad (5.6\text{-}14)$$

where

$$f(f_c') = \frac{5.8}{\sqrt{f_c'}} \le 0.9 \quad (f_c' \text{ in MPa}) \qquad (5.6\text{-}15)$$

$$f(\bar{\varepsilon}_1) = \frac{1}{\sqrt{1+400\bar{\varepsilon}_1}} \qquad (5.6\text{-}16)$$

and

$$f(\beta) = 1 - \frac{|\beta|}{24^\circ} \qquad (5.6\text{-}17)$$

Dividing the experimental softening coefficient by $f(f_c')$, $f(\bar{\varepsilon}_1)$, and $f(\beta)$ gives the values of W_p, which are listed in Table 5.6.2.

Table 5.6.2 Calculation of W_p for Prestressed Concrete Panels

Specimen	ζ (exp.)	$f(f_c')$ (Eq. 5.6-15)	$f(\bar{\varepsilon}_1)$ (Eq. 5.6-16)	$f(\beta)$ (Eq. 5.6-17)	W_p (exp.)	β (Degree)
[1]	[2]	[3]	[4]	[5]	$[6]=\frac{[2]}{[3][4][5]}$	[7]
TA-1	0.284	0.900	0.411	0.267	2.877	17.6
TA-2	0.308	0.900	0.568	0.425	1.416	13.8
TA-3	0.361	0.900	0.691	0.683	0.851	7.6
TA-4	0.265	0.894	0.475	0.483	1.293	12.4
TA-5	0.229	0.900	0.508	0.596	0.841	9.7
TE-3	0.492	0.900	0.413	1	1.321	0
TE-4	0.482	0.900	0.464	1	1.155	0
TE-5	0.390	0.900	0.347	1	1.249	0
TE-6	0.582	0.900	0.406	1	1.593	0
TE-7	0.357	0.891	0.404	1	0.992	0

Figure 5.6.5 relates the W_p factor to the β angle according to Column [6] and [7] in Table 5.6.2. A regression analysis is performed using the Microsoft Excel program. By setting polynomial as the regression type, choosing an order of 2, and setting the intercept at 1.15, the prestressed factor W_p is given as:

$$W_p = 1.15 + \frac{|\beta|(0.09|\beta| - 1)}{6} \tag{5.6-18}$$

The coefficient of determination is calculated to be 0.8896, which means that Eq. 5.6-18 can represent very well the relationship between W_p and β.

Eqs. 5.6-14 to 5.6-18 unify the softening coefficients for reinforced concrete and prestressed concrete. The effect of the deviation angle β on the softening coefficient in prestressed concrete is obviously more complicated than that in reinforced concrete. The complexity stemmed from two sources. First, prestress on the concrete changes the deviation angle even before the application of loading. Second, the properties of the prestressing tendons in the longitudinal

direction are quite different from those of the mild steel in the transverse direction. Apparently, the difference in stiffnesses in the longitudinal and the transverse directions is very large.

Although we cannot explain the shape of the W_p function, the softening coefficient expressed by Eqs. 5.6-14 to 5.6-18 is very general and amazingly accurate. These equations are applicable to reinforced and prestressed concrete, with any ratio of longitudinal steel to transverse steel, any orientation of steel bars with respect to the principal stresses, as well as high-strength concrete up to 100 MPa .

The testing of Group TE and TA panels allowed us to establish the constitutive laws of concrete in compression and in tension, as well as the prestressing tendons. These constitutive laws are included in the Softened Membrane Model to predict the shear behavior of prestressed concrete elements. Fig. 5.6.6 compares the predictions from the Softened Membrane Model for Prestressed Concrete (SMM-PC) with the experimental data of concrete compressive stress-strain relationships. The prediction agrees very well with the experimental data for all five panels of Group TA.

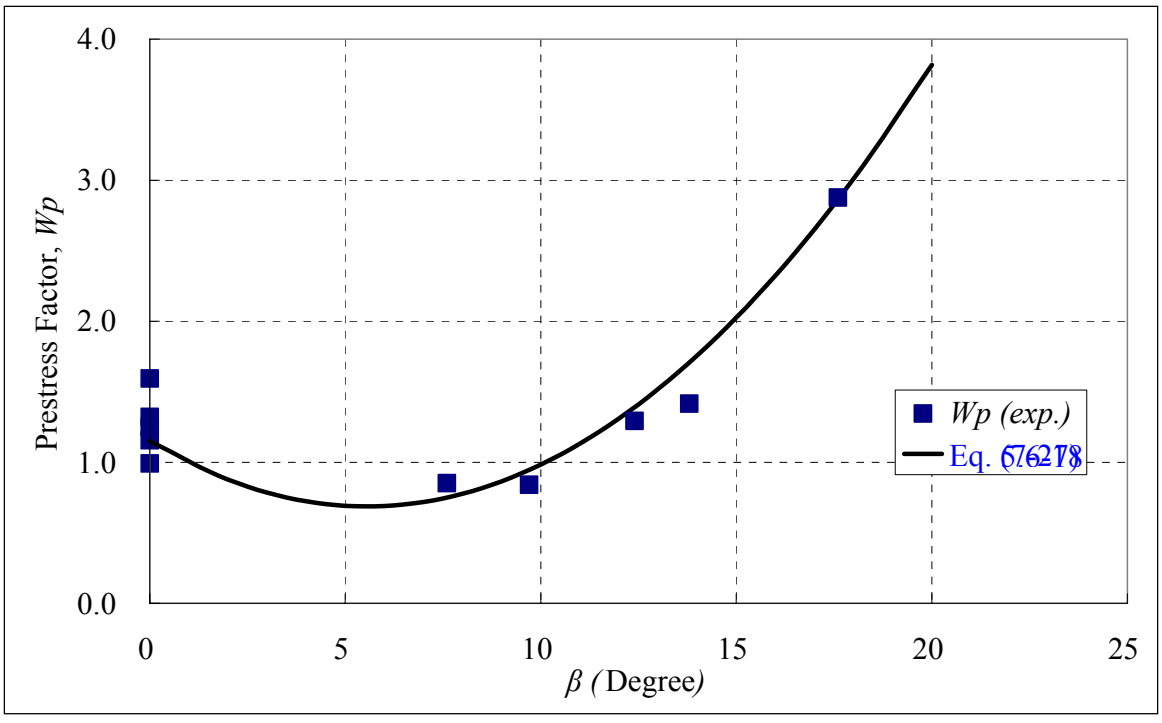

Fig. 5.6.5 W_p versus β Relationships for Prestressed Concrete Panels

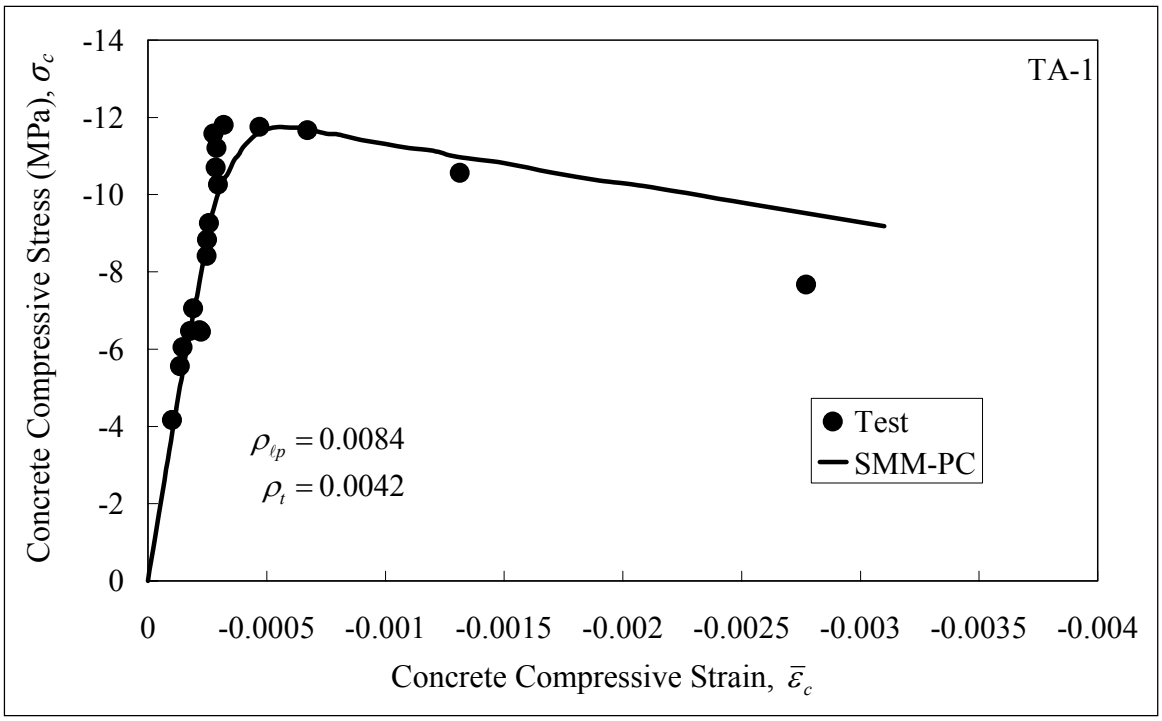

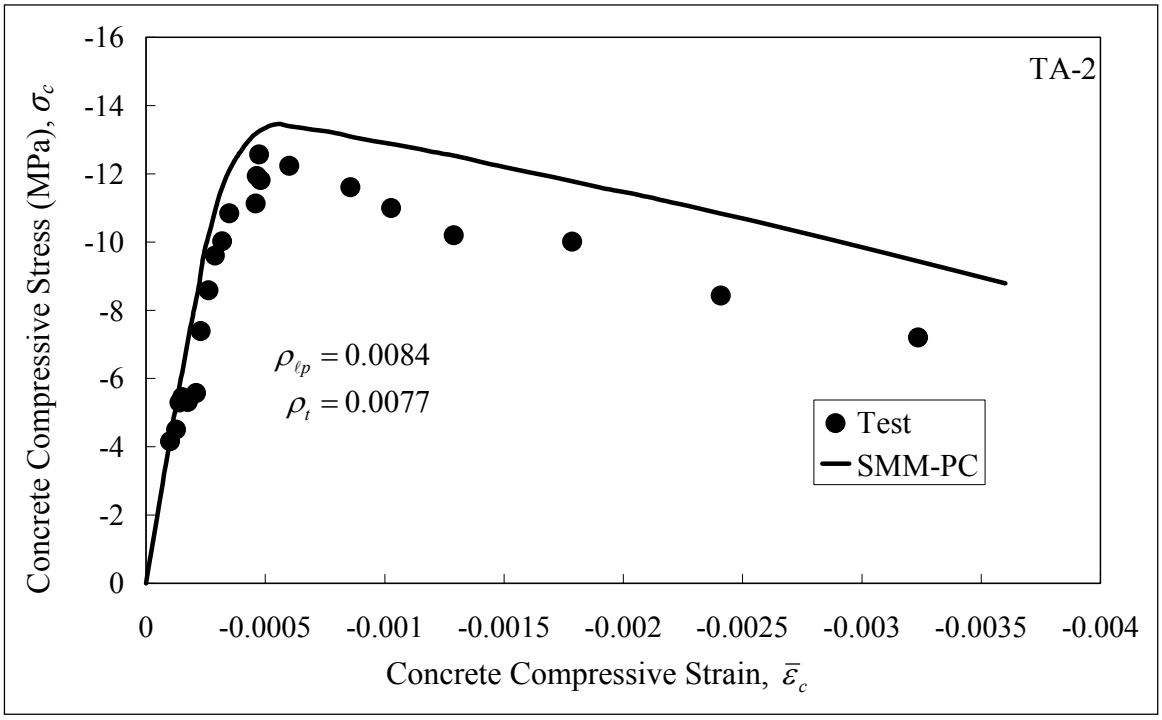

Fig. 5.6.6 Comparison of SMM-PC Predicted Concrete Compressive Stress-Strain Curves with Experimental Data of Panels TA-1 to TA-5

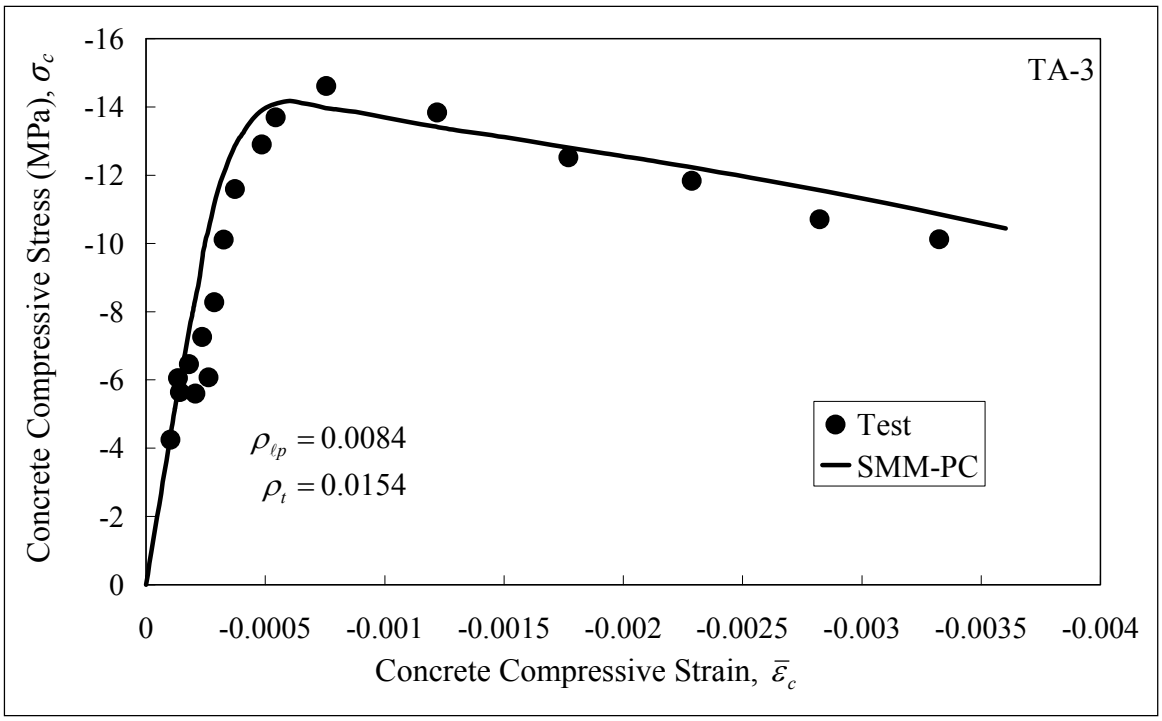

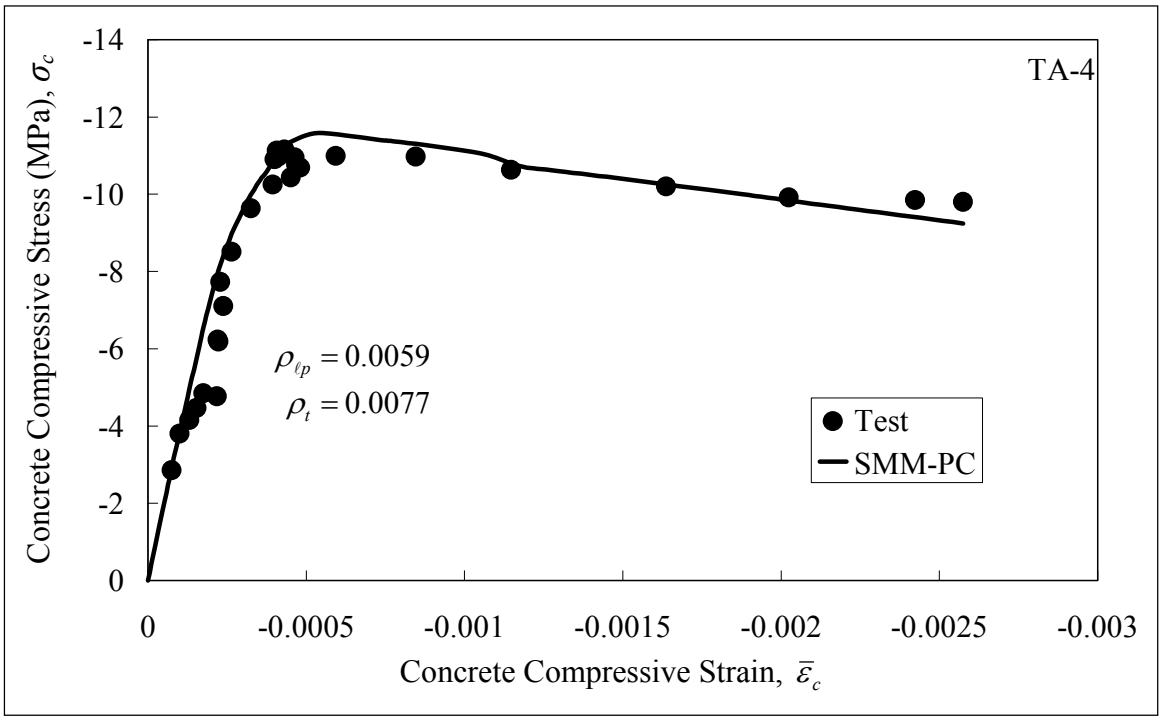

Fig. 5.6.6 Comparison of SMM-PC Predicted Concrete Compressive Stress-Strain Curves with Experimental Data of Panels TA-1 to TA-5 (continued)

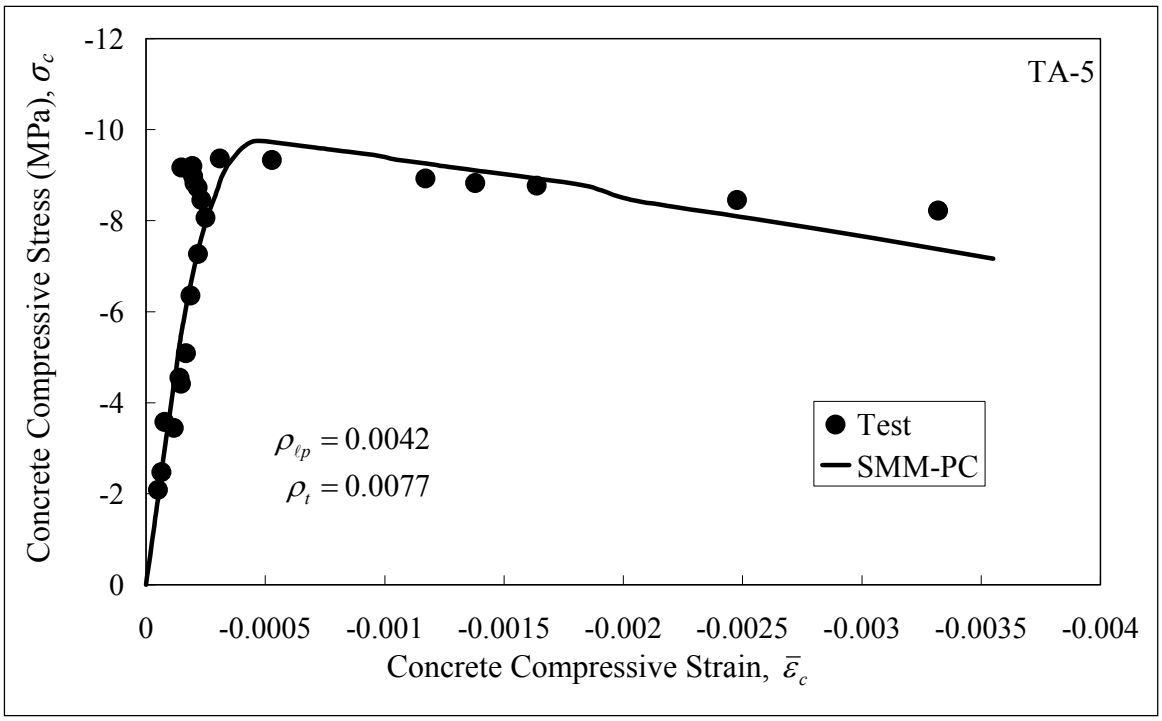

Fig. 5.6.6 Comparison of SMM-PC Predicted Concrete Compressive Stress-Strain Curves with Experimental Data of Panels TA-1 to TA-5 (continued)

CHAPTER 6

ANALYTICAL MODELS OF PRESTRESSED CONCRETE PANELS

6.1 Introduction

Reinforced concrete structures can be visualized as assemblies of membrane elements, and their behavior can be predicted using the finite element method once the constitutive relationships of the elements are established. At the University of Houston, Zhong (2005) developed a nonlinear finite element program, named Simulation of Reinforced Concrete Structures (SRCS), for analysis of reinforced concrete structures. In SRCS, based on the Cyclic Softened Membrane Model (CSMM) (Mansour, 2001; Mansour and Hsu, 2005a and 2005b), a two-dimensional reinforced concrete plane stress material module and three uniaxial material modules of steel and concrete were developed and implemented into the object-oriented finite element framework OpenSees (Fenves 2001). SRCS is proven to successfully predict the behavior of reinforced concrete plane stress structures subjected to static, reversed cyclic, and dynamic loading.

In the present research project, the Softened Membrane Model for Prestressed Concrete (SMM-PC) has been developed to predict the response of prestressed concrete membrane elements under shear loading. Therefore, a new finite element program for prestressed concrete structures can be developed based on SRCS. The key to this program are the following two points: (1) new constitutive relationships of prestressing tendons embedded in concrete; and (2) revised constitutive relationships of concrete considering the effect of prestress. These new constitutive relationships of materials need to be implemented into SRCS based on the OpenSees framework.

This chapter summarizes the equations of equilibrium, compatibility, and constitutive relationships used in the Softened Membrane Model for Prestressed Concrete (SMM-PC). Both the constitutive laws and the analytical model presented in Chapters 4 through 6 will be applied to prestressed concrete beams. Basically, tests on prestressed concrete beams are performed, and an analytical model for the shear behavior of prestressed concrete beams is developed.

The three equilibrium equations and three compatibility equations are summarized in Section 6.2.1; the relationships between the biaxial strains and the uniaxial strains are given in Section 6.2.2; and the constitutive laws of the materials are presented in Section 6.2.3 and Section 6.2.4. The algorithm to solve all the equations is shown in Section 6.2.5. The analytical results of panels in Group TA are presented in Section 6.3 and compared with the test results.

6.2 Fundamentals of Softened Membrane Model for Prestressed Concrete

Fig. 6.2.1(a) shows a prestressed concrete element subjected to in-plane stresses. As with the SMM, two reference Cartesian coordinates are used in the SMM-PC, as shown in Fig. 6.2.1(e). The first reference Cartesian $\ell - t$ coordinate system represents the directions of the longitudinal and transverse reinforcements. The second reference Cartesian $1 - 2$ coordinate system

represents the directions of the applied principal tensile ($1-$axis) and compressive ($2-$axis) stresses.

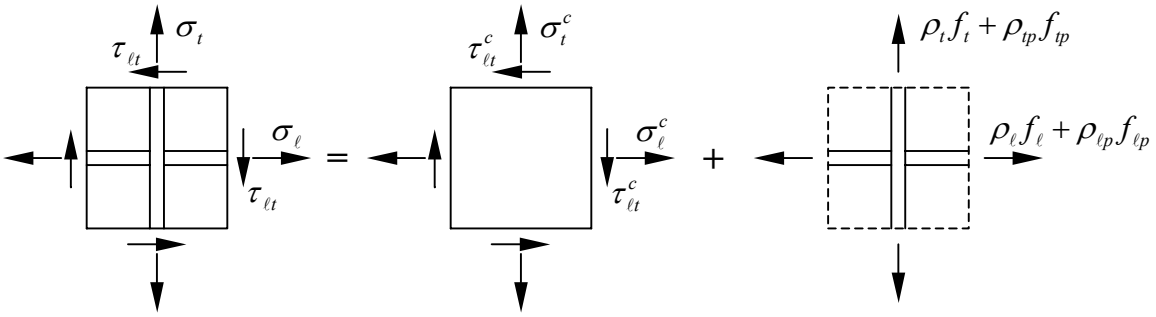

(a) Prestressed Concrete (b) Concrete (c) Reinforcement

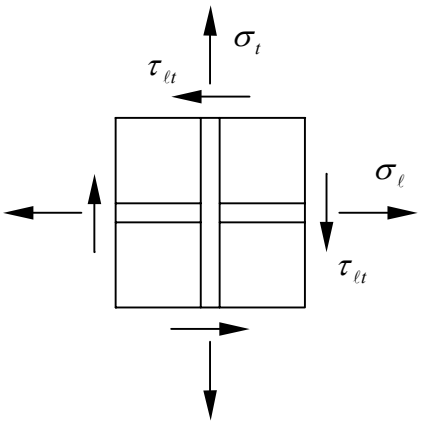

(d) Prestressed Concrete Element

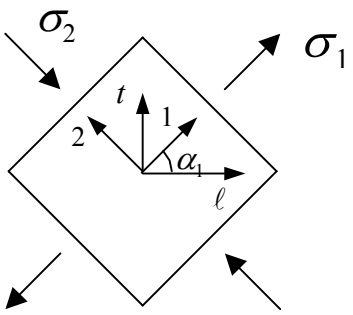

(e) Principal Coordinate $1-2$ for Applied Stresses

Fig. 6.2.1 Coordinate System in a Prestressed Concrete Membrane Element

6.2.1 Equilibrium and Compatibility Equations

The three equilibrium equations, which relate the applied stresses (σ_l, σ_t, and τ_{lt}) to the internal stresses of concrete (σ_1^c, σ_2^c, and τ_{12}^c), mild steel (f_l and f_t), and prestressing steel (f_{lp} and f_{tp}) in a membrane element, are expressed as:

$$\sigma_\ell = \sigma_1^c \cos^2 \alpha_1 + \sigma_2^c \sin^2 \alpha_1 + \tau_{12}^c 2 \sin \alpha_1 \cos \alpha_1 + \rho_\ell f_\ell + \rho_{\ell p} f_{\ell p} \qquad (6.2\text{-}1)$$

$$\sigma_t = \sigma_1^c \sin^2 \alpha_1 + \sigma_2^c \cos^2 \alpha_1 - \tau_{12}^c 2 \sin \alpha_1 \cos \alpha_1 + \rho_t f_t + \rho_{tp} f_{tp} \qquad (6.2\text{-}2)$$

$$\tau_{\ell t} = (-\sigma_1^c + \sigma_2^c) \sin \alpha_1 \cos \alpha_1 + \tau_{12}^c (\cos^2 \alpha_1 - \sin^2 \alpha_1) \qquad (6.2\text{-}3)$$

The three compatibility equations, which represent the relationship between the strains (ε_ℓ, ε_t, and $\gamma_{\ell t}$) in the $\ell - t$ coordinate of the reinforcement and the strains ($\varepsilon_1, \varepsilon_2$, and γ_{12}) in the $1-2$ coordinate of the principal applied stress, are expressed as follows (Pang and Hsu, 1996):

$$\varepsilon_\ell = \varepsilon_1 \cos^2 \alpha_1 + \varepsilon_2 \sin^2 \alpha_1 + \frac{\gamma_{12}}{2} 2 \sin \alpha_1 \cos \alpha_1 \tag{6.2-4}$$

$$\varepsilon_t = \varepsilon_1 \sin^2 \alpha_1 + \varepsilon_2 \cos^2 \alpha_1 - \frac{\gamma_{12}}{2} 2 \sin \alpha_1 \cos \alpha_1 \tag{6.2-5}$$

$$\frac{\gamma_{\ell t}}{2} = (-\varepsilon_1 + \varepsilon_2) \sin \alpha_1 \cos \alpha_1 + \frac{\gamma_{12}}{2} (\cos^2 \alpha_1 - \sin^2 \alpha_1) \tag{6.2-6}$$

6.2.2 Biaxial Strains vs. Uniaxial Strains

To solve the equilibrium and compatibility equations, the stress-strain relationships of concrete and reinforcements have to be provided. As mentioned in Section 2.3.3, the set of strains in the compatibility equations, ε_1, ε_2, ε_l, and ε_t, are biaxial strains, which are functions of the Hsu/Zhu ratios. The constitutive laws between the stresses and the biaxial strains cannot be determined directly from experiments. Therefore, a "bridge" is required to relate the biaxial strains and the uniaxial strains. The relationships between the uniaxial strains ($\bar{\varepsilon}_1$, $\bar{\varepsilon}_2$, $\bar{\varepsilon}_\ell$, and $\bar{\varepsilon}_t$) and the biaxial strains (ε_1, ε_2, ε_l, and ε_t) are given as follows (Zhu, 2000):

$$\bar{\varepsilon}_1 = \frac{1}{1 - \nu_{12}\nu_{21}} \varepsilon_1 + \frac{\nu_{12}}{1 - \nu_{12}\nu_{21}} \varepsilon_2 \tag{6.2-7}$$

$$\bar{\varepsilon}_2 = \frac{\nu_{21}}{1 - \nu_{12}\nu_{21}} \varepsilon_1 + \frac{1}{1 - \nu_{12}\nu_{21}} \varepsilon_2 \tag{6.2-8}$$

$$\bar{\varepsilon}_l = \bar{\varepsilon}_1 \cos^2 \alpha_1 + \bar{\varepsilon}_2 \sin^2 \alpha_1 + \frac{\gamma_{12}}{2} 2 \sin \alpha_1 \cos \alpha_1 \tag{6.2-9}$$

$$\bar{\varepsilon}_t = \bar{\varepsilon}_1 \sin^2 \alpha_1 + \bar{\varepsilon}_2 \cos^2 \alpha_1 - \frac{\gamma_{12}}{2} 2 \sin \alpha_1 \cos \alpha_1 \tag{6.2-10}$$

The Hsu/Zhu ratios are given by:

$$\nu_{12} = 0.2 + 850 \varepsilon_{sf}, \qquad \varepsilon_{sf} \le \varepsilon_y \tag{6.2-11a}$$

$$\nu_{12} = 1.9, \qquad \varepsilon_{sf} > \varepsilon_y \tag{6.2-11b}$$

$$\nu_{21} = 0 \tag{6.2-12}$$

where

ε_{sf} = smeared (average) tensile strain of steel bars in the $\ell-$ and the $t-$directions, whichever yields first, taking into account the Hsu/Zhu ratios.

6.2.3 Constitutive Relationships of Concrete in Prestressed Elements

The constitutive relationships of cracked concrete in tension, compression, and shear in prestressed elements are summarized in this section. The tensile stress is applied in the $1-$direction and the compressive stress in the $2-$direction. Detailed explanations of these constitutive relationships can be found in Chapters 4 and 5.

Concrete in Tension

The constitutive relationships for the tensile stress versus tensile strain of concrete are given in Chapter 4, Eq. 4.6-10. Substituting $\bar{\varepsilon}_c$ by $(\bar{\varepsilon}_1 + \bar{\varepsilon}_{ci})$ (based on Eq. 4.6-7) and σ_c by σ_1^c, the relationships of the tensile stress σ_1^c versus the uniaxial tensile strain $\bar{\varepsilon}_1$ of prestressed concrete are given as follows:

Stage UC: $\sigma_1^c = E_c'\bar{\varepsilon}_1 + \sigma_{ci}$, $\bar{\varepsilon}_1 \le (\bar{\varepsilon}_{cx} - \bar{\varepsilon}_{ci})$ (6.2-13a)

Stage T1: $\sigma_1^c = E_c''(\bar{\varepsilon}_1 + \bar{\varepsilon}_{ci} - \bar{\varepsilon}_{cx})$, $(\bar{\varepsilon}_{cx} - \bar{\varepsilon}_{ci}) < \bar{\varepsilon}_1 \le (\varepsilon_{cr} - \bar{\varepsilon}_{ci})$ (6.2-13b)

Stage T2: $\sigma_1^c = f_{cr}\left(\dfrac{\varepsilon_{cr}}{\bar{\varepsilon}_1 + \bar{\varepsilon}_{ci}}\right)^{0.5}$, $\bar{\varepsilon}_1 > (\varepsilon_{cr} - \bar{\varepsilon}_{ci})$ (6.2-13c)

where

E_c' = decompression modulus of concrete taken as $\dfrac{2f_c'}{\varepsilon_0}$,

$\bar{\varepsilon}_{ci}$ = initial strain in concrete due to prestress,

σ_{ci} = initial stress in concrete,

$\bar{\varepsilon}_{cx}$ = extra strain in concrete after decompression calculated by $\bar{\varepsilon}_{ci} - \dfrac{\sigma_{ci}}{E_c'}$,

E_c'' = modulus of concrete taken as $\dfrac{f_{cr}}{\varepsilon_{cr} - \bar{\varepsilon}_{cx}}$,

ε_{cr} = concrete cracking strain taken as 0.00008, and

f_{cr} = concrete cracking stress taken as $0.31\sqrt{f_c'}$ (f_c' and $\sqrt{f_c'}$ are in MPa).

Concrete in Compression

The smeared (average) constitutive relationships of concrete compressive stress σ_2^c and the uniaxial compressive strain $\bar{\varepsilon}_2$ are given as follows:

$$\sigma_2^c = \zeta f_c' \left[2\left(\frac{\bar{\varepsilon}_2}{\zeta\varepsilon_0}\right) - \left(\frac{\bar{\varepsilon}_2}{\zeta\varepsilon_0}\right)^2 \right], \qquad \frac{\bar{\varepsilon}_2}{\zeta\varepsilon_0} \le 1 \tag{6.2-14a}$$

or

$$\sigma_2^c = \zeta f_c' \left[1 - \left(\frac{\bar{\varepsilon}_2/\zeta\varepsilon_0 - 1}{4/\zeta - 1}\right)^2 \right], \qquad \frac{\bar{\varepsilon}_2}{\zeta\varepsilon_0} > 1 \tag{6.2-14b}$$

where ζ is the softening coefficient.

The softening coefficient in Eq. 6.2-14 can be determined as follows:

$$\zeta = f(f_c')f(\bar{\varepsilon}_1)f(\beta)W_p \le 0.9 \tag{6.2-15}$$

where

$$f(f_c') = \frac{5.8}{\sqrt{f_c'}} \le 0.9 \quad (f_c' \text{ in MPa}) \tag{6.2-16}$$

$$f(\bar{\varepsilon}_1) = \frac{1}{\sqrt{1 + 400\bar{\varepsilon}_1}} \tag{6.2-17}$$

$$f(\beta) = 1 - \frac{|\beta|}{24^\circ} \tag{6.2-18}$$

$$W_p = 1.15 + \frac{|\beta|(0.09|\beta| - 1)}{6} \tag{6.2-19}$$

and

$$\beta = \frac{1}{2}\tan^{-1}\left[\frac{\gamma_{12}}{(\varepsilon_1 - \varepsilon_2)}\right] \tag{6.2-20}$$

Concrete in Shear

The equation relating the shear stress of concrete τ_{12}^c and the shear strain γ_{12} in the $1-2$ coordinate is given by:

$$\tau_{12}^c = \frac{\sigma_1^c - \sigma_2^c}{2(\varepsilon_1 - \varepsilon_2)}\gamma_{12} \tag{6.2-21}$$

6.2.4 Constitutive Relationships of Reinforcements

Two types of reinforcements are embedded in concrete, prestressing tendons and mild steel bars.

Prestressing Tendons Embedded in Concrete

The smeared (average) stress-strain relationships of prestressing tendons embedded in concrete are given as follows:

$$f_{ps} = E_{ps}\bar{\varepsilon}_s, \qquad \bar{\varepsilon}_s < \frac{0.7 f_{pu}}{E_{ps}} \tag{6.2-22a}$$

or

$$f_{ps} = \frac{E''_{ps}\bar{\varepsilon}_s}{\left[1+\left(\frac{E''_{ps}\bar{\varepsilon}_s}{f'_{pu}}\right)^5\right]^{\frac{1}{5}}}, \qquad \bar{\varepsilon}_s \geq \frac{0.7 f_{pu}}{E_{ps}} \tag{6.2-22b}$$

where

E_{ps} = elastic modulus of prestressing tendons taken as 200 GPa (29000 ksi),

f_{pu} = ultimate strength of prestressing tendons taken as 1862 MPa (270 ksi),

E''_{ps} = modulus of prestressing tendons, used in plastic region (Eq. 6.2-22b), taken as 209 GPa (30345 ksi), and

f'_{pu} = revised strength of prestressing tendons taken as 1793 MPa (260 ksi).

In the above equations, *lp* replaces *ps* in the subscript of symbols for the longitudinal tendons, and *tp* replaces *ps* for the transverse tendons.

Mild Steel Embedded in Concrete

The smeared (average) tensile stress-strain relationships of mild steel embedded in concrete in the $\ell - t$ coordinate are the same in SMM. They can be expressed as follows:

Stage 1: $f_s = E_s\bar{\varepsilon}_s, \qquad \bar{\varepsilon}_s \leq \bar{\varepsilon}_n$ (6.2-23a)

Stage 2: $f_s = f_y\left[(0.91-2B)+(0.02+0.25B)\frac{\bar{\varepsilon}_s}{\varepsilon_y}\right], \qquad \bar{\varepsilon}_s > \bar{\varepsilon}_n$ (6.2-23b)

Stage 3 (unloading): $f_s = f_p - E_s(\bar{\varepsilon}_p - \bar{\varepsilon}_s), \qquad \bar{\varepsilon}_s < \bar{\varepsilon}_p$ (6.2-23c)

where

$$\bar{\varepsilon}_n = \varepsilon_y(0.93-2B) \tag{6.2-24}$$

and

$$B = \frac{1}{\rho}\left(\frac{f_{cr}}{f_y}\right)^{1.5} \tag{6.2-25}$$

In the above equations, ℓ replaces s in the subscript of symbols for the longitudinal steel, and t replaces s for the transverse steel.

6.2.5 Solution Algorithm

The solution procedure for the SMM-PC is given in the flow chart of Fig. 6.2.2. Similar to the SMM, two equilibrium equations, Eqs. 6.2-26 and 6.2-27, are also used to make the solution procedure more efficient. Eqs. 6.2-26 and 6.2-27 are derived from Eqs. 6.2-1 and 6.2-2:

$$\rho_\ell f_\ell + \rho_{\ell p} f_{\ell p} + \rho_t f_t + \rho_{tp} f_{tp} = (\sigma_\ell + \sigma_t) - (\sigma_1^c + \sigma_2^c) \tag{6.2-26}$$

$$\rho_\ell f_\ell + \rho_{\ell p} f_{\ell p} - \rho_t f_t - \rho_{tp} f_{tp} = (\sigma_\ell - \sigma_t) - (\sigma_1^c - \sigma_2^c)\cos 2\alpha_1 - 2\tau_{12}^c \sin 2\alpha_1 \tag{6.2-27}$$

Defining $[\rho f]_\ell = \rho_\ell f_\ell + \rho_{\ell p} f_{\ell p}$ and $[\rho f]_t = \rho_t f_t + \rho_{tp} f_{tp}$, the above two equations become:

$$[\rho f]_\ell + [\rho f]_t = (\sigma_\ell + \sigma_t) - (\sigma_1^c + \sigma_2^c) \tag{6.2-28}$$

$$[\rho f]_\ell - [\rho f]_t = (\sigma_\ell - \sigma_t) - (\sigma_1^c - \sigma_2^c)\cos 2\alpha_1 - 2\tau_{12}^c \sin 2\alpha_1 \tag{6.2-29}$$

The solution procedure can also be described as follows (Fig. 6.2.2):

Step 1: Select a value of strain in the $2-$direction, ε_2.

Step 2: Assume a value of shear strain in the $1-2$ coordinate, γ_{12}.

Step 3: Assume a value of strain in the $1-$direction, ε_1.

Step 4: Calculate steel strains ε_l, ε_t, and ν_{12}, from Eqs. 6.2-4, 6.2-5, and 6.2-11, respectively. Hsu/Zhu ratio ν_{21} is taken as zero.

Step 5: Calculate uniaxial strains $\bar{\varepsilon}_1$, $\bar{\varepsilon}_2$, $\bar{\varepsilon}_\ell$, and $\bar{\varepsilon}_t$ from Eqs. 6.2-7 to 6.2-10.

Step 6: Calculate the concrete stresses σ_1^c, σ_2^c and τ_{12}^c from Eqs. 6.2-13, 6.2-14, and 6.2-21, respectively.

Step 7: Calculate the reinforcement stresses f_l, f_t, f_{lp}, and f_{tp} from Eqs. 6.2-22 and 6.2-23.

Step 8: Calculate $([\rho f]_\ell + [\rho f]_t)_1$ and $([\rho f]_\ell - [\rho f]_t)_1$.

Step 9: Calculate $([\rho f]_\ell + [\rho f]_t)_2$ and $([\rho f]_\ell - [\rho f]_t)_2$, from Eqs. 6.2-28 and 6.2-29, respectively.

Step 10: Compare $([\rho f]_\ell + [\rho f]_t)_1$ with $([\rho f]_\ell + [\rho f]_t)_2$. When $([\rho f]_\ell + [\rho f]_t)_2$ is larger than $([\rho f]_\ell + [\rho f]_t)_1$, increase the tensile strain ε_1. Otherwise, decrease

ε_1. Repeat steps 3 to 10 until $([\rho f]_\ell + [\rho f]_t)_1$ and $([\rho f]_\ell + [\rho f]_t)_2$ are close enough within the specified accuracy.

Step 11: Compare $([\rho f]_\ell - [\rho f]_t)_1$ with $([\rho f]_\ell - [\rho f]_t)_2$. When $([\rho f]_\ell - [\rho f]_t)_2$ is larger than $([\rho f]_\ell - [\rho f]_t)_1$, increase the value of shear strain γ_{12}. Otherwise, decrease the shear strain γ_{12}. Repeat steps 2 to 11 until $([\rho f]_\ell - [\rho f]_t)_1$ and $([\rho f]_\ell - [\rho f]_t)_2$ are close enough within the specified accuracy.

Step 12: Calculate the applied shear stress $\tau_{\ell t}$ and the corresponding shear strain $\gamma_{\ell t}$ from Eq. 6.2-3 and 6.2-6, respectively. This will provide one point on the $\tau_{\ell t}$ versus $\gamma_{\ell t}$ curve.

Step 13: Select another value of ε_2 and repeat steps 2 to 12. Calculations for a series of ε_2 values will provide the whole $\tau_{\ell t}$ versus $\gamma_{\ell t}$ curve.

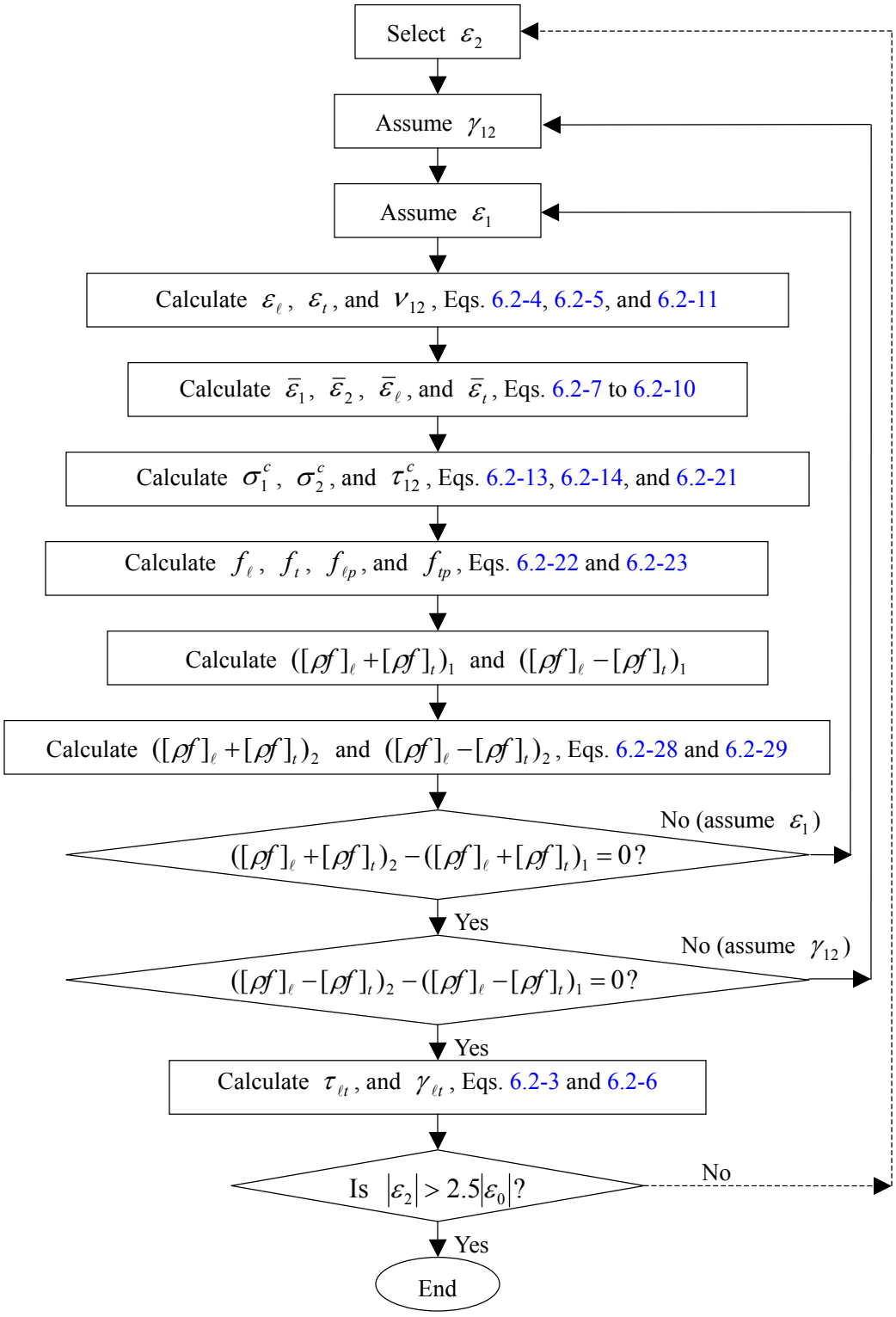

Fig. 6.2.2 Flow Chart of Solution Procedure for SMM-PC

6.3 Applications of SMM-PC to Test Panels TA-1 to TA-5

Following the flow chart shown in Fig. 6.2.2, a computer program was written to predict the shear behavior of the five panels in Group TA. Two features should be emphasized in a computer program for prestressed concrete. First, prestressing tendons were placed in the longitudinal direction and mild steel in the transverse direction for all five panels. Therefore, in Step 7, only $f_{\ell p}$ and f_t were calculated. Second, initial stresses and initial strains exist in prestressing tendons and concrete. These initial stresses were taken into account when applying the constitutive relationships in Step 6 and Step 7.

The applied shear stress versus shear strain relationships predicted by the SMM-PC are compared with the experimental results of five panels TA-1 to TA-5 in Fig. 6.3.1 to Fig. 6.3.5. These five panels have longitudinal prestressing steel ratios, $\rho_{\ell p}$, varying from 0.42% to 0.84% and transverse mild steel ratios, ρ_t, varying from 0.42% to 1.54%. Fig. 6.3.1 to Fig. 6.3.5 show that the predictions of the SMM-PC are very satisfactory.

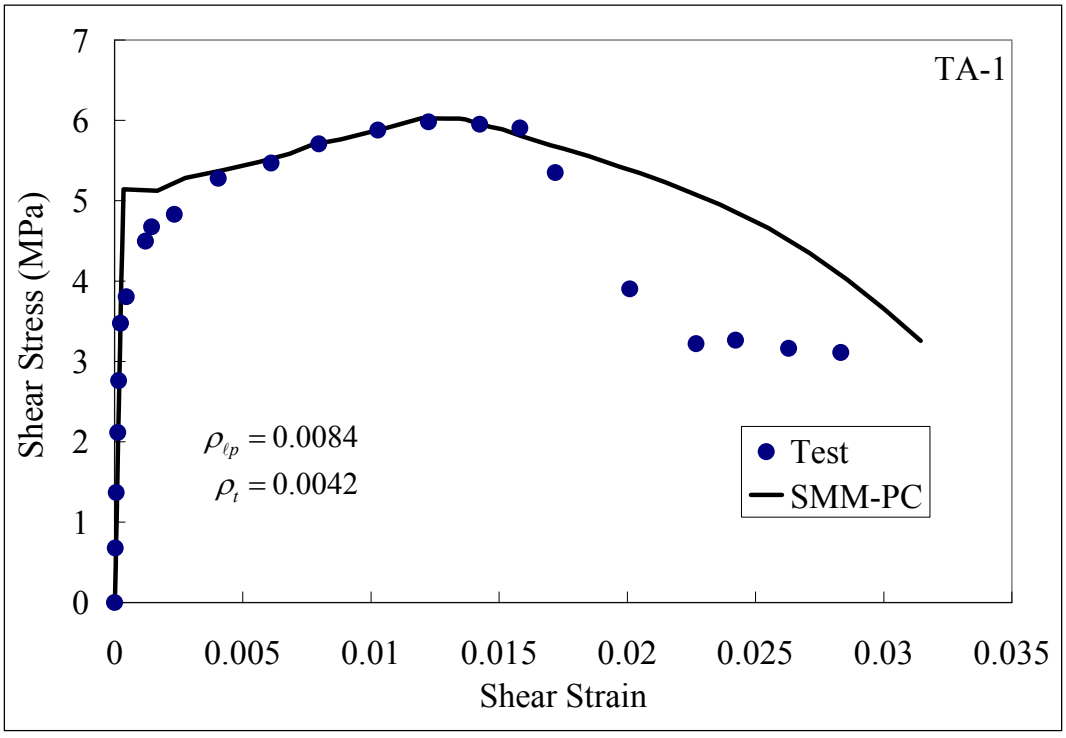

Fig. 6.3.1 Applied Shear Stress $\tau_{\ell t}$ versus Shear Strain $\gamma_{\ell t}$ of Panel TA-1

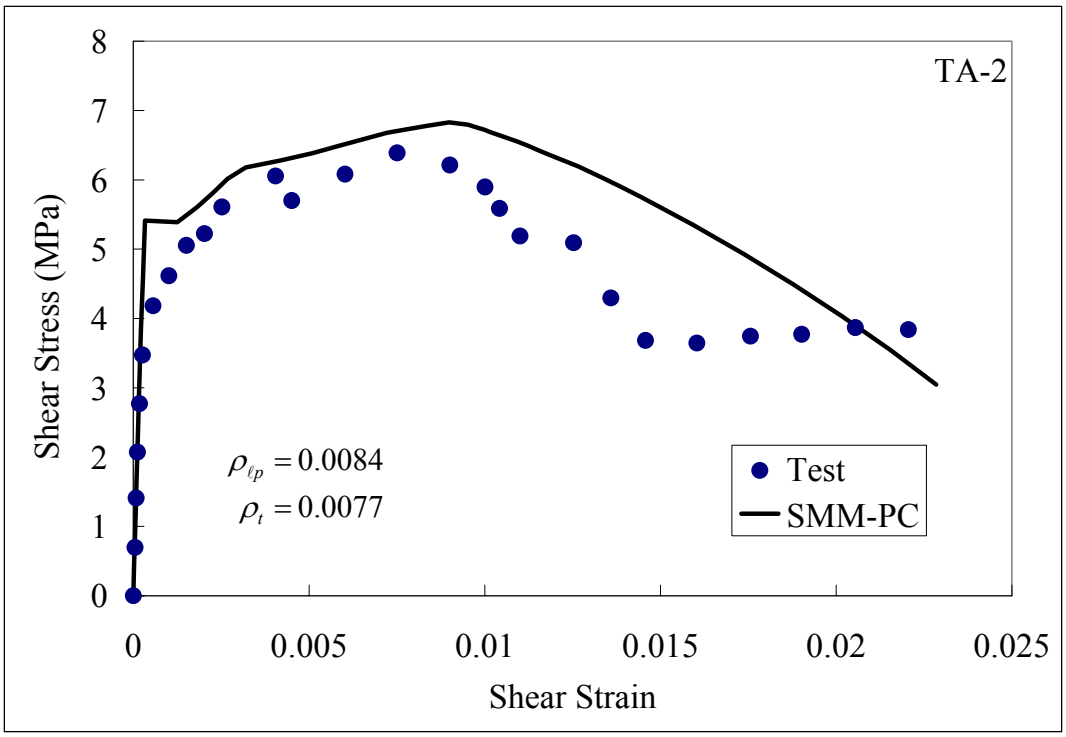

Fig. 6.3.2 Applied Shear Stress $\tau_{\ell t}$ versus Shear Strain $\gamma_{\ell t}$ of Panel TA-2

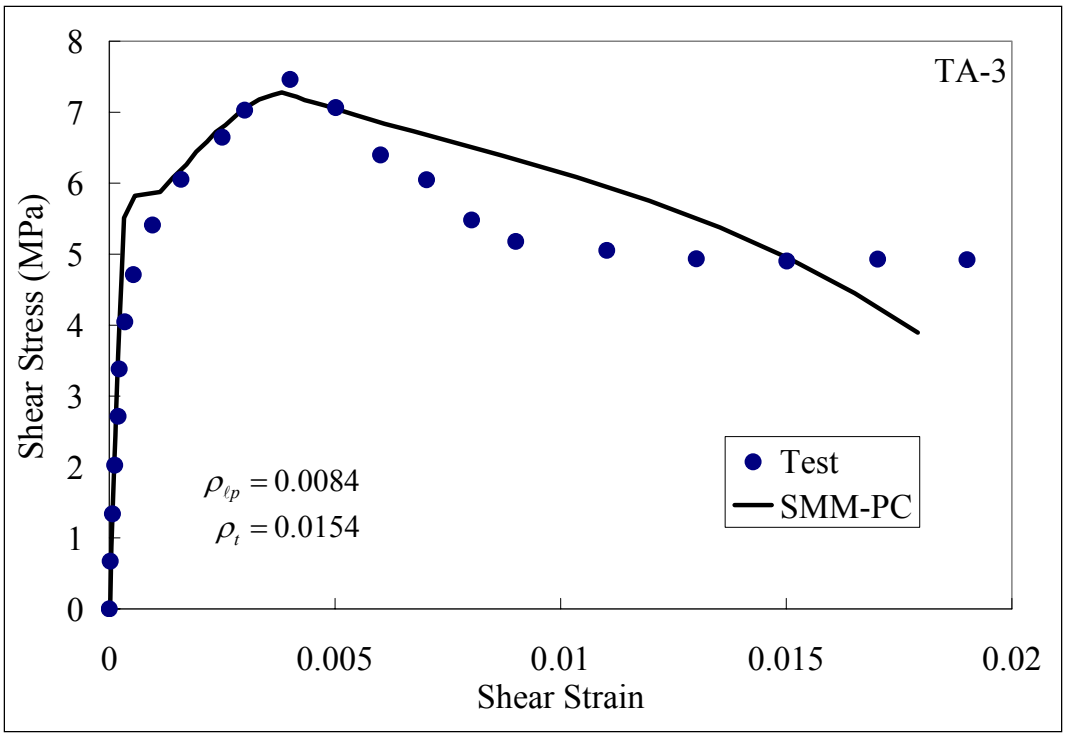

Fig. 6.3.3 Applied Shear Stress $\tau_{\ell t}$ versus Shear Strain $\gamma_{\ell t}$ of Panel TA-3

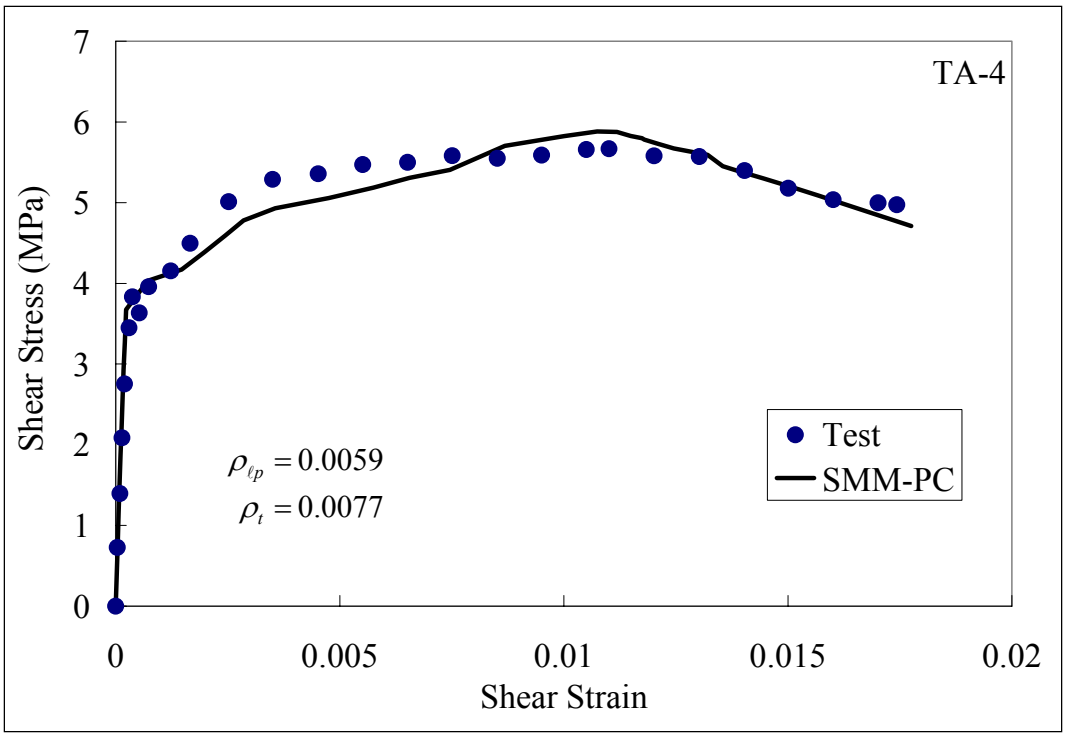

Fig. 6.3.4 Applied Shear Stress $\tau_{\ell t}$ versus Shear Strain $\gamma_{\ell t}$ of Panel TA-4

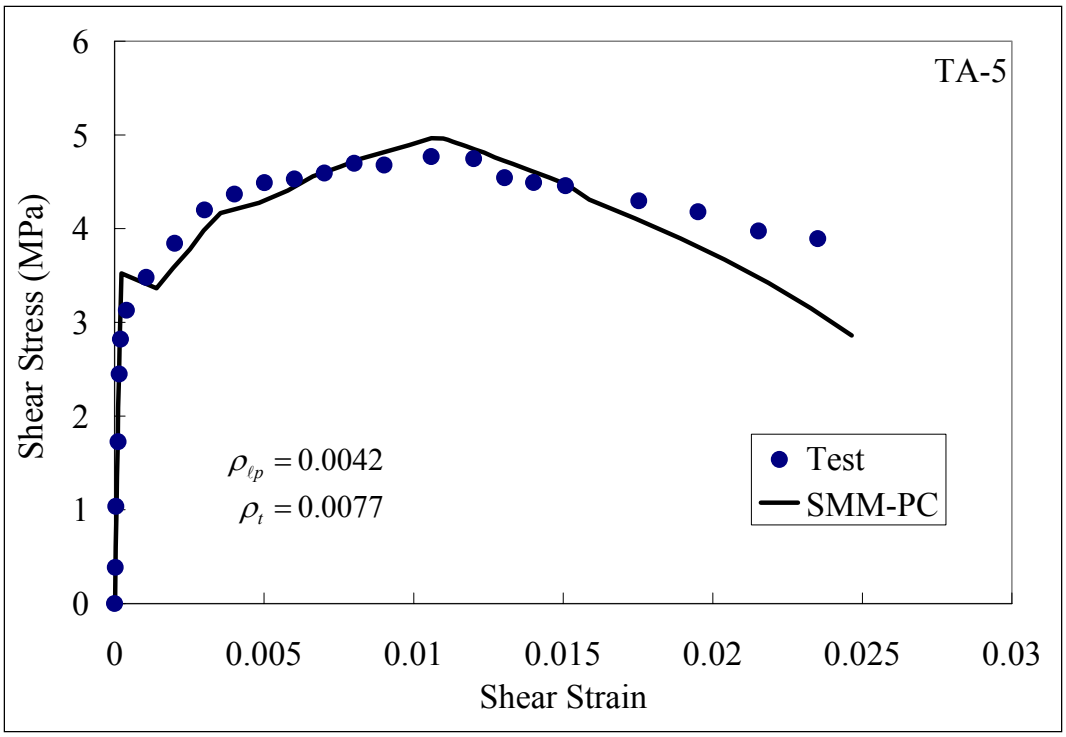

Fig. 6.3.5 Applied Shear Stress $\tau_{\ell t}$ versus Shear Strain $\gamma_{\ell t}$ of Panel TA-5

PART II

SHEAR IN PRESTRESSED CONCRETE BEAMS

CHAPTER 7

SHEAR TESTS OF PRESTRESSED CONCRETE BEAMS

7.1 Introduction

As shown in Part I (Chapters 2 through 6), the constitutive laws of concrete in compression and tension as well as prestressing tendons embedded in concrete were determined by the prestressed concrete panel tests, and the analytical model for prestressed concrete elements (panels) in shear was developed. In Part II (Chapters 7 through 9) both the constitutive laws of materials and the analytical model presented in Part I will be applied to prestressed concrete beams. Chapter 7 reports the test of five prestressed concrete beams. Chapter 8 describes two analytical models, one for the flexural behavior and one for the shear behavior of prestressed concrete beams. Using the shear model to analyze a beam, the shear contribution of concrete (V_c) in prestressed concrete beams is developed from the shear resistance of concrete along an inclined failure plane. In Chapter 9, a new simple design equation for prestressed concrete in shear is proposed. The shear capacities of prestressed concrete beams tested in this project, as well as the other shear test results in the literature (Elzanaty et al., 1987; Rangan, 1991; and Lyngberg, 1976) are used to support the new design equation. The predicted shear strengths are compared with the strengths calculated based on ACI (2005) and AASHTO (2004) provisions. Finally, four design examples are prepared to illustrate the application of the proposed design guidelines.

7.2 Test Program

Test specimens having cross sections of TxDOT Type-A beams were selected for this research project as shown in Figs. 7.2.1 to 7.2.4. Five such beams were designed to study the behavior of the beams in web shear and flexure shear. The aim was to develop a simplified method for shear design of prestressed concrete beams to overcome the complications of the design methods described in the present design codes. Three of the five beams (Beams B1, B2, and B3) were designed to fail in web shear, whereas the remaining two (Beams B4 and B5) were designed to fail in flexure shear. One web shear specimen (Beam B3) and one flexure shear specimen (Beam B5) had draped prestressing strands. Another parameter that was varied in the specimens was the amount of shear reinforcement.

Table 7.2.1 shows the test variables for the five beams, B1 to B5. Beam B1 was designed to fail in web shear and prestressed with 12 straight low-relaxation strands. Transverse shear reinforcement of 0.17% was provided by #2 L rebars at 10 in. spacing or by #3 L rebars at 20 in. The #2 rebars at 10 in. spacing were used at the failure end region to ensure that a sufficient number of stirrups intersect the failure plane. The #3 rebars at 20 in. spacing were used in the remaining parts of the beams.

Similar to B1, Beam B2 was designed to fail in web shear and prestressed with 12 straight low relaxation strands. However, Beam B2 had 1% web shear reinforcement consisting of #4 R rebars at 7 in. spacing.

Beam B3 was also designed to fail in web shear and prestressed with 12 strands. However, four prestressing strands in this beam were draped. Two of the draped strands started from a

distance of 11 ft from the ends of the beam to an additional height of 14 in. at the ends. The draping of the other two strands started at a distance of 8 ft from the ends of the beam to an additional height of 10 in. at the ends. Transverse shear reinforcement of 1% in the web was the same as that provided in Beam B2.

Beam B4 was designed to fail in flexural shear and prestressed with 12 straight low relaxation strands. As in Beam B1, Beam B4 was reinforced with 0.17% shear reinforcement consisting of #2 L rebars at 10 in. spacing for the measured regions and #3 L rebars at 20 in. spacing for the remaining lengths. The measured locations of flexure shear failure was between 5.3 ft to 7.9 ft from the ends.

Beam B5 was also designed to fail in flexural shear. The prestressing strands in Beam B5 were also draped as in Beam B3. The transverse shear reinforcement of 0.17% was identical to that of Beam B4.

Table 7.2.1 Test Specimens

Beam ID	**Mode of failure**	**Shear Reinforcement**	**Prestressing Tendons**	**Casting Schedule**
B1	Web Shear	0.17%	12 straight	12/12/05
B2	Web Shear	1.0%	12 straight	12/12/05
B3	Web Shear	1.0%	8 straight, 4 draped	12/08/05
B4	Flexural Shear	0.17%	12 straight	12/12/05
B5	Flexural Shear	0.17%	8 straight, 4 draped	12/08/05

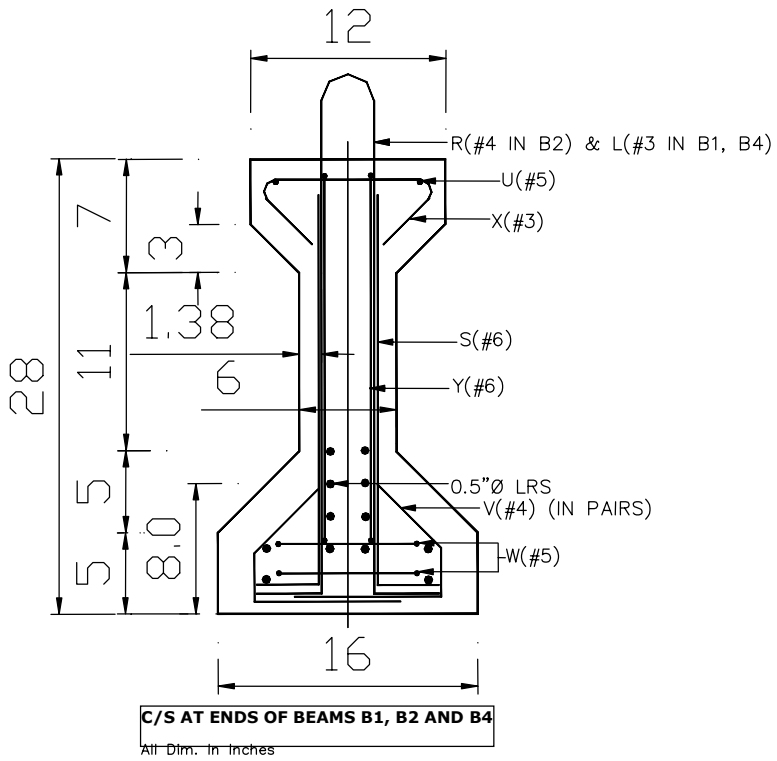

(a) Cross Section of Beams B1, B2 and B4

Fig. 7.2.1 Cross Section of Type-A Beams

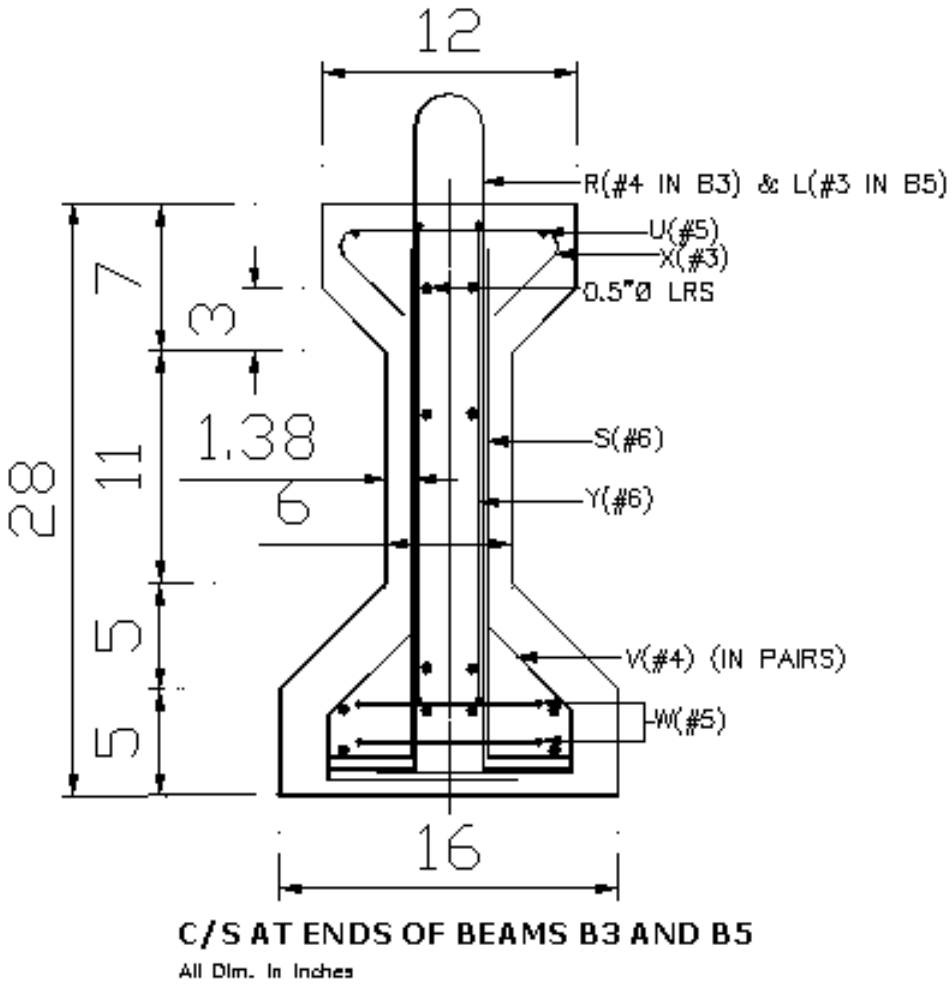

(b) Cross Section of Beams B3 and B5

Fig. 7.2.1 Cross Section of Type-A Beams (continued)

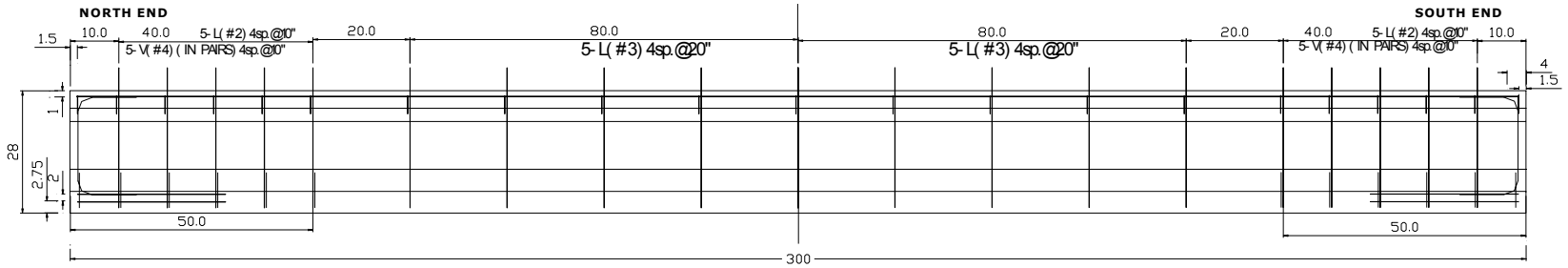

BEAM-B1,

ELEVATION All Dim In Inches

Fig.7.2.2 Elevation and Reinforcement Details of Beam B1

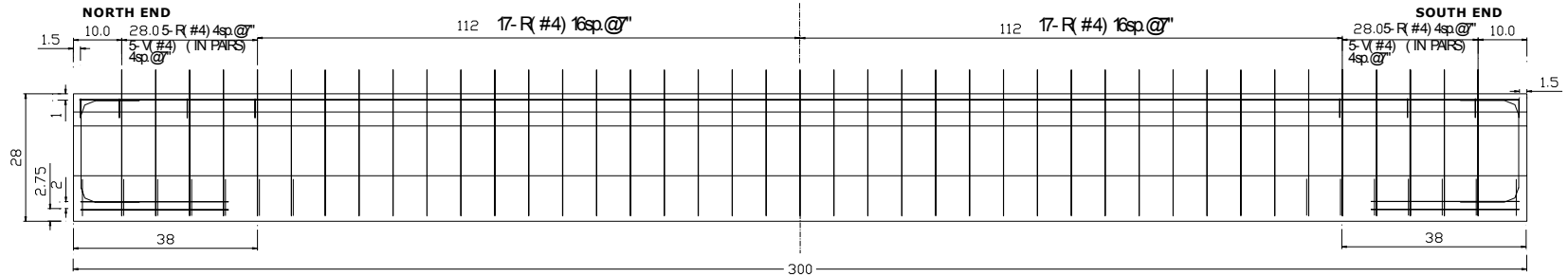

BEAMS-B2 and B3

ELEVATION All Dim In Inches

Fig. 7.2.3 Elevation and Reinforcement Details of Beams B2 and B3

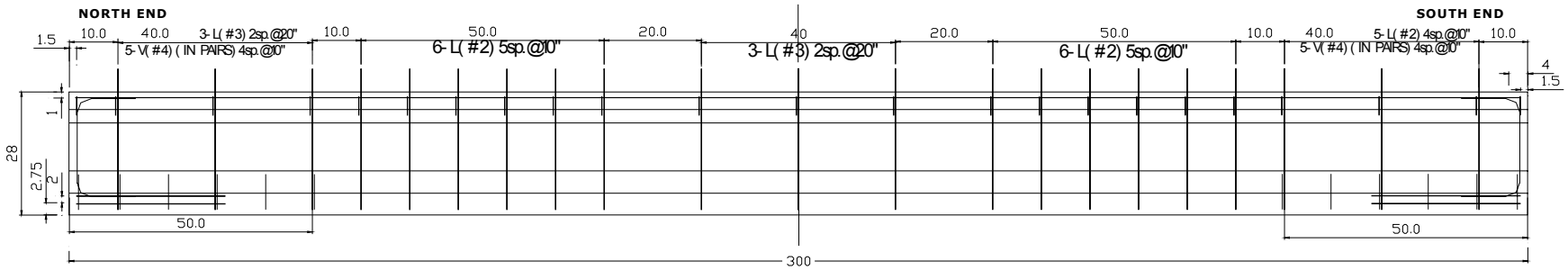

BEAMS-B4,B5

ELEVATION All Dim. In Inches

Fig. 7.2.4 Elevation and Reinforcement Details of Beams B4 and B5

7.3 Test Specimens

The crosssections of the designed beams are shown in Fig. 7.2.1(a) and (b). The total height of the beam was 28 in. and the widths of the top and bottom flange were 12 in. and 16 in., respectively. The width of the web was 6 in. The prestressing tendons in three beams (B1, B2, and B4)were straight while in the other two (B3 and B5) they were draped. The position of the straight prestressing tendons and the type of the reinforcing bars are also shown. The sizes of the rebars are as follows: #3 rebars were used for X rebars, #4 for R and V rebars, #5 for U and W rebars, and #6 for S and Y rebars. In addition to the above, #2 and #3 rebars were used in some beams for L rebars which are similar in shape to the R rebars. X and V rebars were designed to confine the concrete and act as secondary reinforcements in the top and bottom flange, respectively. L, R and S rebars served as transverse reinforcement for shear strength. The W and Y rebars were installed to resist the end zone bearing, spalling, and bursting stresses, whereas the U rebars ran all along the beam to support the R, X, and Y rebars. Twelve 0.5-in. diameter, seven-wire, low-relaxation strands were used as the prestressing steel. The prestressing strands had ultimate strength of 270 ksi.

The elevations of the five designed beams (Beams B1 to B5) are shown in Fig. 7.2.2 through Fig. 7.2.4. The total length of the beams tested was 25 ft while the span length was 24 ft. Fig. 7.3.1 shows the reinforcement and instrumentation details of Beams B1 through B3 that were designed to fail in web shear. Fig. 7.3.2 shows the details of Beams B4 and B5 that were designed to fail in flexure shear.

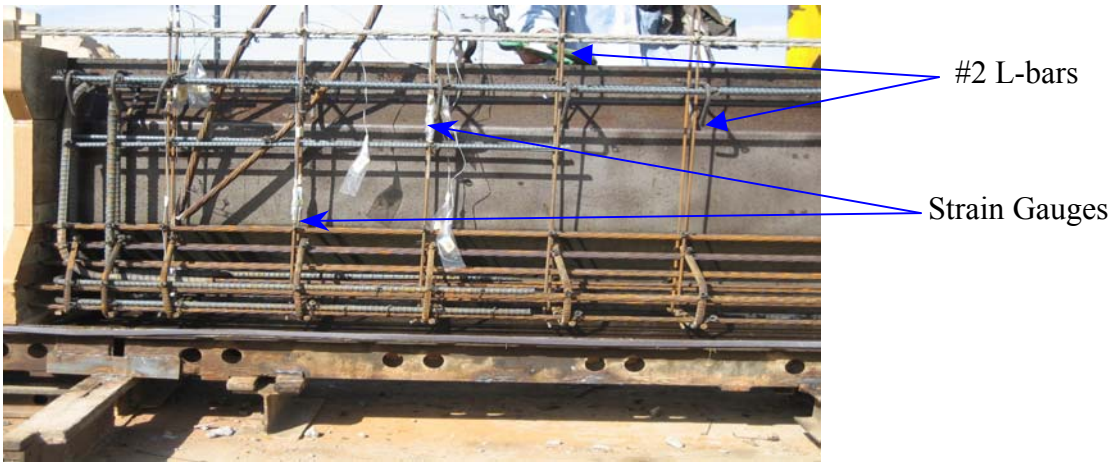

(a) Beam B1 (0.17% steel, straight strands, to be loaded at 3.5 ft from end)

Fig. 7.3.1 Reinforcement and Instrumentation Details of Beams B1, B2, and B3 (Web Shear Specimens)

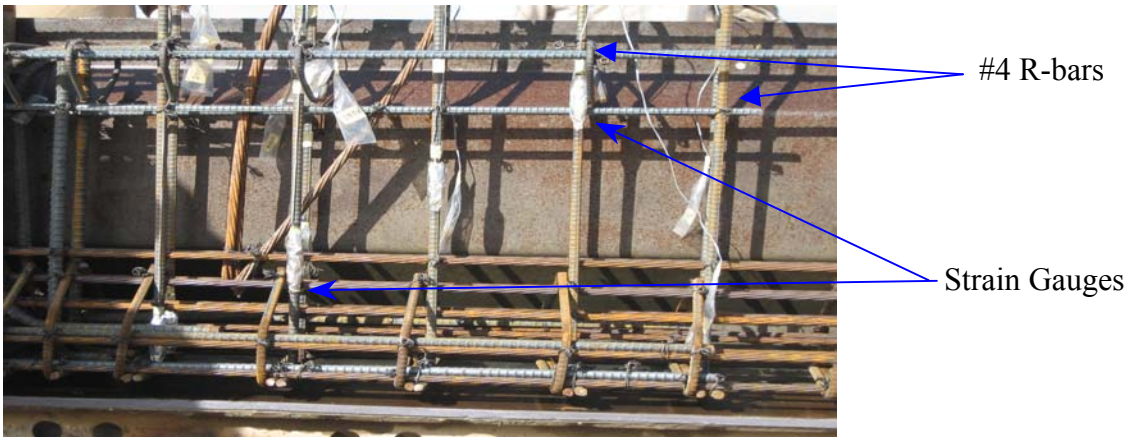

(b) Beam B2 (1% steel, straight strands, to be loaded at 3.5 ft from end)

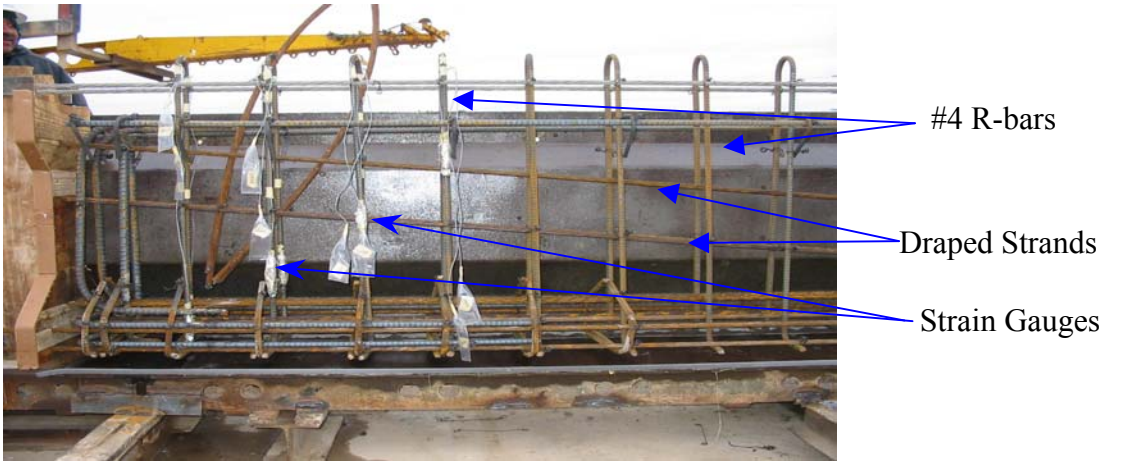

(c) Beam B3 (1% steel, draped strands, to be loaded at 3.5 ft from end)

Fig. 7.3.1 Reinforcement and Instrumentation Details of Beams B1, B2, and B3 (Web Shear Specimens) (continued)

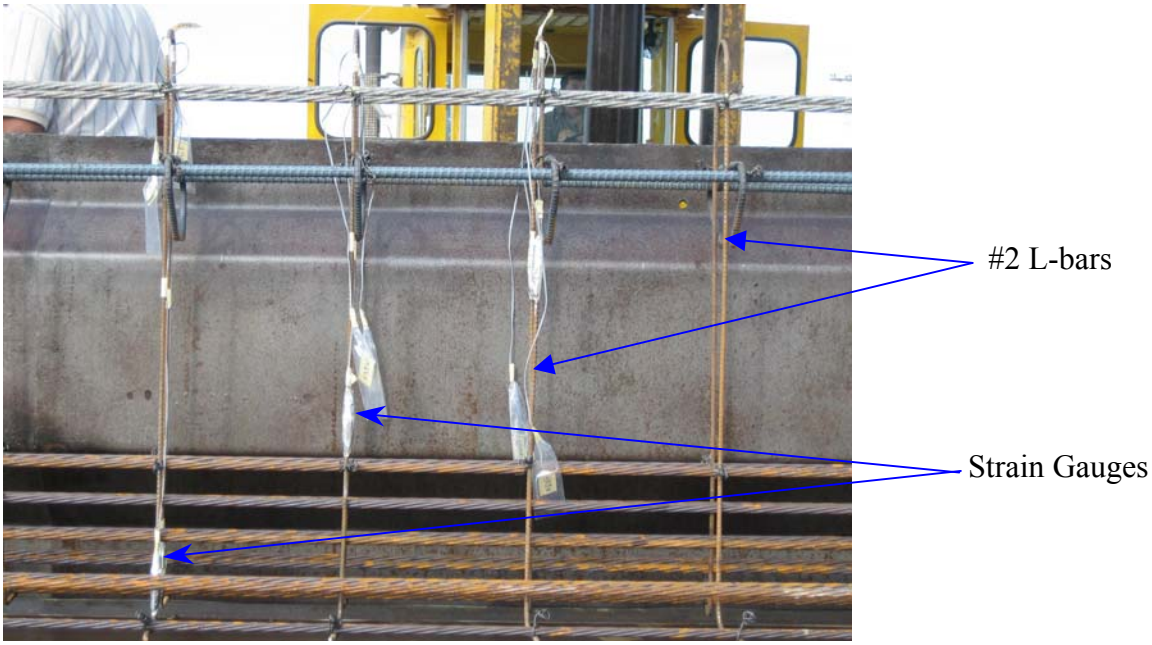

(a) Beam B4 (0.17% steel, straight strands, to be loaded at 8.5 ft from end)

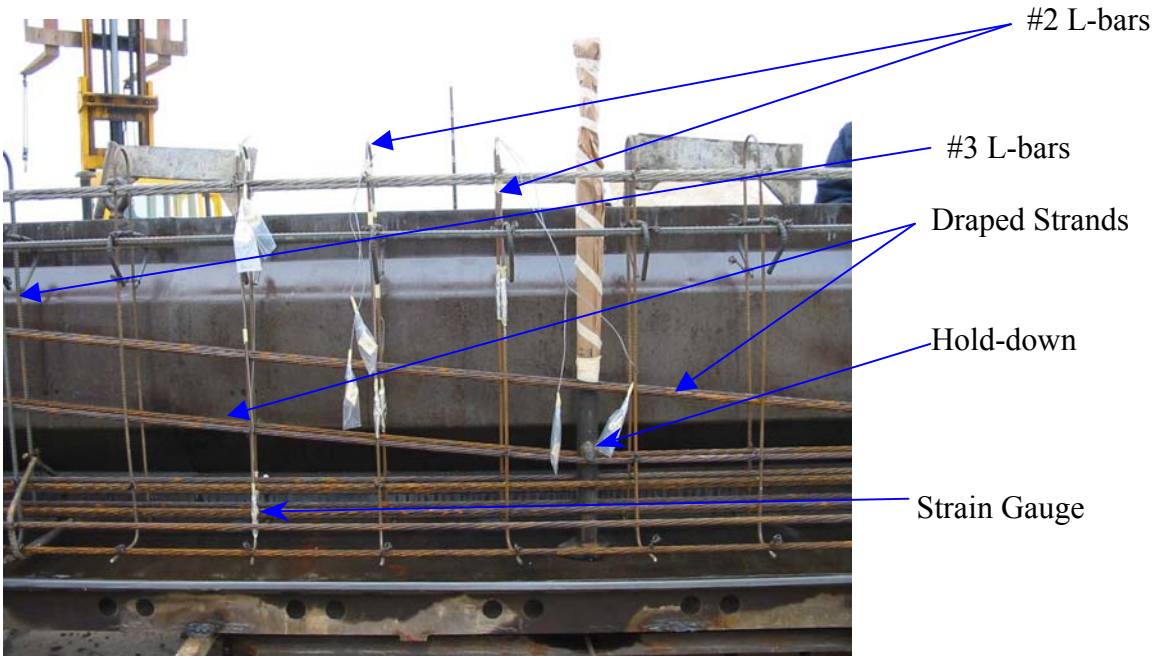

(d) Beam B5 (0.17% steel, draped strands, to be loaded at 8.5 ft from end)

Fig. 7.3.2 Reinforcement and Instrumentation Details of Beams B4 and B5 (Flexure Shear Specimens)

7.4 Manufacturing of Test Specimens

The five beams were cast in two groups on two different days. The two beams, B3 and B5, having draped strands were first cast together in a long-line prestressing bed with Type-A steel form. The strands were prestressed by hydraulic jacks against the prestressing bed. Hold-downs were installed on the bed (Fig. 7.3.2(b)) to drape the strands at the desired inclination. The second group of three beams, B1, B2, and B4, with straight tendons was cast after four days. Concrete was prepared in a plant mixer, transported to the casting site, and deposited into the formworks using a mobile hopper as shown in Fig. 7.4.1(a). During casting, spud vibrators were used for compacting the concrete as shown in Fig. 7.4.1(b).

One day after casting, the prestressing strands were slowly released. The compressive strength of concrete at the time of application of prestress was approximately 4000 psi. For Beams B3 and B5, the anchors of the hold-down rods were removed after the application of the prestress, as shown in Fig. 7.4.1(c).

(a) Concrete Placed in Beam B4 by a Hopper

Fig. 7.4.1 Casting of Test Specimens

(b) Compaction using Needle Vibrators in Beam B4

(c) Removal of Anchors of Hold-down Rod from Beam B3

Fig. 7.4.1 Casting of Test Specimens (continued)

7.5 Test Setup

The beams were subjected to vertical loading up to their maximum shear capacity in a specially built steel loading frame, as shown in Fig. 7.5.1. Two of the four actuators (namely actuator B and actuator C), each attached to a vertical steel frame, were used to apply the vertical loads on the beams. Each of these two actuators had a capacity of 320 kips. Actuator frame B was installed on the north end of the beam, and actuator frame C on the south end of the beam. These two actuator frames were sitting on top of two WF18×97 beams, bolted securely to the strong floor. The two WF18×97 beams were 20 ft long and spaced at 87 in. center to center. The beam specimen was positioned in the middle of this spacing width on top of two load cells placed at each end. The load cells of 500 kips capacity were sitting on top of the steel pedestals fixed to the strong floor. On top of the load cells, bearing plates to support the beams were placed with a roller on the north end and a hinge on the south end, thus allowing the beam to rotate freely at the supports and to expand freely along its length. The actuators were provided with bracings for their lateral stability.

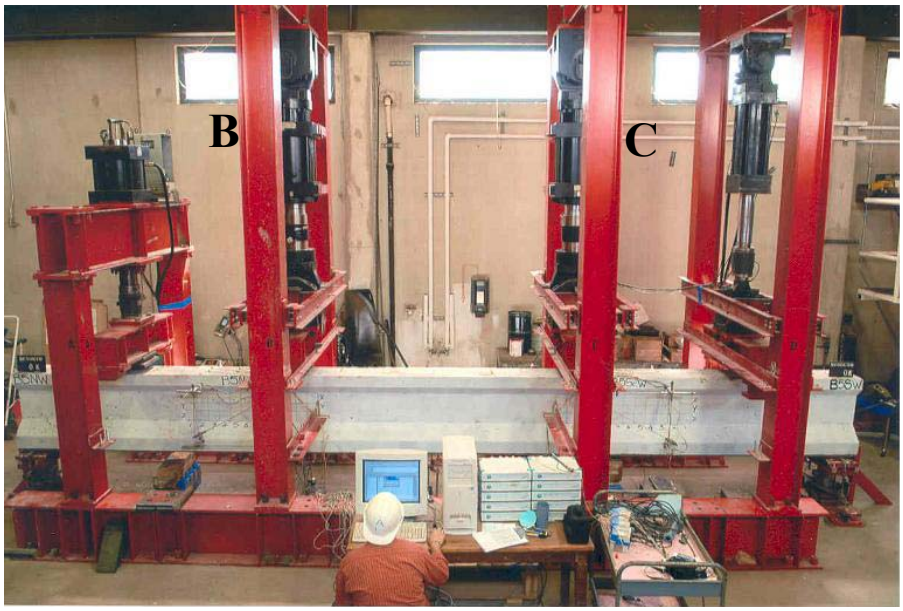

Fig. 7.5.1 Test Setup

The position of the vertical loads on the beams together with the support positions is shown in Fig. 7.5.2. The loads from actuators B and C were applied at 3 ft from the supports (both north and south supports) for Beams B1, B2, and B3; and at 8 ft from the supports for Beams B4 and B5. Actuator loads were applied through a roller assembly consisting of two 6 in.× 12 in.×2 in. bearing plates and two rollers of 2 in. diameter and 12 in. length, so as to ensure uniform and frictionless load transfer from actuators on to the beam surface. All the bearing plates and rollers were heat-treated to maximum possible hardness, in order to minimize local deformations. Lead sheets were also used between the load bearing plates and beam surface.

The loads and displacements of the actuators were precisely controlled by the MTS 'MultiFlex' System. Actuators B and C were first programmed with a load control mode of 5

kips/min. When the slope of the load-displacement curve started decreasing, the control mode was switched to a displacement control of 0.2 in./hour. This step continued until shear failure occurred at either end of the beam. This displacement control feature was essential in capturing the ductility/brittleness behavior of the beam failing in shear.

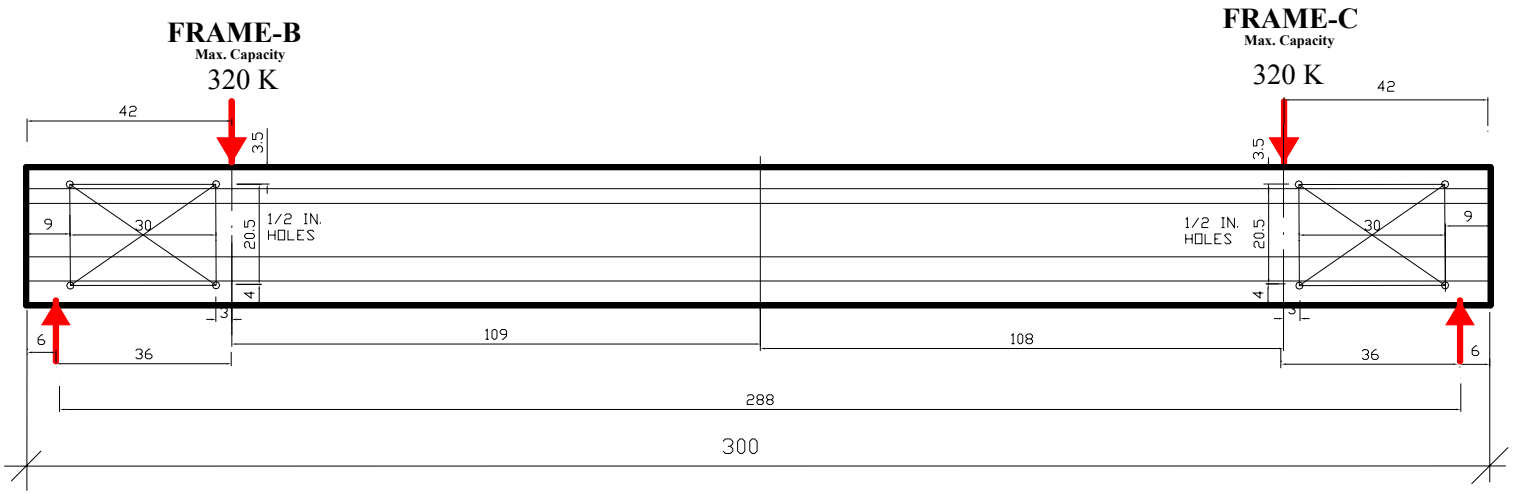

(a) Loading Point and LVDT Locations for Beams B1, B2 and B3

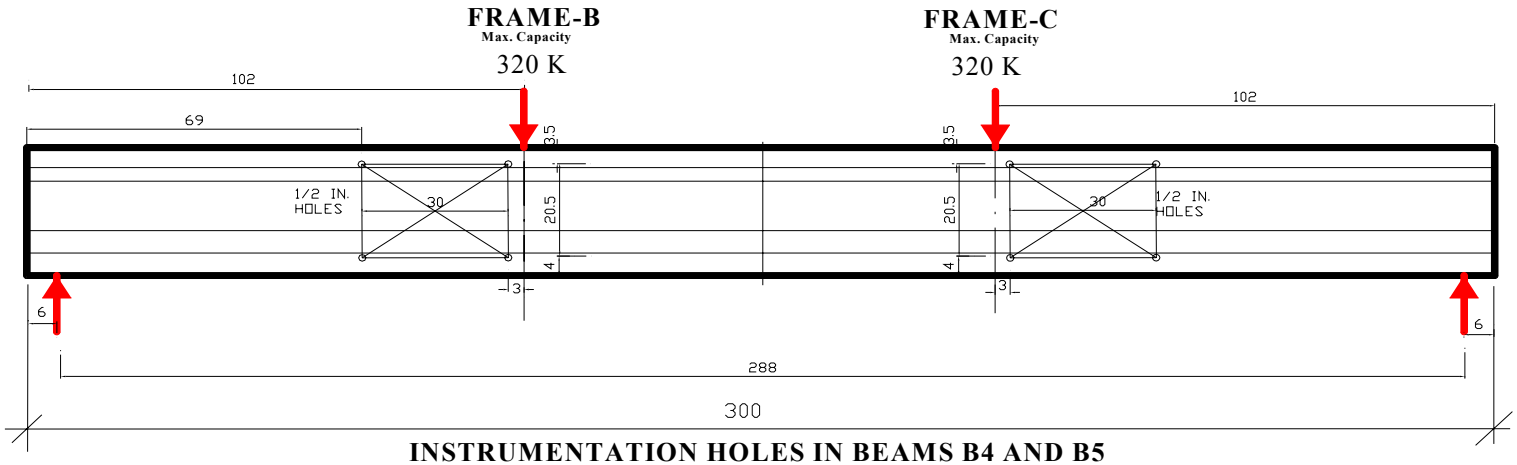

(b) Loading Point and LVDT Locations for Beams B4 and B5

Fig 7.5.2 Loading Positions of Beams

During testing, Linear Voltage Displacement Transducers (LVDTs) were used to measure the displacements at the failure regions of the beam adjacent to the points of load application, as shown in Fig. 7.5.3. The LVDTs were installed on both faces of the beams to get the average displacements. Several LVDTs were also placed under the beam, both at the supports and at the point of loading to measure the total and net displacements of the beam. Strain gauges were installed on both legs of the vertical rebars inside the beams to monitor the rebar strains during the load test. The locations of strain gages on rebars are shown in Fig 7.5.4 through 7.5.6 for various beams. On average, each beam was instrumented with about 30 LVDTs and 16 strain gages to record the structural behavior of the beam. Data from these sensors were continuously monitored and stored by the HBM 'Spider-8' Data Acquisition System. Shear cracks formed on the beam web during the load test were regularly marked on the grid as shown in Fig. 7.5.7. The crack widths were measured using a hand-held microscope having a 0.001 in. measuring precision.

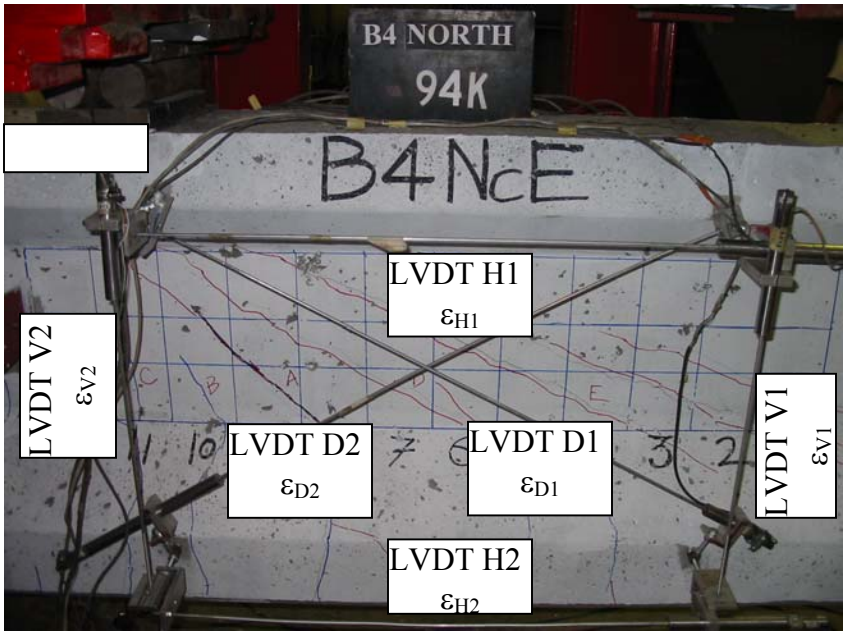

Fig. 7.5.3 LVDT Setup on Beam B4

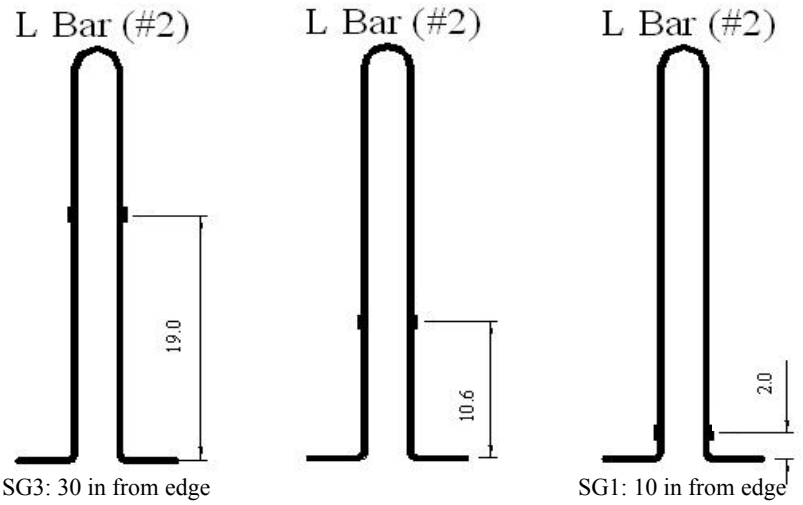

Fig. 7.5.4 Location of Strain Gages on L Bars in Beam B1

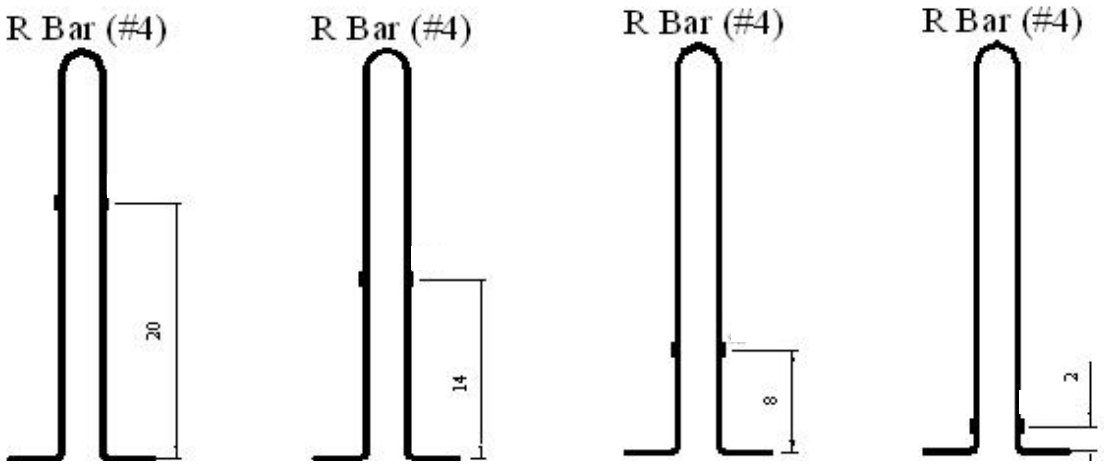

Fig. 7.5.5 Location of Strain Gages on R Bars in Beams B2 and B3

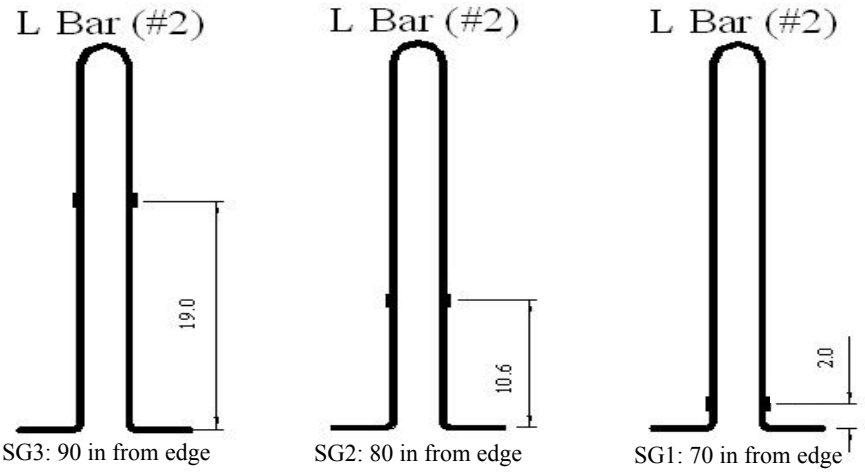

Fig. 7.5.6 Location of Strain Gages on L Bars in Beams B4 and B5

Fig. 7.5.7 Tracking and Measuring Shear Cracks on the Web of Beam B4

7.6 Test Results

Table 7.6.1 shows the ultimate strengths at failure for the five test beams, B1 to B5. It can be seen that both ends of Beams B1 and B2 failed in web shear. Two web shear failures were created in one beam, because such a failure occurred adjacent to the support and damaged only a short length of the beam at one end. It was possible to create a loading scheme to induce a web shear failure at the other end.

Although the north end of Beam B3 failed in flexure, the load deformation curves showed that the north end almost reached its web shear capacity, as the concrete in the web region almost crushed at failure. Since the behavior of the south end was very similar to the north end, it was decided not to test the south end after the failure of the north end.

Beams B4 and B5 were designed to fail in flexural shear in a region adjacent to the load point at one-third span of the beams. As the failure reduced one-third of the beam length, it was not possible to devise a loading scheme to create another flexural shear failure for the remaining length. Hence, each of these two beams could provide only one failure load. Specimen B5 actually failed in flexure at a distance of 11 ft from the end due to a weak section created by the hold-down rod, Fig. 7.4.1(c), as the grouting was weak and full of voids. Similar to Beam B3, the flexural shear capacity of Beam B5 was very close to its failure load in flexure.

From the shape of the load-deflection curves, shown in Fig. 7.6.1. it can be seen that the specimens designed for web shear failure (B1, B2, and B3) had higher shear capacities compared to the specimens designed to fail in flexural shear (B4 and B5). However, the specimens that failed in flexural shear had higher ductility. Both the strength and deflections were well predicted by the flexural analysis given in Chapter 8, Section 8.1.

Table 7.6.1 Failure Loads of Beams

Beam	Tendon Profile (Straight/ Draped)	Transverse Steel (%)	Concrete Strength (ksi)	Failure Mode	Ultimate Shear Capacity (kips)	Ultimate Moment Capacity (kips-ft.)	Max. Shear corresp. to Ultimate Moment (kips)	Max. Moment corresp. to Ultimate Shear (kips-ft.)
B1-North	Straight	0.17	10.5	Web-Shear	**188.9**	**-**	**-**	**566.7**
B1-South	Straight	0.17	10.5	Web-Shear	**173.5**	**-**	**-**	**520.5**
B2-North	Straight	1.0	10.8	Web-Shear	**201.1**	**-**	**-**	**603.3**
B2-South	Straight	1.0	10.8	Web-Shear	**234.0**	**-**	**-**	**702.0**
B3-North	Draped	1.0	9.37	Flexure/ Flexural-Shear	**-**	**684.0**	**228.0**	**-**
B4-South	Straight	0.17	10.3	Flexural-Shear	**96.8**	**-**	**-**	**774.4**
B5-North	Draped	0.17	9.36	Flexure/ Flexural-Shear	**-**	**784.0**	**98.0**	**-**

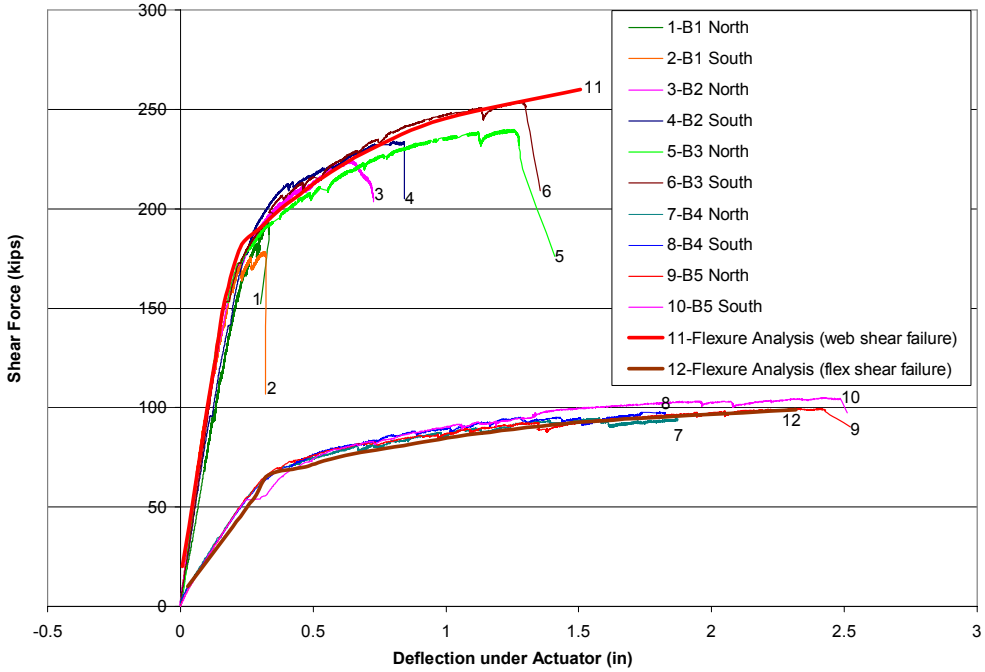

Fig 7.6.1 Load Deflection Curves of Specimens B1 to B5

Table 7.6.2 Ultimate Strains in Specimens B1 to B5 measured by LVDTs

	Strains (x 10^{-6})					
	ε_{V1}	**ε_{V2}**	**ε_{H1}**	**ε_{H2}**	**ε_{D1}**	**ε_{D2}**
B1-North	880	990	-367	377	-1767	2256
B1-South	754	712	-318	1858	-1482	2750
B2-North	982	991	-277	2616	-2629	3881
B2-South	389	165	-276	2514	-1801	2925
B3-North	575	937	-370	2164	-1265	2256
B4-South	4280	678	-665	1982	-290	2202
B5-North	127	687	-954	3406	-309	1448

Table 7.6.2 gives the ultimate strains in Beam B1 to Beam B5 measured by LVDTs at failure. The LVDTs were located adjacent to the loading point as indicated in Fig. 7.5.2. A set of six LVDTs is shown in Fig 7.5.3. Each set had two vertical, two horizontal and two diagonal LVDTs. Out of the two vertical LVDTs, the one that was situated closer to the load was named V2 (strain of ε_{V2}) while the other was named V1 (strain of ε_{V1}). The horizontal LVDT situated on the top flange was named H1 (strain of ε_{H1}) while the one on the bottom flange was named H2 (strain of ε_{H2}). The diagonal LVDT that was connected to the top flange near the load point was

named D1 (strain of ε_{D1}) and was subjected to compressive strains during the loading of the beams. Diagonal LVDT D2 (strain of ε_{D2}) was connected to the lower flange near the load point and subjected to tensile stresses during loading of the beams. The strains shown in Table 7.6.2 for the different LVDTs for all the beams are the average of the two LVDT strains located on both sides of the beams. These strains have been used to calculate the ultimate capacities using the analytical model described in Chapter 8.

Table 7.6.3 Experimental Ultimate Strains in Strain Gages for Specimens B1 to B5

Beams	**Strains (x 10^{-6})**			
	ε_{SG1}	ε_{SG2}	ε_{SG3}	ε_{SG4}
B1-North	2,686	22,918	11,565	-
B1-South	928	22,010	14,854	-
B2-North	1,159	13,255	14,025	11,362
B2-South	1,554	10,737	12,318	5,435
B3-North	1,107	2,398	2,283	2,042
B4-South	235	14,357	8,370	-
B5-North	500	5,052	5,841	-

Table 7.6.3 gives the ultimate strains in Beams B1 to B5 measured by electrical strain gages attached to the rebars in the failure regions. In specimens B1, B4, and B5 three rebars in each measured region were instrumented with strain gages. In specimens B2 and B3, four rebars in each measured region were instrumented. Both legs of a rebar were instrumented with a strain gage. The locations of the strain gages on the rebars were selected to ensure that the strain gages would intersect the failure plane as shown in Figs. 7.5.4 to 7.5.6. The strains shown in Table 7.6.3 have been used to calculate the ultimate stresses and the ultimate forces in the stirrups. The ultimate forces were calculated from the ultimate stresses by multiplying the cross-sectional area of the rebars. The stirrup forces were used to calculate the ultimate shear capacities of the beams using the analytical model described in Chapter 8. However, some strains recorded in Table 7.6.3 are too low. This may be due to the fact that the failure plane did not intersect these strain gages. In such cases, the stresses developed due to the recorded strains have been taken not less than 40 ksi.

CHAPTER 8

ANALYSIS OF PRESTRESSED BEAMS

8.1 Flexural Analysis

A flexural analysis of the beam was performed using the beam theory to check the overall accuracy of the beam tests performed in this research project. For this purpose the load-deflection curves of the beams were obtained for five beams, B1 to B5, and compared with the test results given in Fig. 7.6.1 of Chapter 7. The following procedure was used to obtain the individual points of the load-deflection curve.

Step 1: For a given load, the moments developed at the sections under the loading points were obtained. The sections are at 3 ft from the supports for Beams B1, B2, and B3 and 8 ft for B4 and B5.

Step 2: The stresses developed in concrete and prestressing tendons at the loading section were obtained by equating the compressive and tensile forces in the section. The unbalanced moment at the section was equated to the moment developed at the section due to the external moment (Step 1).

The stress-strain relationship of concrete was assumed to be linear up to the cracking of the section. After cracking, the stress-strain relationship given in Eq. 8.1-1 was used. The cracking stress of concrete was taken as $7.5\sqrt{f_c'}$.

$$\sigma_c = f_c' \left[2\left(\frac{\varepsilon_c}{\varepsilon_0}\right) - \left(\frac{\varepsilon_c}{\varepsilon_0}\right)^2 \right] \tag{8.1-1}$$

where

f_c' = compressive strength of concrete,

ε_c = compressive strain in the extreme concrete fiber at the cross section, and

ε_0 = ultimate compressive strain in concrete.

The stress-strain relationship of prestressing tendons shown in Eqs. 8.1-2 and 8.1-3 were used in this analysis.

$$f_{ps} = E_{ps}\bar{\varepsilon}_s, \qquad \bar{\varepsilon}_s < \frac{0.7 f_{pu}}{E_{pu}} \tag{8.1-2}$$

$$f_{ps} = \frac{E'_{ps}\bar{\varepsilon}_s}{\left[1 + \left(\frac{E'_{ps}\bar{\varepsilon}_s}{f'_{pu}}\right)^m\right]^{\frac{1}{m}}}, \qquad \bar{\varepsilon}_s \geq \frac{0.7 f_{pu}}{E_{pu}} \tag{8.1-3}$$

where

E_{ps} = elastic modulus of prestressing tendons, taken as 29,000 ksi,

f_{pu} = ultimate strength of prestressing tendons, taken as 270 ksi,

E'_{ps} = modulus of prestressing tendons, taken as 30,345 ksi,

f'_{pu} = revised strength of prestressing tendons, taken as 260 ksi, and

m = constant taken as 5.

Step 3: The compressive strain in the extreme concrete fiber at the loading section was obtained corresponding to the external moment in Step 2. This was divided by the depth of the neutral axis of the section to obtain the curvature of the section.

Step 4: The deflection of the beam at the loading section was obtained using the curvature area diagram (Gere and Timoshenko, 1991).

The load-deflection curves were obtained using the above-mentioned procedure for Beams B1, B2, and B3 (web shear) and Beams B4 and B5 (flexure shear). These curves have been shown in Fig 7.5.1. It can be seen that the load deformation behavior predicted from the analysis was very close to the load deformation curves of the test specimens with web shear as well as flexural shear failures.

8.2 Shear Analysis

8.2.1 Analytical Model

The concept of shear resistance developed by Loov (2002) was used to calculate the ultimate shear capacity of Beams B1 to B3 in shear failure. According to this shear model, the contribution of concrete to the shear capacity of the beams stems from the shear stress of the concrete along the failure plane (indicated by S in Fig 8.2.1). Loov's concept is very different from the existing design methods (ACI, 2005 and AASHTO, 2004) which assume that the concrete contribution to the shear capacity of beams arise from the tensile stress across failure planes. The following procedure was used to calculate the ultimate shear capacities of Beams B1 to B3 using the experimental strains measured from these beams.

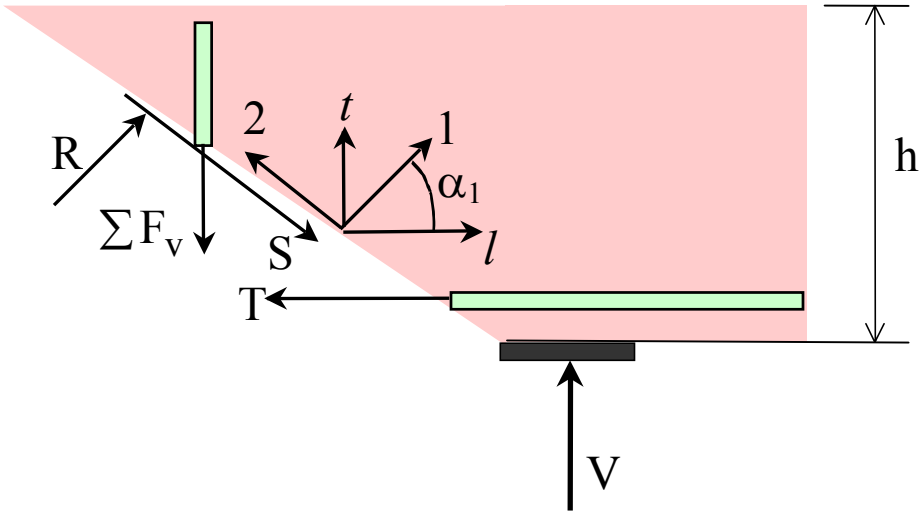

Fig 8.2.1 Analytical Model used for calculating Web Shear Capacities of Beams

Step 1: The shear strain, γ_{lv}, in the horizontal and vertical coordinate (or $\ell - t$ coordinate) were obtained using the strain compatibility relationship shown in Eq. 8.2-1:

$$\varepsilon_d = \varepsilon_h \cos^2\phi + \varepsilon_v \sin^2\phi + 2\frac{\gamma_{hv}}{2}\sin\phi\cos\phi \tag{8.2-1}$$

where

ε_d = strain recorded in either of the diagonal LVDTs,
ε_h = average of the strains recorded in the two horizontal LVDTs,
ε_v = average of the strains recorded in the two vertical LVDTs, and
ϕ = angle between the horizontal and the diagonal LVDTs.

Two values of γ_{hv} were obtained by putting two values of diagonal strains, ε_d, in the above equation along with the strain values of ε_h, ε_v and corresponding ϕ. The average of these two values was taken as the ultimate shear strain γ_{hv} in the ℓ-t coordinate.

Step 2: The values of normal and shear strains ε_1, ε_2 and γ_{12} in the principal $1-2$ coordinate were obtained from the strains in the $\ell - t$ coordinate using the stain compatibility relationships shown in Eqs. 8.2-2 through 8.2-4:

$$\varepsilon_1 = \varepsilon_h \cos^2\alpha_1 + \varepsilon_v \sin^2\alpha_1 + 2\frac{\gamma_{hv}}{2}\sin\alpha_1\cos\alpha_1 \tag{8.2-2}$$

$$\varepsilon_2 = \varepsilon_h \sin^2\alpha_1 + \varepsilon_v \cos^2\alpha_1 - 2\frac{\gamma_{hv}}{2}\sin\alpha_1\cos\alpha_1 \tag{8.2-3}$$

$$\frac{\gamma_{12}}{2} = \left(-\varepsilon_h + \varepsilon_v\right)\sin\alpha_1\cos\alpha_1 + \frac{\gamma_{hv}}{2}\left(\cos^2\alpha_1 - \sin^2\alpha_1\right) \tag{8.2-4}$$

where

α_1 = angle between the horizontal direction ($\ell -$ axis) and the principal tensile stress direction (1—axis).

Step 3: Uniaxial normal strains in the $1-2$ coordinate, $\bar{\varepsilon}_1$ and $\bar{\varepsilon}_2$, were obtained from the biaxial normal strains, $\varepsilon_1$and ε_2, using the Hsu-Zhu ratios in Eqs. 8.2-5 and 8.2-6.

$$\bar{\varepsilon}_1 = \frac{1}{1-\nu_{12}\nu_{21}}\varepsilon_1 + \frac{\nu_{12}}{1-\nu_{12}\nu_{21}}\varepsilon_2 \tag{8.2-5}$$

$$\bar{\varepsilon}_2 = \frac{\nu_{21}}{1-\nu_{12}\nu_{21}}\varepsilon_1 + \frac{1}{1-\nu_{12}\nu_{21}}\varepsilon_2 \tag{8.2-6}$$

Step 4: The tensile and compressive stresses in concrete, σ_1^c and σ_2^c, in the $1-2$ coordinate were obtained from the uniaxial strains $\bar{\varepsilon}_2$ and $\bar{\varepsilon}_1$, respectively, using the constitutive laws of prestressed concrete developed in Section 6.2.3 (Part I, Chapter 6).

Step 5: The shear modulus of concrete was obtained using Eq. 6.2-21:

$$G = \frac{\sigma_1^c - \sigma_2^c}{2\left(\varepsilon_1 - \varepsilon_2\right)} \tag{8.2-7}$$

Step 6: The shear stress in concrete along the failure plane, τ_{12}^{c}, was obtained by multiplying the shear modulus of concrete G (obtained in Step 5) by the shear strain γ_{12} along the failure plane (obtained in Step 2, Eq. 8.2-4).

Step 7: The shear force S along the failure plane was obtained by multiplying the shear stress τ_{12}^{c} by the inclined area of the concrete section along the failure plane.

Step 8: Using the equlibirum relation shown in Eq. 8.2-8, the shear capacity of the beam, V, was calculated as:

$$V = \frac{S - T\sin\alpha_1}{\cos\alpha_1} + \sum F_V \qquad (8.2\text{-}8)$$

where

$\sum F_V$ = summation of forces in the stirrups lying on the failure plane at the ultimate load of the beams. The forces in each stirrup lying on the failure plane can be calculated from the ultimate strains in the stirrups obtained from the strain gages glued on the stirrups. Using the stress-strain relationship of the stirrup rebars, the steel stresses corresponding to the recorded strains can be obtained. Then multiplying the stresses by the cross sectional area of the stirrups gives the individual stirrup forces.

T = tensile force in the prestressing tendons at the ultimate load of the beams. For different beams T was calculated from flexural analysis corresponding to the ultimate moment developed at the loading sections of the beams.

In order to check the validity of the analytical model for shear, the angle of failure plane α_1, defined by its normal, was determined from the equilibrium equation (8.2-8). Using the eight-step procedure described above, the ultimate load of a beam could be calculated by assuming an angle of failure planes. Using an iteration procedure, the angle of failure plane was changed till the calculated ultimate load was close to the experimental capacity of the beam. The above mentioned calculation was done for both ends of Beams B1 and B2. However only the north ends of Beam B3 could be tested up to the ultimate load. Hence, only the failed ends of Beam B3 were included in the calculation.

Table 8.2.1 shows the values of the angles of failure planes for Beams B1 to B3, along with other forces that developed at the ultimate stage of the beams to maintain equilibrium with the external shear loads, as per the analytical model being used here. It can be seen from Table 8.2.1 that the variation of the angle of failure plane with the ultimate load did not follow any specific trend. Hence, it was decided to correlate between the angle of the failure plane with the shear capacity of the beam contributed by the concrete and steel as presented in Section 8.2.2.

Table 8.2.1 Angles of Failure Planes Corresponding to Beam Shear Capacities as per Model

Beam	α_1 (deg)	γ_{12} (x 10^{-6})	G (ksi)	τ_{12}^c (ksi)	A_{incl} (in^2)	S (kips)	T (kips)	$\sum F_V$ (kips)	V_{cal} (kips)	V_{exp} (kips)	$\frac{V_{exp}}{V_{cal}}$
B1 N	42.1	1000	369	0.37	411.7	152.3	34.1	16.0	190.4	188.9	0.992
B1 S	37.0	936	324	0.30	458.6	139.2	22.4	17.4	174.8	173.5	0.993
B2 N	38.2	1228	210	0.26	446.3	115.2	43.5	88.2	200.5	201.1	1.003
B2 S	33.6	974	343	0.33	498.7	166.7	77.0	85.1	234.0	234.0	1.000
B3 N	34.2	944	362	0.34	491.0	167.9	71.6	67.9	228.0	228.0	1.000

Beams B4 and B5 failing in flexural shear are not included in Table 8.2.1. This is because their actual failure surface did not extend all the way from the top to the bottom of these beams. A failure surface actually consisted of a vertical crack at the bottom, joined by an inclined crack at the top. Hence, the total area of the inclined failure plane is not effective in contributing to the shear resistance of these beams as assumed in the shear analysis.

8.2.2 V_c and V_s Terms in the Analytical Model

The term $\frac{S - T\sin\alpha_1}{\cos\alpha_1}$ in Eq. (8.2-8) is the "contribution of concrete in shear," V_c. The variation of the normalized concrete shear, $\frac{V_c}{\sqrt{f_c'}A}$, with the angle of the failure plane was studied for Beams B1 to B3. Table 8.2.2 shows the calculated values of normalized shear capacities of these three beams using the angles of failure planes obtained in Table 8.2.1. The correlation between the normalized shear capacities and the angles of failure planes is shown in Fig 8.2.2. From the trend-line of the variation it was observed that the normalized concrete shear remained essentially constant for the various angles of failure planes. Hence, it was decided not to include the angle of failure plane in the V_c term for the design equation to be developed from this research.

In Eq. (8.2-8) the "contribution of steel in shear," V_s, is equal to $\sum F_V$. For this term no specific trend could be observed in the variation of stirrup forces with the angle of failure. Hence, it was decided to follow Loov's "minimum shear resistance" method to determine the number of stirrups intersecting the failure plane, $\sum F_V$. Instead of locating a 45º crack to obtain an average number of stirrups, d/s, as shown in Fig. 8.2.3(a), Loov's "minimum shear resistance" method gives the number of stirrups as (d/s – 1), as shown in Fig. 8.2.3(b). Hence, the V_s term in the proposed design equation was expressed as:

$$V_s = A_v f_y \left(\frac{d}{s} - 1\right) \tag{8.2-9}$$

Based on the above discussions of the V_c and V_s terms in the analytical model, a new and simple design equation for shear was developed and is presented in Chapter 9.

Table 8.2.2 Normalized Concrete Shear Contributions of Beams B1 through B3

Beam	α_1	f_c' (psi)	$\sqrt{f_c'}$ **(psi)**	**S (kips)**	**T (kips)**	V_s **(kips)**	V_p **(kips)**	V_c **(kips)**	$\frac{V_c}{\sqrt{f_c'}A}$
B1N	42.1	10,500	102.5	152.3	34.1	16.0	0	174.5	6.17
B1S	37.0	10,500	102.5	139.2	22.4	17.4	0	157.4	5.57
B2N	38.2	10,840	104.1	115.2	43.5	88.2	0	112.4	3.91
B2S	33.6	10,840	104.1	166.7	77.0	85.1	0	149.0	5.18
B3N	34.2	9,370	96.8	167.9	71.6	67.9	5.8	154.3	5.78

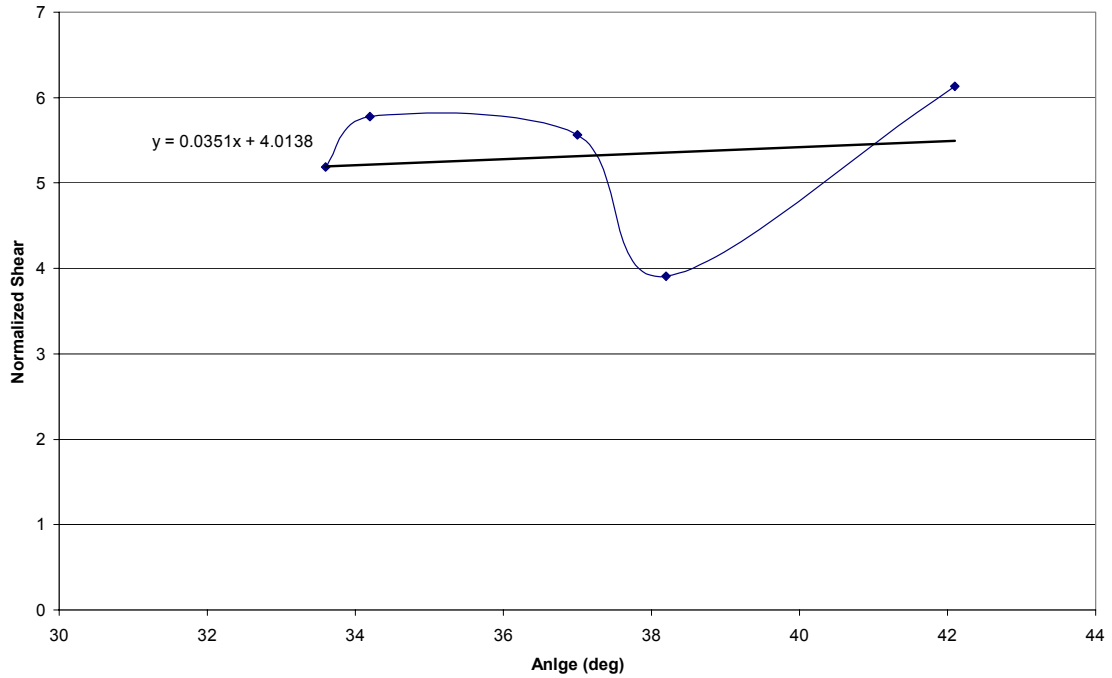

Fig 8.2.2 Variation of Normalized Concrete Shear of Beams Tested in Web Shear

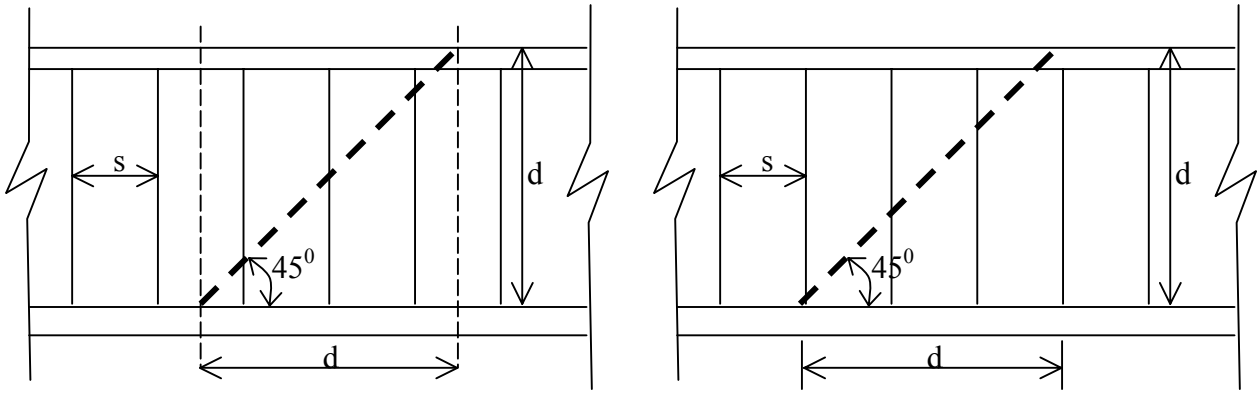

(a) Average Spacing Method (b) Minimum Shear Resistance Method

Fig. 8.2.3 Determination of Number of Stirrups for "Contribution of Steel" V_s

CHAPTER 9

SHEAR DESIGN OF PRESTRESSED BEAMS

9.1 Design Method

A new design method was developed at UH based on the test results reported in Chapter 7. It was found that the shear strength of prestressed beams is a function of the shear span to depth ratio, a/d, and it is not a function of the prestressing force, nor a function of the angle of failure plane. Based on the test results it was decided to implement the shear span to depth ratio (a/d) into the new design equation.

The amount of prestressing force in a prestressed beam did not have a significant effect on its ultimate shear capacity. A series of tests by Lyngberg (1976) specifically indicated the insignificant effect of prestressing force on the ultimate shear capacity of prestressed beams. Tests by Elzanaty and Rangan also had small variations in prestressing forces without any observable variation in the ultimate shear capacities of their beam specimens. Based on these test results it was decided not to include the prestressing force in the new design equation to be developed in this research.

In the case of web-shear failure (B1, B2, and B3), Section 8.2 showed that the concrete contribution to shear, V_c, does not vary significantly with the angle of failure plane. The ultimate strengths of these beams also showed that the steel contribution, V_s, was not strongly effected by the angle of failure plane. In the case of flexural-shear failure (B4 and B5), it is not logical to calculate V_s using the number of stirrups intersecting a failure plane, because the actual failure surface did not extend all the way from the top to the bottom of the beam. A failure surface actually consisted of a vertical crack at the bottom, joined by an inclined crack at the top. Only the stirrups intersecting the top inclined crack would be effective in resisting shear. Hence, it was decided not to include the angle of failure plane in the V_c as well as the V_s parts of the design equation.

The UH observations were supported by three groups of tests in literature. The first group of tests was conducted by Lyngberg (1976) at the University of Denmark. Fig. 9.1.1(a) and (b) shows the cross section and the elevation of a typical Danish specimen. Nine beams were tested, in which the major variable was the intensity of prestress. The cross section, web reinforcement, flexural ultimate moment, and shear span were held constant. The results showed that the shear strength was not influenced by the presence of prestress. The Danish tests also provided another important observation when compared to the UH test specimens. The two groups of test specimens were similar in size and shape, except that the Danish specimens had wide flanges and the UH specimens had narrow flanges. Since good agreement in shear strengths was observed between these two groups of tests, it was concluded that the top flange width was not a significant variable effecting the shear strength, and that the web region was the primary shear-resisting component.

The second group of tests was performed by Rangan (1991). Fig. 9.1.1(c) and (d) shows the cross section and the elevation of a typical specimen. The specimens in these tests were designed with high amounts of steel so that the specimens would fail in web crushing. Hence, these tests were used to determine the upper limit of shear capacities to be specified along with the new design equation.

The third group of tests studied was by Elzanaty et al. (1986) at Cornell University. Specimens of small sizes (height of 14 in. and 18 in.) were used in these tests of flexural shear failures. Fig. 9.1.1(e) and (f) shows the cross section and elevation of a typical specimen tested by Elzanaty. These tests provide the trend of shear strengths as a function of a/d in the range of 3.8 to 5.8. However, the shear strength of these small specimens were found to be much higher than the predicted values based on the larger specimens of UH and Denmark. This is obviously due to size effect. The small size of the Cornell specimens also caused the bottom flange to be very large relative to the web. The large bottom flange will also contribute to the shear resistance of the beams.

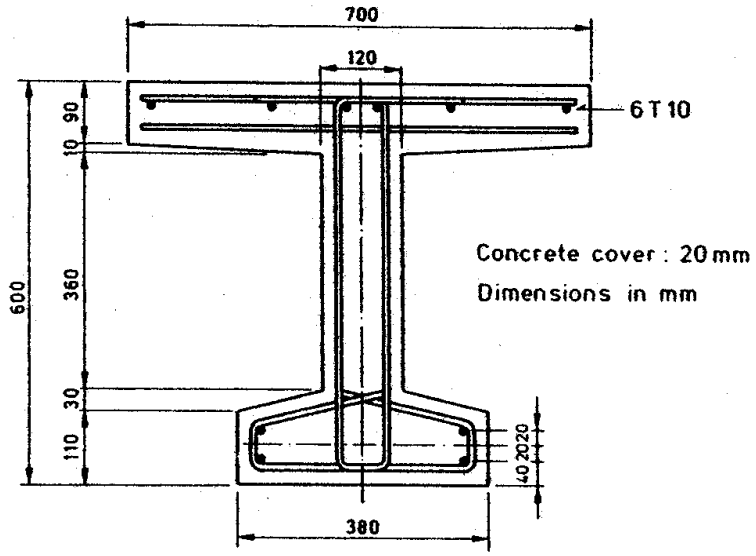

(a) Cross Section of Beams Tested by Lyngberg (1976)

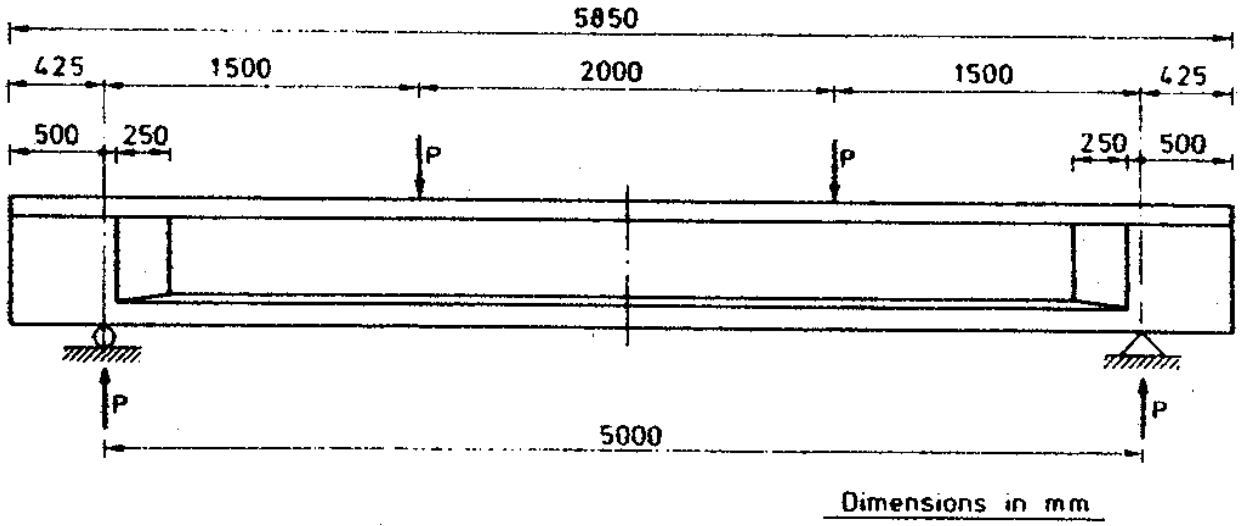

(b) Elevation of Beams Tested by Lyngberg (1976)

Fig. 9.1.1 Details of Beams Tested by Other Researchers

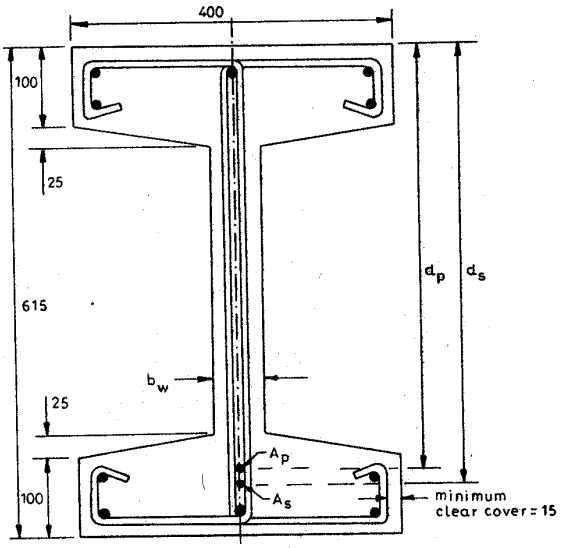

For clarity, detailed layout of longitudinal steel is not shown. Values of d_p, d_s, b_w, A_p and A_s are given in Table 1. All dimensions are in millimeters.

(c) Cross Section of Beams Tested by Rangan (1991)

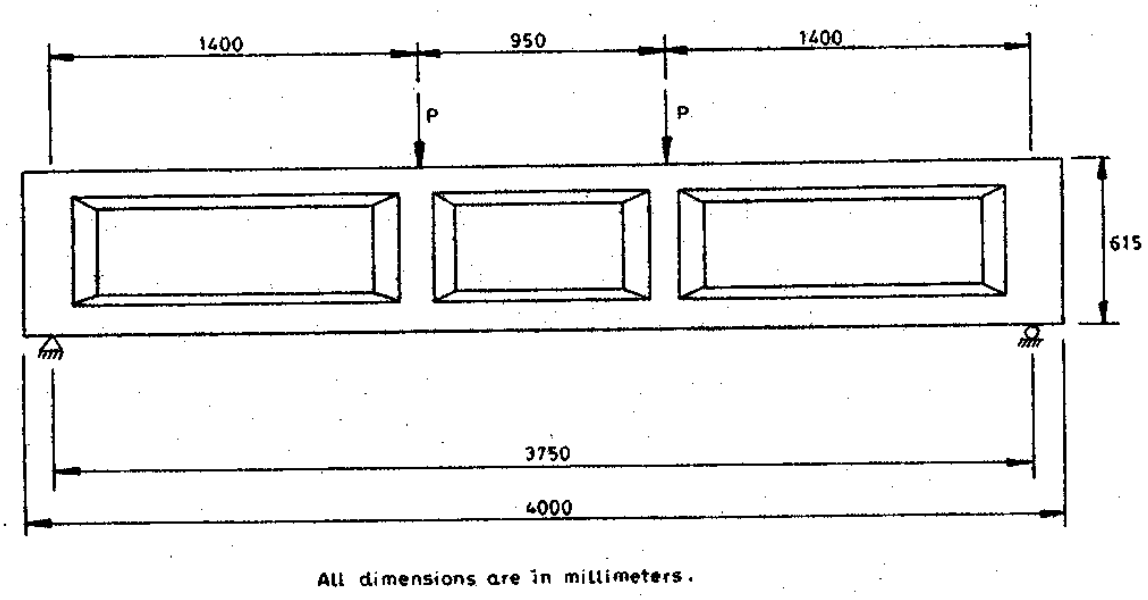

(d) Elevation of Beams Tested by Rangan (1991)

Fig. 9.1.1 Details of Beams Tested by Other Researchers (continued)

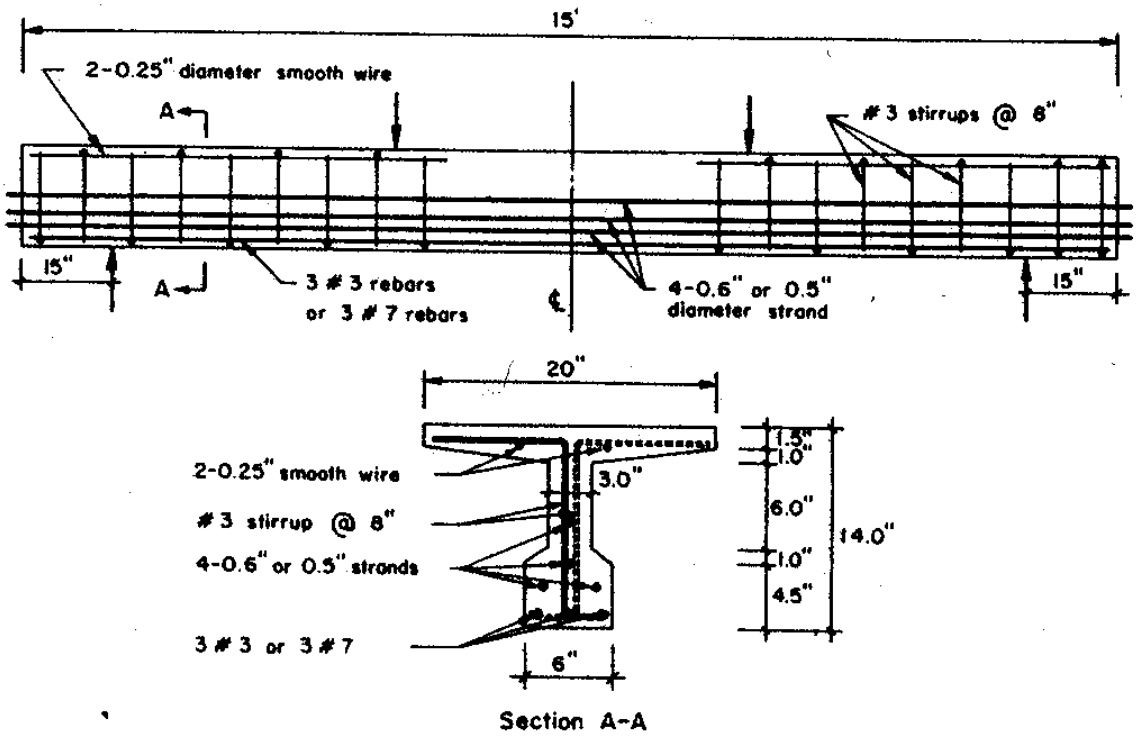

(e) Details of CI Specimens Tested by Elzanaty (1987)

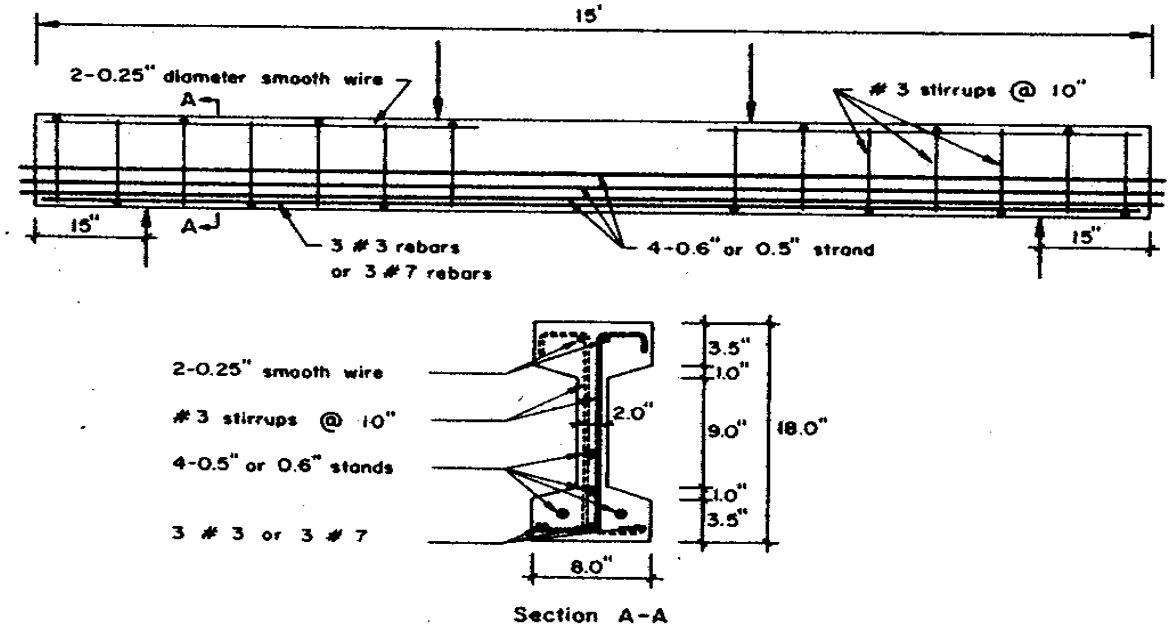

(f) Details of CW Specimens Tested by Elzanaty (1987)

Fig. 9.1.1 Details of Beams Tested by Other Researchers (continued)

To implement the parameter a/d into the design equation, the concrete shear contribution, V_c, of all the specimens were calculated by subtracting the steel contribution, V_s (calculated as per the proposed Eq. 8.2-9) from the total shear capacities of the beams. The normalized concrete shear, $\frac{V_c}{\sqrt{f_c'}\,b_w d}$ of the specimens was obtained thereafter and their variation with a/d was studied. The plot in Fig. 9.1.2 shows the variation of normalized concrete shear with a/d. Taking a conservative trend of the variation, it was observed that the a/d term could be implemented into the V_c part of the design equation as shown in Eq. 9.1-1.

$$V_c = \frac{14}{(a/d)^{0.7}}\sqrt{f_c'}\,b_w d \le 10\sqrt{f_c'}\,b_w d \qquad (9.1\text{-}1)$$

where

b_w = width of the web of the prestressed beam, and

d = depth of the c.g.s of the tendons from the top compression fiber of the prestressed beam. The value of d is not taken to be less than 80% of the total depth of the beam.

V_c should not be greater than $10\sqrt{f_c'}\,b_w d$.

The final design equation for shear capacity of prestressed concrete is shown in Eq. 9.1-2.

$$V_u = \frac{14}{(a/d)^{0.7}}\sqrt{f_c'}\,b_w d + A_v f_y\left(\frac{d}{s} - 1\right) \qquad (9.1\text{-}2)$$

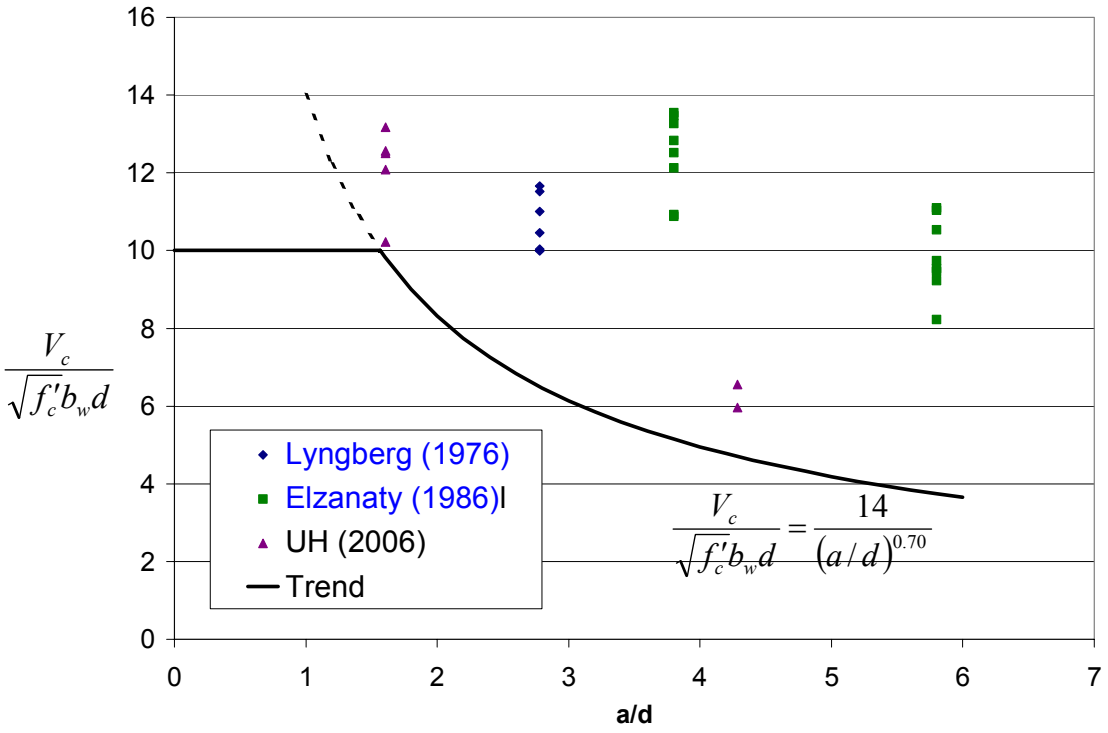

Fig 9.1.2 Variation of Normalized Concrete Shear with a/d

In order to determine the upper limit of the shear capacities for prestressed concrete beams over reinforced in shear, a plot of $\frac{V_u}{\sqrt{f_c'}\,b_w d}$ against a/d was made for all the prestressed concrete beam specimens (Fig. 9.1.3). From the plot it was observed that all specimens tested by Rangan had a $\frac{V_u}{\sqrt{f_c'}\,b_w d}$ value of 18 and above. All these specimens were over-reinforced and failed due to web crushing.

In view of the fact that the actual beams used in highways could be larger than those tested by Rangan, it was decided to choose an upper limit more conservative than the $\frac{V_u}{\sqrt{f_c'}\,b_w d}$ of Rangan's specimens. As a result, the ultimate shear strength of concrete was limited to $16\sqrt{f_c'}\,b_w d$.

For beams subjected to distributed loading, the shear span ratio a/d varies along the length of the beam. Therefore a/d must be generalized to become (M/Vd). In short, the ultimate shear capacity of the prestressed concrete beam can be taken as shown in Eq. 9.1-3.

$$V_u = 14\left(\frac{V_u d}{M_u}\right)^{0.7}\sqrt{f_c'}\,b_w d + A_v f_y\left(\frac{d}{s}-1\right) \le 16\sqrt{f_c'}\,b_w d \qquad (9.1\text{-}3)$$

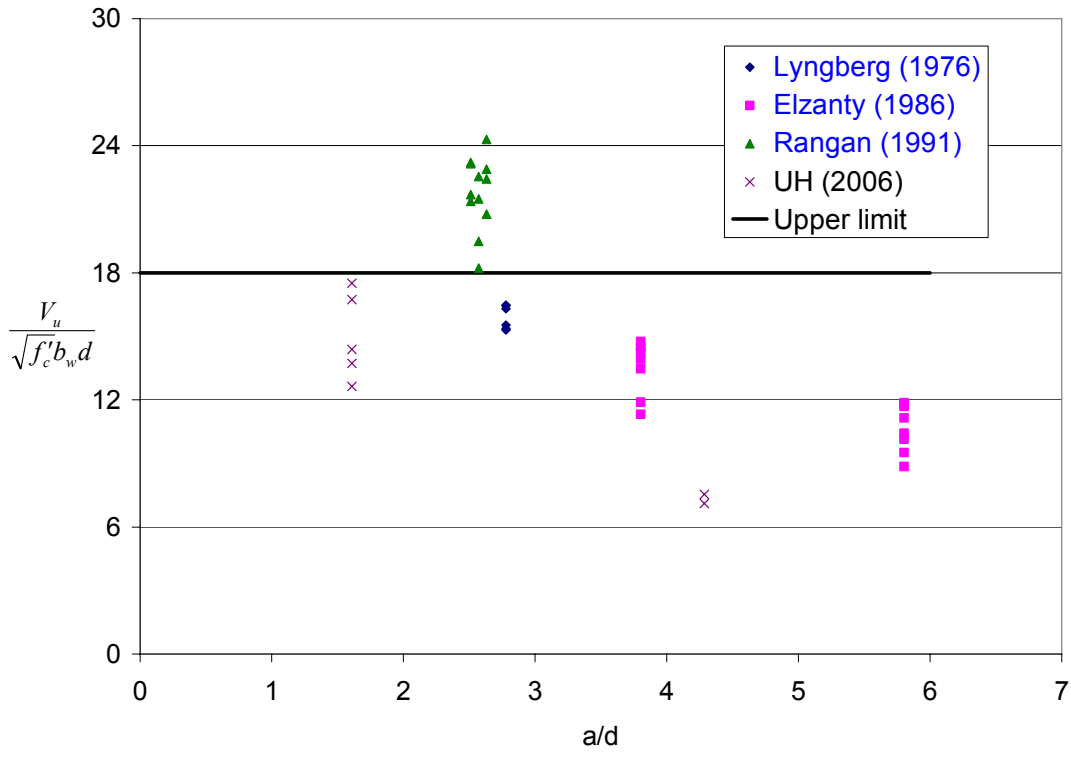

Fig 9.1.3 Variation of Normalized Ultimate Shear Capacities of Beams with a/d

9.2 Shear Capacities of Beams According to ACI and AASHTO Provisions

The shear capacities of all the beam specimens studied in Section 9.1 were also calculated according to the provisions of the ACI Building Code (2005) and the AASHTO Specifications (2004). The results obtained were compared to the shear capacities of the specimens calculated as per the design equations developed in Section 9.1. The results are shown in Tables 9.2.1 through 9.2.4. It can be seen that the proposed shear design equation is not only simple, but quite reasonable.

Table 9.2.4 shows that the results obtained from the new design equation are more conservative than the ones obtained from the ACI and AASHTO provisions. This is desirable because Elzanaty's test specimens were much smaller than the full-scale specimens tested in this project and those used in highway bridges. The relatively large bottom flange in Elzanaty's small specimens also exaggerated the experimental shear strengths.

Table 9.2.3 shows the upper limit of $V_{u,\max} = 16\sqrt{f_c'}b_w d$ is also very reasonable. It is less conservative than the ACI provisions, but safer than the AASHTO provisions. The AASHTO provisions are not sufficiently conservative for two reasons. Firstly, Rangan's specimens have stiffeners under the applied loads and near the failure zone (see Fig. 9.1.1(d)). These stiffeners would exaggerate the shear resistances. Second, beams used in highway bridges are likely to be larger than Rangan's test specimens, and the shear resistance would be lower due to size effect. In short, the upper limit $V_{u,\max}$ in the AASHTO Specifications is not recommended.

Table 9.2.1 Comparison of Test Results for UH Specimens

	V_{exp} (kips)	UH					ACI					AASHTO				
		V_c (kips)	V_s (kips)	V_p (kips)	V (kips)	$\frac{V_{exp}}{V_{cal}}$	V_c (kips)	V_s (kips)	V_p (kips)	V (kips)	$\frac{V_{exp}}{V_{cal}}$	V_c (kips)	V_s (kips)	V_p (kips)	V (kips)	$\frac{V_{exp}}{V_{cal}}$
B1	173.5	137.7	7.4	0	145.1	1.196	72.6	13.4	0	86.0	2.018	32.3	26.7	0	59.0	2.940
B2	201.1	139.9	52.8	0	192.7	1.044	73.3	80.6	0	139.9	1.437	30.9	118.0	0	148.9	1.351
B3	228.0	130.1	52.8	5.8	188.7	1.208	69.9	80.6	5.8	130.1	1.752	25.0	105.2	5.8	136.0	1.676
B4	96.8	69.0	7.4	0	76.4	1.267	59.8	13.4	0	73.2	1.322	46.5	40.7	0	87.2	1.109
B5	98.0	65.7	7.4	10.3	83.4	1.175	57.3	13.4	10.3	70.7	1.386	37.9	34.0	10.3	82.2	1.193

Table 9.2.2 Comparison of Test Results for Lyngberg's Specimens

	V_{exp} (kips)	UH					ACI					AASHTO				
		V_c (kips)	V_s (kips)	V_p (kips)	V (kips)	$\frac{V_{exp}}{V_{cal}}$	V_c (kips)	V_s (kips)	V_p (kips)	V (kips)	$\frac{V_{exp}}{V_{cal}}$	V_c (kips)	V_s (kips)	V_p (kips)	V (kips)	$\frac{V_{exp}}{V_{cal}}$
2A-3	113.8	47.3	31.3	0	78.6	1.448	41.5	47.2	0	69.1	1.647	13.6	73.9	0	87.5	1.300
2B-3	115.8	48.2	31.3	0	79.5	1.457	41.9	49.3	0	70.4	1.645	12.6	75.2	0	87.8	1.318
3A-2	109.9	46.2	31.3	0	77.5	1.418	33.7	50.8	0	67.5	1.628	10.5	72.6	0	83.1	1.323
3B-2	97.3	43.4	31.3	0	74.7	1.303	32.9	47.9	0	63.4	1.535	9.8	67.8	0	77.6	1.253
4A-1	105.4	46.5	32.6	0	79.1	1.332	23.5	49.0	0	67.9	1.552	9.9	66.2	0	76.1	1.387
4B-1	102.1	45.7	32.6	0	78.3	1.304	22.8	50.4	0	66.7	1.531	9.7	67.8	0	77.5	1.318

Table 9.2.3 Comparison of Test Results for Rangan's Specimens

	V_{exp} (kips)	UH					ACI					AASHTO				
		V_c (kips)	V_s (kips)	V_p (kips)	$V_{u,max}$ (kips) *	$\frac{V_{exp}}{V_{cal}}$	V_c (kips)	$V_{s,max}$ (kips) **	V_p (kips)	V (kips)	$\frac{V_{exp}}{V_{cal}}$	V_c (kips)	V_s (kips)	V_p (kips)	$V_{u,max}$ (kips) ***	$\frac{V_{exp}}{V_{cal}}$
II-1	103.6	32.8	62.6	0	71.4	1.451	22.4	35.7	0	44.6	2.323	6.5	92.7	0	82.8	1.251
II-2	85.2	27.0	104.2	0	58.8	1.448	19.5	29.4	0	36.8	2.315	5.5	157.2	0	55.0	1.550
II-3	110.0	37.2	62.6	0	81.1	1.356	25.2	40.6	0	50.7	2.170	7.3	92.6	0	93.5	1.176
II-4	107.8	37.1	104.2	0	80.7	1.336	25.2	40.4	0	50.5	2.135	7.3	153.6	0	91.1	1.183
III-1	82.7	30.7	61.2	0	67.9	1.218	24.6	34.0	0	42.5	1.946	7.4	100.2	0	73.1	1.131
III-2	87.8	29.5	101.8	0	65.3	1.345	24.0	32.7	0	40.8	2.152	6.2	156.0	0	67.1	1.308
III-3	89.1	35.4	61.2	0	78.3	1.138	28.1	39.1	0	48.9	1.822	7.5	94.3	0	83.0	1.074
III-4	101.8	32.7	101.8	0	72.3	1.408	26.2	36.1	0	45.2	2.252	6.9	156.0	0	74.2	1.372
IV-1	84.3	26.8	99.3	0	60.1	1.403	29.3	30.1	0	37.6	2.242	7.9	176.9	0	61.9	1.361
IV-2	75.9	26.0	59.7	0	58.5	1.297	29.4	29.3	0	36.6	2.074	7.8	112.3	0	56.1	1.353
IV-3	104.5	30.6	99.3	0	68.8	1.519	33.1	34.4	0	43.0	2.430	9.2	180.1	0	69.6	1.502
IV-4	87.8	27.3	59.7	0	61.4	1.430	31.5	30.7	0	38.4	2.286	8.0	110.3	0	54.0	1.627

* $V_{u,max} = 16\sqrt{f_c'}b_w d$

** $V_{s,max} = 8\sqrt{f_c'}b_w d$

*** $V_{u,max} = 0.25 f_c' b_w d_v;\ d_v \geq 0.72h$

Table 9.2.4 Comparison of Test Results for Elzanaty's Specimens

	V_{exp} (kips)	UH					ACI					AASHTO				
		V_c (kips)	V_s (kips)	V_p (kips)	V (kips)	$\frac{V_{exp}}{V_{cal}}$	V_c (kips)	V_s (kips)	V_p (kips)	V (kips)	$\frac{V_{exp}}{V_{cal}}$	V_c (kips)	V_s (kips)	V_p (kips)	V (kips)	$\frac{V_{exp}}{V_{cal}}$
CI-10	31.8	15.1	2.8	0	17.9	1.777	11.7	8.8	0	20.5	1.551	10.1	22.3	0	32.4	0.982
CI-11	28.6	13.2	2.8	0	16.0	1.788	11.0	8.8	0	19.8	1.444	8.0	20.8	0	28.8	0.994
CI-12	27.5	11.2	2.8	0	14.0	1.964	10.4	8.8	0	19.2	1.432	6.1	19.0	0	25.1	1.095
CI-13	34.8	15.1	2.8	0	17.9	1.944	14.4	8.8	0	23.2	1.500	9.3	21.7	0	31.0	1.123
CI-14	37.0	15.2	8.6	0	23.8	1.555	14.6	14.1	0	28.7	1.289	9.2	33.2	0	42.4	0.873
CI-15	27.2	14.8	2.8	0	17.6	1.545	11.6	8.8	0	20.4	1.333	9.9	22.3	0	32.2	0.845
CI-16	36.7	15.1	2.8	0	17.9	2.050	14.5	8.8	0	23.3	1.575	9.1	20.8	0	29.9	1.226
CI-17	29.1	14.8	1.3	0	16.1	1.807	14.4	4.0	0	18.4	1.582	10.3	10.6	0	20.9	1.395
CW-10	39.0	16.6	3.0	0	19.6	1.990	17.6	9.7	0	27.3	1.429	7.3	19.3	0	26.6	1.472
CW-11	35.2	14.5	3.0	0	17.5	2.011	16.1	9.7	0	25.8	1.364	6.2	18.8	0	25.0	1.408
CW-12	31.6	12.3	3.0	0	15.3	2.065	14.7	9.7	0	22.0	1.436	4.8	17.4	0	22.2	1.422
CW-13	41.0	16.6	3.0	0	19.6	2.092	20.2	9.7	0	29.6	1.385	7.4	20.8	0	28.2	1.452
CW-14	42.2	16.7	7.3	0	24.0	1.883	20.5	13.8	0	29.8	1.416	7.1	27.9	0	35.0	1.206
CW-15	33.8	16.3	3.0	0	19.3	1.751	17.3	9.7	0	27.0	1.252	7.3	20.0	0	27.3	1.240
CW-16	42.0	16.6	3.0	0	19.6	2.143	20.3	9.7	0	29.7	1.414	7.1	19.5	0	26.6	1.578
CW-17	32.0	16.2	1.4	0	17.6	1.818	20.1	4.4	0	24.5	1.306	7.8	10.1	0	17.9	1.793

9.3 Design Examples for Prestressed Beams

The use of the design equation developed as described in the previous section has been illustrated by four design examples in this section. TXDOT Type-A girders spaced at 8.67 ft c/c and supporting a 30 ft wide and 8 in. thick deck slab are considered. The design of a typical girder described above, using the new design equation, has been shown by varying different parameters in the following four examples.

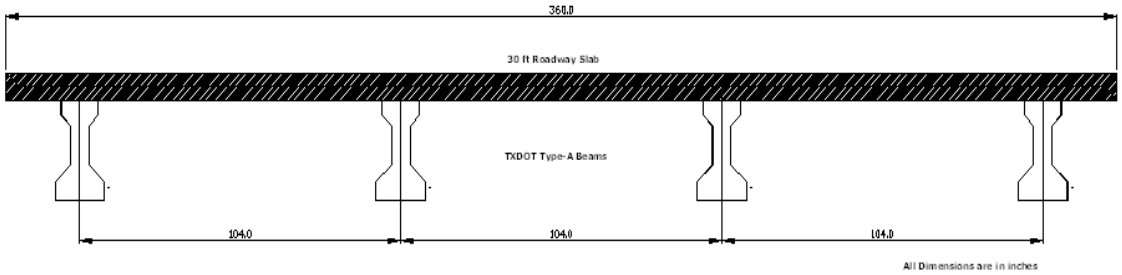

Fig. 9.3.1 Layout of Girders and Roadway Slab considered in Design Examples

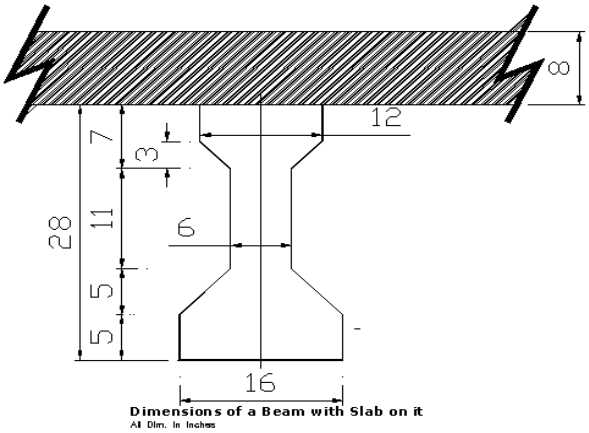

Fig. 9.3.2 Dimensional Details of Beam and Overlaying Slab

9.3.1 Example 1

The values of various quantities required for design are follows:

h = 28 in.	b_w = 6 in.	L_n = 24 ft	f_c' = 10 ksi
f_y = 60 ksi	A_v = 0.62 in.^{2}	d_{bv} = 5/8 in.	w_u = 24 kips/ft

Maximum moment on the girder, $M_u/\phi = \frac{1}{\phi}\frac{w_u l^2}{8} = \frac{24 \times 24^2}{0.9 \times 8} = 1920$ kip-ft

As per calculations for flexural capacities of prestressed concrete girders, provide 18 ½-in. low relaxation strands.

Distance of cg of beam cross section from top fiber = 15.41 in.

Eccentricity of tendons from cg = 8.39 in.

Thickness of deck slab = 8 in.

d = 15.41 + 8.39 + 8 = 31.8 in.

Assuming the critical section of the beam in shear to be at a distance d from the support,

Shear force at critical section of the beam $V_u = \left(\frac{w_u l}{2} - w_u d\right) = \left(\frac{24\times 24}{2} - 24\times\frac{31.8}{12}\right) = 224.4$ kips

Maximum shear capacity of the beam, $V_{u,max} = \phi 16\sqrt{f_c'}\, b_w d = 0.75\times 16\times\sqrt{10{,}000}\times 6\times 31.8$

$= 229.0$ kips > 224.4 kips (ok)

Given cross section is sufficient to resist shear.

The amount of steel required at the critical section of the beam has been shown below.

Factored shear force at the section, $V_u = \left(\frac{w_u l}{2} - w_u x\right) = \left(\frac{24\times 24}{2} - 24\times\frac{31.8}{12}\right) = 224.4$ kips

Factored moment at the section, $M_u = \left(\frac{w_u l}{2}x - \frac{w_u x^2}{2}\right) = \left(\frac{24\times 24}{2}\times\frac{31.8}{12} - \frac{24\times\left(\frac{31.8}{12}\right)^2}{2}\right)$

$= 678.9$ kip-ft

$$\frac{V_u d}{M_u} = \frac{224.4\times 31.8}{678.9\times 12} = 0.876$$

$$V_c = 14\left(\frac{V_u d}{M_u}\right)^{0.7}\sqrt{f_c'}\, b_w d = 14\times 0.876^{0.7}\times\sqrt{10{,}000}\times 6\times 31.8 = 243.5 \text{ kips}$$

Maximum concrete shear capacity of the beam, $V_{c,max} = 10\sqrt{f_c'}\, b_w d = 10\times\sqrt{10{,}000}\times 6\times 31.8$

$= 190.8$ kips < 243.5 kips

$V_s = V_u/\phi - V_c = 224.4/0.75 - 190.8 = 108.4$ kips

Using two-legged #5 rebars ($A_v = 0.62$ in^2) as shear reinforcement, the spacing required to provide the required V_s has been calculated using Eq. 8.2-9.

$$V_s = A_v f_y\left(\frac{d}{s} - 1\right)$$

$$\Rightarrow s = \frac{d}{\left(\frac{V_s}{A_v f_y} + 1\right)} = \frac{31.8}{\left(\frac{108.4}{0.62\times 60} + 1\right)} = 8.1 \text{ in.}$$

Provide two-legged #5 rebars @ 8 in. c/c.

The amount of steel required at a section of the beam 8 ft from the support has been calculated.

Factored shear force at the section, $V_u = \left(\frac{w_u l}{2} - w_u x\right) = \left(\frac{24\times 24}{2} - 18\times 8\right) = 96$ kips

Factored moment at the section, $M_u = \left(\frac{w_u l}{2}x - \frac{w_u x^2}{2}\right) = \left(\frac{18\times 24}{2}\times 8 - \frac{18\times 8^2}{2}\right) = 1536$ kip-ft

$$\frac{V_u d}{M_u} = \frac{96\times 31.8}{1536\times 12} = 0.166$$

$$V_c = 14\left(\frac{V_u d}{M_u}\right)^{0.7}\sqrt{f_c'}\,b_w d = 14\times 0.166^{0.7}\times\sqrt{10{,}000}\times 6\times 31.8 = 75.9 \text{ kips}$$

Maximum concrete shear capacity of the beam, $V_{c,max} = 10\sqrt{f_c'}\,b_w d = 10\times\sqrt{10{,}000}\times 6\times 31.8$

$= 190.8 \text{ kips} > 75.9 \text{ kips}$

$V_s = V_u/\phi - V_c = 96.0/0.75 - 75.9 = 52.1$ kips

Using two-legged #5 rebars (A_v = 0.62 in^2) as shear reinforcement, the spacing required to provide the required V_s has been calculated using Eq. 8.2-9.

$$V_s = A_v f_y\left(\frac{d}{s}-1\right)$$

$$\Rightarrow s = \frac{d}{\left(\frac{V_s}{A_v f_y}+1\right)} = \frac{31.8}{\left(\frac{52.1}{0.62\times 60}+1\right)} = 13.2 \text{ in.}$$

Provide two-legged #5 rebars @ 13 in. c/c.

Table 9.3.1 shows the design of the beam over half span of the beam. It can be seen that the spacing of the two-legged #5 rebars is 8 in. c/c up to a distance 7 ft from the support. At 8 ft from the support, the spacing is increased to 13 in. c/c.

Table 9.3.1 Beam Design 1

x (ft)	**V_u (kips)**	**M_u (kip-ft)**	$\frac{V_u d}{M_u}$	**V_c (kips)**	**V_s (kips)**	**s (#5) (in)**	**s_{prov} (in)**
d=2.65	224.4	678.9	0.876	190.8	108.4	8.1	8
3	216	756	0.757	190.8	97.2	8.8	8
4	192	960	0.530	171.3	84.7	9.7	8
5	168	1140	0.391	138.3	85.7	9.6	8
6	144	1296	0.294	113.5	78.5	10.2	8
7	120	1428	0.223	93.3	66.7	11.4	8
8	96	1536	0.166	75.9	52.1	13.2	13
9	72	1620	0.118	59.8	36.2	16.1	13
10	48	1680	0.076	43.9	20.1	20.6	13
11	24	1680	0.037	26.6	5.4	27.8	13
12	0	1716	-	-	-	-	13

9.3.2 Example 2

The above design example was repeated by using a uniformly distributed load of 12 kips/ft.

Maximum moment on the girder, $M_u/\phi = \frac{1}{\phi}\frac{w_u l^2}{8} = \frac{1}{0.9}\frac{12\times 24^2}{8} = 960$ kip-ft

As per calculations for flexural capacities of prestressed concrete girders, provide 8 ½-in. low relaxation strands.

Distance of cg of beam cross section from top fiber = 15.41 in.

Eccentricity of tendons from cg = 10.11 in.
Thickness of deck slab = 8 in.
d = 15.41 + 10.11 + 8 = 33.52 in.
Assuming the critical section of the beam in shear to be at a distance d from the support,

Shear force at critical section of the beam $V_u = \left(\frac{w_u l}{2} - w_u d\right) = \left(\frac{12\times 24}{2} - 12\times\frac{33.52}{12}\right) = 110.5$ kips

Maximum shear capacity of the beam, $V_{u,max} = \phi 16\sqrt{f_c'}\, b_w d = 0.75\times 16\times\sqrt{10{,}000}\times 6\times 33.52$
$= 241.3$ kips > 110.5 kips (ok)

Given cross section is sufficient to resist shear.
The amount of steel required at a section of the beam 5 ft from the support has been shown below.

Factored shear force at the section, $V_u = \left(\frac{w_u l}{2} - w_u x\right) = \left(\frac{12\times 24}{2} - 12\times 5\right) = 84$ kips

Factored moment at the section, $M_u = \left(\frac{w_u l}{2}x - \frac{w_u x^2}{2}\right) = \left(\frac{12\times 24}{2}\times 5 - \frac{12\times 5^2}{2}\right) = 570$ kip-ft

$$\frac{V_u d}{M_u} = \frac{84\times 33.52}{570\times 12} = 0.412$$

$$V_c = 14\left(\frac{V_u d}{M_u}\right)^{0.7}\sqrt{f_c'}\, b_w d = 14\times 0.412^{0.7}\times\sqrt{10{,}000}\times 6\times 33.52 = 151.3 \text{ kips}$$

Maximum concrete shear capacity of the beam, $V_{c,max} = 10\sqrt{f_c'}\, b_w d = 10\times\sqrt{10{,}000}\times 6\times 33.52$
$= 201.1$kips > 151.3 kips

$V_s = V_u/\phi - V_c = 84.0/0.75 - 151.3 = -39.3$ kips (no steel required)
Hence, provide minimum amount of stirrups as per the ACI Code (2005).
Using Eq. 11-14 of ACI code (2005)

$$A_{v,\min} = \frac{A_{ps} f_{pu}}{80 f_y}\frac{s}{d}\sqrt{\frac{d}{b_w}}$$

$$\Rightarrow \frac{A_{v,\min}}{b_w s} = \frac{A_{ps} f_{pu}}{80 f_y}\frac{1}{b_w d}\sqrt{\frac{d}{b_w}}$$

$$\Rightarrow \rho_w = \frac{(12\times 0.153)(270)}{80(60)(134)}\sqrt{\frac{23.13}{6}} = 0.00151$$

Using Eq. 11-3 of ACI (2005)

$$A_{v,\min} = 0.75\sqrt{f_c'}\frac{b_w s}{f_y}$$

$$\Rightarrow \frac{A_{v,\min}}{b_w s} = \frac{0.75\sqrt{f_c'}}{f_y}$$

$$\Rightarrow \rho_w = \frac{0.75 \times \sqrt{10{,}000}}{60{,}000} = 0.00125$$

Hence use two-legged #2 rebars 10 inches c/c or two-legged #3 rebars @ 20 inches c/c for minimum steel ($\rho_w = 0.17$)

The amount of steel required at a section of the beam 8 ft from the support has been calculated.

Factored shear force at the section, $V_u = \left(\frac{w_u l}{2} - w_u x\right) = \left(\frac{12 \times 24}{2} - 12 \times 8\right) = 48.0$ kips

Factored moment at the section, $M_u = \left(\frac{w_u l}{2} x - \frac{w_u x^2}{2}\right) = \left(\frac{12 \times 24}{2} \times 8 - \frac{12 \times 8^2}{2}\right) = 768$ kip-ft

$$\frac{V_u d}{M_u} = \frac{48 \times 33.52}{768 \times 12} = 0.175$$

$$V_c = 14\left(\frac{V_u d}{M_u}\right)^{0.7} \sqrt{f_c'}\, b_w d = 14 \times 0.175^{0.7} \times \sqrt{10{,}000} \times 6 \times 33.52 = 83.0 \text{ kips}$$

Maximum concrete shear capacity of the beam, $V_{c,max} = 10\sqrt{f_c'}\, b_w d = 10 \times \sqrt{10{,}000} \times 6 \times 33.52$

$= 201.1 \text{kips} > 83.0$ kips

$V_s = V_u/\phi - V_c = 48.0/0.75 - 83.0 = -19.0$ kips (no steel required)

Hence provide minimum amount of stirrups in this case also as calculated for the section at 4 ft from the support. Use two-legged #2 rebars 10 inches c/c or two-legged #3 rebars @ 20 inches c/c for minimum steel ($\rho_w = 0.17$).

Table 9.3.2 shows the concrete shear resistance at different sections along half span of the beam. It can be seen that the concrete shear is greater than the shear force at all sections and no stirrups are required at any section of the beam. Hence, minimum stirrups have been provided throughout

Table 9.3.2 Beam Design 2

x (ft)	**V_u (kips)**	**M_u (kip-ft)**	$\frac{V_u d}{M_u}$	**V_c (kips)**	**V_s (kips)**	**s (#3) (in)**	**s_{prov} (in)**
d=2.8	110.5	355.4	0.868	201.1	-	-	20
3	108	378	0.798	201.1	-	-	20
4	96	480	0.559	187.3	-	-	20
5	84	570	0.412	151.3	-	-	20
6	72	648	0.310	124.1	-	-	20
7	60	714	0.235	102.1	-	-	20
8	48	768	0.175	83.0	-	-	20
9	36	810	0.124	65.4	-	-	20
10	24	840	0.080	48.0	-	-	20
11	12	858	0.039	29.1	-	-	20
12	0	864	-	-	-	-	20

9.3.3 Example 3

The beam designed in Example 1 has been redesigned by increasing its span to 40 ft, and changing the load of 9 kips/ft.

Maximum moment on the girder, $M_u = \frac{1}{\phi}\frac{w_u l^2}{8} = \frac{1}{0.9}\frac{9\times 40^2}{8} = 2000$ kip-ft

As per calculations for flexural capacities of prestressed concrete girders, provide 18 ½-in. low relaxation strands.

Distance of cg of beam cross section from top fiber = 15.41 in.

Eccentricity of tendons from cg = 8.39 in.

Thickness of deck slab = 8 in.

d = 15.41 + 8.39 + 8 = 31.8 in.

Assuming the critical section of the beam in shear to be at a distance d from the support,

Shear force at critical section of the beam $V_u = \left(\frac{w_u l}{2} - w_u d\right) = \left(\frac{9\times 40}{2} - 9\times\frac{31.8}{12}\right) = 156.2$ kips

Maximum shear capacity of the beam, $V_{u,max} = \phi 16\sqrt{f_c'}\, b_w d = 0.75\times 16\times\sqrt{10{,}000}\times 6\times 31.8$

$= 229.0$ kips > 156.2 kips (ok)

Given cross section is sufficient to resist shear.

The amount of steel required at a section of the beam 8 ft from the support has been shown below.

Factored shear force at the section, $V_u = \left(\frac{w_u l}{2} - w_u x\right) = \left(\frac{9\times 40}{2} - 9\times 8\right) = 108$ kips

Factored moment at the section, $M_u = \left(\frac{w_u l}{2}x - \frac{w_u x^2}{2}\right) = \left(\frac{9\times 40}{2}\times 8 - \frac{9\times 8^2}{2}\right) = 1152$ kip-ft

$$\frac{V_u d}{M_u} = \frac{108\times 31.8}{1152\times 12} = 0.248$$

$$V_c = 14\left(\frac{V_u d}{M_u}\right)^{0.7}\sqrt{f_c'}\, b_w d = 14\times 0.248^{0.7}\times\sqrt{10{,}000}\times 6\times 31.8 = 100.8 \text{ kips}$$

Maximum concrete shear capacity of the beam, $V_{c,max} = 10\sqrt{f_c'}\, b_w d = 10\times\sqrt{10{,}000}\times 6\times 31.8$

$= 190.8$ kips > 100.8 kips

$V_s = V_u/\phi - V_c = 108/0.75 - 100.8 = 43.2$ kips

Using two-legged #4 rebars ($A_v = 0.4$ in^2) as shear reinforcement, the spacing required to provide the required V_s has been calculated using Eq. 8.2-9.

$$V_s = A_v f_y\left(\frac{d}{s} - 1\right)$$

$$\Rightarrow s = \frac{d}{\left(\frac{V_s}{A_v f_y} + 1\right)} = \frac{31.8}{\left(\frac{43.2}{0.4\times 60} + 1\right)} = 11.4 \text{ in.}$$

Provide two-legged #4 rebars @ 11 in. c/c.

The amount of steel required at a section of the beam 16 ft from the support has been calculated.

Factored shear force at the section, $V_u = \left(\frac{w_u l}{2} - w_u x\right) = \left(\frac{9\times 40}{2} - 9\times 16\right) = 36$ kips

Factored moment at the section, $M_u = \left(\frac{w_u l}{2} x - \frac{w_u x^2}{2}\right) = \left(\frac{9\times 40}{2}\times 16 - \frac{9\times 16^2}{2}\right) = 1728$ kip-ft

$$\frac{V_u d}{M_u} = \frac{36\times 31.8}{1728\times 12} = 0.055$$

$$V_c = 14\left(\frac{V_u d}{M_u}\right)^{0.7}\sqrt{f_c'}\, b_w d = 14\times 0.055^{0.7}\times\sqrt{10{,}000}\times 6\times 31.8 = 35.2 \text{ kips}$$

Maximum concrete shear capacity of the beam, $V_{c,max} = 10\sqrt{f_c'}\, b_w d = 10\times\sqrt{10{,}000}\times 6\times 31.8$

$= 190.8$ kips > 35.2 kips

$V_s = V_u/\phi - V_c = 36/0.75 - 35.2 = 12.8$ kips

Using two-legged #4 rebars ($A_v = 0.4$ in^2) as shear reinforcement, the spacing required to provide the required V_s has been calculated using Eq. 8.2-9.

$$V_s = A_v f_y\left(\frac{d}{s} - 1\right)$$

$$\Rightarrow s = \frac{d}{\left(\frac{V_s}{A_v f_y} + 1\right)} = \frac{31.8}{\left(\frac{12.8}{0.4\times 60} + 1\right)} = 20.7 \text{ in.}$$

Provide two-legged #4 rebars @ 20 in. c/c.

Table 9.3.3 shows the design of the beam over half span of the beam. It can be seen that with the increase of beam span the $\frac{V_u d}{M_u}$ values are lower than the ones obtained in Example 1. This in turn gives lower values of concrete shear resistance in comparison to Example 1. However, since the value of distributed load applied in this case is less than half of what is applied in Example 1, the shear resistance required at any section is much lower. Hence, the amount of transverse steel required is lower even though the concrete contribution is lower.

Table 9.3.3 Beam Design 3

x (ft)	V_u (kips)	M_u (kip-ft)	$\frac{V_u d}{M_u}$	V_c (kips)	V_s (kips)	s (#4) (in)	s_{prov} (in)
d=2.65	156.2	445.4	0.929	190.8	25.2	18.4	11
4	144	648	0.589	184.4	7.6	24.1	11
6	126	918	0.364	131.6	36.4	12.6	11
8	108	1152	0.248	100.8	43.2	11.4	11
10	90	1350	0.177	79.4	40.6	11.8	11
12	72	1512	0.126	62.7	33.3	13.2	13
14	54	1638	0.087	48.5	23.5	16.1	13
16	36	1728	0.055	35.2	12.8	20.7	20
18	18	1782	0.027	21.2	2.8	28.5	20
20	0	1800	-	-	-	-	20

9.3.4 Example 4

The beam in Example 3 has been redesigned by reducing the uniformly distributed load acting on it to 6 kips/ft.

Maximum moment on the girder, $M_u/\phi = \frac{1}{\phi}\frac{w_u l^2}{8} = \frac{1}{0.9}\frac{6\times 40^2}{8} = 1333$ kip-ft.

As per calculations for flexural capacities of prestressed concrete girders, provide 10 ½-in. low relaxation strands.

Distance of cg of beam cross section from top fiber = 15.41 in.

Eccentricity of tendons from cg = 9.81 in.

Thickness of deck slab = 8 in.

d = 15.41 + 9.81 + 8 = 33.22 in.

Assuming the critical section of the beam in shear to be at a distance d from the support,

Shear force at critical section of the beam $V_u = \left(\frac{w_u l}{2} - w_u d\right) = \left(\frac{6\times 40}{2} - 6\times\frac{33.22}{12}\right) = 103.4$ kips

Maximum shear capacity of the beam, $V_{u,max} = \phi 16\sqrt{f_c'}\, b_w d = 0.75\times 16\times\sqrt{10{,}000}\times 6\times 33.22$

$= 239.2$ kips > 103.4 kips (ok)

Given cross section is sufficient to resist shear.

The amount of steel required at a section of the beam 10 ft from the support has been shown below.

Factored shear force at the section, $V_u = \left(\frac{w_u l}{2} - w_u x\right) = \left(\frac{6\times 40}{2} - 6\times 10\right) = 60$ kips

Factored moment at the section, $M_u = \left(\frac{w_u l}{2}x - \frac{w_u x^2}{2}\right) = \left(\frac{6\times 40}{2}\times 10 - \frac{6\times 10^2}{2}\right) = 900$ kip-ft

$\frac{V_u d}{M_u} = \frac{60\times 33.22}{900\times 12} = 0.185$

$$V_c = 14\left(\frac{V_u d}{M_u}\right)^{0.7}\sqrt{f_c'}\,b_w d = 14\times 0.185^{0.7}\times\sqrt{10{,}000}\times 6\times 33.22 = 85.5 \text{ kips}$$

Maximum concrete shear capacity of the beam, $V_{c,max} = 10\sqrt{f_c'}\,b_w d = 010\times\sqrt{10{,}000}\times 6\times 33.22$
$= 199.3 \text{ kips} > 85.5 \text{ kips}$

$V_s = V_u/\phi - V_c = 60.0/0.75 - 85.5 = -5.5$ kips (no steel required)
Hence, provide minimum amount of stirrups in this case also as calculated for Example 2.
Use two-legged #2 rebars 10 inches c/c or two-legged #3 rebars @ 20 in. c/c for minimum steel ($\rho_w = 0.17$)
The amount of steel required at a section of the beam 16 ft from the support has been calculated.

Factored shear force at the section, $V_u = \left(\frac{w_u l}{2} - w_u x\right) = \left(\frac{6\times 40}{2} - 6\times 16\right) = 24$ kips

Factored moment at the section, $M_u = \left(\frac{w_u l}{2}x - \frac{w_u x^2}{2}\right) = \left(\frac{6\times 40}{2}\times 16 - \frac{6\times 16^2}{2}\right) = 1152$ kip-ft

$$\frac{V_u d}{M_u} = \frac{24\times 33.22}{1152\times 12} = 0.058$$

$$V_c = 14\left(\frac{V_u d}{M_u}\right)^{0.7}\sqrt{f_c'}\,b_w d = 14\times 0.058^{0.7}\times\sqrt{10{,}000}\times 6\times 33.22 = 37.9 \text{ kips}$$

Maximum concrete shear capacity of the beam, $V_{c,max} = 10\sqrt{f_c'}\,b_w d = 010\times\sqrt{10{,}000}\times 6\times 33.22$
$= 199.3 \text{ kips} > 37.9 \text{ kips}$

$V_s = V_u/\phi - V_c = 24.0/0.75 - 37.9 = -5.9$ kips (no steel required)
Hence, provide minimum amount of stirrups in this case also as calculated for Example 2. Use two-legged #2 rebars 10 in. c/c or 2 legged #3 rebars @ 20 in. c/c for minimum steel ($\rho_w = 0.17$)

Table 9.3.4 shows the design of the beam over half span of the beam. It can be seen that with after reducing the load to half the value, no stirrups are required in this case also (similar to Example 2). Hence, provide minimum stirrups.

Table 9.3.4 Beam Design 4

x (ft)	V_u (kips)	M_u (kip-ft)	$\frac{M_u}{V_u d}$	V_c (kips)	V_s (kips)	s (#3) (in)	s_{prov} (in)
d=2.77	103.4	309.2	0.926	199.3	-	-	20
4	96	432	0.615	198.6	-	-	20
6	84	612	0.380	141.7	-	-	20
8	72	768	0.260	108.5	-	-	20
10	60	900	0.185	85.5	-	-	20
12	48	1008	0.132	67.6	-	-	20
14	36	1092	0.091	52.2	-	-	20
16	24	1152	0.058	37.9	-	-	20
18	12	1188	0.028	22.8	-	-	20
20	0	1200	-	-	-	-	20

9.4 Shear Design of Non-Prestressed Beams

The design equation proposed in Section 6.1 can be extended to reinforced concrete structures by implementing a factor K_r into the concrete contribution to the shear capacity, to take into account the absence of prestressing effect. A value of $K_r = 0.4$ was chosen to be used in design. However the upper limits of shear capacities of reinforced concrete structures is not as high as prestressed concrete structures. Hence, following the provisions of the ACI code (2005) it was decided to restrict the upper limit of shear capacities to $10\sqrt{f_c'}\,b_w d$. The upper limit of concrete contribution to the shear, however, has been taken as $4\sqrt{f_c'}\,b_w d$. Hence, Eq. 9.4-1 gives the new design equation for non-prestressed structures. The application of this design equation has been illustrated through an example problem in Section 9.4.1.

$$V_u = V_c + V_s \le 10\sqrt{f_c'}\,b_w d \qquad (9.4\text{-}1)$$

$$V_c = 14K_r\left(\frac{V_u d}{M_u}\right)^{0.7}\sqrt{f_c'}\,b_w d \le 4\sqrt{f_c'}\,b_w d \qquad (9.4\text{-}2)$$

$K_r = 0.4$

$$V_s = A_v f_y\left(\frac{d}{s} - 1\right) \qquad (9.4\text{-}3)$$

9.4.1 Design Example for Non-Prestressed T-Beam

The following problem has been considered to show application of new design equation for non-prestressed members:

An isolated T-beam has an effective span of 25 ft and carries a factored load of 18 kips/ft. Other properties of the beam are as follows:

h = 30 in. b_f = 40 in. h_f = 5 in.

b_w = 15 in. d = 26 in. f_c' = 7 ksi

f_y = 60 ksi

Maximum moment on the girder, $M_u/\phi = \frac{1}{\phi}\frac{w_u l^2}{8} = \frac{1}{0.9}\frac{18\times 25^2}{8} = 1562.5$ kip-ft

Using the compressive stress-strain relations given in the ACI code (2005) and assuming the NA lies in the flange:

$$0.85 f_c' ba\left(d - \frac{a}{2}\right) = M_u,$$

where a = depth over which the compressive stresses exist in the cross section.

Substituting the numerical values of all other parameter in the above equation, the value of a can be obtained:

$a = 3.23$ in.

Equating the compressive and steel forces we get:

$$A_s f_y = 0.85 f_c' ba$$

$$\Rightarrow A_s = \frac{0.85 f_c' ba}{f_y}$$

$$\Rightarrow A_s = \frac{0.85\times 7\times 40\times 3.23}{60}$$

Therefore $A_s = 12.8$ in^2

Provide ten #10 bars as longitudinal tension steel (total area = 12.70 in.^{2} ~ 12.8 in.^{2})

Assuming the critical section of the beam in shear to be at a distance d from the support,

Shear force at critical section of the beam $V_u = \left(\frac{w_u l}{2} - w_u d\right) = \left(\frac{18\times 25}{2} - 18\times\frac{26}{12}\right) = 186$ kips

Maximum shear capacity of the beam, $V_{u,max} = \phi 10\sqrt{f_c'}\, b_w d = 0.75\times 10\times\sqrt{7{,}000}\times 15\times 26$

$= 244.7$ kips > 186 kips (ok)

Given cross section is sufficient to resist shear.

The amount of steel required at the critical section of the beam has been shown below.

Factored shear force at the section, $V_u = \left(\frac{w_u l}{2} - w_u x\right) = \left(\frac{18\times 25}{2} - 18\times\frac{26}{12}\right) = 186$ kips

Factored moment at the section, $M_u = \left(\frac{w_u l}{2}x - \frac{w_u x^2}{2}\right) = \left(\frac{18\times 25}{2}\times\frac{26}{12} - \frac{18\times\left(\frac{26}{12}\right)^2}{2}\right)$

$= 445.3$ kip-ft

$$\frac{V_u d}{M_u} = \frac{186\times 26}{445.3\times 12} = 0.905$$

$$V_c = 14 K_r \left(\frac{V_u d}{M_u}\right)^{0.7}\sqrt{f_c'}\, b_w d = 14\times 0.4\times 0.905^{0.7}\times\sqrt{7{,}000}\times 15\times 26 = 170.4 \text{ kips}$$

Maximum concrete shear capacity of the beam, $V_{c,max} = 4\sqrt{f_c'}\, b_w d = 4\times\sqrt{7000}\times 15\times 26$

$= 130.5$ kips < 170.4 kips

$V_s = V_u/\phi - V_c = 186/0.75 - 130.5 = 117.5$ kips

Using two-legged #5 rebars ($A_v = 0.62$ in^2) as shear reinforcement, the spacing required to provide the required V_s has been calculated using Eq. 8.2-9.

$$V_s = A_v f_y \left(\frac{d}{s} - 1\right)$$

$$\Rightarrow s = \frac{d}{\left(\frac{V_s}{A_v f_y} + 1\right)} = \frac{26}{\left(\frac{117.5}{0.62 \times 60} + 1\right)} = 6.3 \text{ in.}$$

$s_{max} = 0.5d = 13$ in.

Provide two-legged #5 rebars @ 6 in. c/c

The amount of steel required at a section of the beam 10 ft from the support has been calculated.

Factored shear force at the section, $V_u = \left(\frac{w_u l}{2} - w_u x\right) = \left(\frac{18 \times 25}{2} - 18 \times 10\right) = 45$ kips

Factored moment at the section, $M_u = \left(\frac{w_u l}{2} x - \frac{w_u x^2}{2}\right) = \left(\frac{18 \times 25}{2} \times 10 - \frac{18 \times 10^2}{2}\right) = 1350$ kip-ft

$$\frac{V_u d}{M_u} = \frac{45 \times 26}{1350 \times 12} = 0.072$$

$$V_c = 14 K_r \left(\frac{V_u d}{M_u}\right)^{0.7} \sqrt{f_c'} b_w d = 14 \times 0.4 \times 0.072^{0.7} \times \sqrt{7{,}000} \times 15 \times 26 = 29.0 \text{ kips}$$

Maximum concrete shear capacity of the beam, $V_{c,max} = 4\sqrt{f_c'} b_w d = 4 \times \sqrt{7000} \times 15 \times 26$

$= 130.5$ kips > 29.0 kips (ok)

$V_s = V_u/\phi - V_c = 45/0.75 - 29.0 = 31.0$ kips

Using two-legged #5 rebars ($A_v = 0.62$ in^2) as shear reinforcement, the spacing required to provide the required V_s has been calculated using Eq. 8.2-9.

$$V_s = A_v f_y \left(\frac{d}{s} - 1\right)$$

$$\Rightarrow s = \frac{d}{\left(\frac{V_s}{A_v f_y} + 1\right)} = \frac{26}{\left(\frac{31.0}{0.62 \times 60} + 1\right)} = 14.2 \text{ in.}$$

$s_{max} = 0.5d = 13$ in.

Provide 2 legged #5 rebars @ 13 in. c/c.

Table 9.4.1 shows the design of the beam over half span of the beam.

Observations: Comparing prestressed beam (Example 1 in Section 9.3) to non-prestressed beam (Example in Section 9.4), the amount of transverse steel required for a 24 ft prestressed beam with 6 in. wide web, carrying a load of 24 kips/ft is lower than the amount of transverse steel required for the non-prestressed beam with a 15 in. wide web carrying a load of 18 kips/ft and having a span of 25 ft. This is because the concrete contribution to shear is much higher in the case of a prestressed beam.

Table 9.4.1 Design of Non-Prestressed Beam

x (ft)	**V_u (kips)**	**M_u (kip-ft)**	$\frac{V_u d}{M_u}$	**V_c (kips)**	**V_s (kips)**	**s (#5) (in)**	**s_{prov} (in)**
d=2.17	186	445.3	0.905	130.5	117.5	6.3	6
3	171	594	0.624	130.5	97.5	7.2	6
4	153	756	0.438	102.6	101.4	7.0	6
5	135	900	0.325	83.2	96.8	7.2	6
6	117	1026	0.247	68.7	87.3	7.8	6
7	99	1134	0.189	57.0	75.0	8.6	6
8	81	1224	0.143	46.9	61.1	9.8	9
9	63	1296	0.105	37.8	46.2	11.6	9
10	45	1350	0.072	29.0	31,0	14.2	13
11	27	1386	0.042	19.9	16.1	18.2	13
12	9	1404	0.014	9.2	2.8	24.2	13
12.5	0	1406.25	0	-	-	-	13

CHAPTER 10

CONCLUSIONS AND SUGGESTIONS

10.1 Conclusions

The purpose of this research is to study the behavior of prestressed concrete elements and beams under shear and to finally develop a simplified equation for the shear design of prestressed concrete girders. The following conclusions are made from this research:

(1) The Softened Membrane Model for Prestressed Concrete (SMM-PC) is presented in this research as an analytical model to predict shear behavior of prestressed concrete elements. The SMM-PC is an extension of the SMM developed at the University of Houston (Hsu and Zhu, 2002; Zhu, 2000; Zhu and Hsu, 2002). This new model is applicable to reinforced and prestressed concrete, with any ratio of longitudinal steel to transverse steel, and in any orientation of steel reinforcement with respect to the applied principal stresses. Although this model was verified for application to concrete of normal strength (42 MPa) in this research project, future research is likely to prove that it is also applicable to high-strength concrete up to 100 MPa.

(2) To implement the new model SMM-PC, new constitutive laws are established for prestressed concrete under sequential and proportional loading. The constitutive laws of concrete in tension include the decompression load stage.

(3) Prestress causes a 15% increase of concrete compressive strength under sequential loading. In the case of proportional loading, a prestress factor W_p is proposed for incorporation into the softening coefficient of prestressed concrete. W_p is expressed in terms of the deviation angle β, and takes care of the effect of prestress on concrete compressive strength.

(4) The constitutive laws of prestressing strands embedded in concrete are obtained. Compared to bare prestressing strands, the smeared (average) stress-strain relationships of prestressing strands has a lower ultimate strength, a lower elastic limit, and a knee region of smaller curvature.

(5) A post-tensioning system was developed for seven-wire strands to simulate the bond condition of pre-tensioning strands. A system of self-compacting concrete grout (SCCG) in flexible conduits was developed to create the same crack patterns in post-tensioned concrete as those in pre-tensioned concrete.

(6) The shear behavior of prestressed concrete beams was critically examined by full-scale tests on five TXDOT Type-A beams with web shear or flexural shear failure

(7) Using the constitutive laws developed in this research, an analytical model is developed to calculate the ultimate shear capacity of the prestressed concrete beams. Using this model, ultimate capacities of beams can be calculated corresponding to given angles of failure planes.

(8) A new design equation is developed using the results of the beam tests performed in this research as well as test results from other tests available in literature. Four design examples are shown to illustrate the use of the developed design equation for prestressed girders.

(9) The new design equation is extended to include non-prestressed girders, and a design example for the same is also prepared.

10.2 Suggestions

Future research in this area are suggested as follows:

(1) Whereas the prestressed concrete panels were subjected to pure shear in this research, future research is desired to study the effect of normal stresses on the shear strength of elements. The Universal Panel Tester can be used to apply a combination of normal and shear stresses to prestressed concrete panels.

(2) Because high-strength concrete is widely used in prestressed concrete construction, the application of the SMM-PC model to high-strength prestressed concrete elements needs to be validated.

(3) Finite element programs should be developed based on the SMM-PC model to predict the behavior of whole prestressed concrete structures.

REFERENCES

AASHTO (2004), "AASHTO LRFD Bridge Design Specifications," 1998, (also 1999 and 2000 Interim Revisions), American Association of State Highway and Transportation Officials (AASHTO), Washington, D. C.

ACI Committee 318 (2005), "Building Code Requirements for Structural Concrete (ACI 318-02) and Commentary (ACI 318R-02)," American Concrete Institute, Farmington Hills, MI.

Ayoub, Amir and Filippou, Filip C. (1998), "Nonlinear Finite-Element Analysis of RC Shear Panels and Walls," *Journal of Structural Engineering*, ASCE, Vol. 124, No. 3, Mar. 1998, pp. 298-308.

Balakrishnan, S. and Murray, D. W. (1988a), "Concrete Constitutive Model for NLFE Analysis of Structures," *Journal of Structural Engineering*, ASCE, Vol. 114, No. 7, July 1988, pp. 1449-1466.

Balakrishnan, S. and Murray, D. W. (1988b), "Strength of Reinforced Concrete Panels," *Canadian Journal of Civil Engineering*, Vol. 15, No. 5, Oct. 1988, pp. 900-911.

Balakrishnan, S. and Murray, D. W. (1988c), "Prediction of R/C Panels and Deep Beam Behavior by NLFEA," *Journal of Structural Engineering*, ASCE, Vol. 114, No. 10, Oct. 1988, pp. 2323-2342.

Belarbi, A. and Hsu, T. T. C. (1994), "Constitutive Laws of Concrete in Tension and Reinforcing Bars Stiffened by Concrete," *Structural Journal of the American Concrete Institute*, Vol. 91, No. 4, pp. 465-474.

Belarbi, A. and Hsu, T. T. C. (1995), "Constitutive Laws of Softened Concrete in Biaxial Tension-Compression," *Structural Journal of the American Concrete Institute*, Vol. 92, No. 5, pp. 562-573.

Belletti, B., Cerioni, R., and Iori, I. (2001), "Physical Approach for Reinforced-Concrete (PARC) Membrane Elements," *Journal of Structural Engineering*, ASCE, Vol. 127, No. 12, Dec. 2001, pp. 1412-1426.

Bhide, B. S. and Collins, M. P. (1989), "Influence of Axial Tension on Shear Capacity of Reinforced Concrete Members," *ACI Structural Journal*, Vol. 86, No. 5, pp. 570-580.

Carreira, D. J. and Chu, K. H. (1986), "Stress-Strain Relationship of Reinforced Concrete in Tension," *Journal of the American Concrete Institute*, Vol. 83, No. 1, Jan.-Feb. 1986, pp. 21-28.

Chintrakarn, R. (2001), "Minimum Shear Steel and Failure Modes Diagram of Reinforced Concrete Membrane Elements," *Master's Thesis*, Department of Civil and Environmental Engineering, University of Houston, Houston, TX.

Collins, M. P., Vecchio, F. J., and Mehlhorn, G. (1985), "An International Competition to Predict the Response of Reinforced Concrete Panels," *Canadian Journal of Civil Engineering*, Ottawa, Vol. 12, No. 3, pp. 626-644.

Crisfield, Michael A. and Wills, John (1989), "Analysis of R/C Panels Using Different Concrete Models," *Journal of Engineering Mechanics*, ASCE, Vol. 115, No. 3, Mar. 1989, pp. 578-597.

Elzanaty, Ashraf H., Nilson, Arthur H., and Slate, Floyd O. (1986), "Shear Capacity of Prestressed Concrete Beams Using High Strength Concrete," *ACI Journal*, Vol. 83, No. 3, May-June 1986, pp. 359-368.

Fenves, G. L. (2001), "Annual Workshop on Open System for Earthquake Engineering Simulation," Pacific Earthquake Engineering Research Center, UC Berkeley, http://opensees.berkeley.edu/.

Foster, Stephen J. and Marti, Peter (2003), "Cracked Membrane Model: Finite Element Implementation," *Journal of Structural Engineering*, ASCE, Vol. 129, No. 9, Sept. 2003, pp. 1155-1163.

Freyssinet, E. (1956), "The Birth of Prestressing," *Cement and Concrete Association Translation No. 29*, London.

Gere, James M. and Timoshenko, Stephen P. (1991), *Mechanics of Materials*, Chapman and Hall, London, UK, 807 pp.

Hsu, T. T. C. (1993), *Unified Theory of Reinforced Concrete*, CRC Press, Inc., Boca Raton, FL, 336 pp.

Hsu, T. T. C. (1998), "Stresses and Crack Angles in Concrete Membrane Elements," *Journal of Structural Engineering*, ASCE, Vol. 124, No. 12, Dec. 1998, pp. 1476-1484.

Hsu, T. T. C. (2002), "Rational Shear Design of Reinforced Concrete Bridges," Presented at ACI 343/445 Session "Concrete Bridges in Shear," ACI Fall Convention, Phoenix, AZ, Oct. 27 – Nov. 1, 2002.

Hsu, T. T. C., Belarbi, A., and Pang, X. B. (1995), "A Universal Panel Tester," *Journal of Testing and Evaluations*, ASTM, Vol. 23, No. 1, pp. 41-49.

Hsu, T. T. C. and Zhang, L. X. (1996), "Tension Stiffening in Reinforced Concrete Membrane Elements," *Structural Journal of the American Concrete Institute*, Vol. 93, No. 1, pp. 108-115.

Hsu, T. T. C. and Zhang, L. X. (1997), "Nonlinear Analysis of Membrane Elements by Fixed-Angle Softened-Truss Model," *Structural Journal of the American Concrete Institute*, Vol. 94, No. 5, pp. 483-492.

Hsu, T. T. C. and Zhu, R. R. H. (2002), "Softened Membrane Model for Reinforced Concrete Elements in Shear," *Structural Journal of the American Concrete Institute*, Vol. 99, No. 4, pp. 460-469.

Kaufmann, Walter and Marti, Peter (1998), "Structural Concrete: Cracked Membrane Model," *Journal of Structural Engineering*, Vol. 124, No. 12, Dec. 1998, pp. 1467-1475.

Loov, R. E. (1978), "Design of Precast Connections," Paper presented at a *seminar* organized by Compa International Pte, Ltd., September 25-27, Singapore, pp. 8.

Loov, R. E. (1997), "The Direct Computation of Stirrup Spacing Based on Shear-Friction," Symposium on *Advanced Design of Concrete Structures*, Chalmers University of Technology, Goteborg, June 12-14.

Loov, R. E. (2002), "Shear Design of Uniformly Loaded Beams," Presented at *the Sixth International Conference on Short and Medium Span Bridges*, Vancouver, Canada, July 31 – August 2, 2002.

Lyngberg, Bent S. (1976), "Ultimate Shear Resistance of Partially Prestressed Reinforced Concrete I-Beams," *ACI Journal*, Vol. 73, No. 4, April 1976, pp. 214-222.

Mansour, M. (2001), "Behavior of Reinforced Concrete Membrane Elements under Cyclic Shear: Experiments to Theory," *Ph.D. Dissertation*, Department of Civil and Environmental Engineering, University of Houston, Houston, TX.

Mansour, M. and Hsu, T. T. C. (2005a), "Behavior of Reinforced Concrete Elements under Cyclic Shear: Part 1 – Experiments," *Journal of Structural Engineering*, ASCE, Vol. 131, No. 1, January, 2005, pp. 44-53.

Mansour, M. and Hsu, T. T. C. (2005b), "Behavior of Reinforced Concrete Elements under Cyclic Shear: Part 2-Theoretical Model," *Journal of Structural Engineering*, ASCE, Vol. 131, No. 1, January 2005, pp. 54-65.

Marti, P. and Meyboom, J. (1992), "Response of Prestressed Concrete Elements to In-plane Shear Forces," *ACI Structural Journal*, Vol. 89, No. 5, Sept.-Oct. 1992, pp. 503-514.

Meyboom, J. (1987), "An Experimental Investigation of Partially Prestressed, Orthogonally Reinforced Concrete Elements Subjected to Membrane Shear," *Thesis*, Department of Civil Engineering, University of Toronto, Toronto, Canada.

Morsch, E. (1902), "Der Eisenbetonbau, seine Anwendung und Theorie," Wayss and Freytag, A.G., Im Selbstverlag der Firma, Neustadt, A.D. Haardt, May 1902, pp. 118.

Nawy, E. G. (1985), *Reinforced Concrete: A Fundamental Approach*, Prentice-Hall Press, Inc., Englewood Cliffs, NJ, 701 pp.

Pang, X. B. (1991), "Constitutive Laws of Reinforced Concrete in Shear," *Ph.D. Dissertation*, Department of Civil and Environmental Engineering, University of Houston, Houston, TX.

Pang, X. B. and Hsu, T. T. C. (1995), "Behavior of Reinforced Concrete Membrane Elements in Shear," *Structural Journal of the American Concrete Institute*, Vol. 92, No. 6, pp. 665-679.

Pang, X. B. and Hsu, T. T. C. (1996), "Fixed-Angle Softened-Truss Model for Reinforced Concrete," *Structural Journal of the American Concrete Institute*, Vol. 93, No. 2, pp. 197-207.

Rahal, K. N. (2002), "Membrane Elements Subjected to In-plane Shearing and Normal Stresses," *Journal of Structural Engineering*, ASCE, Vol. 128, No. 8, August 2002, pp. 1064-1072.

Rangan, B. Vijaya (1991), "Web Crushing Strength of Reinforced and Prestressed Concrete Beams," *ACI Structural Journal*, Vol. 88, No. 1, Jan.-Feb. 1991, pp. 12-16.

Ritter, W. (1899), " Die Bauweise Hennebique," Schweizerische Bauzeitung, Vol.33, No. 5, 6, and 7, Zurich, pp. 41-43, 49-52, and 59-61.

Robinson, J. R. and Demorieux, J. M. (1968), "Essai de Traction-Compression sur Modeles d'Ames de Poutre en Beton Arme," Compte Rendu Partiel I, U.T.I., Institut de Recherches Appliquees du Beton Arme, Paris, France, 43 pp.

Tamai, S., Shima, H., Izumo, J., and Okamura, H. (1987), "Average Stress-Strain Relationship in Post Yield Range of Steel Bar in Concrete," *Concrete Library of JSCE*, No. 11, June 1988, pp.117-129. (Translating from *Proceeding of JSCE*, No. 378/V-6, Feb. 1987.)

Vecchio, F. J. (1990), "Reinforced Concrete Membrane Element Formulation," *Journal of Structural Engineering*, ASCE, Vol. 116, No. 3, pp. 730-750.

Vecchio, F. J. (2000), "Disturbed Stress Field Model for Reinforced Concrete: Formulation," *Journal of Structural Engineering*, ASCE, Vol. 126, No. 9, Sept. 2000, pp. 1070-1077.

Vecchio, F. J. (2001a), "Disturbed Stress Field Model for Reinforced Concrete: Implementation," *Journal of Structural Engineering*, ASCE, Vol. 127, No. 1, Jan. 2001, pp. 12-20.

Vecchio, F. J. and Collins, M. P. (1981), "Stress-Strain Characteristic of Reinforced Concrete in Pure Shear," IABSE Colloquium, Advanced Mechanics of Reinforced Concrete, Delft, *Final Report*, International Association of Bridge and Structural Engineering, Zurich, Switzerland, pp. 221-225.

Vecchio, F. J. and Collins, M. P. (1982), "Response of Reinforced Concrete to In Plane Shear and Normal Stresses," *Report*, No. 82-03, University of Toronto, Toronto, Canada.

Vecchio, F. J. and Collins, M. P. (1986), "The Modified Compression Field Theory for Reinforced Concrete Elements Subjected to Shear," *ACI Journal*, Vol. 83, No. 2, pp. 219-231.

Vecchio, F. J., Lai, D., Sim, W., and Ng, J. (2001), "Disturbed Stress Field Model for Reinforced Concrete: Validation," *Journal of Structural Engineering*, ASCE, Vol. 127, No. 4, April 2001, pp. 350-358.

Wang, J. (2006), "Constitutive Relationships of Prestressed Concrete Membrane Elements," *Ph.D. Dissertation*, Department of Civil and Environmental Engineering, University of Houston, Houston, TX.

Zhang, L. X. (1992), "Constitutive Laws of Reinforced Elements with Medium-High Strength Concrete," *Ph.D. Dissertation*, Department of Civil and Environmental Engineering, University of Houston, Houston, TX.

Zhang, L. X. and Hsu, T. T. C. (1998), "Behavior and Analysis of 100Mpa Concrete Membrane Elements," *Journal of Structural Engineering*, ASCE, Vol. 124, No. 1, Jan. 1998, pp. 24-34.

Zhong, J. X. (2005), "Model-Based Simulation of Reinforced Concrete Plane Stress Structures," *Ph.D. Dissertation*, Department of Civil and Environmental Engineering, University of Houston, Houston, TX.

Zhu, R. R. H. (2000), "Softened-Membrane Model for Cracked Reinforced Concrete Considering Poisson Effect," *Ph.D. Dissertation*, Department of Civil and Environmental Engineering, University of Houston, Houston, TX.

Zhu, R. H., Hsu, T. T. C., and Lee, J. Y. (2001), "Rational Shear Modulus for Smeared Crack Analysis of Reinforced Concrete," *Structural Journal of the American Concrete Institute*, Vol. 98, No. 4, pp. 443-450.

Zhu, R. R. H., and Hsu, T. T. C. (2002), "Poisson Effect of Reinforced Concrete Membrane Elements," *Structural Journal of the American Concrete Institute*, Vol. 99, No. 5, pp. 631-640.

APPENDIX

Recommendations for Shear Design of Prestressed and Non-Prestressed Bridge Girders

A.1 Design Recommendations for Prestressed Beam

The step-by-step procedure involved for shear design of a prestressed concrete beam using the new design equation has been described below:

Step 1: Calculate the maximum bending moment, M_{max} acting on the beam. Provide the number of prestressing strands required to carry the bending moment by calculating the flexural capacity.

Step 2: Calculate the effective depth of the beam, d from the eccentricity of the arrangement of tendons finalized in **Step 1**.

Step 3: Calculate the maximum shear force, V_u acting at the critical section of the beam located at a distance d from the support.

Step 4: Check if the shear force at the critical section of the beam is greater than the maximum shear capacity of the beam given by Eq. A.1-1. If so, then increase the concrete strength or the size of the beam.

$$V_{u,\max} = \phi 16\sqrt{f_c'}b_w d \tag{A.1-1}$$

Step 5: Calculate the shear force, V_u and bending moment M_u at different sections over the span of the beam at intervals not exceeding $L_n/20$, where L_n is the span of the beam.

Step 6: Calculate shear span to depth ratios $\frac{M_u}{V_u d}$ for different design sections.

Step 7: Calculate the concrete contribution to shear capacity of the different sections, V_c using Eq. A.1-2.

$$V_c = 14\left(\frac{V_u d}{M_u}\right)^{0.7}\sqrt{f_c'}b_w d < 10\sqrt{f_c'}b_w d \tag{A.1-2}$$

Step 8: Calculate the amount of shear force to be carried by steel at different sections, V_s using Eq. A.1-3.

$$V_s = V_u/\phi - V_c \tag{A.1-3}$$

Step 9: For selected sizes of stirrup having cross-sectional area A_v, find the spacing of stirrups required at different design sections using Eq. A.1-4.

$$s = \frac{d}{\left(\frac{V_s}{A_v f_y} + 1\right)} \tag{A.1-4}$$

A design problem has been solved below to illustrate the various steps described above:

Design Problem TXDOT Type-A girders spaced at 8.67 ft c/c and supporting a 30 ft wide and 8 in. thick deck slab are designed. The step-by-step design procedure of a typical girder described above, using the new design equation, has been shown below.

The values of various quantities required for design are as follows:

h = 28 in.	b_w = 6 in.	L_n = 24 ft	f_c' = 10 ksi
f_y = 60 ksi	A_v = 0.62 in.^{2}	d_{bv} = 5/8 in.	w_u = 24 kips/ft

d = 22.33 + 0.8 = 23.13 in.

Step 1:

Maximum moment on the girder, $M_u/\phi = \frac{1}{\phi}\frac{w_u l^2}{8} = \frac{24 \times 24^2}{0.9 \times 8} = 1920$ kip-ft

As per calculations for flexural capacities of prestressed concrete girders, provide 18 ½-in. low relaxation strands.

Step 2:

Distance of cg of beam cross section from top fiber = 15.41 in.
Eccentricity of tendons from cg = 8.39 in.
Thickness of deck slab = 8 in.
d = 15.41 + 8.39 + 8 = 31.8 in.

Step 3:

Assuming the critical section of the beam in shear to be at a distance d from the support,

Shear force at critical section of the beam $V_u = \left(\frac{w_u l}{2} - w_u d\right) = \left(\frac{24 \times 24}{2} - 24 \times \frac{31.8}{12}\right) = 224.4$ kips

Step 4:

Maximum shear capacity of the beam, $V_{u,max} = \phi 16\sqrt{f_c'}\, b_w d = 0.75 \times 16 \times \sqrt{10{,}000} \times 6 \times 31.8$

= 229.0 kips > 224.4 kips (ok)

Given cross section is sufficient to resist shear.

The amount of steel required at the critical section of the beam has been shown below.

Step 5:

Factored shear force at the section, $V_u = \left(\frac{w_u l}{2} - w_u x\right) = \left(\frac{24 \times 24}{2} - 24 \times \frac{31.8}{12}\right) = 224.4$ kips

Factored moment at the section, $M_u = \left(\frac{w_u l}{2} x - \frac{w_u x^2}{2}\right) = \left(\frac{24 \times 24}{2} \times \frac{31.8}{12} - \frac{24 \times \left(\frac{31.8}{12}\right)^2}{2}\right)$

= 678.9 kip-ft

Step 6:

$\frac{V_u d}{M_u} = \frac{224.4 \times 31.8}{678.9 \times 12} = 0.876$

Step 7:

$V_c = 14\left(\frac{V_u d}{M_u}\right)^{0.7} \sqrt{f_c'}\, b_w d = 14 \times 0.876^{0.7} \times \sqrt{10{,}000} \times 6 \times 31.8 =$ **219.9** kips

Maximum concrete shear capacity of the beam, $V_{c,max} = 10\sqrt{f_c'}\, b_w d = 10 \times \sqrt{10{,}000} \times 6 \times 31.8$

= 190.8 kips < 219.9 kips

Step 8:

$V_s = V_u/\phi - V_c = 224.4/0.75 - 190.8 = 108.4$ kips

Step 9:

Using two-legged #5 rebars (A_v = 0.62 in^2) as shear reinforcement, the spacing required to provide the required V_s has been calculated using Eq. 8.2-9.

$$V_s = A_v f_y \left(\frac{d}{s} - 1\right)$$

$$\Rightarrow s = \frac{d}{\left(\frac{V_s}{A_v f_y} + 1\right)} = \frac{31.8}{\left(\frac{108.4}{0.62 \times 60} + 1\right)} = 8.1 \text{ in.}$$

Provide two-legged #5 rebars @ 8 in. c/c.

Table A.1 shows the design of the beam over half span of the beam. It can be seen that the spacing of the two-legged #5 rebars is 8 in. c/c upto a distance 7 ft from the support. At 8 ft from the support, the spacing is increased to 13 in. c/c.

Table A.1 Prestressed Beam Design

x (ft)	**V_u (kips)**	**M_u (kip-ft)**	$\frac{V_u d}{M_u}$	**V_c (kips)**	**V_s (kips)**	**s (#5) (in)**	**s_{prov} (in)**
d=2.65	224.4	678.9	0.876	190.8	108.4	8.1	8
3	216	756	0.757	190.8	97.2	8.8	8
4	192	960	0.530	171.3	84.7	9.7	8
5	168	1140	0.391	138.3	85.7	9.6	8
6	144	1296	0.294	113.5	78.5	10.2	8
7	120	1428	0.223	93.3	66.7	11.4	8
8	96	1536	0.166	75.9	52.1	13.2	13
9	72	1620	0.118	59.8	36.2	16.1	13
10	48	1680	0.076	43.9	20.1	20.6	13
11	24	1680	0.037	26.6	5.4	27.8	13
12	0	1716	-	-	-	-	13

A.2 Design Recommendation for Non-Prestressed Beam

A unified shear design method is proposed for both prestressed and non-prestressed beams. The primary difference between these two types of beams lies in the concrete contribution V_c. A generalized V_c can be expressed as follows:

$$V_c = 14 K_r \left(\frac{V_u d}{M_u}\right) \sqrt{f_c'} b_w d \qquad \text{(A.2-1)}$$

where

K_r = prestress factor. K_r is taken as unity (1) for beams with effective prestress force not less than 40 percent of the tensile strength of flexural reinforcement. K_r will be taken as 0.4 for non-prestressed beams.

The step-by-step procedure to design a non-prestressed beam using the new design equation has been described below:

Step 1: Calculate the maximum bending moment M_{max} acting on the beam. Calculate the amount of longitudinal tension steel required to carry this moment.

Step 2: Calculate the maximum shear force, V_u acting at the critical section of the beam located at a distance d from the support.

Step 3: Check if the shear force at the critical section of the beam is greater than the maximum shear capacity of the beam given by Eq. A.1-1. If so then increase the concrete strength or the size of the beam.

$$V_{u,\max} = \phi 10\sqrt{f_c'}b_w d \tag{A.2-2}$$

Step 4: Calculate the shear force V_u and bending moment M_u at different sections over the span of the beam at intervals not exceeding $L_n/20$, where L_n is the span of the beam.

Step 5: Calculate shear span to depth ratios $\frac{V_u d}{M_u}$ for different design sections.

Step 6: Calculate the concrete contribution to shear capacity of the different sections V_c using Eq. A.2-3.

$$V_c = 14K_r\left(\frac{V_u d}{M_u}\right)^{0.7}\sqrt{f_c'}b_w d < 4\sqrt{f_c'}b_w d \tag{A.2-3}$$

Step 7: Calculate the amount of shear force to be carried by steel at different sections V_s using Eq. A.2-4.

$$V_s = V_u/\phi - V_c \tag{A.2-4}$$

Step 8: For selected sizes of stirrup having cross-sectional area A_v find the spacing of stirrups required at different design sections using Eq. A.2-5.

$$s = \frac{d}{\left(\frac{V_s}{A_v f_y} + 1\right)} \tag{A.2-5}$$

Design Problem An isolated T-beam has an effective span of 25 ft and carries a factored load of 18 kips/ft. Other properties of the beam are as follows:

h = 30 in. b_f = 40 in. h_f = 5 in.

b_w = 15 in. d = 26 in. f_c' = 7 ksi

f_y = 60 ksi

Step 1:

Maximum moment on the girder, $M_u/\phi = \frac{1}{\phi}\frac{w_u l^2}{8} = \frac{1}{0.9}\frac{18\times 25^2}{8} = 1562.5$ kip-ft

Using the compressive stress-strain relations given in the ACI Code (2005) and assuming the NA lies in the flange:

$0.85 f_c' b a\left(d - \frac{a}{2}\right) = M_u$,

where

a = depth over which the compressive stresses exist in the cross section.

Substituting the numerical values of all other parameter in the above equation, the value of *a* can be obtained:

$a = 3.23$ in.

Equating the compressive and steel forces we get:

$$A_s f_y = 0.85 f_c' b a$$

$$\Rightarrow A_s = \frac{0.85 f_c' b a}{f_y}$$

$$\Rightarrow A_s = \frac{0.85 \times 7 \times 40 \times 3.23}{60}$$

Therefore $A_s = 12.8$ in.^{2}

Provide ten #10 bars as longitudinal tension steel (total area = 12.70 in.^{2} ~ 12.8 in.^{2})

Step 2:

Assuming the critical section of the beam in shear to be at a distance d from the support,

Shear force at critical section of the beam $V_u = \left(\frac{w_u l}{2} - w_u d\right) = \left(\frac{18 \times 25}{2} - 18 \times \frac{26}{12}\right) = 186$ kips

Step 3:

Maximum shear capacity of the beam, $V_{u,max} = \phi 10 \sqrt{f_c'}\, b_w d = 0.75 \times 10 \times \sqrt{7{,}000} \times 15 \times 26$

= 244.7 kips > 186 kips (ok)

Given cross section is sufficient to resist shear.

Step 4:

The amount of steel required at the critical section of the beam has been shown below.

Factored shear force at the section, $V_u = \left(\frac{w_u l}{2} - w_u x\right) = \left(\frac{18 \times 25}{2} - 18 \times \frac{26}{12}\right) = 186$ kips

Factored moment at the section, $M_u = \left(\frac{w_u l}{2} x - \frac{w_u x^2}{2}\right) = \left(\frac{18 \times 25}{2} \times \frac{26}{12} - \frac{18 \times \left(\frac{26}{12}\right)^2}{2}\right)$

= 445.3 kip-ft

Step 5:

$$\frac{V_u d}{M_u} = \frac{186 \times 26}{445.3 \times 12} = 0.905$$

Step 6:

$$V_c = 14 K_r \left(\frac{V_u d}{M_u}\right)^{0.7} \sqrt{f_c'}\, b_w d = 14 \times 0.4 \times 0.905^{0.7} \times \sqrt{7{,}000} \times 15 \times 26 = 170.4 \text{ kips}$$

Maximum concrete shear capacity of the beam, $V_{c,max} = 4\sqrt{f_c'}\, b_w d = 4 \times \sqrt{7000} \times 15 \times 26$

= 130.5 kips < 170.4 kips

Step 7:

$V_s = V_u/\phi - V_c = 186/0.75 - 130.5 = 117.5$ kips

Step 8:

Using two-legged #5 rebars ($A_v = 0.62$ in^2) as shear reinforcement, the spacing required to provide the required V_s has been calculated using Eq. 8.2-9.

$$V_s = A_v f_y \left(\frac{d}{s} - 1\right)$$

$$\Rightarrow s = \frac{d}{\left(\frac{V_s}{A_v f_y} + 1\right)} = \frac{26}{\left(\frac{117.5}{0.62 \times 60} + 1\right)} = 6.3 \text{ in.}$$

$s_{max} = 0.5d = 13$ in.

Provide two-legged #5 rebars @ 6 in. c/c.

Table A-2 shows the design of the beam over half span of the beam.

Table A-2 Non-Prestressed Beam Design

x (ft)	**V_u (kips)**	**M_u (kip-ft)**	$\frac{V_u d}{M_u}$	**V_c (kips)**	**V_s (kips)**	**s (#5) (in)**	**s_{prov} (in)**
d=2.17	186	445.3	0.905	130.5	117.5	6.3	6
3	171	594	0.624	130.5	97.5	7.2	6
4	153	756	0.438	102.6	101.4	7.0	6
5	135	900	0.325	83.2	96.8	7.2	6
6	117	1026	0.247	68.7	87.3	7.8	6
7	99	1134	0.189	57.0	75.0	8.6	6
8	81	1224	0.143	46.9	61.1	9.8	9
9	63	1296	0.105	37.8	46.2	11.6	9
10	45	1350	0.072	29.0	31.0	14.2	13
11	27	1386	0.042	19.9	16.1	18.2	13
12	9	1404	0.014	9.2	2.8	24.2	13
12.5	0	1406.25	0	-	-	-	13